

DISS. ETH NO 23615

**Correlating Synthetic Protocols and Activity of
Lewis Acid β -Zeolites by Physicochemical Properties
and Active Site Structures**

A thesis submitted to attain the degree of

DOCTOR OF SCIENCES of ETH ZURICH

(Dr. sc. ETH Zurich)

presented by

PATRICK WOLF

M.Sc. Chem. Bio. Eng. ETH, ETH Zürich, Switzerland

born on 20.04.1989

citizen of Germany

accepted on the recommendation of

Prof. Dr. C. Copéret, examiner

Prof. Dr. I. Hermans, co-examiner

Prof. Dr. C. Müller, co-examiner

2016

“You miss 100 % of the shots you don’t take”

-Wayne Gretzky

Acknowledgments

The work presented in this thesis would not have been possible without the contributions of many great individuals. I would like to use this opportunity to express my sincere gratitude for their support in so many ways.

First and foremost, I would like to thank Prof. Dr. Ivo Hermans for giving me the opportunity to conduct my doctoral thesis in a unique research environment. In particular I would like to thank him for the exceptional research facilities and his excellent supervision, guidance and motivation. Ivo, I greatly appreciate all the efforts and time you invested in my academic and personal development. I am also very grateful that you gave me the chance to experience the American grad school life in the Midwest and, although it was related to a lot of work, being part of building up a lab from scratch. You give me a lifetime of unforgettable memory, full of advice, lessons learned, and invaluable experience.

Secondly, I would like to thank Prof. Dr. Christophe Copéret for kindly taking over the responsibility for me after the Hermans research group moved to Madison. His contagious enthusiasm for science has always been a great driving force for me. I'm very thankful for your unconditional support and excellent guidance throughout our collaboration over the last 2.5 years. Thank you for your excellent scientific input and for giving me the opportunity to finish my Ph.D. in your group.

Prof. Dr. Christophe Müller is kindly acknowledged for agreeing to act as co-examiner to my thesis.

Special thanks go to the DNP-NMR guys, Wei-Chi Liao, Dr. Ta-Chung Ong and in particular Dr. Maxence Valla and Prof. Dr. Aaron Rossini as well as the computational team Dr. Francisco Nuñez-Zarur and Dr. Aleix Comas-Vives. Without their contributions this thesis would not have been possible. Further, I want to kindly acknowledge my collaborator Dr. Anne Lesage, Prof. Dr. Bernard Malaman and Prof. Dr. Lyndon Emsley for their contribution.

The research in this thesis has also benefited from the support of a number of people who have helped me with logistical and technical issues throughout. As such, my thanks go to Jan Kovacovic, Andreas Dutly and Erol Dedeoglu (Zurich), as well as Kat Myhre, Kristi Heming, Mike Bradely, Jeff Nielsen and Steve Meyers (Madison).

I also want to thank my undergraduate students Lukas Langenegger, Bolis Vasco, Sven Linster (Zurich) and Hana Kallas, Megan Ewel, Justin Carrington (Madison). In particular I want to thank Connor Firth for his continuous help over two years.

Throughout the whole time the Hermans group always provided a very constructive, enjoyable, humorous and positive working atmosphere. Therefore I would like to thank the Hermans group at ETH (2012-2013), in particular Dr. Christof Aellig and Dr. Ceri Hammond who were very helpful in the beginning of my Ph.D. I also want to thank the Hermans group at UW Madison for making the time in Madison unforgettable. Over the last years I did not only meet a lot of great people, more important, I also won a lot of new friends from all over the world for which I am very grateful. Very special thanks go to Sabrina, my roommate in Madison and Phil. Sabrina, your cooking skills are amazing. Phil, thank you for all the scientific discussions we had and for your company in so many fun trips from Mt. Bohemia down south to Atlanta.

Last but not least, I would like to express my deepest gratitude to my family and friends who always supported me and believed in my goals. My ETH colleagues Sandro, Daniel, Nicolas, Fabian and Anna ... as well as Philipp, who brought some franconian home to Zürich. Stephanie, for her support and for sharing a lot of fun adventures during the last 6 months in Madison with me. I also would like to thank my friends and family from home, especially Issy, Schnuppi, Mare, Ali and Cedi who were very helpful in giving diversity to my life, thereby allowing me to recharge my batteries and return very motivated to university. My mom (Heidi), my dad (Udo) and Jasmin for their unconditional support and care, and for showing me day-by-day what is important. Without my family as my backbone I would not be at the point in life, where I am today. Thank you for everything. You are the best!

Table of Contents

Acknowledgements	iii
Table of Contents	v
Summary	vii
Zusammenfassung	xi
1 Introduction	1
2 Post-synthetic Preparation of Sn-, Zr-, Nb-, and Ti- β ; A Facile Route to Water-Tolerant, Highly Active Lewis Acid Zeolites	17
3 NMR Signatures of the Active Sites in Sn- β Zeolites	31
4 Correlating Synthetic Methods, Morphology, Atomic-Level Structure and Catalytic Activity of Sn- β Catalysts	41
5 Conclusions and Outlook	77
Bibliography	85
Appendix A Annexes	95
Appendix B List of Publications	155
Appendix C List of Presentations	157
Appendix D Curriculum Vitae	159

Summary

The dwindling supply of fossil resources and the emerging awareness of their polluting nature and environmental impact compels us to develop new sustainable routes for the production of value-added chemicals and fuels from renewable resources. Within this area, the utilization of biomass feedstocks into value-added chemicals shows high potential. However, due to the fundamentally different chemical composition of biomass feedstocks (20-50 % oxygen) compared to fossil resources, new technologies need to be developed. To do so, the design of catalytic systems that are able to valorize biomass-derived oxygenates in an atom-efficient way is key.

In this regard, Lewis acid doped zeolites have been explored because of their water-tolerant behavior and ability to efficiently activate carbonyl groups. Major breakthroughs in their development are the discovery of titanosilicate TS-1 and the synthesis of Lewis acid doped zeolite β in fluoride media. While TS-1 was already commercialized about 30 years ago, Lewis acid β -zeolites are still restricted to lab-scale applications. The main challenges to overcome are the intricate synthesis procedure and the lack of fundamental understanding about the nature of the active sites.

Typically these materials are prepared in lengthy hydrothermal crystallizations, which involve the use of toxic chemicals. Therefore, new, convenient synthesis protocols would be desirable to make this promising class of materials readily available. In Chapter 2 of this thesis we address the challenge to facilitate the synthesis of Lewis acid β -zeolites by applying a two-step post-synthesis approach. In this synthetic route Al is removed from commercially available Al- β zeolite by acid-leaching, resulting in the creation of vacant tetrahedral sites. In a second step, these vacant sites can be filled with a heteroatom *via* solid-state ion-exchange or impregnation. Compared to traditional methods, a 5 times higher heteroatom incorporation could be achieved. Postsynthetically synthesized Sn-, Zr-, Nb- and Ti- β zeolites are active catalysts in the intramolecular 1,2-hydride shift of glyceraldehyde to dihydroxyacetone and follow the reactivity order Sn>Zr>Ti>Nb. Ti- β and Nb- β also facilitate the epoxidation of bulky olefins with H₂O₂. Interestingly, Nb- β shows a 4 times higher catalytic activity than the typically used titanosilicate in this reaction. The synthesis strategy presented here shows high potential toward an industrial implementation.

Concerning the nature of the active sites in Lewis acid zeolites, many questions still exist. Several different potential active sites have been proposed in literature for Sn- β .

Thus, our fundamental aim in Chapter 3 was to determine the precise nature of the active sites in the post-synthetically prepared Sn- β zeolite. For this purpose, we picked a multidisciplinary approach consisting of material synthesis, catalytic testing, spectroscopic characterization and theory. A series of Sn- β with varying Sn loading (0.5-10 wt%) showed decreasing catalytic activity in the aqueous phase glucose isomerization, suggesting a difference in the active site speciation within these materials. ^{119}Sn Mössbauer spectroscopy experiments revealed that hexacoordinated Sn^{IV} centers with a distorted octahedral geometry are present independent of the loading. ^{119}Sn NMR spectroscopy and DFT calculations corroborate this finding and further provide structural information on the active sites in Sn- β on an atomic level. This structural information was derived from the chemical shift anisotropy parameter, which could be obtained in magic-angle turning experiments with the aid of dynamic nuclear polarization. A correlation of the experimental NMR parameters with computational predictions allowed us to create an atomic-level structure for each of the active sites present. In agreement with literature hypotheses, the presence of the two proposed active sites, *i.e.* closed and open sites, were shown for the first time based on direct spectroscopic evidence.

In Chapter 4 of this thesis, we want to address how different synthetic protocols of Sn- β affect the physicochemical properties and the active site speciation of the resulting materials and correlate these features with catalytic activities. Accordingly, Sn- β zeolites were prepared *via* different synthesis protocols and tested in the aqueous phase isomerization of glucose to fructose. For post-synthetic materials prepared *via* solid-state ion-exchange, a 2-5 times lower activity per Sn compared to traditional hydrothermal Sn- β was observed suggesting a fundamental difference in these materials. ^{29}Si NMR, X-ray diffraction and water adsorption isotherms show that post-synthetic materials possess a hydrophilic, defective framework, which mainly cause the lower activity. This applies to post-synthetic materials, unless the parent Al- β zeolite is prepared in fluoride media and all silanol vacancies are filled with Sn. In this case a highly hydrophobic framework with little or no defects is obtained, resulting in high activity. However, the post-synthetic hydrophobic material is still less active by a factor of 2 compared to the hydrothermal Sn- β 's. Since the physicochemical properties of these materials are almost identical, a difference in accessibility of the Sn-sites and/or the local geometry of the active site is hypothesized to cause the difference in activity. In addition to the two configurations of open and closed sites identified in Chapter 3,

we also aim to address the exact location of the Sn atom within the zeolite lattice. Therefore, we extended the previously developed methodology for the active site determination and calculated the NMR parameter for the Sn sites at different degrees of hydration from fully dehydrated to triply hydrated sites for all 9 different T-sites. Correlation of the ^{119}Sn chemical shift for the dehydrated and hydrated state provides a NMR signature map. Together with the experimentally determined NMR parameters for different Sn- β samples, which were measured in both their hydrated and dehydrated state, we were able to identify the dominant active sites. For highly active hydrothermal Sn- β zeolites, mainly closed sites in T6 and T5/T7 were determined. The less active post-synthetic materials most likely consist of closed T8, hydrolyzed-open T5 sites and also some T9 defect-open sites. We conclude from this that a high hydrophobicity with accessible Sn sites in T6 and/or T5/T7 position are important for high activity in the aqueous phase isomerization of glucose to fructose. This study demonstrates that the morphology and the distribution of the active sites of Lewis acid β -zeolites are highly dependent on the synthetic protocol employed.

Overall, this thesis presents significant developments toward a rationale for the design of Lewis acid doped zeolites, with a focus set on Sn- β . As such, we describe a robust and versatile synthesis procedure to tailor the physicochemical properties of Lewis acid β -zeolites. Further, we provide a NMR signature map of various Sn sites that allows for the determination of the active site distribution in terms of nature and lattice position of the Sn centers in Sn- β zeolites. Ultimately, this enables us to systematically investigate the influence of synthetic parameters with respect to the formation of specific sites and to rationally optimize the synthesis protocols toward the formation of the desired active sites.

Zusammenfassung

Hervorgerufen durch die schwindenden Reserven an fossilen Brennstoffen und dem zunehmenden Bewusstsein ihrer umweltbelastenden Wirkung herrscht ein dringendes Verlangen zur Entwicklung nachhaltiger Prozesse für die Herstellung von hochwertigen Chemikalien und Treibstoffen aus erneuerbaren Energien. Großes Potenzial zeigt insbesondere die Nutzung von Biomasse als Rohstoff für wertschöpfende Chemikalien. Aufgrund der grundlegend verschiedenen chemischen Zusammensetzung von Biomasse (20-50% Sauerstoff) im Vergleich zu fossilen Brennstoffen bedarf es der Entwicklung von neuen Technologien. Schlüssel hierzu sind neue katalytische Systeme, welche die Aufwertung von aus Biomasse gewonnenen sauerstoffhaltigen Verbindungen auf atomeffiziente Weise ermöglichen.

Wegen ihrer Fähigkeit Carbonylgruppen wirkungsvoll zu aktivieren und ihrer Kompatibilität mit Wasser, wurden überwiegend Lewis saure Zeolithe in diesem Zusammenhang verwendet. Bedeutende Meilensteine in deren Geschichte stellen die Entdeckung des Titansilikats TS-1 und die Synthese Lewis saurer β Zeolithe in fluoridhaltigem Medium dar. Während TS-1 schon vor ungefähr 30 Jahren kommerzialisiert wurde, sind Lewis saure β Zeolithe noch auf Anwendungen im Labormaßstab beschränkt. Die wesentlichen Probleme, die es hierbei zu bewältigen gilt sind die aufwendige und komplizierte Synthese sowie das fehlende grundlegende Verständnis über die Beschaffenheit des aktiven Zentrums.

In der Regel werden solche Materialien in zeitintensiven hydrothermalen Kristallisationen unter Verwendung toxischer Chemikalien hergestellt. Deshalb sind neue, praktische Herstellungsverfahren wünschenswert, die Lewis saure β Zeolithe einfach zugänglich machen. In Kapitel 2 dieser Dissertation befassen wir uns mit den Problemen während der Synthese solcher Katalysatoren indem wir einen zweistufigen postsynthetischen Ansatz zur Herstellung von Lewis sauren β Zeolithen wählen. Ausgehend von kommerziell verfügbaren Al- β Zeolithen kreieren wir durch Entfernung des Al mit Säure unbesetzte tetraedrische Zentren, welche im zweiten Schritt durch Ionenaustausch im festen Zustand oder Imprägnierung mit Heteroatomen gefüllt werden. Verglichen zur konventionellen hydrothermalen Synthese können auf diese Weise die 5 fache Menge an Heteroatomen inkorporiert werden. Die so hergestellten Sn-, Zr-, Nb-, und Ti- β Zeolithe katalysieren die intramolekulare Verlagerung von Wasserstoff in der Isomerisierung von Glycerinaldehyd zu Dihydroxyaceton und folgen der

Reaktivitätsordnung $\text{Sn} > \text{Zr} > \text{Ti} > \text{Nb}$. $\text{Ti-}\beta$ und $\text{Nb-}\beta$ ermöglichen darüber hinaus die Epoxidierung von sperrigen Olefinen mit Wasserstoffperoxid. Interessanterweise zeigte $\text{Nb-}\beta$ in dieser Reaktion eine 4 mal höhere Aktivität als das gewöhnlich verwendete Titansilikat. Die präsentierte Strategie zur Synthese zeigt viel Potenzial für eine mögliche industrielle Realisierung von Lewis sauren β -Zeolithen.

In Bezug auf die Beschaffenheit der aktiven Zentren bestehen noch einige offene Fragen. Für den $\text{Sn-}\beta$ Zeolith wurden viele mögliche Modelle für das aktive Zentrum in der Literatur vorgeschlagen. Aufgrund dessen haben wir uns das fundamentale Ziel gesetzt die genaue Struktur der aktiven Zentren in postsynthetischem $\text{Sn-}\beta$ zu bestimmen (Kapitel 3). Hierzu verwenden wir einen multidisziplinären Ansatz, welcher Materialsynthese und katalytische Tests mit der Charakterisierung durch Spektroskopie und Theorie kombiniert. Eine Reihe von $\text{Sn-}\beta$ Katalysatoren mit verschiedener Beladung an Sn (0,5-10 Gew.-%) ergaben unterschiedliche Aktivitäten in der Glukoseisomerisierung in Wasser, was auf einen Unterschied in der Beschaffenheit und/oder Verteilung der aktiven Zentren hinweist. Unabhängig von der Beladung fanden wir durch ^{119}Sn Mössbauer Spektroskopie hexakoordinierten Sn^{IV} Zentren mit verzerrter oktaedrischer Geometrie. Dies wurde mit Hilfe von ^{119}Sn NMR Spektroskopie und DFT Berechnungen bestätigt, welche zusätzliche Strukturinformationen auf atomarer Ebene lieferten. Die Strukturinformation des geprobten Kerns wurde den Parametern der chemischen Verschiebungsanisotropie entnommen, welche mittels dynamischer Kernpolarisation in Experimenten mit Drehung um den magischen Winkel (MAT) bestimmt wurden. Korrelation von experimentellen und berechneten NMR Parametern ermöglichte es uns Strukturmodelle auf atomarem Level aufzustellen. In Übereinstimmung mit den Hypothesen in der Literatur konnten wir zwei verschiedene aktive Zentren im Zeolithgerüst beobachten, ein geschlossenes und ein offenes Zentrum. Dies konnte zum ersten Mal durch direkte spektroskopische Beweise gezeigt werden.

In Kapitel 4 dieser Dissertation untersuchen wir, welchen Einfluss verschiedene Rezepte zur Synthese von $\text{Sn-}\beta$ auf die physikalisch-chemischen Eigenschaften sowie die vorhandenen aktiven Zentren hat und verknüpfen diese Eigenschaften mit der katalytischen Aktivität. $\text{Sn-}\beta$ Zeolithe wurden mit postsynthetischen sowie hydrothermalen Methoden hergestellt und in der Isomerisierung von Glukose zu Fruktose in Wasser getestet. Die Materialien, welche mit der postsynthetischen Methode hergestellt wurden zeigten im Vergleich zu hydrothermalen $\text{Sn-}\beta$ Zeolithen

eine 2-5 mal geringere Aktivität pro Sn atom. Dies deutet auf einen fundamentalen Unterschied zwischen diesen Materialien hin. Mittels ^{29}Si NMR, Röntgenbeugung und der Adsorption von Wasser konnte im Fall der postsynthetischen Materialien ein hydrophiles Zeolithgerüst mit Defekten nachgewiesen werden, welches für die niedrige Aktivität verantwortlich ist. Dies gilt für alle postsynthetischen Zeolithe, es sei denn der ausgehende Zeolith wurde in fluoridhaltigem Medium hergestellt und alle unbesetzten Zentren wurden mit Sn gefüllt. In dem Fall wurden außerordentlich hydrophobe Zeolithe ohne Defekte mit guter Aktivität beobachtet. Allerdings sind diese Katalysatoren immer noch 2 mal weniger aktiv als diejenigen aus hydrothermalen Synthesen. Da die physikalisch-chemischen Eigenschaften fast identisch sind, wird ein Unterschied in der Erreichbarkeit der aktiven Zentren und/oder der lokalen Geometrie dieser vermutet. Zusätzlich zu den in Kapitel 3 identifizierten Konfigurationen von geschlossenem und offenem Zentrum ist es unser Ziel die exakte Position derer im Zeolithgerüst zu bestimmen. Deshalb erweiterten wir die zuvor entwickelte Methodik zur Bestimmung der aktiven Zentren und berechneten die NMR Parameter der Sn Zentren für verschiedene Hydrierungsgrade, von komplett dehydrierten bis hin zu dreifach hydrierten Zentren für alle 9 T-Positionen. Durch die Korrelation von dehydrierten und hydrierten chemischen Verschiebungen für ^{119}Sn kann eine NMR Signaturkarte erzeugt werden. In Verbindung mit den experimentellen NMR Parametern, ebenfalls in dehydrierter und hydrierter Form können die vorhandenen aktiven Zentren in den unterschiedlichen Materialien bestimmt werden. Für die sehr aktiven hydrothermalen Sn- β Zeolithe wurden demnach geschlossene Zentren in T6 und T5/T7 Position und keine defekt-offenen Zentren gefunden. Für die weniger aktiven postsynthetischen Materialien fanden wir geschlossene T8 Zentren, hydrolysiert-offene Zentren in T5, sowie defekt-offene Zentren in T9 Position. In Verbindung mit den beobachteten katalytischen Daten lässt sich daraus schließen dass ein hydrophobes Gerüst mit erreichbaren Sn Zentren in T6 und/oder T5/T7 Position wichtig ist für eine hohe Aktivität. Diese Studie zeigt, dass die Morphologie und die Verteilung der aktiven Zentren von Lewis sauren β -Zeolithen stark von der Methode ihrer Herstellung abhängig sind.

Umfassend beinhaltet die vorliegende Dissertation maßgebliche Entwicklungen auf dem Weg zur kontrollierten Herstellung von Lewis sauren Zeolithen mit definierten Eigenschaften, im Besonderen Sn- β . Wir beschreiben ein zuverlässiges und flexibles Syntheseverfahren zur Herstellung von Lewis sauren β -Zeolithen mit kontrollierbaren

physikalisch-chemischen Eigenschaften. Des Weiteren stellen wir eine Karte mit den NMR Signaturen verschiedener Sn Zentren zur Verfügung, welche es ermöglicht die Verteilung der aktiven Zentren in Bezug auf Konfiguration und Position zu bestimmen. Schlussendlich ermöglicht dies den Einfluss von spezifischen Parametern während der Zeolithsynthese systematisch zu untersuchen und mit der daraus resultierende Bildung von bestimmten Zentren zu verknüpfen sowie gezielt das Syntheseprotokoll hin zu der Bildung der gewünschten aktiven Zentren zu optimieren.

1.1. Background

One of the greatest challenges for the modern chemical society is the mismatch between the demand and supply of fossil resources. To ensure that the needs of our present generation can be met without denying future generations thereof, the development of sustainable technologies is necessary. Often this sustainability is associated with environmentally friendly technologies; however, sustainability also comprises economy and society.¹ According to the so-called Triple Bottom Line, the needs of all three stakeholders – environment, economy and society – have to be addressed simultaneously so that a technology, process or product is considered sustainable.²

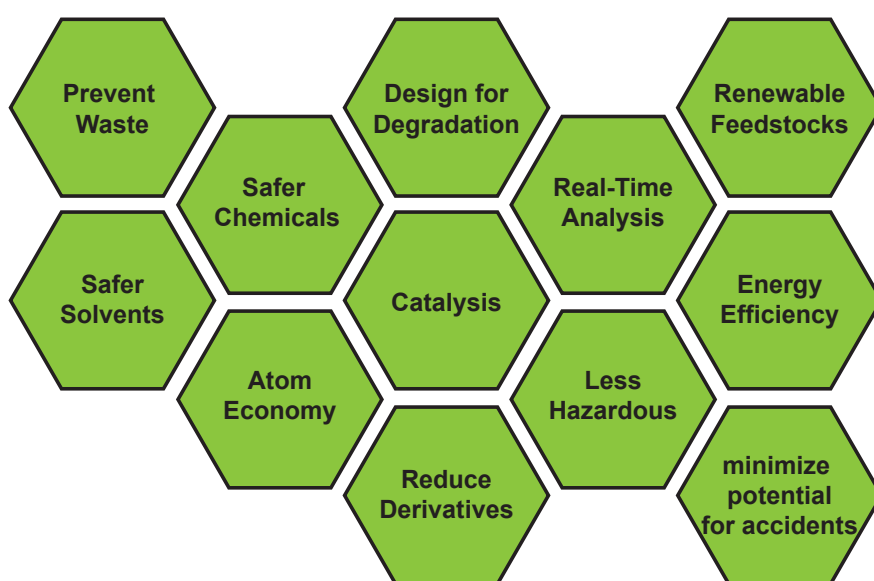


Figure 1.1. The 12 principles of green chemistry.³

A term that is often associated with sustainability is “Green Chemistry”. In 1998 Anastas and Warner defined the twelve principles of Green Chemistry as guidelines for the design of chemical processes and products.³ In brief, the goal of Green Chemistry is to use resources, preferably renewable, efficiently. At the same time both the formation of waste and the use of toxic/hazardous reagents should be minimized. Out of the twelve principles, catalysis in particular has been identified as a key tool toward

sustainability.⁴ By lowering a reaction's activation energy, catalysts beneficially alter chemical reactions in terms of their rates and selectivities. As a consequence productivity increases, energy consumption decreases and the formation of undesired by-products is inhibited. This leads to a more efficient utilization of resources, a reduction of waste and hence a pare down of extensive downstream processing, which improves the overall sustainability of chemical processes.^{1,5,6} Thus, the importance of catalysis has steadily increased over the last 200 years, and today, a considerable amount of all chemicals (95 % by volume) are produced with the aid of a catalyst.⁷ The global catalyst market itself was valued at 33.5 billion USD in 2014.⁸ Although homogeneous catalysts typically possess higher activity and selectivity than their heterogeneous alternatives, 80 % of the industrial catalysts are in solid state.⁷ Especially in terms of process intensification, process safety and downstream processing, heterogeneous catalysts offer several advantages, which make them attractive from both an economical and environmental point of view. In fact, the possibility to operate under continuous flow conditions in a fixed bed or fluidized bed reactor allows easy catalyst separation and better process control, which results in safer operation conditions, enhanced productivity and in many cases in reduced capital and operational costs. Moreover, heterogeneous catalysts generally exhibit good thermal stability, which allows for higher operating temperatures, thus increasing the activity of the catalyst.^{4,9}

1.2. Lewis acids doped zeolites

Acid catalyzed reactions constitute one of the most important types of catalytic transformations used in industrial catalysis. While solid Brønsted acids are well established in the sectors of petrochemicals¹⁰⁻¹² and fine chemicals^{6,13,14}, Lewis acid catalysis typically relies on the use of homogeneous materials. Conventional inorganic Lewis acids, such as AlCl_3 , ZnCl_2 or SnCl_4 are commonly used in organic syntheses for the production of fine chemicals.¹⁵ Such inorganic Lewis acids are not only corrosive and hazardous but also frequently used in stoichiometric amounts, which leads to the formation of significant quantities of solid waste during hydrolytic work-up.^{16,17} In view of more restrictive environmental regulations and the on-going urge for sustainable technologies, the development of recyclable heterogeneous Lewis acids is thus highly desired.^{6,15,17}

Over the past decades, Lewis acid zeolites have attracted significant attention as potential candidates to replace homogeneous industrial catalysts.¹⁸⁻²¹ Historically, zeolites are crystalline aluminosilicates with pores and cavities of molecular dimension (0.3 – 1 nm diameter). Today more than 200 different framework types are known, all of which differ in the connectivity of corner sharing SiO_4^{4-} and AlO_4^{5-} tetrahedra.²² However, less than 10% of these framework types are applied in industry. The great interest in zeolites as industrial catalysts originates from their (i) thermal stability, (ii) shape selectivity due to their pores of molecular dimension and (iii) ion-exchange properties due to the trivalency of Al, which introduces a negative framework charge. This framework charge is balanced by extra-framework cations (*e.g.* Na^+ , NH_4^+ , H^+) which allow introducing different acid/base functionalities that trigger catalysis in zeolites.^{13,22,23}

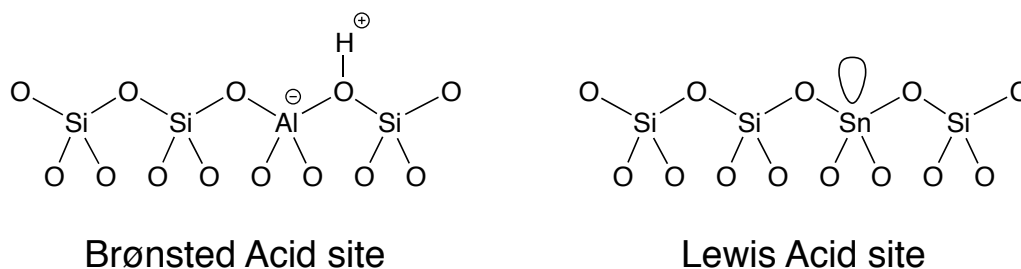


Figure 1.2. Brønsted and Lewis Acid sites in zeolites.

Another possibility for introducing catalytic functionality into zeolites is the incorporation of heteroatoms into the zeolite framework.^{22,24} In 1983, Eni S.p.A. realized that the isomorphous substitution of Ti for Si in the MFI zeolite framework isolated Lewis acid centers are formed, which possess unique catalytic activity. The development of so-called titanium silicalite-1 (TS-1) is considered one of the biggest breakthroughs in modern heterogeneous catalysis. Not only because it serves as a catalyst in several oxidation processes which involve aqueous hydrogen peroxide as a green oxidant in industry,²⁵⁻²⁷ but also because it revolutionized zeolite chemistry by pioneering the development of Lewis acid doped zeolites through heteroatom incorporation. Since then, various Lewis acid heteroatoms, such as Ti, Sn, Zr, Nb, Ta and Hf have been incorporated into a number of zeolite topologies (MFI, BEA, CHA, MWW, MOR, MEL)²⁸⁻³⁵ and mesoporous silicas (SBA-15, MCM-41).^{36,37} All of these isolated metal centers have an open coordination site to which the reagent can coordinate. Identical to homogeneous Lewis acids, the substrate gets activated by donating electron density into the LUMO of the Lewis acid, forming a Lewis acid-base adduct.³⁸⁻⁴⁰ In addition, the siliceous framework provides a hydrophobic confined space around the Lewis acid

center, hence protecting it from decomposition and hindering coordination of bulk solvent. Conventional Lewis acids often suffer from these problems, especially when they are employed in combination with polar protic solvents, such as water or alcohols.

1.3. Application of Lewis acid zeolites

As a consequence of the described advantageous properties, Lewis acid zeolites have been the topic of extensive research for the production of fine chemicals and the upgrading of renewable biomass resources. As such, isolated titanium sites have been found to be highly selective in activating hydrogen peroxide by forming a hydroperoxo species. Thus, titanosilicates have been utilized for the epoxidation of alkenes,^{34,41-43} the ammoximation of ketones,^{33,44-46} aromatic hydroxylations^{44,47} and the oxidation of primary alcohols and alkanes^{27,48} with hydrogen peroxide as green oxidant. In contrast, in the Baeyer-Villiger-Oxidation (BVO) of ketones with hydrogen peroxide, no activity toward the desired lactones was observed. Studies on the mechanism reveal that the carbonyl group of the ketone has to be activated by the Lewis acid for the reaction to proceed. Since isolated titanium sites are excellent in activating hydrogen peroxide but not in activating ketones, no reaction is observed.⁴⁹ As demonstrated by Corma *et al.*, Sn Lewis acid centers on the other hand show excellent C=O activation without activating H₂O₂, resulting in high activity and selectivity toward lactones even in the presence of other functional groups.³⁰ Stimulated by their ability to efficiently activate carbonyl groups, stannosilicates were tested for several other catalytic reactions. As such, after discovering the exceptional activity of Sn-β (*i.e.* Sn incorporated into the BEA zeolite framework) in the BVO reaction, the same research group also reported on the high catalytic activity of Sn-β in the Meerwein-Ponndorf-Verley (MPV) reduction of aldehydes and ketones *via* transfer-hydrogenation with an alcohol,⁵⁰ the carbonyl-ene reaction in the cyclization of citronellal to isopulegol⁵¹ and etherifications⁵². Depending on the substrate and the reaction, it was found that the Zr-incorporated analogue shows similar or even higher activity than the Sn.^{32,52,53}

Inspired by the fact that Sn-β is an active catalyst for intermolecular hydride transfer reactions, Davis *et al.* reported that the aqueous phase isomerization of glucose to fructose – one of the most important reactions in the upgrading of biomass to value-added chemicals – is catalyzed by Sn-β, *via* intramolecular 1,2-hydride shift.³⁷ In view of process intensification and profitability the Lewis acidic zeolite offers several

advantages over the conventionally used enzyme xylose isomerase. Sn- β performs well over a wide temperature range and is less sensitive to process impurities and acidic reaction conditions. Indeed, the combination of Sn- β with HCl allowed converting glucose directly into 5-Hydroxymethylfurfural (5-HMF) in a one-pot reaction with high yields.⁵⁴ The reaction proceeds *via* Lewis acid catalyzed glucose isomerization followed by Brønsted acid catalyzed dehydration of fructose. The resulting product 5-HMF constitutes an essential intermediate in the production of high-value polymers and fuels from bio-renewable resources.^{55,56} Oxidation of 5-HMF results in 2,5-furandicarboxylic acid (FDCA), which is considered as a bio-based substituent for para-terephthalic acid (PTA), one of the monomers in polyethylene terephthalate (PET).

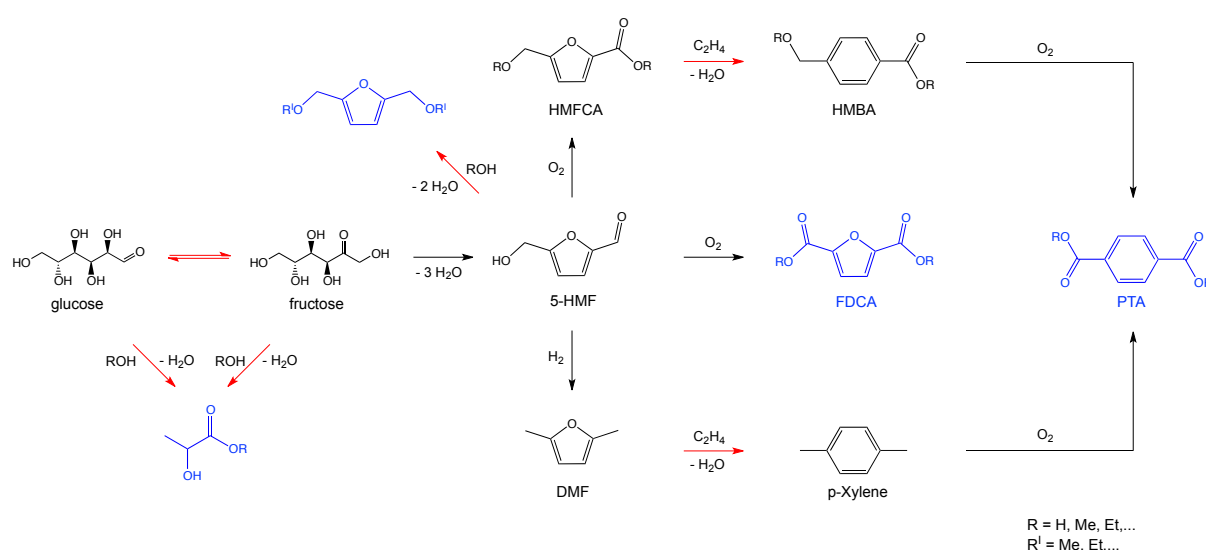


Figure 1.3. Reaction scheme for the production of bio-based polymer building blocks (blue) from glucose. Reactions involving Lewis acid zeolites are indicated with a red arrow.

More recently, Davis *et al.* showed that PTA derivatives can also be synthesized through a Diels-Alder reaction of oxidized 5-HMF derivatives with ethylene over Lewis acid zeolites, thus enabling the synthesis of 100% bio-based PET.⁵⁷ Similarly, dimethylfuran and ethylene can be converted to p-xylene over Lewis acid zeolites.⁵⁸ Other examples for the synthesis of biomass derived polymer building blocks with the aid of metal incorporated zeolites are the production of lactic acid derivatives from hexoses⁵⁹⁻⁶¹ and the synthesis of itaconic acid diesters through self-aldol condensation of pyruvates.⁶² Furthermore, the activity of Lewis acid zeolites in aldol condensation reactions was demonstrated for the production of the specialty chemical α -hydroxy- γ -butyrolactone from triose sugars and formaldehyde.⁶³

Other reactions catalyzed by Lewis acid zeolites are the epoxide rearrangement of β -pinene into myrtanal,⁶⁴ the epimerization of monosaccharides *via* intramolecular carbon shift^{65,66} and the ring opening hydration of epoxides.⁶⁷

1.4. Synthesis of Lewis acid Zeolites

The success of Lewis acid zeolites over the last two decades was strongly influenced by the improvements made in the synthesis of heteroatom-substituted zeolites. Besides the discovery of TS-1, the fluoride-mediated synthesis of heteroatom-incorporated β -zeolites represents a major breakthrough. First reported by Corma *et. al.* for defect free Ti- β zeolite,⁶⁸ the synthesis of β zeolites in fluoride media, near to neutral pH, enabled the use of otherwise poorly soluble metal precursors. This led to the incorporation of various metals such as Sn, Zr, Nb, Ta and Hf into the β -framework^{30-32,69} and more recently, also into the small pore CHA structure.²⁸ However, the higher solubility of the inorganic precursors causes a retarded nucleation resulting in long crystallization times and the formation of large crystals. Therefore some of the reported synthesis procedures involve the addition of seeds to facilitate crystallization.⁷⁰⁻⁷² Independent of seeding, these materials typically exhibit very high thermal stability and crystallinity as well as excellent hydrophobicity, due to very few to no silanol defects.^{73,74} As a consequence of their improved physicochemical properties these materials show superior catalytic activity and selectivity compared to the hydroxide mediated analogue, as has been shown for the epoxidation of olefins⁶⁸ or the isomerization of glucose to fructose in aqueous phase over Ti- and Sn- β zeolites.⁷⁵⁻⁷⁷ Indeed, in many Lewis acid catalyzed reactions in fine chemistry and the upgrading of biomass-derived oxygenates (*vide infra*), defect-free metal-doped β -zeolite has been demonstrated to be a very efficient catalyst.²¹ Besides the excellent stability even in polar protic solvents, the wide applicability of β -zeolite is a result of its 3D pore system consisting of 12-membered rings. Although it is a highly faulted intergrowth of two distinct, but closely related polymorphs, it exhibits straight channels of 7.6 x 6.4 Å in the a- and b-direction and sinusoidal channels of 5.5 x 5.5 Å in the c-direction.⁷⁸ Compared to the medium pore-sized (5.5 Å) MFI topology found in TS-1, β -zeolite thus possesses enhanced accessibility of the active sites toward bulky organic molecules.⁷⁹

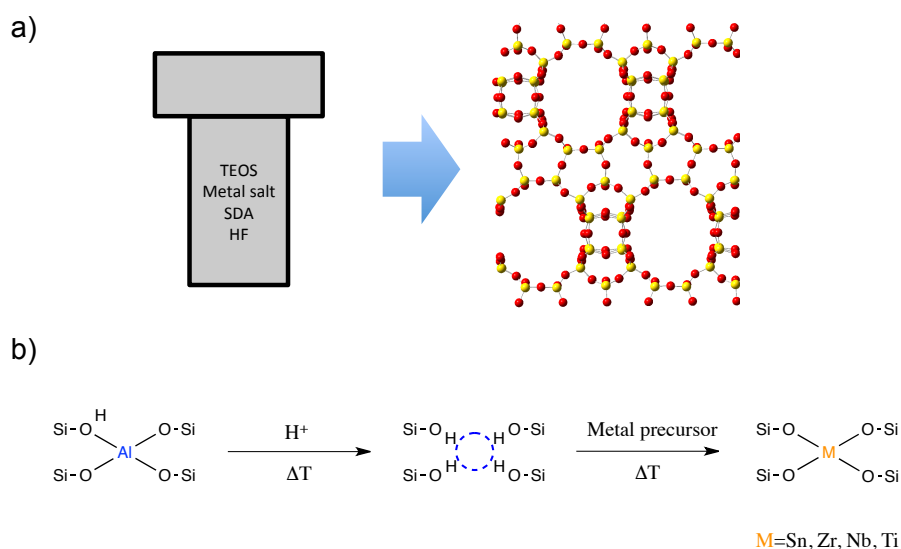


Figure 1.4. Schematic outline of a) conventional hydrothermal synthesis and b) postsynthesis via atom-planting.

Despite these clear advantages, the crystallization in a fluoride media also poses substantial drawbacks, which limit the synthesis procedures of Lewis acid zeolites to lab-scale. In particular the use of toxic hydrofluoric acid and the lengthy synthesis (up to 40 days) constitute the biggest challenges toward industrial implementation. Therefore significant efforts have been taken to overcome these hurdles. Owing to the unparalleled activity of Sn- β in numerous reactions, most studies on improved Lewis acid heteroatom substitution have been devoted to this system. Nonetheless, the developed synthesis protocols are generally transferable to the synthesis of other Lewis acid metals with minor modifications (see Chapter 2).

Fan and coworkers demonstrated that by carefully controlling the dispersion and morphology of β -zeolite nano-seeds the crystallization of hydrophobic Sn- β can be achieved in only 2 days.⁸⁰ Other strategies to reduce crystallization time involve steam-assisted conversion (SAC) from a dry gel⁸¹ or the crystallization from Sn-Si mixed oxides, which is prepared by mechanochemistry.⁸² However, these syntheses all require fluoride ions in the synthesis gel. Interestingly, the first successful hydrothermal synthesis of Sn- β in a non-fluoride medium was achieved very recently. It was found that besides well-defined seed crystals, the addition of alkali ions and the ion-exchange of the as-synthesized material with ammonium nitrate were crucial to obtain highly crystalline β -zeolite with framework Sn sites. Nevertheless, the resulting material showed a lower activity in the aqueous phase glucose isomerization, which was attributed to the higher amount of silicon defects and possibly a different local environment of the active site.⁸³

Simultaneously to the development in the hydrothermal synthesis routes, several research groups reported alternative post-synthesis strategies. In such methods the Lewis acid center is incorporated into a crystalline zeolite framework in two steps. First, framework Al (or B) sites are removed from the framework by acid leaching (7-15 M HNO₃, 80-110°C, 8-20 h) to create vacant lattice positions, so called vacant T-sites. These silanol nests can then be filled with a metal by means of chemical vapor deposition (CVD),⁸⁴ solid-state ion-exchange (SSIE)^{67,85} or chemical grafting.^{86,87} Generally, these methods do not require the use of toxic hydrofluoric acid, they show significantly reduced synthesis times and result in nano-sized crystals. Furthermore, the threshold of heteroatom incorporation for hydrothermal synthesis (ca. 2 wt% in case of Sn-β) could be overcome, which is highly favorable for industrial applications. However, some extra-framework (EF) species were observed at high Sn-loadings. For materials prepared by CVD and chemical grafting the presence of an EF oxide phase was verified by UV-Vis spectroscopy at Sn-loadings higher than 2 wt%.^{84,88} In case of the SSIE-based material, Hammond *et al.* detected small amounts of SnO₂ nanocluster by ¹¹⁹Sn solid-state nuclear magnetic resonance (NMR) spectroscopy already at loadings of 2 wt% with increasing cluster sizes and quantities at loadings higher than 5 wt%.⁸⁹ In terms of sustainability, the SSIE (or dry impregnation) methods are advantageous, since they proceed solvent-free and all the metal introduced in the synthesis remains in the final material. On the other hand, both the CVD and the chemical grafting methods use excess amounts of the metal precursor. Albeit, in case of liquid grafting from an isopropanol solution, recyclability of the grafting solution has been shown.⁸⁶

Regarding their catalytic activity the different materials behave very differently depending on their preparation. While materials prepared *via* CVD and SSIE show similar activity in the BVO compared to fluoride mediated Sn-β,^{84,85} chemical grafted materials were demonstrated to possess similar activity in the aqueous phase glucose isomerization.⁸⁶ Sels *et al.* recently tested both hydrothermal Sn-β samples and a series of post-synthetic samples prepared following different atom-planting methods in a number of reactions. They determined different reactivity trends on the reaction, suggesting that each synthesis method leads to the formation of a unique material with different physicochemical properties.⁸⁸ However, the rationalization of which material characteristics are favorable for a certain type of reaction and further identification of the influence of specific synthesis parameter on the final properties of the material is extremely difficult.

1.5. Characterization of Lewis acid Zeolites

The catalytic activity and selectivity of Lewis acid zeolites depend on a number of different material characteristics, such as hydrophobicity, crystallinity, site accessibility and the local geometry of the active site. In a recent review, Román-Leshkov *et al.* divided the effects of the zeolite environment on the catalytic activity into direct and extended factors.²¹ Direct factors include characteristics of the active site itself, such as site flexibility and electronic properties of both the metal center and the adsorbed species. Extended factors primarily address properties which affect the diffusion and conformation of reagents and solvents within the zeolite pores. Characterization techniques to investigate extended factors are well established and routinely applied. As such, the framework topology, (i.e. the structure of the pore channel system) and the relative crystallinity of a zeolite is determined by powder X-ray diffraction (PXRD).⁹⁰ The porosity of zeolites is assessed by physical adsorption measurements of inert gases, such as N₂ and Ar.^{91,92} The hydrophobicity of the material can be determined if H₂O is used as an adsorbent instead.^{75,77,91,93} Scanning electron microscopy (SEM) provides information on the crystal size and morphology.^{94,95}

Based on these techniques, it was found that fluoride mediated zeolite crystals are in general significantly larger than post-synthetic and hydroxide mediated crystals, owing to the retarded nucleation in this reaction media. Additionally, they generally possess higher hydrophobicity due to their (almost) defect-free framework, which has been confirmed by H₂O adsorption measurements.⁷⁴ By combining SEM with wavelength-dispersive spectroscopy (WDS), Tolborg *et al.* also showed that in the fluoride mediated syntheses Sn preferentially accumulates in the outer rim of a zeolite crystal.⁹⁵

The characterization of the direct factors (i.e. the local environment at the active site) is, on the other hand, more challenging as the typically low loading (< 2 wt%) and the variety of potential sites in zeolites cause sensitivity and resolution issues in various techniques. This often makes the interpretation of the collected data very difficult, so that a multidisciplinary approach with the combination of a variety of corroborative techniques is needed. In general, the nature of the active site can be separated into three aspects: framework vs. extra-framework (EF) species, open vs. closed sites and the distinct T-site within the zeolite lattice.

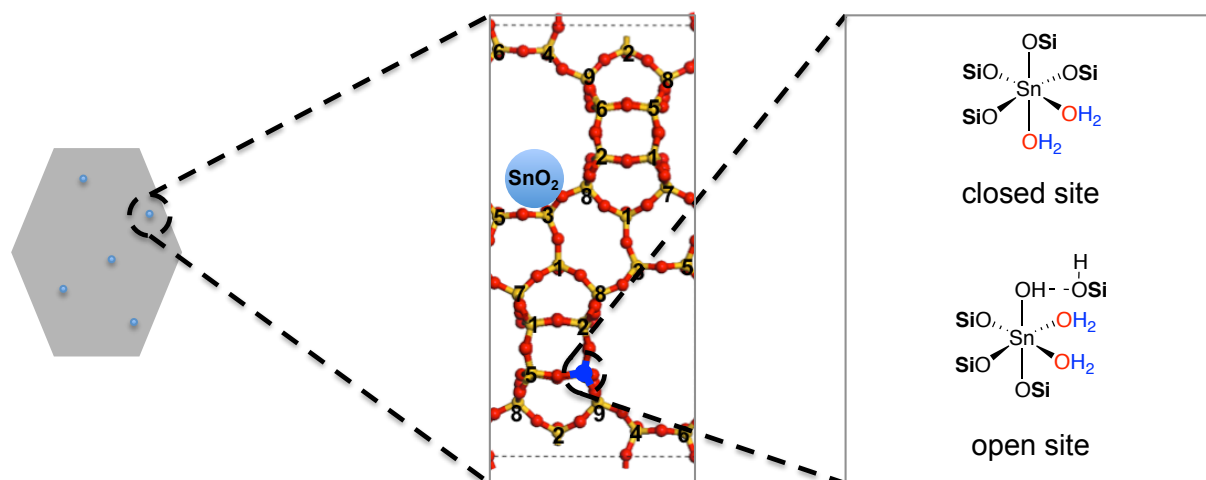


Figure 1.5. Schematic showing the different aspects for the description of the active sites in Sn-β: framework vs. extra-framework, T-site position within the zeolite lattice and closed vs. open site.

The most common way to check for undesired EF oxide species is diffuse reflectance UV/Vis spectroscopy (DR-UV/Vis). Typically, the successful heteroatom-incorporation into the zeolite framework is verified based on a characteristic absorption band at 200–220 nm resulting from the ligand-to-metal charge transfer from O²⁻ to the tetrahedral M⁴⁺ center.^{96,97} However, DR-UV/Vis only allows to qualitatively assess the presence of framework and EF species and cannot unambiguously prove the absence of EF species. Similarly, X-ray photoelectron spectroscopy (XPS) can only differentiate between framework and EF species in a non-quantitative manner and is a surface-sensitive technique. Additionally, information on the oxidation state and a rough estimate about the spatial distribution of the heteroatom within the zeolite crystal can be gained with this technique.^{35,67,98,99} Larger amounts of EF species can also be detected by PXRD, even though the detection limit is typically higher than the total metal loading in most Lewis acid zeolites.⁸⁹ Vibrational spectroscopy such as Raman or Fourier-Transform infrared spectroscopy (FTIR) can be used to probe M-O-Si vibrations, but due to the low loading none of the vibrational spectroscopic techniques is sensitive enough to detect the M-O-Si vibration at the given concentration.

In contrast to UV/Vis and vibrational spectroscopy, Solid-state NMR is in general an ideal technique to probe the local environment at the active site.^{100,101} Indeed, NMR has been shown to unambiguously detect EF species in Lewis acid zeolites, even at low loadings. However, due to the large quadrupole moment and the small gyromagnetic moment of ⁹¹Zr (I=5/2) and ^{47/49}Ti (I=5/2), solid-state NMR studies, which directly probe the heteroatom have only been performed for ¹¹⁹Sn (I=1/2). Nonetheless, long acquisition times and ¹¹⁹Sn enriched samples are necessary to allow the acquisition of

spectra with reasonable signal-to-noise ratios.^{29,89,94,97,102} Recently it was shown that the application of Carr-Purcell-Meiboom-Gill (CPMG) echo train acquisition¹⁰³ or dynamic nuclear polarization (DNP)¹⁰⁴ can significantly reduce acquisition times, thus allowing to collect ¹¹⁹Sn NMR spectra of natural abundance Sn-β samples with loadings as low as 1 wt% in short acquisition times (decrease in acquisition time up to a factor of 50).

Characteristically EF SnO₂ species give resonance at around -600 ppm, while framework species give rise to resonances at -650 to -740 ppm and -420 to -460 ppm in their hydrated and dehydrated state, respectively.^{89,97} Furthermore, ¹¹⁹Sn NMR of dehydrated samples has been used to discriminate between open vs. closed sites. By performing ¹H-¹¹⁹Sn cross-polarization (CP) experiments Davis *et al.* assigned a signal at around -420 ppm in the spectrum of dehydrated Sn-β to the open and a resonance at -445 ppm to the closed sites.^{65,94} The main difference between these two sites is their coordination to the zeolite framework. An open site is three-fold bound to the siliceous zeolite framework and has one Sn-OH group, while the closed site is four-fold bound to the zeolite framework. For the different chemical shifts that are observed in the spectra of hydrated samples no assignments have been made thus far, except that they have been stated to be hexacoordinated.

The assignment of NMR signals from ¹H-¹¹⁹Sn CP measurements to open vs. closed Sn sites is based on previously proposed active site structures developed from an FTIR adsorption study with Lewis base acetonitrile as probe molecule.¹⁰⁵ In this study Corma and co-workers demonstrated that the open sites are more Lewis acidic than the closed sites, indicated by a more pronounced redshift of the C≡N stretching vibration of adsorbed deuterated acetonitrile (2316 cm⁻¹ vs. 2308 cm⁻¹), which was confirmed by DFT calculations. Therefore the open site was suggested to be the primary active site in Sn-β, which is supported by several experimental and computational studies.^{65,94,105-108} The quantification of the two proposed sites by titration with deuterated acetonitrile was only recently established when the integrated molar extinction coefficients were determined.⁷⁶ With these extinction coefficients, the molar ratios between open and closed sites were measured for a series of Sn-β samples prepared with different Si/Sn ratios and following different synthesis protocols (hydrothermal and post-synthetic). No correlation between the preparation method and the observed molar ratio between the two proposed sites could be observed.⁷⁶ Instead, correlation with the initial catalytic activity of these materials in the aqueous phase glucose isomerization led to further evidence that the open site (2316 cm⁻¹ upon the adsorption of deuterated acetonitrile) is

the dominant active site. However, the assignment of the IR signal at 2316 cm^{-1} is not unambiguous as it was claimed that the 2316 cm^{-1} feature arises from adsorbed solvent molecules and does not present different types of sites.⁹⁶ Other probe molecules that have been used in combination with FTIR for the characterization of Lewis acid zeolites are pyridine,^{76,88} cyclohexanone¹⁰⁹ and CO^{110,111}.

Surprisingly, almost all of the described studies neglect the presence of different crystallographic tetrahedral sites (T-sites), which are occupied by the heteroatom. Intrinsically, each zeolite framework (except for CHA) has multiple distinct T-sites, which can potentially be populated by the Lewis acid heteroatom. Each of these T-sites has a different geometry and thus different electronic properties resulting in different acidities.^{36,112,113} So far, an experimental investigation of the T-site location has only been performed for TS-1 and Sn- β using Neutron- and X-ray diffraction¹¹⁴⁻¹¹⁶ and EXAFS¹¹⁷. The preferred location of the heteroatom within the zeolite framework has also been addressed by computational modeling.^{113,118-120} In these studies, the preferred order of heteroatom substitution is based on the different stabilities of the T-sites. The resulting acidities are generally described by calculating the adsorption energies of water.¹¹⁹ However, kinetic factors influencing the distribution of the heteroatom are not considered in these calculations. Since zeolites are in general metastable phases, kinetic factors may play a crucial role in the crystallization process and affect the location of the heteroatom within the zeolite framework.¹²¹

Other characterization techniques that have been applied are Mössbauer spectroscopy,^{122,123} and temperature programmed desorption^{76,124}.

1.6. Scope of the Thesis

The goal of this thesis is to develop a robust and versatile synthesis protocol for the preparation of Lewis acid zeolites and to gain an understanding how these post-synthetic materials differ from their conventional analogues synthesized *via* hydrothermal crystallization. Focus will be put on identifying the differences in the precise geometry of the active site structure on an atomic level.

Based on a two-step post-synthetic approach for the preparation of the Lewis acid Sn- β which was previously developed in our research group, other heteroatoms such as Zr, Nb, and Ti will be incorporated to prove the versatility of the optimized method. The resulting materials will be subjected to detailed material characterization and catalytic testing to assess their characteristic properties.

Further, we aim to better understand Sn- β and compare our post-synthetic material to conventional hydrothermally synthesized materials. Special attention will be placed on the determination of the precise local environment at the active site. With this in mind, first, the active site speciation for a series of post-synthetic materials with different Sn loadings will be determined. To do so, we aim to gain structural information on the active sites by measuring the chemical shift and the chemical shift anisotropy as a NMR signature of the different sites in Sn- β . From this in combination with theoretical calculations of the NMR parameter, the active site structures can be described on an atomic level. In a second step, the influence of the synthesis procedures on morphology and active site speciation is approached. A series of Sn- β catalysts from different synthesis protocols, *i.e.* post-synthetic solid-state ion-exchange and conventional hydrothermal synthesis, will be prepared. This set of materials will be subjected to an in-depth physicochemical characterization including adsorption isotherms, powder X-ray diffraction and microscopy. Applying our previously developed approach of combining NMR signatures with theoretical calculations, focus will be put on the determination of the active site speciation. Like this, a signature map can be created to identify possible active sites present in as-synthesized Sn- β catalysts. Correlation of the physicochemical properties and active site structures for different Sn- β catalysts will allow to develop structure-activity relationships and identify material characteristics which are essential for high activity.

We expect that the improved and extended synthesis protocol and the development of a characterization tool for the determination of the active site speciation will enable the systematic investigation of synthesis parameters and their influence on the formation of specific active sites in the resulting Lewis acid zeolite. Ultimately this allows to rationally optimize the synthesis protocols toward the formation of the desired active sites.

1.7. Outline of the Thesis

The results of this thesis are presented in three chapters (**Chapter 2 – 4**) followed by the conclusions and outlook of the challenges ahead (**Chapter 5**). The research presented in this thesis has been carried out in the frame of a Swiss National Science Foundation grant titled (project no. 200021_146661) titled "Hybrid catalytic systems for the upgrading of renewable feedstocks".

Brønsted acid zeolites are an important class of industrial catalysts, while their Lewis acid doped analogues have only been poorly exploited. Owing to their inconvenient and complex synthesis these materials have mainly been restricted to academic research. In **Chapter 2** we address the synthesis issues and establish a convenient and versatile post-synthetic preparation of Lewis acid zeolites via a two-step approach, based on previous developed work in our research group. Since different types of Lewis acid catalyzed chemical transformations require different acid properties we slightly modify the developed methodology for Sn- β to other Lewis acid metals, such as Zr, Ti and Nb. To confirm the successful heteroatom incorporation, the resulting catalysts are characterized by means of spectroscopy and catalytic testing.

To get a better understanding about the incorporated heteroatom on an atomic level, we determine the nature of the active sites present in Sn- β . For this, we prepare a series of Sn- β samples with varying Sn loading and investigate these materials by advanced characterization techniques, as shown in **Chapter 3**. ^{119}Sn Mössbauer spectroscopy is used to gain information on the Sn coordination. The precise local geometry of the active sites present in Sn- β is investigated by measuring the ^{119}Sn chemical shift and chemical shift anisotropy of each individual site. This is enabled by the use of dynamic nuclear polarization, which results in signal enhancement. Combining the experimental results with the theoretical NMR parameter from DFT calculations finally allows us to attain the local structure of the active sites.

In **Chapter 4**, we combine both our synthetic and characterization techniques to compare conventional and post-synthetic Sn- β zeolites. Focus is put on the identification of crucial material characteristics for high activity in the aqueous phase isomerization of glucose to fructose. With an in-depth characterization of the physicochemical properties and the active site speciation of the different materials we aim to correlate specific material properties to catalytic activity. Exploration of the zeolite morphology is undertaken by adsorption measurements, microscopy, X-ray diffraction and ^{29}Si NMR. The active site distribution is determined by an improved methodology of the one developed in **Chapter 3**. ^{119}Sn NMR spectra are collected for Sn- β in their hydrated and dehydrated state. By correlating these data sets with the chemical shift anisotropy and the theoretical calculations on all proposed active site models found in present literature we are able to propose active site distributions in the different materials. Finally correlating the information gathered from

physicochemical analysis and the active site speciation with the catalytic activity allows us to determine a structure-activity relationship.

Chapter 5 summarizes the key results of the research performed throughout this thesis and identifies challenges ahead.

Chapters 2-4 were each written as one publication and can be read independently. Accordingly, some overlap between the chapter introductions and experimentals occur.

Post-synthetic preparation of Sn-, Zr-, Nb- and Ti- β ; a facile route to water tolerant, highly active Lewis acidic zeolites

Myself performed the triose sugar isomerization experiments as well as part of the material synthesis and most of the catalyst characterization. Ceri Hammond conducted part of the material synthesis and the cyclooctene epoxidation experiments. Sabrina Conrad performed the CD_3CN adsorption experiment for Sn- β (Figure 2.4).

2.1. Introduction

In recent times, water tolerant, heterogeneous Lewis acids have found widespread applicability for a number of liquid phase oxidation and isomerization reactions.^{15,125} Most notable amongst this class of materials are Lewis acid-containing zeolites. Unlike traditional stoichiometric and/or homogeneous Lewis acids, e.g. Zn^{II} and Al^{III} , these heterogeneous materials avoid the (co)-production of copious amounts of inorganic and/or toxic waste, and avoid a number of downstream handling problems *viz.* separation. Moreover, the encapsulation of the Lewis acid inside a water-resistant, hydrophobic framework (as found for highly siliceous zeolites) prevents the hydrolysis and subsequent deactivation of the Lewis acid, and thereby allows these promising materials to be utilized for aqueous phase oxidation and isomerization reactions.^{31,126} Of particular interest is Sn^{IV} -containing zeolite β (Sn- β). This catalyst has demonstrated an exceptional ability to activate carbonyl-containing molecules, and has thus found widespread applicability as a promising catalyst for the Baeyer–Villiger oxidation of ketones to lactones using H_2O_2 ,^{30,127,128} and the upgrading of bio-renewable platform molecules, such as glucose.^{37,60,61,129} Indeed, Sn- β -catalyzed isomerization of glucose to fructose is the first step in perhaps the most promising route towards the upgrading of glucose (and eventually cellulose) to various fuels and chemicals.^{54,130-132} In addition to the

promising catalytic results obtained with Sn- β , exciting results have also been obtained by other Lewis acidic zeolites. For example, Zr^{IV}-containing β -zeolite has recently been shown to be a promising catalyst for the production of γ -valerolactone from bio-renewable furfural,¹³³ and the cascade transformation of citral to \pm -menthol.⁵³ Zr^{IV}-containing silicates have recently also shown promising activity as CO₂ adsorbents.^{134,135} Interestingly Nb^V-containing β -zeolite has also shown high activity in the cyclization reaction of the citral to \pm -menthol transformation.³¹ Other Nb silicates were utilized for the gas-phase Beckmann-Rearrangement of cyclohexanone oxime to ϵ -caprolactam.¹³⁶⁻¹³⁸ Furthermore, Ti^{IV} is also the critical component of many highly active and selective oxidation catalysts, such as TS-1, Ti- β and Ti-MWW zeolites.^{68,139,140}

Despite increasing academic and industrial interest in this class of catalyst, some significant practical hurdles remain that currently curtail industrial implementation. Amongst these, the lengthy and complicated hydrothermal synthesis procedure, the low amount of active metal typically incorporated per kilogram of the final catalyst, and the large crystallite sizes remain the most prohibitive. Therefore alternative methods, which do not suffer from these drawbacks, are of great interest.^{80,84,86,141}

Recently, some of us reported a convenient post-synthetic route for the incorporation of Sn^{IV} into the framework of zeolite β .⁸⁵ In brief, the desired Lewis acid was incorporated into the vacant tetrahedral (T)-sites of a dealuminated framework by solid-state ion-exchange. Not only does this approach avoid the long synthesis times associated with conventional hydrothermal synthesis routes, but also it allows for the synthesis of a material with significantly smaller crystallite sizes, higher metal content, and more favorable catalytic properties. Indeed, the catalytic productivity of post-synthetically prepared Sn- β was found to be five to ten times larger than previously reported for the Baeyer–Villiger oxidation of cyclohexanone with H₂O₂, and the conversion of dihydroxyacetone into ethyl lactate. In this publication, we extend our post-synthetic route for the preparation of Sn- β to other Lewis acids, such as Zr^{IV}, Nb^V and Ti^{IV}, with the aim of developing more convenient synthetic routes for other promising Lewis acidic zeolites.

2.2. Experimental

2.2.1. Catalyst synthesis

Commercial zeolite H- β (ZeoChem, SiO₂:Al₂O₃ =25) was dealuminated by treatment in HNO₃ solution (13 M HNO₃, 100 °C, 20 h, 20 mL g⁻¹ zeolite). Solid-state ion-exchange was performed by grinding the appropriate amount of tin(II)acetate or zirconium(IV)ethoxide with the necessary amount of pre-dealuminated zeolite. Impregnation was performed by stirring dealuminated zeolite β in an ethanolic solution of niobium(IV)- or titanium(IV)ethoxide. Following this procedure, the samples were heated in a combustion furnace to 550 °C for 3 h (20 °C min⁻¹ ramp rate) under a dry airflow.

2.2.2. Catalyst Characterization

FT-IR spectroscopy was performed on self-supporting wafers using a Bruker Alpha Spectrometer inside a glovebox in transmission mode. Intensities were normalized to the Si–O–Si overtones of the zeolite framework. DRUV-Vis analysis was performed with an Ocean Optics UV-Visible Spectrophotometer in diffuse reflectance mode. Si, Al, and other metal contents were determined by ICP-OES. Porosimetry measurements were performed on a Micromeritics Asap 2020 apparatus. The samples were degassed prior to use (275 °C, 3 h). Adsorption isotherms were obtained at 77 K and analyzed using BET and t-plot methods.

2.2.3. Catalytic activity measurements

The isomerization of glyceraldehyde to dihydroxyacetone was carried out in a 50 mL round-bottomed flask equipped with a reflux condenser. The vessel was charged with the reactant solution (5 mL, 0.25 M glyceraldehyde in H₂O) and heated to the desired reaction temperature (50–100 °C). The reaction was initiated by adding the desired amount of catalyst (corresponding to a substrate/metal ratio of 100) and stirred vigorously for the required reaction period. Samples were taken periodically and quantified by HPLC.

The oxidation of cyclooctene was carried out in a 50 mL round-bottomed flask equipped with a reflux condenser. The vessel was charged with the reactant solution (10 mL, 0.5 M cyclooctene in 2-butanol) and heated to the desired reaction temperature (80 °C). The desired amount of catalyst was added to the vessel, and the reaction was subsequently initiated by adding the desired amount of H₂O₂ (0.25 or 0.5 M, H₂O₂/olefin = 0.5 or 1) and stirred vigorously for the required reaction period. Samples were taken

periodically and quantified by GC-FID against a biphenyl internal standard (30 m FFAP column).

2.3. Results and Discussion

2.3.1. Dealumination of H-zeolite β

To create the necessary vacant framework sites for the incorporation of the desired Lewis acidic species, a parent alumino-silicate zeolite β ($\text{SiO}_2/\text{Al}_2\text{O}_3$ molar ratio = 25 (3.1 wt% Al), H-Al-Beta-OH-25) was first dealuminated via an established literature procedure¹⁴² by treatment with concentrated HNO_3 (13 M, 100 °C, 20 h). Unlike steaming, dealumination by HNO_3 ensures that little or no extra-framework Al^{III} , a strong Lewis acid, remains in the material, thereby ensuring a clean, naked framework into which other Lewis acid centers can be incorporated. ICP-OES analysis demonstrated that Al^{III} was easily removed from the material (Table 2.1), with no negative changes to the structural integrity of the zeolite *cf.* pore volume, surface area and XRD patterns (Figure 2.1). The resulting material was denoted as deAl-Beta-OH-25.

Table 2.1. Physicochemical properties of Lewis acidic zeolites.^[a]

Entry	Catalyst	Treatment ^[a]	S_{BET} ($\text{m}^2 \text{g}^{-1}$) ^[b]	Metal loading (wt. %)
1	H-Al-Beta-OH-25	-	600	3.1
2	deAl-Beta-OH-25	H^+	620	< 0.1
3	10Sn/deAl-Beta-OH-25	H^+ /SSIE (Sn^{II} acetate)	600	10.1
4	8Zr/deAl-Beta-OH-25	H^+ /SSIE (Zr^{IV} ethoxide)	580	7.7
5	8Nb/deAl-Beta-OH-25	H^+ /IMP (Nb^{V} ethoxide)	600	7.8
6	4Ti/deAl-Beta-OH-25	H^+ /IMP (Ti^{IV} ethoxide)	610	4.0

[a] H^+ = acidic pre-treatment (HNO_3 , 13 M, 100 °C, 20 h); SSIE = solid-state ion-exchange reaction; IMP = impregnation. [b] Brunauer-Emmett-Teller surface area calculated by N_2 physisorption.

Transmission FT-IR spectroscopy of the parent H-zeolite β demonstrates that the untreated material contains both Brønsted acid sites (charge compensatory protons occupying the cation-exchange sites, Si-O(H)-Al , 3610 cm^{-1}) and isolated silanol groups ($-\text{SiOH}$, 3740 cm^{-1}) at the external surface(s) of the zeolite (Figure 2.2). Following HNO_3 treatment, the Si-O(H)-Al stretch is completely removed from the FT-IR spectrum, further indicating the complete removal of framework Al^{III} and the corresponding loss

of cation-exchange sites. Along with an increased signal associated with isolated silanol species (3740 cm^{-1}), the dealuminated material also contains a broad absorbance at $\pm 3550\text{ cm}^{-1}$. This broad feature is indicative of a network of hydrogen bonding within the structure of the zeolite, and has been attributed to the presence of silanol nests, $(\text{SiOH})_4$.¹⁴²

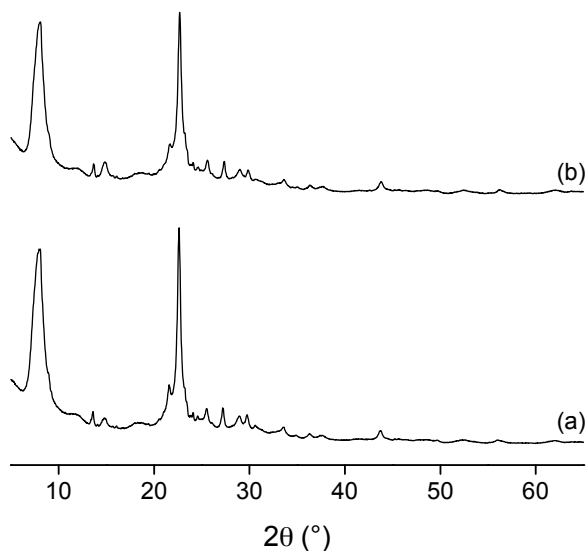


Figure 2.1. XRD patterns for (a) untreated H-zeolite ($\text{SiO}_2/\text{Al}_2\text{O}_3 = 25$) and (b) HNO_3 -treated zeolite ($\text{SiO}_2/\text{Al}_2\text{O}_3 \geq 1000$).

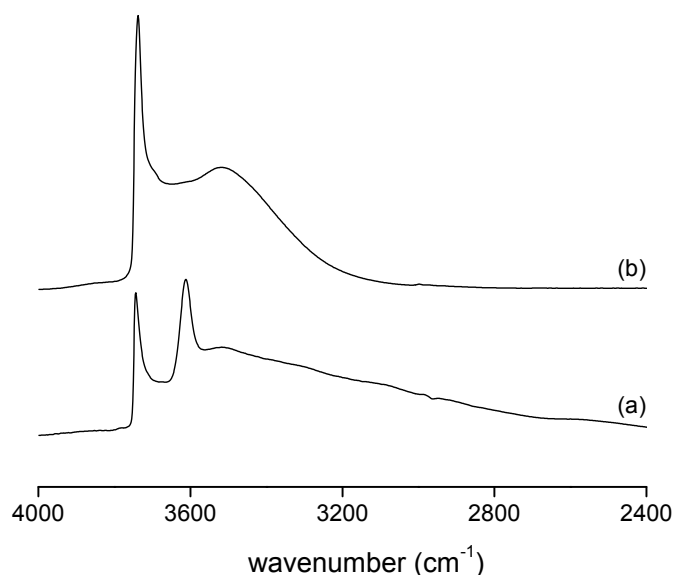


Figure 2.2. FT-IR spectra for (a) untreated H-zeolite ($\text{SiO}_2/\text{Al}_2\text{O}_3 = 25$) and (b) HNO_3 -treated zeolite β ($\text{SiO}_2/\text{Al}_2\text{O}_3 \geq 1000$). This data was partly published previously in *Angew. Chem. Int. Ed.*, 2012, 51, 11736.

2.3.2. Synthesis of Sn-, Zr- Nb and Ti-zeolite β

Our previous work in this area has demonstrated that the formation of silanol nests is a pre-requisite for incorporating Lewis acids or other transition metals into the framework of zeolite β . Having achieved this aim, we subsequently turned our focus to the incorporation of Sn^{IV}, Zr^{IV}, Nb^V and Ti^{IV}. In order to prepare these samples, two preparation procedures were employed. For Sn- and Zr- β , we employed a solid-state ion-exchange procedure, which involves the mechanical grinding of dealuminated zeolite β with an appropriate solid metal precursor (Sn(II) acetate and Zr(IV) ethoxide, respectively). For Nb- β and Ti- β , the absence of a suitable solid precursor forced us to employ an impregnation methodology, involving the wet impregnation of dealuminated zeolite β with an ethanolic solution of Nb(V)- and Ti(IV) ethoxide, respectively. The preparation of each as synthesized sample was completed by a high-temperature calcination procedure (550 °C, 3 h, flowing air) in order to remove the residual acetate/ethoxide species, and to ensure complete encapsulation of the Lewis acid into the vacant framework sites. We note that each sample was prepared to contain the same molar ratio (i.e. 0.84 mmol metal per g catalyst), but that for simplicity each sample will be denoted by its total metal content, i.e. wt%. Therefore, Sn^{IV} zeolite β , containing 10.1 wt% Sn, will be denoted as 10Sn/deAl-Beta-OH-25.

2.3.3. Characterisation of Sn-, Zr- Nb and Ti-zeolite β

Unlike trivalent metals, e.g. Al^{III}, the coordination of tetravalent metals into the zeolite framework, e.g. Sn^{IV}, does not give rise to a negatively charged framework or cation-exchange sites. Thus, other than the complete consumption of the silanol nests feature ($\pm 3550\text{ cm}^{-1}$),¹⁴³ FT-IR spectroscopy provides very little information on these Lewis acidic zeolites. However, analysis of the Diffuse Reflectance spectra in the UV-Vis region (DRUV-Vis) provides a great deal of information on the nature of the as synthesized species. The spectrum obtained for 10Sn/deAl-Beta-OH-25 features a sharp maximum at ca. 216 nm, which is indicative of isolated, tetrahedral Sn^{IV} species in the zeolite framework. As can be observed (Figure 2.3), the spectrum for 10Sn/deAl-Beta-OH-25 is significantly blue-shifted with respect to the bulk metal oxide, SnO₂. In contrast, the spectra obtained for 8Zr/deAl-Beta-OH-25, 8Nb/deAl-Beta-OH-25 and 4Ti/deAl-Beta-OH-25 are somewhat broader and less defined than 10Sn/deAl-Beta-OH-25. Originally, we presumed that the broad patterns indicated the formation of multiple metal species, e.g. isolated metal sites, dimers/oligomers and/or bulk metal oxides.

Nevertheless, no indication of absorbance at ± 350 nm was observed for 4Ti/deAl-Beta-OH-25, suggesting little or no presence of TiO₂ (nano)particles, and the observed UV-Vis spectrum is very similar to those reported by Mania et al., Hereijgers et al., and Blasco et al., where isolated Ti^{IV} sites were found following detailed spectroscopic analysis.^{72,144,145} Similarly, despite the DRUV-Vis pattern of 8Zr/deAl-Beta-OH-25 being somewhat broader than that of 10Sn/deAl-Beta-OH-25, no absorbance was found above ± 250 nm. From this, we conclude that each catalyst contains (predominantly) isolated, tetrahedrally coordinated Lewis acids within the framework of the zeolite, and few (or no) bulk oxides. However, in the absence of e.g. XAS or STEM analysis, the complete absence of bulk oxides is not yet conclusive.

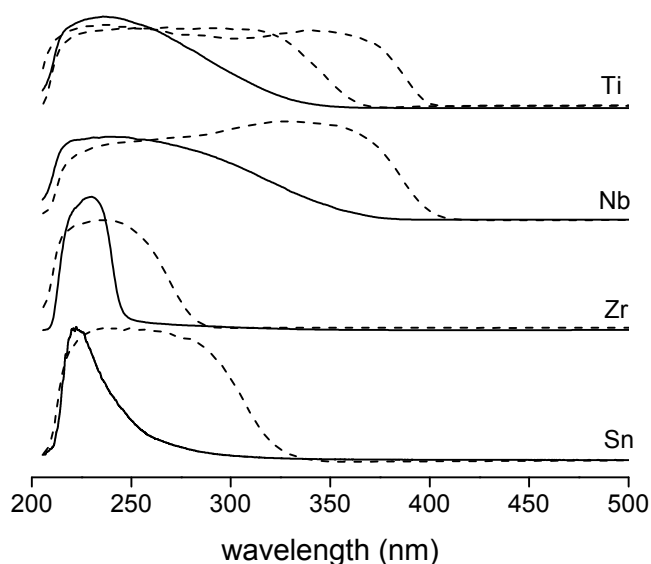


Figure 2.3. DRUV-Vis spectra for (a) 10Sn/deAl-Beta-OH-25 (b) 8Zr/deAl-Beta-OH-25 and (c) 4Ti/deAl-Beta-OH-25. Dashed lines overlaid with each spectrum are the DRUV-Vis spectrum obtained for the corresponding bulk metal oxide (SnO₂, ZrO₂, Nb₂O₅ and TiO₂ (anatase and rutile)).

For further information on the Lewis acid speciation within each sample, we subsequently turned to in situ analysis of the catalysts with CD₃CN absorption (i.e. probe molecule studies). It has previously been demonstrated¹⁶ that when coordinated within the zeolite framework, Lewis acidic centers dosed with CD₃CN give rise to an absorption in the FT-IR spectrum at ± 2310 cm⁻¹. This feature has been attributed to the coordination of CD₃CN onto the isolated, framework-incorporated Lewis acidic center (CD₃CN–Lewis acid), and is not observed for bulk metal oxides. The presence of this band at 2310 cm⁻¹ thus provides information on the degree of Lewis acidity in a sample. Figure 2.4 presents the full adsorption/desorption spectrum for 10Sn/deAl-Beta-OH-25. Following adsorption of CD₃CN, two major adsorption features are observed at ± 2270

and $\pm 2310\text{ cm}^{-1}$. The first feature is indicative of CD_3CN weakly physisorbed onto the sample. The second feature at 2310 cm^{-1} corresponds to CD_3CN coordinated onto the Sn^{IV} Lewis acid center, and conclusively demonstrates that Sn^{IV} is isolated and present in the zeolite framework. It is noticeable that a shoulder at $\pm 2275\text{ cm}^{-1}$ is present on the physisorbed CD_3CN feature. This has previously been attributed to CD_3CN coordinated to a Brønsted acid site. Its presence in the adsorption spectrum for 10Sn/deAl-Beta-OH-25 is likely due to the residual silanol species that are present in the material; even at a loading of 10 wt%, only around 90% of the silanol nests have been fully occupied by Sn, and thus a small fraction of vacant silanol nests – imparting weak Brønsted acidity – remain. This fraction could also be somewhat larger if not all the metal is present in the framework. Following desorption under static vacuum for various time periods, it is clear that the weakly-bound physisorbed CD_3CN is first removed, followed by the CD_3CN species bound to the Brønsted acid sites. It is apparent that the strength of the CD_3CN –Lewis acid species is quite high, as full removal of these species was not observed even following 16 minutes of evacuation.

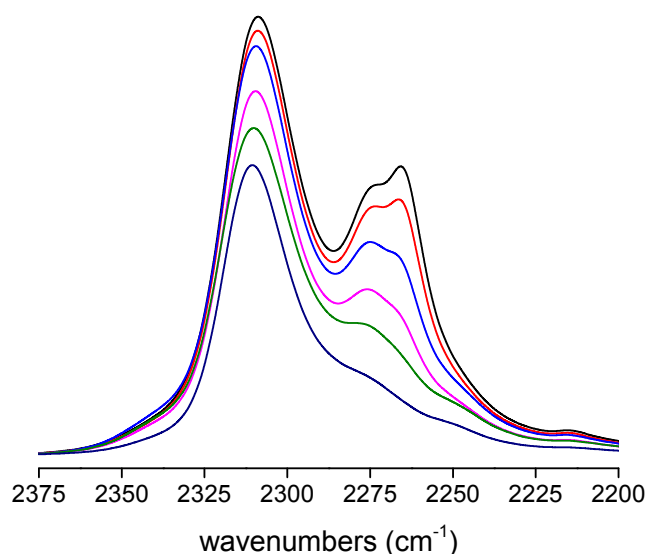


Figure 2.4. In situ CD_3CN adsorption/desorption profile for 10Sn/deAl-Beta-OH-25. CD_3CN was desorbed under a static vacuum for various time periods (increasing from top to bottom), and all spectra are background-referenced against the dehydrated zeolite sample.

A similar analysis of 8Zr/deAl-Beta-OH-25 and 4Ti/deAl-Beta-OH-25 demonstrated that these samples also contain isolated Lewis acid sites (Figure 2.5), though the strength of these Lewis acidic centers appears to be somewhat lower than those found in 10Sn/deAl-Beta-OH-25. For example, whilst evacuation of 10Sn/deAl-Beta-OH-25 for 4 minutes removed only weakly physisorbed CD_3CN , a similar treatment of 8Zr/deAl-Beta-OH-25 and 4Ti/deAl-Beta-OH-25 had a larger influence on the spectra (Figure 2.5),

with around one half of the CD_3CN -Lewis acid absorption feature being lost. Whilst both 8Zr/deAl-Beta-OH-25 and 4Ti/deAl-Beta-OH-25 are apparently much less Lewis acidic than 10Sn/deAl-Beta-OH-25, it is clear that the order of acidity follows the trend $\text{Sn} \gg \text{Zr} > \text{Ti}$.

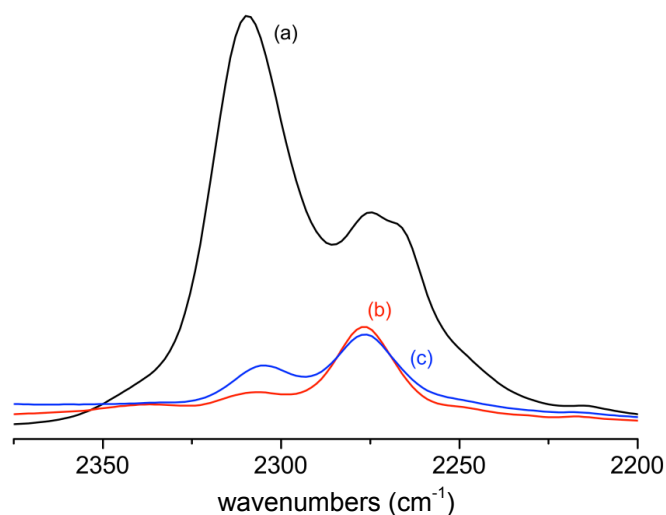


Figure 2.5. CD_3CN adsorption/desorption profile for (a) 10Sn/deAl-Beta-OH-25, (b) 8Zr/deAl-Beta-OH-25, and (c) 4Ti/deAl-Beta-OH-25, following desorption for 4 minutes.

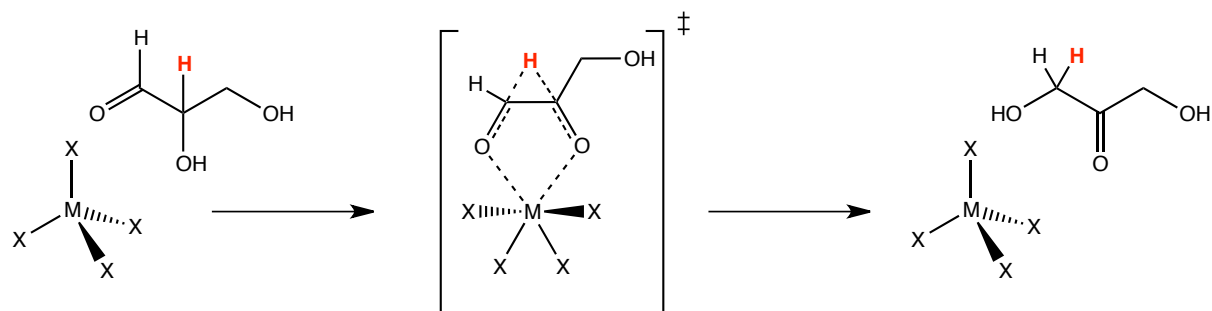
2.3.4. Isomerization of glyceraldehyde to dihydroxyacetone

Having established that each material contains isolated Lewis acid sites within the zeolite framework, we aimed to explore their relative catalytic activities for a series of reactions. As mentioned above, Lewis acid catalyzed isomerization has emerged as one of the most promising routes towards utilizing cellulose-based feedstocks for the synthesis of chemicals and fuels.^{36,96,105,146} Although there remains much debate as to the structure of the active Lewis acid site (whether the Lewis acid is fully coordinated to the zeolite framework (closed) or partially hydrolyzed (open)), this isomerization is known to proceed via a 1,2-hydride shift, and is catalyzed by the bidentate coordination of the reacting molecule (glucose) to the Lewis acidic center (Scheme 2.1).¹⁴⁷ The isomerization of glyceraldehyde to dihydroxyacetone is therefore an ideal model reaction to investigate the catalytic activity of Lewis acidic zeolites for such isomerization reactions.

However, despite its potential as a route towards utilizing bio-renewable feedstocks, this isomerization is a relatively slow reaction, and many consecutive and/or side products can also be formed. Thus, as a simpler and more facile model reaction, we utilized the analogous 1,2-hydride shift reaction involving isomerization of glyceraldehyde to dihydroxyacetone as a means of exploring the relative reactivities of

the synthesized catalysts. Nevertheless, in order to be fully representative of the isomerization of glucose to fructose, the isomerization of glyceraldehyde to dihydroxyacetone was performed in the aqueous phase.

Scheme 2.1. Schematic representation of the isomerisation of glyceraldehyde to dihydroxyacetone, catalysed by Lewis acidic zeolites.



M = Sn, Zr, Nb or Ti
X=siloxane bridge (M-O-Si) or OH

A recent theoretical analysis has proposed that for this specific aqueous phase reaction, the order of reactivity for these catalysts should be: $\text{Sn} \gg \text{Zr} > \text{Ti}$.¹⁰⁶ As can be seen (Figure 2.6), all synthesized solids demonstrate catalytic activity for this reaction, confirming their successful synthesis by post-synthetic methods.

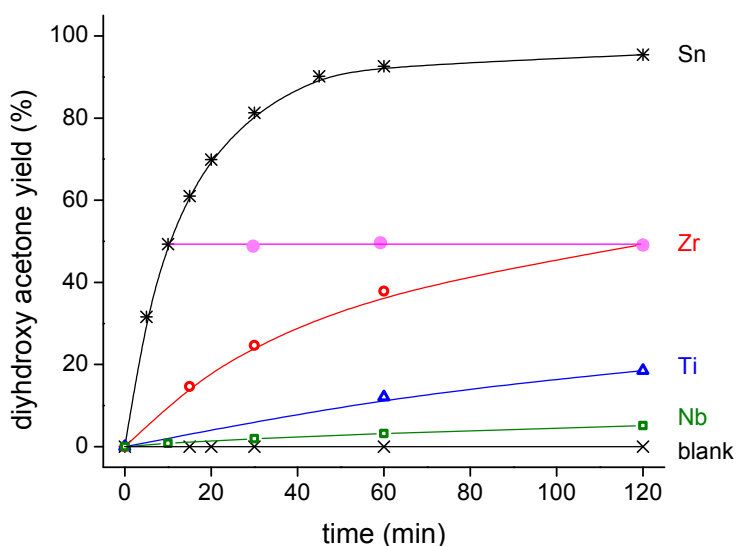


Figure 2.6. Catalytic activity of (*) 10Sn/deAl-Beta-OH-25, (○) 8Zr/deAl-Beta-OH-25, (□) 8Nb/deAl-Beta-OH-25, (△) 4Ti/deAl-Beta-OH-25, and (×) no catalyst, for the isomerisation of glyceraldehyde to dihydroxyacetone. Catalytic activity of supernatant solution after removal of 10Sn/deAl-Beta-OH-25 at 10 minutes is also indicated (●). Reaction conditions: 5 mL solution, 0.25 M glyceraldehyde in H₂O, 90 °C, substrate/metal ratio = 100.

Furthermore, and in excellent agreement with the theoretical calculations, our preliminary experiments demonstrate that 10Sn/deAl-Beta-OH-25 displays exceptional activity for the isomerization of glyceraldehyde ($R_{\text{init}} = 15.8 \text{ mmol min}^{-1}$), and that 8Zr/deAl-Beta-OH-25, 8Nb/deAl-Beta-OH-25 and 4Ti/deAl-Beta-OH-25 are at least one order of magnitude less active (2.8, 0.2 and 0.5 mmol min^{-1} , respectively). Similar observations were made for the 1,2-hydrate shift in the aqueous phase glucose isomerization, where the activity of Ti- β is also two orders of magnitude lower than the activity of Sn- β .⁷⁷ In all cases, dihydroxyacetone was the major product obtained at >95% selectivity, though trace quantities of pyruvic aldehyde were observed above 95% conversion.

It is clear that the order of reactivity is in agreement with both the apparent Lewis acid strength as obtained from in situ CD_3CN adsorption studies and the order of reactivity proposed by theoretical studies. To further examine this link between experiment and theory, we explored the catalytic activity of 10Sn/deAl-Beta-OH-25 over a temperature range of 50–100 °C, and found that the obtained Arrhenius temperature dependence ($16.6 \text{ kcal mol}^{-1}$) for 10Sn/deAl-Beta-OH-25 agrees to an excellent degree with the theoretical predictions of Assary and Curtiss ($15.4 \text{ kcal mol}^{-1}$; Figure 2.7).¹⁰⁶

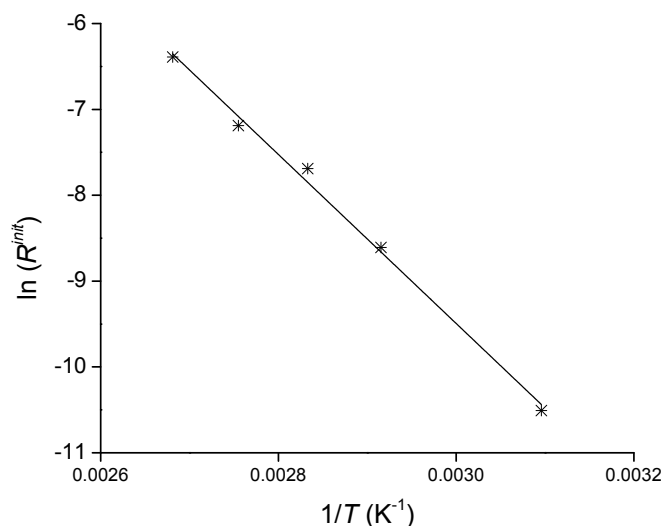


Figure 2.7. Arrhenius plot for 10Sn/deAl-Beta-OH-25 for the isomerisation of glyceraldehyde to dihydroxyacetone between 50 and 100 °C. An Arrhenius expression of $k(T) = 16.8 \text{ s}^{-1} \exp(-16.6 \pm 0.7 \text{ kcal mol}^{-1}/RT)$ was obtained.

2.3.5. Epoxidation of cyclooctene with H₂O₂

Despite the activity of all the catalysts for the isomerization of glyceraldehyde to dihydroxyacetone, the low activity of 8Nb/deAl-Beta-OH-25 and 4Ti/deAl-Beta-OH-25 makes an overall assessment of its synthesis difficult, particularly since its activity for isomerization reactions is predicted to be very low. Thus, to further verify the activity and nature of 8Nb/deAl-Beta-OH-25 and 4Ti/deAl-Beta-OH-25, we also explored the epoxidation of bulky olefins by H₂O₂ with this catalyst. The epoxidation of olefins is a key reaction in the bulk and fine chemical industries, and when performed with H₂O₂, is a particularly green method for introducing functionality into key platform molecules.

Table 2.2. Catalytic activity of 4Ti/deAl-Beta-OH-25 and 8Nb/deAl-Beta-OH-25 for cyclooctene epoxidation.^[a]

Entry	Catalyst	Preparation route ^[a]	TON ^[b]	TOF ^[c] [h ⁻¹]	Ref.
1	4Ti/deAl-Beta-OH-25	dealumination/ impregnation	96	17	This work
2	8Nb/deAl-Beta-OH-25	dealumination/ impregnation	99	99	This work
3	Ti-Beta ^[d]	hydrothermal synthesis	20	10	41
3	Ti-MWW ^[d]	hydrothermal synthesis	147	73.5	41

[a] reaction conditions: 80 °C, 0.5 M in 2-butanol, olefin/H₂O₂ = 1, 1 mol. % catalyst, [b] defined as mole epoxide produced per mole Ti, [c] mole epoxide produced per mole metal per hour, over the entire time course of the reaction. [d] reaction temperature 60 °C and acetonitrile as solvent.

As can be seen (Table 2.2), 4Ti/deAl-Beta-OH-25 demonstrates good catalytic activity for the epoxidation of cyclooctene, and is somewhat comparable in activity to other reported Ti-β catalysts prepared by more established preparation procedures, though it is still significantly lower in activity than the current state of the art Ti-containing epoxidation zeolite (Ti-MWW).⁴¹ The 8Nb/deAl-Beta-OH-25 on the other hand, showed excellent catalytic activity in the cyclooctene epoxidation with a 4 times larger TOF than the post-synthetic Ti-β material (Table 2.2 and Figure 2.8). We note here that both Zr and Sn-containing β zeolites are known to be inactive for such epoxidation reactions.

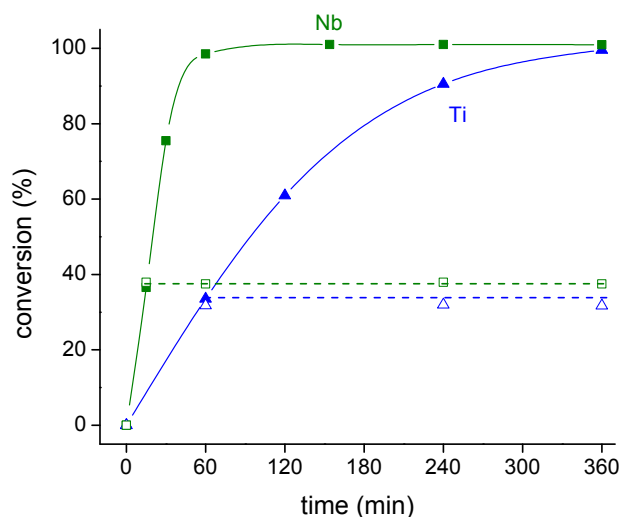


Figure 2.8. Catalytic activity of (\square)8Nb/deAl-Beta-OH-25 and (\triangle)4Ti/deAl-Beta-OH-25, for the epoxidation of cyclooctene. Catalytic activity of supernatant solution after removal of 8Nb/deAl-Beta-OH-25 and 4Ti/deAl-Beta-OH-25 after 15 and 60 minutes, respectively is also indicated with empty symbols. Reaction conditions: 10mL solution 80 °C, 0.5 M in 2-butanol, olefin/H₂O₂ = 1, 1 mol. % catalyst.

2.4. Conclusion

A two-step procedure for the post-synthetic preparation of Lewis acidic Sn-, Zr-, Nb- and Ti-zeolite β has been reported. Following dealumination of a parent aluminosilicate H- β zeolite, Lewis acidic centers can be incorporated into the vacant framework sites by solid-state ion-exchange (for Sn and Zr) or impregnation (Nb and Ti). The synthesized catalysts demonstrate excellent catalytic activity for the isomerization of glyceraldehyde to dihydroxyacetone and/or the epoxidation of bulky olefins with H₂O₂. We believe that the ability to post-synthetically prepare such Lewis acidic zeolites from readily available aluminosilicate analogues will lead to significant increases in the utilization of these promising catalysts on an academic and industrial scale.

Chapter 3

NMR Signatures of the Active Sites in Sn- β Zeolites

In this Chapter glucose isomerization and the physicochemical characterization of the materials was performed by myself. All NMR data was collected by Maxence Valla and Aaron Rossini. The DFT calculations were performed by Francisco Nunez-Zarur and Aleix Comas-Vives. Mössbauer spectroscopy was performed by Bernard Malaman.

3.1. Introduction

Heterogeneous catalysts with well-defined isolated active sites do not only facilitate mechanistic investigations, but can also show unparalleled activity in a variety of important reactions. One example is TS-1 for the epoxidation of propene with H_2O_2 .^{26,139,148} A more recent example is Sn- β , which consists of Sn^{IV} -sites embedded in the zeolite- β framework.^{125,149,150} The uniform distribution of isolated Lewis acid sites, in combination with the unique hydrophobic pore architecture of the material, results in an unrivalled catalytic performance. Of particular interest is the Lewis acid-catalyzed isomerization and epimerization of sugars, key transformations in the upgrading of cellulose-based renewable feedstocks.^{37,61,66,147} Sn- β is also active for other reactions, including the Baeyer–Villiger oxidation of ketones and aldehydes,^{30,128,151} the carbonyl-ene cyclization of citronellal,⁵¹ and the Meerwein–Ponndorf–Verley–Oppenauer reaction.^{50,126,152} Today, Sn- β can be conveniently synthesized with Sn-loadings varying between 0 and 10 wt %.^{84–86}

Despite the potential of this catalyst, the nature of its active site (distribution) is not fully determined. Various experimental investigations, including the adsorption of deuterated acetonitrile, point towards the presence of several different sites in the material, proposed as closed and open Sn^{IV} -sites, having three and four Sn-O-Si linkages with the zeolite framework, respectively.^{105,153} X-ray absorption fine structure (XAFS) spectroscopy on a 1.6 wt % sample¹¹⁷ showed that Sn was located in the six-

membered ring of the b-framework. The preferred location of Sn within the framework (so-called T-sites) is however still the topic of intense experimental and theoretical research.^{119,154} Another open question is how the Sn-loading and -distribution would affect the ratio between closed and opened Sn^{IV}-sites, and which of those sites would be active.

In principle, ¹¹⁹Sn solid-state NMR is an ideal method to probe the local structure at the Sn^{IV} sites. Indeed, major spectral differences have been observed between hydrated and de-hydrated samples, in particular when using isotopically enriched ¹¹⁹Sn (as a result of the low Sn loading, typically a low signal-to-noise ratio is obtained, necessitating ¹¹⁹Sn isotopic labeling).⁹⁴ For hydrated samples, the signals observed between $\delta_{\text{iso}} = -685$ and -736 ppm were assigned to octahedral Sn^{IV}. Dehydrated samples are characterized by signals at much higher chemical shift (between $\delta_{\text{iso}} = -425$ and -445 ppm), which based on CD₃CN adsorption studies have been proposed to correspond to tetrahedral open and closed Sn^{IV} sites, respectively.⁹⁷ However, the precise structure of the active sites remains unknown.

Herein we report the determination of the structure of the active sites in Sn- β as a function of Sn loading, by combining Mössbauer, dynamic nuclear polarization surface-enhanced NMR spectroscopy (DNP-SENS) and DFT calculations.

3.2. Experimental

3.2.1. Catalyst synthesis and characterization

Sn- β samples were synthesized and characterized as described elsewhere.⁸⁵ Glucose isomerization reactions in H₂O were carried out in a 25 mL sealed round bottom flask. The vessel was charged with aqueous glucose solution (10 mL of 5 wt%) and heated to 100°C for 15 min, prior to the addition of catalyst (100 mg). The reaction mixture was stirred vigorously at 500 rpm for the required reaction period. Samples were taken periodically and quantified by HPLC equipped with an RI detector. Monosaccharides were separated using a Ca²⁺ column (Phenomenex). ¹¹⁹Sn Mössbauer measurements were carried out using a constant-acceleration spectrometer in standard transmission geometry with a Ba^{119m}SnO₃ source (10 mCi) kept at room temperature as a reference for the isomer shifts. Spectra of each sample were recorded at 300 and 15 K in a liquid helium cryostat. The velocity scale was calibrated with a ⁵⁷CoRh source (25 mCi) and a metallic iron foil at room

temperature. A polycrystalline absorber with natural abundance of ^{119}Sn isotope and thickness of 15 mg cm^{-2} was used. A palladium foil of 0.5 mm thickness was used as a critical absorber for Sn X-rays. The Mössbauer spectra were fitted by using a unique doublet with a FWHM value of around 1.0 mm s^{-1} (see Table A1) with a least-squares method program assuming Lorentzian.¹⁵⁵ DNP solid-state NMR experiments were performed on a BrukerAvance III 9.4 T (400 MHz/263 GHz ^1H /electron Larmor frequencies) DNP spectrometer¹⁵⁶ equipped with a gyrotron microwave source. The sweep coil of the main superconducting NMR coil was set so that microwave irradiation occurred at the positive enhancement maximum for the TOTAPOL diradical.¹⁵⁷ Samples were prepared for DNP-SENS experiments by applying incipient wetness impregnation with a 16 mm solution of the TEKPol¹⁵⁸ biradical in 1,1,2,2-tetrachloroethane to the Sn- β zeolite materials. Typically the material (25 mg) was impregnated with biradical solution (20 mL) then packed into 3.2 mm outer diameter sapphire rotors. The ^{119}Sn spectra were acquired with a rotor synchronized CP spin echo pulse sequence and the full spin echo signal was acquired. CP experiments were typically performed with a $2.5\text{ }\mu\text{s}$ ^1H $\pi/2$ pulse for excitation and ^1H and ^{119}Sn spin lock rf fields of ca. 72 kHz and MAS frequencies of 12.5 kHz. The amplitude of the ^1H spin lock pulse was linearly ramped from 90 to 100% of its maximum value. Optimized contact times of 3.0 to 3.5 ms were used. SPINAL-64 heteronuclear ^1H decoupling was applied in all experiments.¹⁵⁷ The constant time five- π pulse MAT experiment of Grant and co-workers was employed for acquisition of the 2D ^{119}Sn chemical shift correlation spectra.¹⁵⁹ CS tensor parameters were obtained by fitting the sideband manifolds with the HBA-Graphic Analysis Program v1.7.3 (Dr. K. Eichele, University of Tübingen).

3.3. Results and Discussions

Sn- β zeolites with a Sn loading ranging from 0.5–10 wt% were prepared by a two-step post-synthetic method.⁸⁵ The synthesized materials were tested for the isomerization of glucose-to-fructose in water, and showed a decreasing turnover frequency (TOF) with increasing Sn loading (Table 3.1), similar to what has been observed by Dijkmans *et al.*⁸⁶ This observation suggests the presence of distinct Sn sites with different activities. No major difference is observed between samples of various loadings in ^{119}Sn Mössbauer spectroscopy, performed at 300 K and 15 K

(Figure A1). At 15 K, all spectra show a doublet with the hyperfine parameters, that is, an isomer shift, IS $0.07(3) \text{ mm s}^{-1}$ and a quadrupole splitting, QS $0.75(3) \text{ mm s}^{-1}$ (Table A1). The observed IS is consistent with a hexacoordinated Sn^{IV} site, with the large QS suggesting a distorted geometry.^{160,161} Moreover, based on the relative increase in spectral area between 300 K and 15 K, the Sn signals were assigned to framework sites. The small asymmetry in the experimental spectra may be due to either texture effects or the presence of minor (less than 2%) additional Sn^{IV} sites. Note that no SnO_2 was detected, consistent with Diffuse Reflectance UV/Vis and Raman data, while small amounts (less than 4%) of Sn^{II} are present, presumably arising from the initial Sn^{II} precursor used for the synthesis of Sn- β . For NMR spectroscopy in these systems, isotopic enrichment is usually required. Roy *et al.* have shown that conventional natural isotopic abundance direct polarization ^{119}Sn solid-state NMR spectra of Sn- β can be acquired, but such experiments required between 14 to 60 h of signal averaging for a single 1D ^{119}Sn NMR spectrum.⁹⁶

Table 3.1. Catalytic activity of Sn- β with different Sn loadings for glucose isomerization in H_2O .^[a]

Entry	Catalyst	$\text{TOF}_{\text{init}}^{\text{[b,c]}} [\text{h}^{-1}]$
1	0.5Sn/deAl-Beta-OH-25	76 ± 15
2	1Sn/deAl-Beta-OH-25	64 ± 11
3	2Sn/deAl-Beta-OH-25	34 ± 3
4	5Sn/deAl-Beta-OH-25	22 ± 0.6
5	10Sn/deAl-Beta-OH-25	10 ± 0.2
6	deAl-Beta-OH-25	n.d. ^[d]
7	SnO_2 / deAl-Beta-OH-25	n.d. ^[d]

[a] Reaction conditions: 100 mg of catalyst in 10 mL of a 5 wt % aqueous glucose solution at 373 K. [b] Defined as the mole product generated per mole Sn per hour calculated at the initial stage of the reaction. [c] Error estimated based on ICP-determined Sn-loading. [d] no product detected by HPLC after 4 h of reaction.

In a DNP experiment,¹⁶² the nuclear polarization is enhanced by microwave induced polarization transfer from unpaired electrons to nuclei (usually protons). For DNP-SENS the unpaired electrons are introduced by contacting the material by incipient wetness impregnation with a solution of a nitroxide diradical, specifically bulky 2,6-spirocyclohexylnitroxide derivatives¹⁶³⁻¹⁶⁵ in tetrachloroethane solutions.¹⁶³⁻¹⁶⁵ In the case

of nanoparticulate and mesoporous samples, impregnation brings the radical solution into direct contact with the surface of the material allowing the polarization of the protons near the surface to be highly enhanced by DNP. This enhanced ^1H polarization is then transferred to the hetero-nuclei (e.g., ^{13}C , ^{27}Al , ^{29}Si , ^{119}Sn) at the surface.¹⁶⁶⁻¹⁶⁸ Some of us recently demonstrated the rapid acquisition of natural abundance ^{119}Sn signals in core-shell ligand-capped Sn/SnO_x nanoparticles using DNP-SENS NMR.¹⁶⁹ In our current work, an analogous methodology is used to investigate the molecular structure of the Sn^{IV}-sites in Sn- β .¹⁷⁰ Samples for ^{119}Sn DNP-SENS were prepared by impregnating the zeolites with a 16 mM solution of TEKPol¹⁵⁸ in tetrachloroethane.

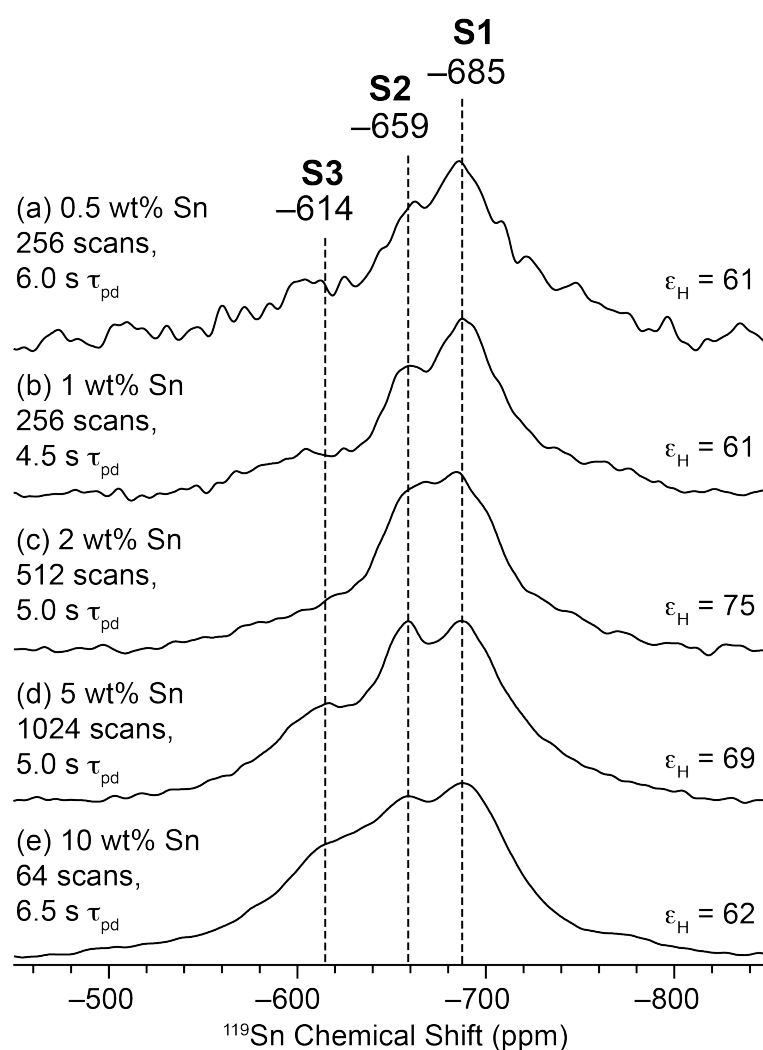


Figure 3.1. 9.4 T 105 K ^1H - ^{119}Sn DNP-SENS magic-angle spinning cross-polarization spin echo spectra of a) 0.5Sn/deAl-Beta-OH-25 zeolite, b) 1Sn/deAl-Beta-OH-25 zeolite, c) 2Sn/deAl-Beta-OH-25 zeolite, d) 5Sn/deAl-Beta-OH-25 zeolite, e) 10Sn/deAl-Beta-OH-25 zeolite. All samples were impregnated with a 16 mM TEKPol 1,1,2,2-tetrachloroethane solutions. All spectra were acquired with a MAS frequency of 12.5 kHz and CP contact times between 3.0 and 3.5 ms. The number of scans and polarization delay (τ_{pd}) are indicated for each spectrum together with the proton DNP enhancements (ϵ_{H}) measured with separate ^1H spin echo experiments. The signals around $\delta = -580$ and -780 ppm, as observed for the 10 wt % sample, correspond to spinning sidebands. See text for details.

Since the pores of Sn- β are quite small (ca. 7 Å diameter), the TEKPol radical is not able to enter the material and cannot interact with the Sn sites. The pores of the Sn- β will be filled with tetrachloroethane and/or water from ambient moisture. Enhanced ^1H polarization will be generated at the surface of the Sn- β particles and then transported into the interior of the particles by ^1H spin diffusion along the channels (as has been observed for MOF samples).¹⁷¹⁻¹⁷⁴ Since the Sn- β particles are quite small (200–400 nm), high ^1H DNP enhancements (greater than 60, corresponding to an acceleration by a factor of 3600 in time) were obtained in all cases, enabling the rapid acquisition of natural abundance ^{119}Sn cross-polarization magic-angle spinning (CPMAS) NMR spectra even for low loading levels (0.5 wt% Sn). By comparison, the ^{119}Sn CP NMR spectra acquired without microwave irradiation, and the same number of scans showed no signal, even for high loaded samples. The total spectrometer time required to obtain all the data in Figure 3.1 was only 3 h. Acquisition can be further accelerated by the application of CP-CPMG pulse sequences (Figure A2).¹⁷⁵ In all spectra, three isotropic Sn chemical shifts centered at approximately $\delta = -614$ (**S3**), -659 (**S2**), and -685 ppm (**S1**) were identified from both 1D CP spin echo (Figure 3.1) and 2D CPMAT ^{119}Sn spectra (see below). The relative intensity of these sites varies as a function of Sn-loading level (Figure 3.1 and Figure A3). Cross-polarization magic-angle turning (CPMAT) experiments¹⁵⁹ were recorded on the 1Sn/deAl-Beta-OH-25 and 5Sn/deAl-Beta-OH-25 samples. A CPMAT spectrum correlates the MAS sideband manifolds to a single isotropic chemical shift in the indirect dimension. This method allows the chemical shift anisotropy (CSA) to be measured for each ^{119}Sn site of the overlapping sideband manifolds. The Sn CSA arises from the anisotropy of the electronic distribution around the Sn nucleus. CSA parameters are often described by the isotropic chemical shift (δ_{iso}), the span (Ω) and the skew ($-1 \leq \kappa \leq +1$) which are calculated from the principal tensor components of the chemical shift tensor $\delta_{11} \geq \delta_{22} \geq \delta_{33}$:¹⁷⁶ [Eq. (3.1)-(3.3)].

$$\delta_{iso} = (\delta_{11} + \delta_{22} + \delta_{33})/3 \quad (3.1)$$

$$\Omega = (\delta_{11} - \delta_{33}) \quad (3.2)$$

$$\kappa = 3(\delta_{22} - \delta_{iso})/\Omega \quad (3.3)$$

δ_{iso} is the average of the three components of the CSA tensor and is analogous to the chemical shift that is observed in solution NMR spectroscopy. Ω describes the magnitude of the anisotropy and reports on the degree of spherical symmetry of the electronic distribution at the nuclear site, while κ describes the axial symmetry of the tensor. The 2D-CPMAT of the 5Sn/deAl-Beta-OH-25 is shown in Figure 3.2, where the isotropic NMR spectrum can be observed in the indirect dimension (F1) and the normal CP spectrum (isotropic peaks and spinning sidebands) can be observed in the direct dimension (F2). Fitting of the sideband manifolds extracted from the direct dimension at the position of the corresponding provides the CS tensor parameters (δ_{iso} , Ω and κ). The signal S3 at $\delta = -614$ ppm is similar to that observed for bulk SnO₂, and this site is found to have a Ω of 162 ppm and a κ of + 0.13, consistent with the octahedral environment of Sn in SnO₂. This resonance has previously been assigned to extra-framework SnO₂ and is typically observed at high Sn-loadings (greater than 1 wt%). In addition, the two other signals at $\delta = -659$ (S2) and $\delta = -685$ ppm (S1) are associated with slightly different CSA parameters (S2: $\Omega = 155$ ppm and $\kappa = + 0.05$ and S1: $\Omega = 146$ ppm and $\kappa = + 0.21$). The chemical shifts and the skews (κ) close to 0 point toward a slightly distorted octahedral Sn environments (see below).

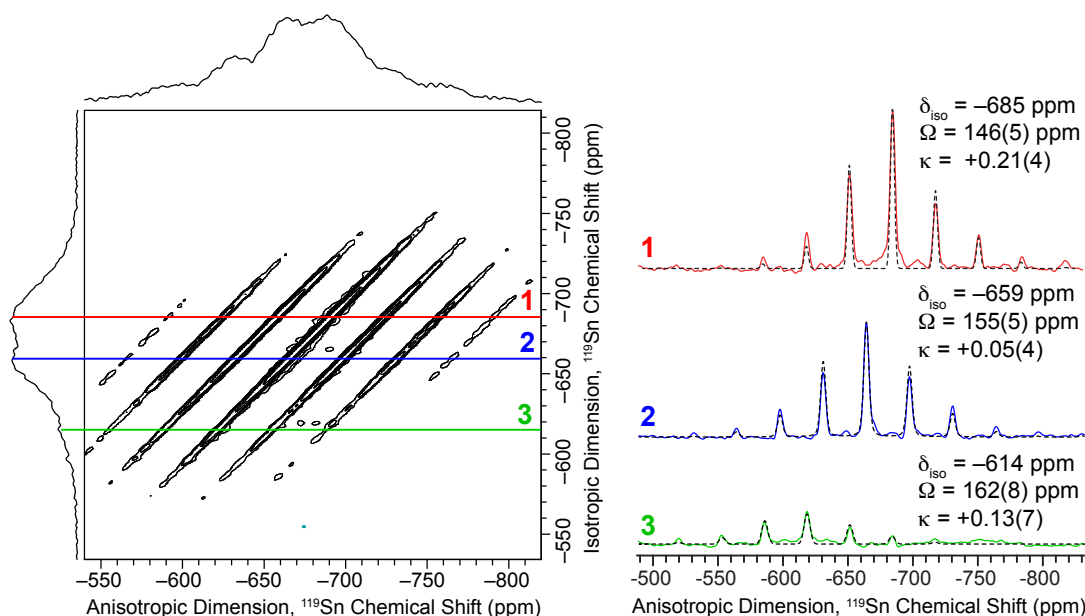


Figure 3.2. 105 K ¹¹⁹Sn DNP SENS CP Magic Angle Turning (CP-MAT) spectra of 5Sn/deAl-Beta-OH-25 zeolite impregnated with a 16 mM solution of TEKPol in tetrachloroethane. The spectrum was acquired on a 400 MHz DNP spectrometer, with a sample spinning frequency of 5 kHz and a polarization delay of 5 s. 512 scans per increment and 160 t_1 increments were acquired. A ¹H DNP enhancement of ca. 85 was obtained. Spinning sideband manifolds are shown for the three different isotropic shifts and the extracted CS tensor parameters are indicated. Fits of the sideband manifolds are also shown (dashed black lines).

The 2D-CPMAT experiment on $^{119}\text{Sn}/\text{deAl-Beta-OH-25}$ (Figure A4) shows the two peaks at $\delta = -659$ ppm and $\delta = -685$ ppm with similar CSA parameters as observed in the $^{119}\text{Sn}/\text{deAl-Beta-OH-25}$ sample, consistent with the presence of similar species, suggesting that increased loading does not change the nature of Sn species, but only their ratio. The one-dimensional ^{119}Sn DNP-SENS CPMAS spectra were deconvoluted (Figure A5) and the relative ratio of each species evaluated (Table 3.2). Note that since DNP and CP are used to obtain the spectra, it is not possible to quantitatively evaluate the amount of each site, but that this analysis should provide an estimate of the variation of the relative ratio of each site. At low loading, Sn- β is constituted mainly of S1, and increased loading leads to increased intensity of S3, associated with extra framework SnO_2 , while the relative amount of S2 is approximately constant as a function of the loading level. Reconciling these deconvoluted spectroscopic data with the catalytic activity results in Table 3.1 suggests that the sites associated with signals S1 and S2 are both active in the glucose-to-fructose isomerization (see Figure A6). Note that a significant amount of SnO_2 is detected by DNP-SENS even though it was not observed with Mössbauer, Raman and UV/Vis spectroscopies. It is therefore likely that the SnO_2 clusters are located outside the zeolite framework, closer to the polarizing agent where the DNP enhancement will be higher.

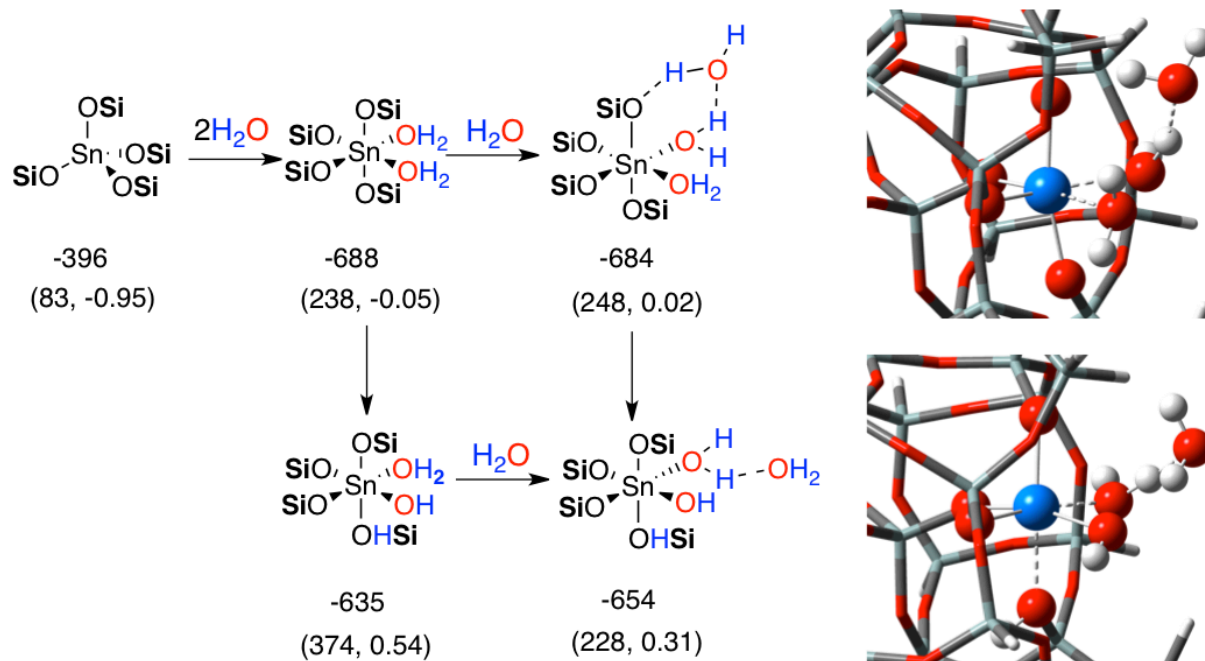
Table 3.2. Relative contribution of the three ^{119}Sn signals (deconvoluted areas in percentage) as a function of the Sn loading as determined from DNP-SENS showing a qualitative trend in active site-distribution.

Entry	Catalyst	S3 [%] $\delta = -614$ ppm	S2 [%] $\delta = -659$ ppm	S1 [%] $\delta = -685$ ppm
1	0.5Sn/deAl-Beta-OH-25	8	27	65
2	1Sn/deAl-Beta-OH-25	8	28	64
3	2Sn/deAl-Beta-OH-25	11	36	53
4	5Sn/deAl-Beta-OH-25	16	35	49
5	10Sn/deAl-Beta-OH-25	24	29	47

To relate these observations directly to the local structure of the Sn environment, DFT calculations on cluster models were carried out to assign the observed NMR signatures. We first used a small cluster model of the T-site to screen several structural possibilities and to calibrate the methodology. Details on the models and the methodologies are given in the Supporting Information (see for example, Table

A2) for an overview of all structures that were investigated). For the most realistic cluster model, that includes the zeolite framework, the tetrahedral site has a calculated δ_{iso} of -396 ppm, in good agreement with experimental values (see above), and the chemical shift decreases by approximately 100 ppm with the addition of each (1 or 2) coordinated water molecule (see Supporting Information). The hexacoordinated Sn sites, resulting from the coordination/reaction of at least two water molecules, have calculated NMR parameters consistent with the experimental values. When Sn-sites have two water molecules in the first coordination sphere and one additional water molecule H-bonded to the coordinated H_2O , the calculated NMR parameters are in very good agreement with the experimental chemical shift parameters: $\delta_{\text{iso}}/\Omega/\kappa$ of $-654/228/0.31$ and $-684/248/0.02$ for open or closed sites, respectively, allowing the assignment of S2 ($\delta = -654$ ppm) to an open site and S1 ($\delta = -685$ ppm) to a closed site, coordinated by two H_2O molecules (Scheme 3.1). It has to be noted that the defect-open site model was used to for calculations on the open site. This means that one of the Si atoms adjacent to the Sn atom is removed, which results in the presence of dangling O atoms terminated with H.

Scheme 3.1. Computed ^{119}Sn isotropic chemical shifts in ppm (δ_{iso} , upper numbers outside of parenthesis). The span Ω (in ppm) and skew κ are shown in parenthesis. The optimized geometries including the zeolite framework are depicted for the two structures on the right.



The low Ω and a value of κ close to 0 are consistent with distorted octahedral sites. In terms of stability, the T1 sites with two coordinated water molecules (closed site) are energetically more favored by approximately 5 kcal mol⁻¹ than the corresponding opened site with one coordinated H₂O and one Sn-O-Si bridge opened by H₂O (Table A4). However, the presence of an additional water molecule on the second coordination sphere is crucial to stabilize the opened site structure by hydrogen bonding (see Table A4), which is otherwise highly unstable (+ 19 kcal mol⁻¹).

3.4. Conclusions

In summary, combining Mössbauer spectroscopy, DNP-SENS, and DFT calculations show that the active sites of Sn- β zeolite correspond to octahedrally coordinated Sn^{IV}, involving the tetrahedral Sn-sites and two water molecules. In agreement with earlier literature hypotheses two types of Sn are determined herein: one where two water molecules are coordinated to Sn (closed site), and another where one of the water molecules has opened one of the Sn-O-Si bridges (open site). These two species, with distinct NMR signatures, are the active sites of Sn- β zeolite.

Correlating Synthetic Methods, Morphology, Atomic-Level Structure and Catalytic Activity of Sn- β Catalysts

In this Chapter the catalytic data and the physicochemical characterization of the materials was performed by myself. All NMR data was collected by Maxence Valla and Aaron Rossini. The DFT calculations were performed by Francisco Nunez-Zarur and Aleix Comas-Vives.

4.1. Introduction

Isomorphous substitution of a small fraction of the Si^{IV} centers in the crystalline framework of zeolites with Lewis acids results in promising heterogeneous catalysts.³⁶ In particular, Sn^{IV} centers incorporated into zeolite β (BEA topology) catalyze a number of atom-efficient and industrially attractive transformations, such as the Baeyer-Villiger oxidation with hydrogen peroxide,^{30,128} the Meerwein-Ponndorf-Verley-Oppenauer hydrogen-transfer reaction^{50,109,126} and the isomerization of monosaccharides.^{37,177} More recently, Sn- β has also been found to promote direct aldol reactions⁶⁹ and other C-C coupling reactions in the development of new routes for the production of important intermediates such as α -hydroxy- γ -butyrolactone⁶³ and 4-(hydroxymethyl)benzoic acid derivatives⁵⁷.

Sn- β is traditionally synthesized by direct incorporation of Sn^{IV} centers into the zeolite β framework during hydrothermal synthesis.^{30,37,126,128,177,178} Unfortunately, this procedure is typically associated with long synthesis timescales, and only limited amounts of Sn may be incorporated. For these reasons, there has been a large effort in developing faster synthesis protocols^{80,81} and post-synthetic methods (*i.e.*, incorporating Sn into dealuminated β zeolite) to produce Sn- β .^{67,85,86} However, the catalytic activities of the resulting materials strongly depend on the synthetic method. It is, however, not clear that materials obtained by different synthetic routes result in Sn^{IV} sites having the same molecular environment. In addition, the nature and identity of the active sites in

Sn- β themselves are still matter of intense debate. The challenge in determining the active sites is pronounced as the crystal structure of the zeolite BEA shows nine crystallographically distinct sites,¹¹⁷ referred to as “T-sites” as depicted in Figure 4.1 (top). All of these sites can potentially be substituted by Sn, a problem generally observed for zeolites containing heteroatoms.¹¹⁶ Vjunov *et al.* recently combined EXAFS and solid state NMR to quantitatively probe the Al-distribution in the corresponding commercial Al- β .¹⁷⁹

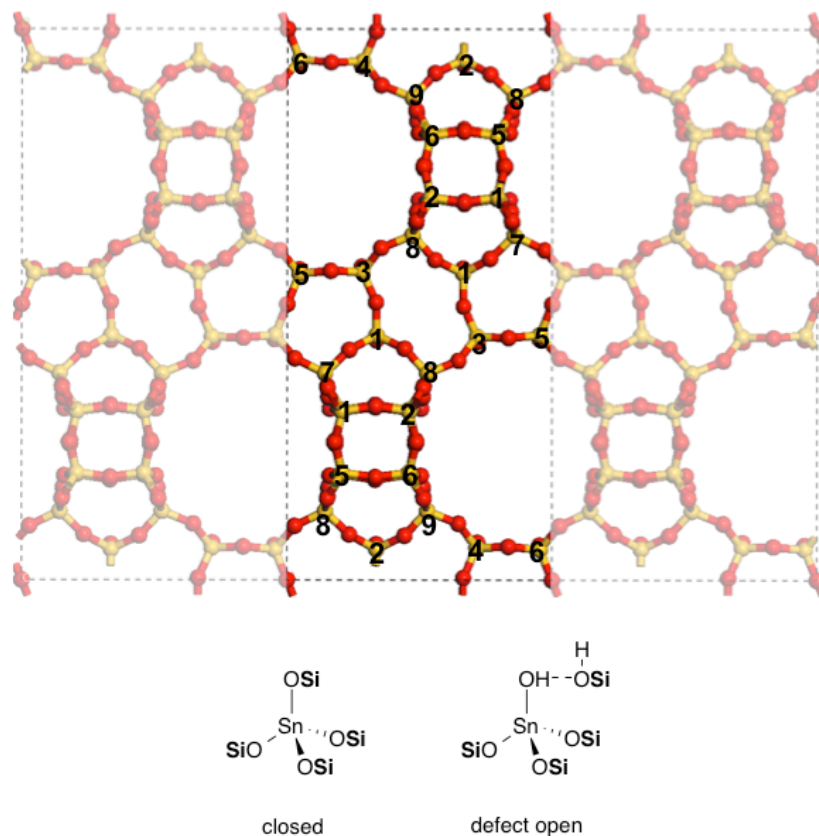


Figure 4.1. Crystal structure of the BEA zeolite framework with labeling of the distinct T-sites (*top*). The proposed “closed” and “defect-open” Sn^{IV}-sites in dehydrated form resulting from substitution of Sn^{IV} into a Si^{IV} T-site (*bottom*).

Solid-state NMR spectroscopy has emerged as a powerful technique to identify the structure of Sn-containing materials and can be used to investigate the differences in structures and environments of Sn^{IV} centers in different Sn- β materials. Davis and co-workers acquired ¹¹⁹Sn solid-state NMR spectra of ¹¹⁹Sn-labeled Sn- β obtained from hydrothermal synthesis.⁶⁵ In their study, ¹¹⁹Sn isotopic enrichment was required because of the combined low natural abundance of ¹¹⁹Sn (NA = 8.6 %) and the low Sn-content of the samples (typically 1-2 wt%). It was proposed that both “closed” [(SiO)₄Sn] and “open” [(SiO)₃Sn(OH)] Sn sites are present in these materials¹⁰⁵ (Figure 4.1, bottom) and

that the open sites would be most active for the glucose isomerization.^{65,102} Density functional theory (DFT) calculations on cluster models also suggest a higher inherent activity of the open site due to enhanced site flexibility and a synergistic effect with the adjacent silanol group.^{107,108}

More recently Dynamic Nuclear Polarization Enhanced NMR Spectroscopy (DNP-NMR)^{162,166,168} was shown to be an expedient method to obtain ¹¹⁹Sn NMR signatures of Sn-β zeolites with natural isotopic abundance ¹¹⁹Sn within short acquisition time (minutes to hours).¹⁷⁰ (Chapter 3) In particular, the significant reduction in experimental time made possible by DNP-NMR allows for recording two dimensional ¹¹⁹Sn magic angle turning (MAT) NMR spectra and thereby obtaining both isotropic ¹¹⁹Sn chemical shifts and ¹¹⁹Sn chemical shift anisotropy (CSA) parameters, which is not possible by conventional solid-state NMR due to the low sensitivity (Chapter 3). Since the CSA is very sensitive to the symmetry and the chemical nature around the Sn center, its measurement provides direct information on the Sn-site structure and further insight to the Sn sites in Sn-β zeolites. In particular we have shown that the incorporation of Sn in a post-synthetic approach led to the presence of mainly two isolated Sn sites in hydrated samples with NMR chemical shifts of -659 ppm and -685 ppm, consistent with the presence of two octahedral Sn sites in different environments (Chapter 3). It is worth noting that the DNP enhanced ¹¹⁹Sn solid-state NMR spectra of Sn-β prepared *via* direct hydrothermal synthesis showed a distinct resonance at -700 ppm.¹⁷⁰ Earlier work, using conventional ¹¹⁹Sn solid-state NMR (with ¹¹⁹Sn isotopic labeling), showed isotropic chemical shifts ranging from $\delta_{\text{iso}} = -685$ to -736 ppm.⁹⁷ The observation of distinct ¹¹⁹Sn chemical shifts in Sn-β prepared by different synthetic routes suggests the presence of different Sn^{IV}-sites in the otherwise seemingly similar Sn-β samples.

Sels *et al.* recently presented a detailed experimental study using EXAFS, XANES, UV-Vis and TPR to compare the active sites in post-synthetically grafted Sn-β and hydrothermal Sn-β. A new Sn-site for post-synthetic liquid phase grafted Sn-β was proposed, where the Sn is coordinated with three framework SiO⁻ and one distant charge-balancing SiO⁻.¹⁸⁰ Furthermore, a different T-site occupancy was suggested for post-synthetic Sn-β vs. hydrothermal Sn-β. Sn sites in different T-sites could have different electronic properties, site accessibility, and also different proximity to silanol groups, which could all contribute to the catalytic activity.

With the fundamental aim of understanding the differences between various Sn-β catalysts at an atomic level and to correlate the structure of the active sites and the

catalytic activity, we prepared Sn- β catalysts by solid-solid ion-exchange from dealuminated β zeolite and by traditional hydrothermal synthesis. Microscopy, powder X-ray diffraction (pXRD) and adsorption isotherms (N_2 , Ar, H_2O) were used as complementary characterization techniques. ^{119}Sn and ^{29}Si DNP-NMR, combined with DFT calculations, are used to obtain an atomic description of the surface sites. Correlation between catalytic activity for the aqueous phase glucose-fructose isomerization and the presence of specific sites according to DNP-NMR and DFT calculations allows the construction of a map of spectroscopic signatures of the different Sn sites. This enables structure-activity relationship and shows that the most active materials in our series consist of predominantly closed sites in T6 and T5/T7 of a hydrophobic zeolite β framework in the as-synthesized sample.

4.2. Experimental

4.2.1. Synthesis of Al- β in Fluoride media

Al- β in fluoride media was prepared by hydrothermal synthesis according to a literature procedure.⁷³ First Aluminum powder (99.99%, Acros) was dissolved in an aqueous solution of tetraethyl ammonium hydroxide, TEAOH (35%, SACHEM). After complete dissolution of the aluminum the solution was added to a tetraethyl-orthosilicate (TEOS; 98%, Sigma-Aldrich) plus TEAOH solution. The resulting mixture is stirred until complete evaporation of ethanol, formed upon TEOS hydrolysis. To the resulting viscous gel, hydrofluoric acid (48%, Sigma-Aldrich) was added to result in a gel with the following composition: 1 SiO_2 : x Al_2O_3 : (0.54+2x) TEAOH : (0.54+2x) HF : (7+2x) H_2O . Crystallization was carried out at 140 °C in 45 mL scale teflon-lined stainless-steel autoclaves, tumbled at 60 rpm for 7 days. After cooling down, the samples were filtered and subsequently washed with deionized water and acetone before drying them in an oven at 110 °C over night. To remove the structure directing agent, samples were calcined at 580 °C under a steady air flow for 6 h.

4.2.2. Solid-solid ion-exchange post synthesis of Sn- β .

Post-synthetic incorporation of Sn was performed in two steps as described elsewhere.¹⁸¹ Dealumination of the parent Al- β zeolites was done by acid leaching (13 M HNO_3 , 20 mL g^{-1} , 100 °C, 20 h). Sn was incorporated via solid-solid ion-exchange by grinding the dealuminated β with the appropriate amount of the tin(II) acetate precursor (Sigma Aldrich) followed by subsequent 3 h heat treatments under N_2 and air

at 550 °C. Sn/deAl-Beta-OH represents the post-synthetic material from starting from commercial Al- β zeolite ($\text{SiO}_2/\text{Al}_2\text{O}_3=25$ Zeochem and $\text{SiO}_2/\text{Al}_2\text{O}_3=300$, Zeolyst), while the Sn/deAl-Beta-F ($\text{SiO}_2/\text{Al}_2\text{O}_3=30,400$) is synthesized from the Al- β synthesized in fluoride media *vide supra*.

4.2.3. Hydrothermal synthesis of Sn- β

Sn- β zeolites via direct incorporation of Sn during hydrothermal synthesis with and without the use of β seeds were prepared following literature protocols.^{95,182} TEOS was added to a TEOH solution under stirring. After a single phase was obtained, the desired amount of Sn ($\text{SnCl}_4 \cdot 5 \text{H}_2\text{O}$, 98%, STREM) dissolved in H_2O was added dropwise. The solution was stirred open to evaporate ethanol and water until a viscous gel was obtained. Addition of hydrofluoric acid resulted in a solid gel with the molar composition 1.0 SiO_2 : 0.01 SnCl_4 : 0.55 TEOH : 0.55 HF : 7.5 H_2O . In case of Sn-Beta-seed a solution of dealuminated Beta seeds in water was added. Crystallization was carried out at 140 °C in 45 mL scale teflon-lined stainless-steel autoclaves, tumbled at 60 rpm for 14 days. After cooling down, the samples were filtered and subsequently washed with deionized water and acetone before drying them in an oven at 110 °C over night. To remove the structure directing agent, samples were calcined at 580 °C under a steady air-flow for 6 h.

4.2.4. Catalyst Characterization

Powder diffraction patterns were recorded on a Bruker D8 advance diffractometer using $\text{Cu-K}\alpha_1$ radiation and a Lynxeye detector. Relative crystallinity was calculated by integration of the d_{302} -reflection at 22.4 2θ using the Bruker DIFFRAC.EVA software. Al, Si and Sn contents were determined by ICP-AES on a Perkin Elmer Optima 2000 at 396.152, 251.611 and 189.927 nm respectively after acid digestion. Scanning electron microscopy (SEM) was performed using a LEO SUPRA 55 VP S3 field-emission scanning electron microscope operated at 5 kV. N_2 sorption measurements were performed on a Micromeritics 3Flex apparatus at 77K. Samples were degassed under vacuum at 350°C for 3h prior to analysis. The surface area and the pore volume were calculated using the Brunauer-Emmett-Teller (BET) and the t-plot theory respectively. The linear range of the BET plot was chosen following Rouquerol et al.¹⁸³ and is $p/p_0 = 0.005-0.03$. Argon adsorption experiments were performed at 87 K. The nonlinear density functional theory (NLDFT) model describing argon adsorption in cylindrical micro- and mesopores of metal oxides was used to calculate the pore size distribution. Water sorption

experiments were performed on a Micromeritics 3Flex instrument at 298 K. Water was purified by three freeze and thaw cycles and zeolite samples were degassed under vacuum at 350 °C for 3h prior to analysis. Microporous water uptake was determined at the relative pressure p/p_0 that showed complete filling of the micropores in the N_2 adsorption.

Dynamic Nuclear Polarization NMR Spectroscopy (DNP NMR) was used to reduce the acquisition time of solid-state NMR by several orders of magnitude. The nitroxide biradical polarizing agents was TEKPol.¹⁵⁸ Incipient wetness impregnation with 1,1,2,2-tetrachloroethane (TCE) biradical solution with a concentration of approx. 16 mM biradical was used to prepare the samples for DNP NMR experiments. The impregnated samples were packed into sapphire rotors and the samples were frozen at around 105 K inside the low temperature 3.2 mm MAS probe head. Samples were typically subjected to multiple insert-eject cycles and left under an eject gas flow prior to insertion in order to reduce the amount of oxygen in the TCE solution and increase DNP enhancements.¹⁸⁴ Dehydrated samples were subjected to a heat treatment at 500 °C (ramp of 10 °C per min) under high vacuum (10^{-5} mbar) over night. Experiments were performed with a 400 MHz (9.4 T)/263 GHz Bruker DNP system.¹⁵⁶ The sweep coil of the main magnetic field was set so that microwave irradiation occurred at the 1H positive enhancement maximum of nitroxide biradicals. Cross Polarization Magic Angle spinning (CPMAS)¹⁸⁵ with a ramped 1H spin lock pulse¹⁸⁶ was then used to transfer polarization from the 1H nuclei to the nucleus of interest (^{119}Sn or ^{29}Si). A radio frequency field of 100 kHz was always used for the 1H excitation while 50 to 100 kHz RF field was used for either ^{119}Sn or ^{29}Si excitation. In some cases, ^{119}Sn CPMAS spectra were also acquired with total suppression of spinning sidebands (TOSS)¹⁸⁷. For all the samples, the 1H longitudinal relaxation time (T_1) was measured using a saturation recovery type experiment. For subsequent CPMAS experiments the polarization delay was then set to $1.3 \cdot T_1$ to obtain optimal sensitivity. 2D CP-magic angle turning (CPMAT) NMR spectra correlating isotropic ^{119}Sn chemical shifts to their spinning sideband manifolds (containing isotropic and anisotropic shifts) were acquired with the $5-\pi$ pulse sequence of Grant and co-workers.¹⁸⁸

4.2.5. Catalytic testing

All reactions were performed in 10 mL thick wall tube reactors capped with a PTFE/silicone seal, capable of holding 15 bar over-pressure. For the glucose isomerization reactions in H_2O , the reactor was charged with aqueous glucose solution

(5 mL of 5 wt %) and heated to 100 °C for 15 min, prior to the addition of catalyst (50 mg). The reaction mixture was stirred vigorously at 500 rpm for the required reaction period. Samples were taken periodically and quantified by HPLC equipped with an RI detector. Monosaccharides were separated using a Ca²⁺ column (Phenomenex Rezex RCM).

Isotopic tracer studies were performed similar to a literature procedure.⁷⁶ To 1 mL of a 5 wt% aqueous glucose solution of D-glucose-d₂ (Cambridge Isotope Laboratories, 2-D, 98%) in a 1.5 mL GC vial equipped with a magnetic stir bar, 10 mg of Sn-β were added. The reaction mixture was stirred in a heated oil bath to 100 °C. After 2 h of reaction the reaction mixture was quenched, the catalyst separated by centrifugation and the product mixture concentrated by rotary evaporation. The concentrated product mixture was then dissolved in D₂O (99.9 atom% D, Sigma Aldrich). Solution ¹H-NMR spectra were measured on a Bruker Avance 400 MHz spectrometer averaging 8 scans at a rate of 2 scans per second.

4.3. COMPUTATIONAL DETAILS

The structures of the nine T clusters and their corresponding hydrated species were fully optimized with the Gaussian 09 code.¹⁸⁹ These geometries were obtained with the B₃LYP-D₃ density functional, which accounts for the B₃LYP functional¹⁹⁰⁻¹⁹³ with Grimme empirical dispersion corrections and Becke-Johnson damping (D₃BJ)^{194,195}. A combination of different basis sets was used in order to obtain the ground state geometries and energies: Sn was described by the LanL2DZ effective core pseudopotential (ECP)¹⁹⁶⁻¹⁹⁸ augmented with a *d* polarization function, whereas the O-atoms directly bonded to Sn (including O-atoms of water in hydrated species) were described by a 6-31+G(*d*) basis set. The Si atoms, the rest of O atoms and the H atoms were described by the 6-31G(*d,p*) basis set.

Calculations of the NMR parameters^{199,200} were carried out at the B₃LYP-D₃ level as implemented in the ADF code.²⁰¹ The all electron TZP basis set²⁰² for all atoms was used in this case. Relativistic and spin-orbit coupling were taken into account through the ZORA method^{203,204} for the calculation of the isotropic chemical shift (δ_{iso}), the span (Ω) and skew (κ) of all considered species. For the calculation of δ_{iso} the chemical shielding of Sn(CH₃)₄ was used as reference. The applied methodology has been previously tested for molecular and surface Sn species and showed excellent agreement with experiments within ca. 10 ppm.²⁰⁵

4.4. Results and Discussions

4.4.1. Catalyst performance and characterization

Sn- β zeolites with metal loadings of 1.0 ± 0.2 wt % were prepared by both hydrothermal synthesis and post-synthetic incorporation into dealuminated β zeolites. Direct hydrothermal synthesis was carried out in fluoride media with and without the use of β zeolite seeds. The seeded sample was formed by adding nano-sized dealuminated β zeolite crystals. Post-synthetic Sn- β samples were prepared starting from two commercial Al- β zeolites, which were synthesized in a hydroxide media, with $\text{SiO}_2/\text{Al}_2\text{O}_3$ ratios of 25 or 300 (denoted as Sn/deAl-Beta-OH-25 and Sn/deAl-Beta-OH-300, respectively). We also prepared our own Al- β zeolite synthesized in fluoride media with $\text{SiO}_2/\text{Al}_2\text{O}_3$ ratios of 30 or 400 and then synthesized post-synthetic Sn- β zeolite (denoted as Sn/deAl-Beta-F-30 and Sn/deAl-Beta-F-400, respectively).

The materials were tested for the equilibrated isomerization of glucose-to-fructose in water, where Sn- β samples obtained from post-synthetic modification (Table 4.1, entries 1-4) in general showed a 2-5 times lower initial activity per total amount of Sn compared to the hydrothermal materials (Table 4.1, entry 5 and 6). The formation of fructose *via* the base-catalyzed enolization pathway by hydroxide ions in solution was excluded performing isotopic tracer studies with D-glucose-d₂. All catalysts selectively formed fructose products with the deuterium labeling at the first carbon, indicated by the absence of the ¹H resonance at $\delta = 3.47$ ppm (Figure 4.2). This unambiguously confirms that fructose is exclusively formed *via* intramolecular 1,2-hydride shift over Lewis acid Sn centers.¹⁴⁷ In agreement, no indication for the presence of interzeolite SnO₂ was found (*vide infra*). Moreover, reacting glucose with dealuminated β zeolite did not show any activity and performing a hot filtration test confirmed the heterogeneous nature of the catalysis, since after removal of the catalyst no further production of fructose was observed. The observation of the different activity per Sn therefore suggests an inherent difference in the physical and/or chemical properties of the Sn- β zeolites prepared *via* the two different methods.

Table 4.1. Activity and activation energies of different Sn- β zeolites in the aqueous phase isomerization reaction of glucose.^{a,f}

Entry	Catalyst ^b	Activity per Sn _{init} ^{c,d} [h ⁻¹]	Fructose Yield ^e [%]	Fructose Selectivity ^e [%]	E_{app}^f [kcal mol ⁻¹]	Pre-exponential factor $A^{f,g}$
<i>Sn-β From Post-Synthetic Incorporation</i>						
1	Sn/deAl-Beta-OH-25	55 ± 12	8	68	23.7 ± 2.8	34.0 ± 3.8
2	Sn/deAl-Beta-OH-300	50 ± 10	8	68	21.4 ± 2.3	30.8 ± 3.2
3	Sn/deAl-Beta-F-30	48 ± 10	9	68	22.2 ± 1.9	32.3 ± 2.6
4	Sn/deAl-Beta-F-400	128 ± 16	21	68	21.3 ± 1.0	32.0 ± 1.4
<i>Sn-β From Hydrothermal Synthesis</i>						
5	Sn-Beta-seed	280 ± 50	28	67	-	-
6	Sn-Beta	279 ± 32	29	66	21.4 ± 0.9	33.1 ± 1.1

^aReaction conditions: 50 mg of catalyst in 5 mL of a 5 wt % aqueous glucose solution (0.3 M) at 100 °C.

^bSn/deAl-Beta: Sn incorporated into dealuminated β by solid-solid ion-exchange; OH: parent Al-Beta zeolite synthesized in hydroxide media; F: parent Al-Beta zeolite synthesized in fluoride media; 25: SiO₂/Al₂O₃ ratio of parent zeolite; Sn-Beta: hydrothermally synthesized Sn- β zeolite; seed: β seed crystals added to the synthesis gel. ^cDefined as the mole product generated per mole Sn per hour calculated at the initial stage of the reaction. ^dError based on ICP-OES determined Sn-loading. ^eAfter 1h of reaction. ^frates are measured in mole product formed per second normalized per total mole metal in the catalyst; temperatures for Arrhenius plot range from 80-110°C (Figure A16). ^g units: (mol · dm³)(mol Sn · s · mol glucose)⁻¹

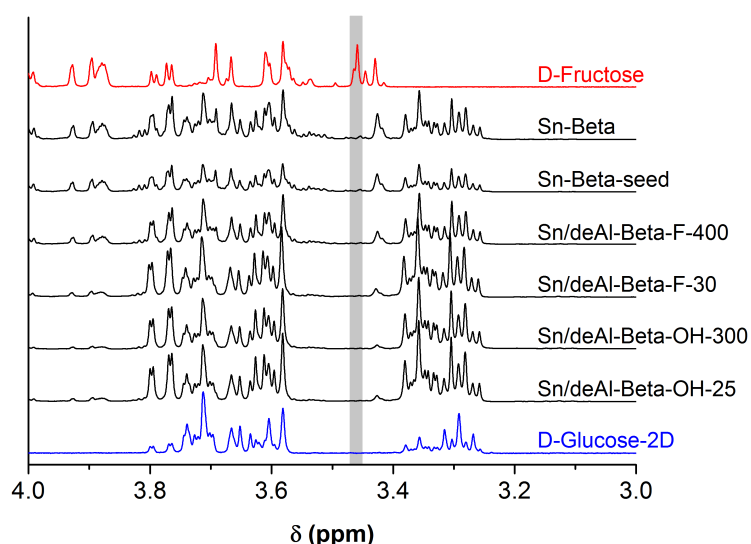


Figure 4.2. ¹H NMR spectra of reaction mixtures from D-glucose-2D isomerization after 2h at 100°C with the Sn- β samples tested in this study. The $\delta=3.47$ ppm is characteristic for the ¹H in the C1 position of the D-fructose. The absence of this resonance confirms the selective formation of D-Fructose-1D from D-glucose-2D *via* 1,2-hydride shift over the Lewis acid Sn sites.

It was shown that the hydrophobicity of micro- and mesoporous oxides has a strong influence on the efficiency of aqueous phase biomass conversions.^{93,76} Therefore, H₂O adsorption isotherms were recorded to measure the hydrophobicity of all the different Sn- β zeolites (Figure 4.3). Independent of seeding, a Type III adsorption isotherm²⁰⁶ was observed for both of the Sn- β zeolites prepared *via* direct hydrothermal Sn incorporation. On the other hand, the H₂O isotherms for the Sn- β samples prepared from commercial Al- β zeolites (Sn/deAl-Beta-OH-25 and Sn/deAl-Beta-OH-300) showed a Type II adsorption isotherm.²⁰⁶

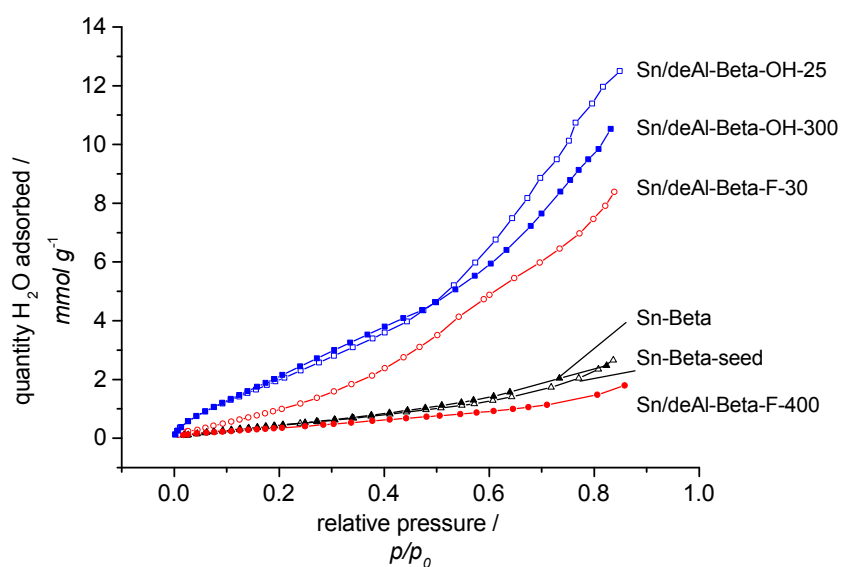


Figure 4.3. H₂O adsorption isotherms at 298 K for post synthetic Sn- β catalysts obtained from parent zeolites synthesized in hydroxide media (*blue*), post synthetic Sn- β obtained from parent zeolites synthesized in fluoride media (*red*) and Sn- β catalysts prepared *via* traditional hydrothermal synthesis (*black*).

The amount of water adsorbed in both the micro- and mesopores was significantly higher (see Table A5), indicating a more hydrophilic framework, probably associated with the presence of defect sites within the BEA framework (Si-OH groups, see below). In the case of the Sn/deAl-Beta-OH-25, this observation is not surprising since at Sn-loadings of 1 wt%, less than 10% of the vacant T-sites created during dealumination are filled. Parent deAl-Beta-OH-300 can theoretically fit 1.25 wt% of Sn, so ca. 80% of the silanol nests should be closed after Sn incorporation. However, very similar H₂O adsorption behavior, especially in the microporous region, was observed for both of the Sn/deAl-Beta-OH zeolites (Figure 4.3, blue), suggesting that the majority of the hydrophilic defect sites are already present in the parent Al- β zeolites (²⁹Si solid-state NMR confirms this, see below). From literature, it is well known that zeolites synthesized in a fluoride media possess less connectivity defects than those obtained

from hydroxide media, resulting in a material with higher hydrophobicity.²⁰⁷ Indeed the H₂O adsorption isotherms of post-synthetic Sn-β zeolites prepared from Al-β synthesized in fluoride media show a significant improvement in the hydrophobicity of the catalyst (Figure 4.3, red). As for the hydroxide mediated Sn/deAl-Beta-OH samples, slightly more water was adsorbed at higher relative pressure on the sample with lower SiO₂/Al₂O₃ ratio. This is likely due to silanol nests created during acid treatment of the dealumination step. For the Sn/deAl-Beta-F-400, where all vacant T-sites should be filled with Sn^{IV}, a Type III adsorption isotherm identical to the ones obtained for the Sn-β zeolites from direct hydrothermal synthesis was observed. The total water uptake per gram of catalyst was determined to be around 5 times lower than for the Sn/deAl-Beta-OH-25. We conclude from these experiments that the post-synthetic Sn/deAl-Beta-F-400 material has very similar hydrophobicity properties to the direct hydrothermal

Sn-β samples. Although improved catalytic performance was observed, Sn/deAl-Beta-F-400 did not reach the benchmark activity of the materials obtained through direct incorporation of the metal (Table 4.1, entries 5 and 6).

BET areas between 610 and 650 m² g⁻¹ were obtained from N₂ adsorption measurements at 77 K for all Sn-β samples, except for the Sn/deAl-Beta-F-400 where a BET area of 554 m² g⁻¹ was obtained. Micropore and mesopore volume, as well as the external surface area, were extracted from the t-method²⁰⁸ (Table A5). Slightly smaller micropore volume is observed for all post-synthetic materials, while the mesopore volume and the external surface area was higher for the two samples obtained from commercial zeolites and the Sn/deAl-Beta-F-30. The Sn/deAl-Beta-F-400 and both direct hydrothermal Sn-β zeolites exhibit significantly lower external surface area, *i.e.* larger crystal size resulting from retarded crystallization in fluoride mediated synthesis. Scanning Electron Microscopy (SEM) confirmed the difference of one order-of-magnitude in crystal size (Figure A12). To assess the microporosity of the β zeolites more accurately, argon adsorption measurements at 87 K were performed for the different materials. A pore size of 6.2 ± 0.1 Å was determined for both, post-synthetic Sn/deAl-Beta zeolites and hydrothermal Sn-β (Figure A13).

Another possible explanation for the superior catalytic performance of the materials prepared by direct incorporation vs. post-synthetic incorporation of the Lewis acid center could be a higher crystallinity of the zeolitic material. Therefore, powder X-ray diffractograms (pXRD) were collected and the degree of crystallinity of the different

zeolites was assessed by integration of the d_{302} -reflection at $2\theta = 22.4$ (Table A5). The characteristic powder pattern of the BEA type was observed for all samples (Figure 4.4). No direct correlation between the crystallinity of the post-synthetic Sn- β catalysts and the activity in the aqueous phase glucose isomerization could be observed. However, a higher crystallinity was detected for the materials known to exhibit less defect sites, *i.e.* those featuring a more hydrophobic framework (*vide supra*).

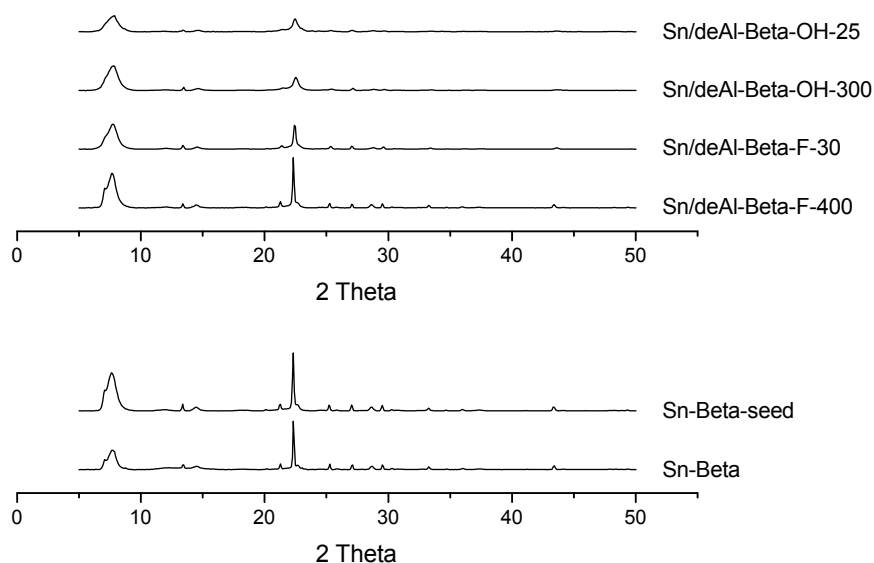


Figure 4.4. Powder X-ray diffraction patterns obtained for post-synthesis Sn- β (*upper*) and hydrothermal Sn- β catalysts (*lower*).

Considering the physical properties of the Sn- β samples, *i.e.* hydrophobicity, particle size, pore size distribution and crystallinity, one can conclude that when starting from a parent zeolite prepared *via* the fluoride route with a high Si/Al ratio, a post-synthetic Sn- β , *i.e.* Sn/deAl-Beta-F400 can be obtained which is very similar to traditional hydrothermal Sn- β . However, the hydrothermal Sn- β still shows a 2.2 times higher activity than post-synthetic Sn/deAl-Beta-F400 in terms of initial activity per Sn in the aqueous phase glucose isomerization. We also evaluated the apparent activation energies for the different Sn- β samples. Therefore, aqueous phase glucose isomerization reactions were performed at temperatures between 353-383 K allowing measuring activation energies of 21-24 kcal mol⁻¹, in agreement with literature data.^{4b} Moreover, from the Eyring equation activation enthalpies of 16-19 kcal mol⁻¹ were determined (Figure A17). Both confirm that catalytic tests were not run under mass transfer limitations. However, this does not explain the difference by a factor of 2.2 in the activity between the Sn/deAl-Beta-F400 and the two hydrothermal zeolites that

have very similar if not identical physicochemical properties. Possible explanations for the difference in activity are site accessibility of the active Sn-site for glucose and a different site distribution in terms of the nature of the active Sn site and the T-site occupancy. The latter results in a different local site geometry and possibly restrictions of bound intermediates and transition states. Recently it was demonstrated that by titrating the active sites in Sn-Beta, the amount of open and closed sites could be quantified.⁷⁶ Correlating the number of active sites with the catalytic activity showed that the open sites in Sn-Beta are the dominant active sites for aqueous glucose isomerization. However different hydrophobic Sn-Beta zeolites showed heterogeneity in activity per open Sn site, which has been hypothesized to result from the different local environment of the Sn site (T-site position).⁷⁶

Table 4.2. Activity of different Sn- β zeolites in the aqueous phase isomerization reaction of glyceraldehyde.

Entry	Catalyst ^b	Activity per Sn _{init} ^{c,d} [h ⁻¹]	DHA Yield ^e [%]	DHA Selectivity ^e [%]
<i>Sn-β From Post-Synthetic Incorporation</i>				
1	Sn/deAl-Beta-OH-25 ^f	144 ± 18	13	>99
2	Sn/deAl-Beta-OH-300	122 ± 4	10	>99
3	Sn/deAl-Beta-F-30	156 ± 36	14	>99
4	Sn/deAl-Beta-F-400 ^f	868 ± 107	43	95
<i>Sn-β From Hydrothermal Synthesis</i>				
5	Sn-Beta-seed	-	-	-
6	Sn-Beta	764 ± 74	43	98

^aReaction conditions: 27 mg of catalyst in 5 mL of a 0.3 M aqueous glyceraldehyde solution at 70 °C.

^bSn/deAl-Beta: Sn incorporated into dealuminated β by solid-solid ion-exchange; OH: parent Al-Beta zeolite synthesized in hydroxide media; F: parent Al-Beta zeolite synthesized in fluoride media; 25: SiO₂/Al₂O₃ ratio of parent zeolite; Sn-Beta: hydrothermally synthesized Sn- β zeolite; seed: β seed crystals added to the synthesis gel. ^cDefined as the mole product generated per mole Sn per hour calculated at the initial stage of the reaction. ^dError based on ICP-OES determined Sn-loading. ^eAfter 20 min of reaction. ^f activation energies for this sample can be found in Table A6.

Therefore we first tested the different materials in the aqueous phase glyceraldehyde isomerization where all sites are assumed to be accessible due to the smaller size of the glyceraldehyde molecule compared to the glucose. Similar to glucose, zeolites having a hydrophilic framework showed significant lower activity per Sn for the isomerization of glyceraldehyde to dihydroxyacetone (Table 4.2, entry 1-3). On the other hand the

hydrophobic materials show a more than 5 times higher initial catalytic activity (Table 4.2 entry 4-6). In contrast to the glucose isomerization the Sn/deAl-Beta-F-400 performs as good as, if not slightly better than, the hydrothermal Sn-Beta. Initial activity per Sn was in general about 3 times higher than for the glucose isomerization. For the Sn/deAl-Beta-F400 the activity per Sn was even 7 times higher for glyceraldehyde compared to glucose isomerization. Thus it is feasible to hypothesize that not all active Sn-sites are accessible for the glucose (as they are for glyceraldehyde).

In order to provide an atomic level description of the Sn- β zeolites, *i.e.* to identify the local environment of the Sn sites and to evaluate the corresponding nature of the active sites, we performed NMR measurements of all the synthesized materials. This complements the other physical measurements and catalytic activity data and provides further insights into the differences at atomic level between all the zeolite materials. For this purpose, ^{29}Si and ^{119}Sn DNP NMR experiments were performed to investigate the molecular structure of the Sn^{IV} centers. Incipient wetness impregnation with a tetrachloroethane (TCE) solution of a stable bulky 2,6-spirocyclohexyl nitroxide derivative,^{163,164,1747} here TEKPol,¹⁵⁸ was used to prepare the Sn- β samples for the DNP experiments. Since the pores of Sn- β are ca. 6 Å (*vide supra*), the TEKPol radicals do not enter the pores of the material, and hence they do not directly interact with the Sn^{IV}-sites. Instead, DNP enhances the polarization of the ^1H nuclei of adsorbed water and TCE molecules near the surface of the zeolite particles. The enhanced ^1H polarization at the surface of the particles is then relayed into the interior of the zeolite particles by ^1H spin diffusion amongst the ^1H nuclei of the TCE and the absorbed water (from ambient moisture) that fills the pores (Chapter 3).¹⁷⁰⁻¹⁷⁴ The DNP enhanced ^1H polarization can then be transferred to hetero-nuclei such as ^{119}Sn or ^{29}Si by conventional ^1H -X cross polarization (CP)²⁰⁹ experiments. DNP signal enhancements of 10-200 can typically be realized in this way, resulting in a dramatic reduction in experiment time and allowing natural isotopic abundance ^{119}Sn NMR experiments at low Sn loadings.

To also ensure that the TCE molecules do not interfere with the Sn Lewis acid center a DNP experiment with a d3/d8-toluene (ratio=1/9) solution of TEKPol and a dehydrated 1Sn/deAl-Beta-OH sample was performed. As expected significantly lower enhancement compared to the TCE solution of TEKPol was observed (Figure 4.5). Importantly, the spectrum obtained with the toluene mixture and the one with the TCE mixture are qualitatively the same. In case an interaction of TCE with the Sn-site would

be present, a clear shift upfield, similar to the coordination of a water molecule would be expected. Calculations on a closed Sn-site with TCE nearby confirmed the experimental findings. A distance around 5 Å between the Sn center and the TCE molecule was obtained in the optimized structure. The calculated NMR parameter with and without TCE are almost identical, therefore the interaction of TCE with the Sn-site can be excluded.

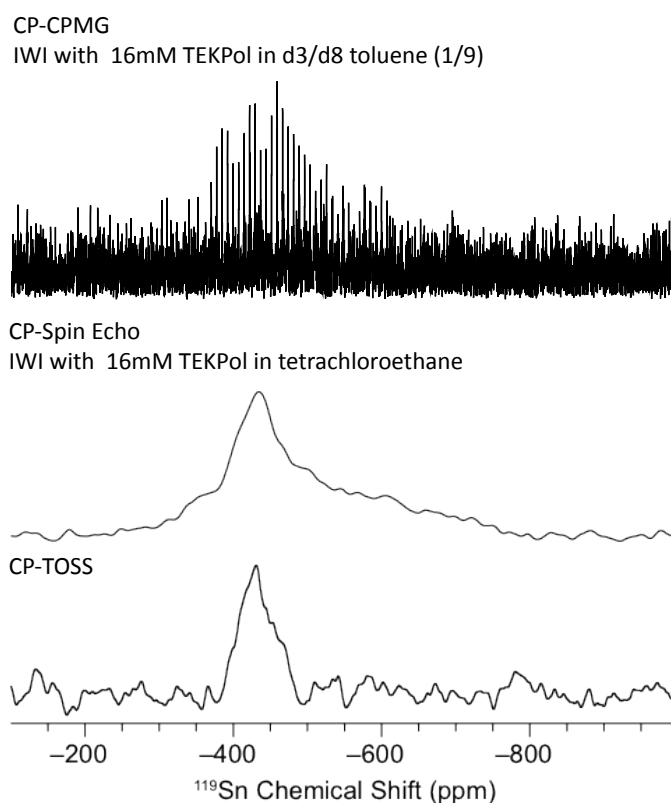


Figure 4.5. Comparison of DNP enhanced ^1H - ^{119}Sn CP-CPMG with TEKPol in d_3/d_8 toluene (1/9) solution and CP-echo (A) and CP-TOSS (B) spectrum with TEKPol in TCE of dehydrated Sn/deAl-Beta-OH-25.

DNP enhanced ^{29}Si and ^{119}Sn cross-polarization magic-angle spinning (CPMAS) NMR spectra were collected for all of the different Sn- β catalysts (Figure 4.6). We note that ^{29}Si solid-state NMR experiments are useful to understand how DNP and spin diffusion proceed in the zeolites. ^{29}Si NMR spectra allow the proton DNP enhancement *inside the pores of the zeolite* to be measured, since ^{29}Si CPMAS provides enough sensitivity to acquire a reference NMR spectrum without DNP. On the other hand, direct measurement of the ^1H DNP enhancements (ϵ_{H}) by ^1H solid-state NMR provides a measure of the DNP enhancement wherever the impregnating solvent is located, in this case inside and outside the pores. Therefore, during the process of optimizing sample preparation for DNP, the DNP enhancement inside the pores of the zeolite should be measured by ^{29}Si CPMAS experiments, rather than relying upon direct

measurements of proton DNP enhancements. Since ^1H spin diffusion transports DNP enhanced ^1H polarization into the zeolite smaller zeolite particles should yield the highest $\epsilon_{\text{Si CP}}$.^{171,172} However there are many factors which influence the absolute DNP enhancement such, hydration level, dielectric properties and degree of de-oxygenation, therefore, we do not observe a strong correlation between particle size and the observed $\epsilon_{\text{Si CP}}$.

The ^{29}Si DNP CPMAS spectra corroborate the results obtained by H_2O adsorption and pXRD. The ^{29}Si DNP NMR spectra of the different Sn- β catalysts show Q_3 $[(\text{SiO})_3\text{SiOH}]$ and Q_4 $[(\text{SiO})_4\text{Si}]$ Si^{IV} -sites with characteristic ^{29}Si isotropic chemical shifts centered around $\delta_{\text{iso}} = -104$ and -115 ppm, respectively. Q_3 sites correspond to defect sites in the material, *i.e.* hydroxylated Si^{IV} sites that are only partially bound to the zeolite framework. The ^{29}Si DNP CPMAS spectra of both the post-synthetic Sn- β 's prepared in hydroxide media and the post-synthetic Sn/deAl-Beta-F-30 prepared in fluoride media (where there is not enough Sn^{IV} to fill the vacant silanol nests), show very intense Q_3 $[(\text{SiO})_3\text{SiOH}]$ peaks. This is consistent with the pXRD and H_2O adsorption measurements indicating that these materials are the most defected and hydrophilic, respectively. For the post-synthetic Sn/deAl-Beta-F-400 Sn- β there are few, if any, defect sites present in the parent zeolite, and all of the created T-site vacancies are filled with Sn. In this case, little or no Q_3 sites were observed in the ^{29}Si NMR spectra. The same is true for the Sn- β prepared *via* hydrothermal synthesis where Q_3 ^{29}Si NMR signals are weak or absent. This is consistent with the high degree of crystallinity and hydrophobicity of these Sn- β samples.

DNP enables the rapid acquisition of ^{119}Sn solid-state NMR spectra and can be used to probe the structure of the Sn sites in order to understand the molecular level origin of the activity differences amongst the different Sn- β . 2D ^{119}Sn DNP-NMR magic angle turning (MAT) spectra of the different hydrated Sn- β catalysts were acquired (Figure A21-A25) in order to measure both isotropic Sn chemical shifts and Sn chemical shift tensors. Projections of the indirect isotropic dimension of the DNP enhanced ^{119}Sn MAT NMR spectra (which only show isotropic Sn chemical shifts, *i.e.*, spinning sidebands are absent) are shown in Figure 4.6. The projections were fit with simple mixed Gaussian/Lorentzian lineshapes in order to determine distinct isotropic chemical shifts (δ_{iso}). Table 4.3 summarizes the chemical shifts at the center of each peak and their relative integrated intensities. To evaluate how quantitative are the DNP enhanced ^{119}Sn solid-state NMR spectra and that relative integrated intensity are not affected by

the DNP enhancements we performed experiments on Sn/deAl-Beta-OH-25 with variable polarization delays and variable CP contact times. DNP enhanced ^{119}Sn CPMAS spectra acquired with polarization delays ranging from 2 to 30 seconds (Figure A18) show that the relative intensities within the ^{119}Sn NMR spectrum are constant. This suggests that the DNP enhancements for all Sn sites are similar; sites with higher DNP enhancements should be characterized by faster signal build-ups since they would reside closer to the polarizing agents at the surface of the zeolite particles. DNP enhanced ^{119}Sn NMR acquired with variable CP contact times (0.5 ms to 8 ms, Figure A19) show that the relative intensities in the ^{119}Sn NMR spectra are constant. These experiments suggest that intensities observed in the DNP enhanced ^{119}Sn CPMAS spectra are pseudo-quantitative since all ^{119}Sn sites exhibit the same CP dynamics and signal build-up rates, and suggest that the integrated intensities in Table 4.3 are not substantially biased.

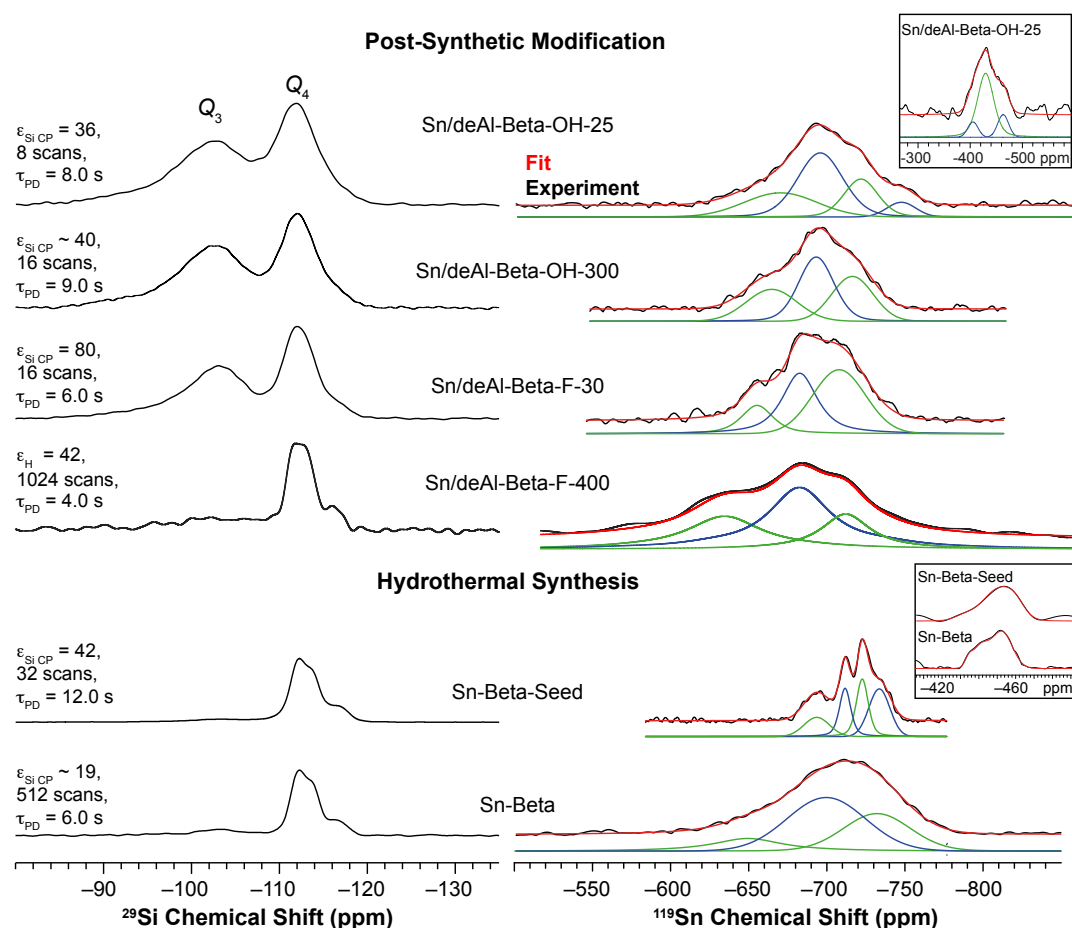


Figure 4.6. 9.4 T 105 K ^1H - ^{29}Si (left) DNP-NMR magic-angle spinning cross-polarization spin echo spectra and the 1D projections of ^1H - ^{119}Sn (right) DNP-NMR cross-polarization magic-angle turning spectra (see Figure A21-A25) of various Sn- β catalysts in the hydrated form. For the Sn/deAl-Beta-F-400 a ^1H - ^{119}Sn cross-polarization spectra with total suppression of spinning sidebands (TOSS)^{210,211} is shown. ^1H - ^{119}Sn DNP-NMR magic-angle spinning cross-polarization spin echo spectra of dehydrated Sn/deAl-Beta-OH-25 and both hydrothermal Sn- β samples are shown in the insets.

The corresponding chemical shift (CS) tensor parameters¹⁷⁶ for each isotropic shift were obtained from 2D magic angle turning (MAT) experiments. For Sn/deAl-Beta-F-400, MAT experiments were not collected, since poor sensitivity prevented the acquisition of a 2D MAT spectrum in a reasonable experiment time. The poor sensitivity likely arises from a low DNP enhancement, which is caused by the larger zeolite particle size (as confirmed by SEM, see Figure A12). However, for hydrothermal synthesized Sn catalysts, which possess a similar crystal size to Sn/deAl-Beta-F-400, sensitivity of the DNP enhanced ¹¹⁹Sn NMR experiments was good enough to allow rapid acquisition of MAT spectra, which suggests that the Sn indirect DNP enhancements were high. Therefore we hypothesize that a difference in the spatial distribution of the Sn centers within the zeolite crystal is causing the lower sensitivity. Tolborg *et al.* recently showed that Sn is preferentially located in the outer rim of Sn zeolite crystals prepared by hydrothermal synthesis.³³ A more uniform distribution in Sn/deAl-Beta-F-400 could explain the lower DNP enhancement due to a longer diffusion length into the crystal to polarize the Sn-site (see SEM-EDX of Sn/deAl-Beta-F-400 in Figure A14).

For all tested materials no SnO₂, associated with a ¹¹⁹Sn signal at -600 ppm, was detected by ¹¹⁹Sn NMR, which is consistent with the UV-Vis of all materials (Figure S5). For post-synthetic Sn/deAl-Beta zeolites in all cases the ¹¹⁹Sn MAS spectra could satisfactorily fit with a maximum of four distinct Sn-sites (Table 4.3) and the most intense ¹¹⁹Sn NMR resonances were centered around -680 to -690 ppm. The ¹¹⁹Sn DNP SENS CP-TOSS spectrum of the dehydrated Sn/deAl-Beta-OH-25 was also acquired. ¹¹⁹Sn NMR chemical shifts characteristic of the dehydrated four fold coordinated Sn sites in Sn-β were observed. It is important to note that the DNP enhanced ¹¹⁹Sn CP spin echo showed substantial intensity ranging from a chemical shift of -380 ppm to -780 ppm (Figure 4.5), indicating that not all adsorbed water molecules could be removed although the sample was dehydrated at 500°C over night under high vacuum (10⁻⁵ mbar). This observation is consistent with the higher hydrophilicity of Sn/deAl-Beta-OH-25 in comparison to hydrothermal Sn-β samples and was also observed for post-synthetic Sn-β prepared via liquid phase grafting.¹⁸⁰ Moreover, a chemical shift of -560 ppm was observed, consistent with the presence of penta-coordinated Sn and a mono-hydrated species as proposed by Hwang *et al.* in a recent study¹⁰² and further supported by our calculations (*vide infra* and Figure A39). In the case of the hydrothermal Sn-β the ¹¹⁹Sn resonances are clearly shifted to lower chemical shifts. Fits of the ¹¹⁹Sn DNP NMR spectra yielded three to four distinct Sn^{IV} sites with δ_{iso} as low as -734 ppm.

Table 4.3. ^{119}Sn solid-state NMR signatures of the different Sn-b catalysts prepared by different synthetic methods.

δ_{iso} (ppm)	Ω (ppm)	$\kappa(-)$	Peak width at half height (ppm)	Relative intensity (%)
<i>Sn/deAl-Beta-OH-25 (dehydrated)</i>				
-464	–	–	25	17
-430	–	–	37	71
-405	–	–	23	11
<i>Sn/deAl- Beta-OH-25 (hydrated)^a</i>				
-748 ^b	–	–	22	6
-722	114	0.4	26	21
-696	124	0.2	34	47
-670	131	0.1	55	26
<i>Sn/deAl- Beta-OH-300 (hydrated)</i>				
-716	141	0.1	31	32
-693	133	0.2	27	41
-664	129	0.2	38	27
<i>Sn/deAl- Beta-F-30 (hydrated)</i>				
-708	126	0.1	40	47
-683	139	0.0	27	38
-655	140	0.0	24	15
<i>Sn/deAl- Beta-F-400 (hydrated)</i>				
-716	–	–	64	27
-689	–	–	59	43
-653	–	–	63	30
<i>Sn-Beta-seed (dehydrated)</i>				
-460	–	–	12	14
-451	–	–	20	78
-432	–	–	13	8
<i>Sn-Beta-seed (hydrated)</i>				
-734	127	-0.2	16	25
-723	127	0.1	9	30
-712	121	0.1	9	24
-693	158	0.6	20	22
<i>Sn-Beta (dehydrated)</i>				
-452	117	-0.3	13	66
-445	101	-0.9	10	29
-435	115	-0.3	5	5
<i>Sn-Beta (hydrated)</i>				
-732	115	-0.1	51	32
-700	132	0	49	52
-649	139	0.2	53	16

^aRemeasured sample from Chapter 4, stored under ambient conditions for 2 years. ^bFitting of the CS tensor not possible due to weak signal.

For the two hydrothermally synthesized samples Sn-Beta-seed and Sn-Beta, ^{119}Sn DNP NMR spectra of the corresponding dehydrated materials were also acquired. The spectra of the dehydrated materials show peaks covering a shift range of ca. -430 and -465 ppm, in agreement with previous studies (inset, Figure 4.6 and Figure A25).^{94,97} Similar to the hydrated samples, the center of the ^{119}Sn NMR resonances of hydrothermal Sn- β zeolites are shifted upfield (-450 ppm) compared to post-synthetic Sn/deAl-Beta-OH-25 where highest intensity was observed around -430 ppm.

Comparing the isotropic ^{119}Sn DNP SENS spectra of the different hydrated Sn- β zeolites, the differences in Sn chemical shifts most likely reflect (i) substitution of Sn^{IV} in different T-sites of the zeolite framework (Figure 4.1, top), and/or (ii) the presence of closed and/or open Sn^{IV} -sites (Figure 4.1, bottom), which could also explain the difference in activity. Combining the catalytic data in Table 4.1 with the insights obtained from various characterization techniques leads us to conclude that the Sn^{IV} -site giving rise to ^{119}Sn isotropic chemical shifts around -730 ppm in combination with a hydrophobic zeolite framework are most likely provide highest activity for the glucose-to-fructose isomerization.

4.4.2. Computational modeling and Calculated Chemical Shift Map of Sn^{IV} -sites in Sn- β

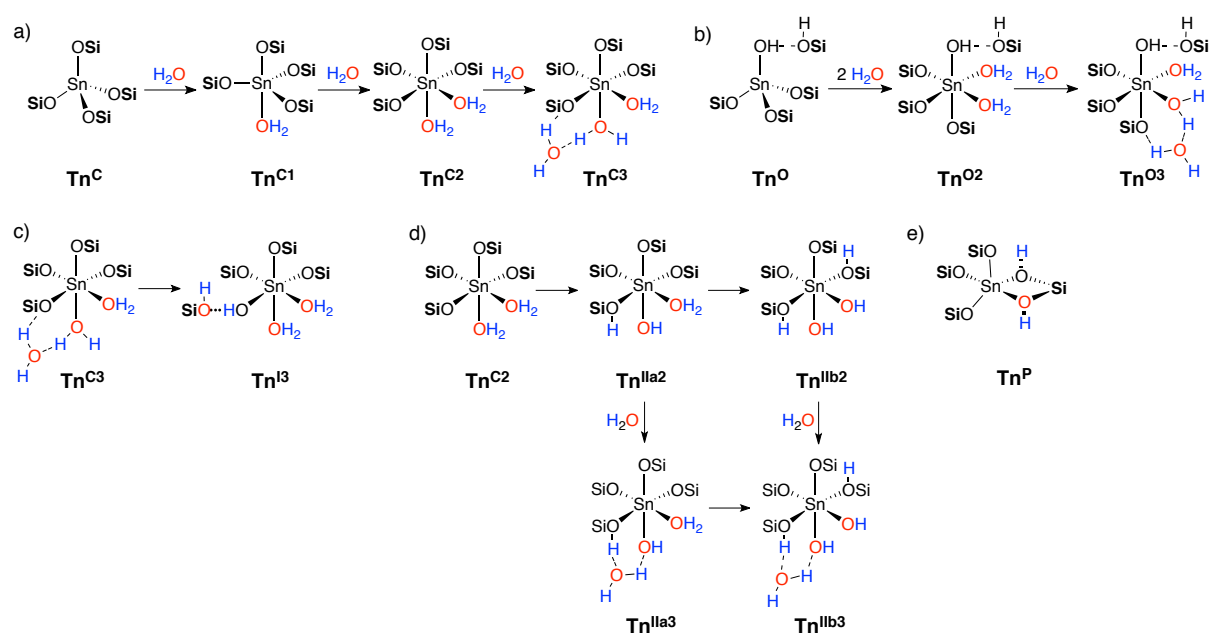
To corroborate on our hypothesis that the Sn^{IV} -sites (closed or open) are located in different T-sites in the different zeolite samples, computational modeling based on Density Functional Theory (DFT) was performed. DFT has been extensively used to study structures and reactivity of Sn- β and similar zeolites.^{105,113,117,119,120,154,212} Structures, relative energies, and the spectroscopic signatures such as the ^{119}Sn NMR parameters of Sn^{IV} -sites in Sn- β were calculated using cluster models for all proposed T-sites at different hydration levels in order to relate a structure to specific isotropic chemical shift and chemical shift tensors, which were measured experimentally.

4.4.2.1 Models of T-sites in Sn- β zeolite.

The starting structure of the model catalyst is the polymorph A of zeolite β (framework type BEA).^{78,118} In this structure, there are nine unique crystallographic lattice positions for Si^{IV} , referred to as T1-T9 sites (see Figure 4.1, top). It is important to note that the BEA topology is a mixture of the two polymorphs A and B. The difference in the two polymorphs results from the stacking of the same building layer.²¹³ Thus, we only expect minor changes in the local geometry of the Sn within the different polymorphs

and performed the calculations exclusively on polymorph A. In order to assign the experimentally observed ^{119}Sn NMR spectra, five different cluster models were constructed from the experimentally determined X-Ray structure zeolite β .⁷⁸ These five models represent the structures corresponding to the nine T-sites, where sites T1/T2, T3/T4, T5/T6 and T7/T8 share the same cluster, with 108, 121, 131 and 128 atoms, respectively. The cluster model for T9 is unique, with 98 atoms. In order to construct Sn^{IV} sites in these clusters, the Si atom of a particular T-site was substituted by Sn, giving rise to the nine Sn- β cluster models. In the construction of the clusters all the rings that are part of the evaluated T-site have been included, whereas the dangling bonds that connect the Si atoms to the rest of the zeolite framework were saturated with H-atoms. The models with Sn bonded to four OSi groups correspond to closed sites (Tn^{C}). We also consider sites where one Si atom is substituted by Sn and an adjacent Si atom is removed, which results in the presence of dangling O-atoms terminated with H (see Figure 4.7), referred to hereafter as defect-open sites (Tn^{O}).^{119,154} Hydrated closed (Tn^{C1} , Tn^{C2} , Tn^{C3}) and defect-open sites (Tn^{O2} , Tn^{O3}) were modeled by coordinating one or two water molecules to Sn, and with a third water molecule in the second coordination sphere, as shown in Schemes 1a and 1b for closed and defect-open sites, respectively.

Scheme 4.1. Formation of hydrated species for a) closed sites; b) defect-open sites; c) hydrolyzed-open sites of type I, d) hydrolyzed-open sites of type II and e) penta-coordinated sites with a bridging OH group in Sn-b. All of the Si atoms are bound to three O atoms of the zeolite framework, however, for clarity connections to the framework are not shown.



Alternative structures, corresponding to open sites created by hydrolysis of framework Sn-O bonds in doubly- and triply-hydrated closed sites were also considered. Two types of hydrolyzed-open sites can be envisioned: in Type I (Scheme 4.1, **Tn^b**) a water molecule in the second coordination sphere of Sn breaks a Sn-O bond, leading to one Si-OH and one Sn-OH group interacting with each other, while the Sn^{IV} remains coordinated to two water molecules. In Type II (Scheme 4.1d, **Tn^{iv}**, v=a2, b2, a3, b3), the reaction of coordinated water molecules on Si-O-Sn generates a Si(OH)Sn bridge and a terminal Sn(OH). Up to two water molecules can be split. Hydrolyzed-open sites of type I (Scheme 4.1c) were studied for all nine T-sites, while hydrolyzed-open sites of Type II (Scheme 4.1d) were only evaluated for T1, T5 and T9 sites. We also studied some structures where Sn is in a penta-coordinated (**Tn^p**) environment with two bridging OH groups between Sn and a neighboring Si, that is, Sn(μ -OH)₂-Si, as recently proposed (Scheme 4.1e).²¹⁴ These sites can result from the splitting of the water molecule in the Sn-O-Si group in mono-hydrated sites (**Tn^{c1}**). As for Type II hydrolyzed sites, only T1, T5 and T9 were considered for these sites.

4.4.2.2 Structures of dehydrated and hydrated closed and defect-open T-sites

The optimized structures and geometrical parameters (in terms of average values) of all nine dehydrated closed (hereafter **Tn^c**) and defect-open T-sites (hereafter **Tn^o**) can be found in Figure A26-A28 and Table A7. As an example, Figure 4.7a shows the optimized structures of the T9 site, in the closed and defect-open forms. Similar geometries are found for other sites. All the sites present a distorted-tetrahedral Sn coordination environment. In the case of the closed sites the average Sn-O distances range between 1.886 and 1.895 Å, which is in very good agreement with the Sn-O distance obtained from EXAFS experiments.¹¹⁷ The six O-Sn-O angles vary from 102.0° to 113.8°, with an average value of 109.5°. The dehydrated defect-open sites also present average O-Sn-O angles of *ca.* 109°, similar to what was found for the closed sites, and the Sn-OH average distances range from 1.886 to 1.923 Å.

The average values of the main geometrical parameters of the hydrated closed and defect-open sites are presented in Table A8-A12, while Figure A29-A34 show the optimized geometries of all sites in the hydrated form. The optimized structures of the triply-hydrated closed and defect-open T9 site are shown in Figure 4.7 as an example. While for mono-hydrated sites the geometry around Sn corresponds to a distorted trigonal bi-pyramid (TBP, Figure A28), doubly-hydrated closed sites exhibit a geometry at the Sn^{IV}-site that corresponds to a distorted octahedron. The coordination of two

water molecules increases the Sn-O bond distances to average values between 1.931 and 1.950 Å, while the average values the O-Sn-O angles of framework O atoms in *cis* position range between 96.3-99.8°, and the O-Sn-O^w angles (O and O^w are framework and water oxygen atoms in *trans* position, respectively) vary from 166.3 to 175.5°. The presence of a third water molecule in the second coordination only slightly increases the Sn-O bond distances to values between 1.939 and 1.960 Å (Table A10).

Coordination of two water ligands to defect-open sites increases the Sn-OH bond to values in the range 1.925-1.990 Å, and the Sn-O bond distances to values between 1.935 and 1.959 Å, similar to what was found for closed sites species (Table A11). The average O-Sn-O angles for framework oxygen atoms in *cis* position range between 96.8 and 100.7°. The presence of a third water molecule in the second coordination sphere of Sn causes only minor variations to the optimized parameters of the double-hydrated defect sites (Table A12).

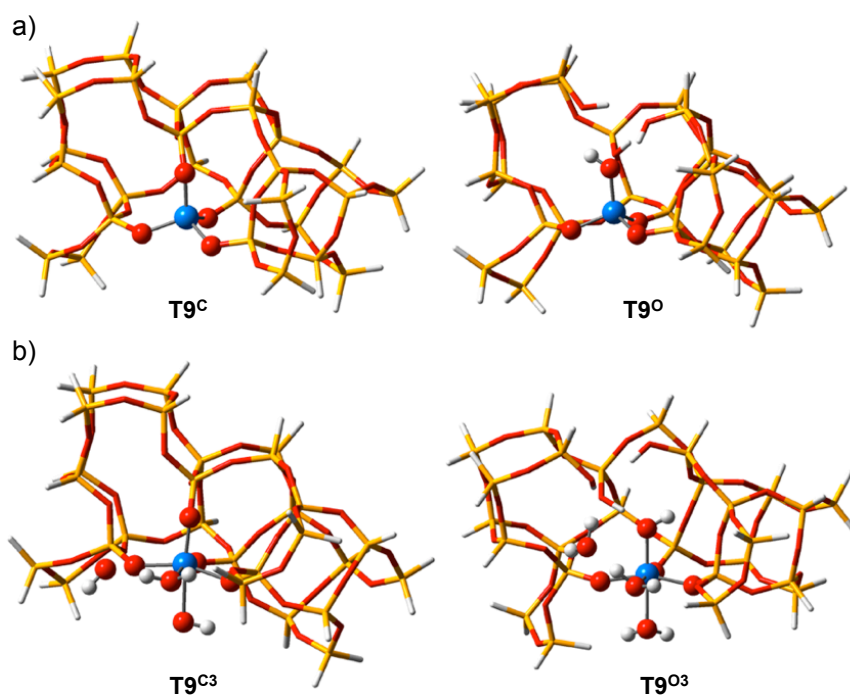


Figure 4.7. Optimized structures of a) dehydrated closed and defect-open T₉ site and b) triply-hydrated closed and defect-open T₉ site of Sn-β. The Sn atom and its first coordination sphere are highlighted with balls and sticks models. Sn atoms are shown in blue, oxygen in red, silicon in yellow and hydrogen in white.

4.4.2.3 Stabilities of T-sites in Sn-β

The relative stability of all nine T-sites was obtained by comparing the energy of substituting one Si atom by Sn at a specific T-site in all nine clusters in the dehydrated closed form. The results are shown in Table A13. In summary, the most stable site for substitution is T₁, however, the relative stability of most sites with respect to T₁ is

within 1-4 kcal·mol⁻¹, indicating that there is not a very strong thermodynamic bias for a preferred location for the Sn substitution. However, the preference of substitution can also be influenced by kinetic factors, which have not been considered in the calculations. We also evaluated the reaction free energies at 298 K (ΔG_{ads}) for the adsorption of water on the T-sites, which was calculated according to equation 4.1:

$$\Delta G_{ads} = G(\text{Tn}-(\text{H}_2\text{O})_x) - G(\text{Tn}) - xG(\text{H}_2\text{O}) \quad (4.1)$$

where $\text{Tn}-(\text{H}_2\text{O})_x$ corresponds to the adduct between the Tn-site of the zeolite and x molecules of water (either as coordinated water molecule or split over a Sn-O bond, $x=1, 2, 3$), and Tn and H_2O refer to the corresponding isolated Tn-site cluster model and the water molecule, respectively.

Table 4.4. Reaction free energies at 298 K (ΔG_{ads}) of various Sn^{IV}-sites in both closed ($x=1, 2, 3$) and open sites ($x=2, 3$) of Sn- β , calculated using equation 4.1. Energies are given in kcal·mol⁻¹

Site	Closed sites			Open sites						
	Tn ^{C1}	Tn ^{C2}	Tn ^{C3}	Tn ^{O2}	Tn ^{O3}	Tn ^{I3}	Tn ^{IIa2}	Tn ^{IIa3}	Tn ^{IIb2}	Tn ^{IIb3}
T1	-3.7	-10.6	-13.3	-18.1	-29.6	18.6	-1.7	-9.5	12.1	4.8
T2	-5.6	-10.3	-16.2	-6.7	-30.1	17.3				
T3	-4.3	-5.1	-12.5	-14.9	-22.8	-3.4				
T4	-8.3	-14.0	-22.3	-14.1	-25.5	-8.3				
T5	-4.4	-11.7	-21.5	-20.9	-26.7	-13.5	-6.7	-11.6	0.5	-2.5
T6	-9.6	-17.2	-24.3	-26.2	-24.6	-6.3				
T7	-8.8	-15.3	-21.6	-19.0	-22.4	-6.2				
T8	-5.0	-15.5	-19.6	-16.5	-23.6	-0.9				
T9	-1.9	-11.9	-17.4	-16.0	-25.7	-8.3	-3.5	-10.1	0.0	0.2

The free energies for adsorption of water at all T-sites are given in Table 4.4. According to these results, the adsorption of one water molecule (**Tn^{C1}**, $x=1$) by any closed T-site is favorable, with the reaction free energies ranging from -9.6 to -1.9 kcal · mol⁻¹. Adsorption of two (**Tn^{C2}**, $x=2$) and three water molecules (**Tn^{C3}**, $x=3$) is even more favorable at all sites. In the latter case ΔG_{ads} ranges from -24.3 to -12.5 kcal · mol⁻¹. In general, thermodynamics points toward the formation of hydrated species on the Sn^{IV}-sites by coordination of two water molecules as previously proposed,^{30,94,96,97} with a third water molecule in the second coordination sphere involved in H-bonding with the other water molecules. ΔG_{ads} for defect-open sites **Tn^{O2}** and **Tn^{O3}** in Sn- β are also shown

in Table 4.4. The adsorption of two water molecules is favorable for all defect-open sites, and, in general, for these species the coordination of water molecules to Sn^{IV} is more exoergic compared to the corresponding closed sites, except for **T2**. The presence of a third water molecule in the second coordination sphere of Sn increases the stability of all species, similar to the effect already observed for closed sites, and the adsorption of three water molecules becomes more exoergic than the similar process for closed sites (compare **Tn^{C3}** and **Tn^{O3}** columns in Table 4.4). The most favorable adsorption of water molecules by the acidic defective open Sn^{IV}-sites compared to closed ones is in agreement with previous theoretical results for the adsorption of CH₃CN at T1, T5 and T9 sites in Sn-β.¹⁰⁵

For hydrolyzed-open sites of Type I (**Tn^{l3}**; Scheme 1c), ΔG_{ads} is reported in Table 4.4. Except for the **T1^{l3}** and **T2^{l3}** sites, the formation of these hydrolyzed-open sites is exoergic, ranging from -13.5 to -0.9 kcal · mol⁻¹ with respect to separate reactants, although the formation of these hydrolyzed-open sites is always endoergic when compared to the corresponding triply-hydrated closed sites (**Tn^{C3}**). For hydrolyzed-open sites of Type II (**Tn^{llv}** in Scheme 1d), we observed that the splitting of one water molecule in **Tn^{lla2}** and **Tn^{lla3}** sites is still favorable, but the splitting of the second water molecule in **Tn^{llb2}** and **Tn^{llb3}** sites makes the process thermodynamically unfavorable with respect to separate reactants (only **T5^{llb3}** is slightly exoergic).

4.4.2.4 ¹¹⁹Sn NMR calculations

In order to shed light on the local environment of the Sn^{IV}-sites in Sn-β, ¹¹⁹Sn NMR calculations at the B3LYP-D3/TZP level of theory, including relativistic effects (RE) and spin-orbit coupling (SOC), of all sites in both dehydrated and hydrated forms were performed. The chemical shift (CS) tensor is often parameterized with the following equations (4.2)-(4.4):

$$\delta_{iso} = (\delta_{11} + \delta_{22} + \delta_{33})/3 \quad (4.2)$$

$$\Omega = (\delta_{11} - \delta_{33}) \quad (4.3)$$

$$\kappa = 3(\delta_{22} - \delta_{iso})/\Omega \quad (4.4)$$

where $\delta_{11} \geq \delta_{22} \geq \delta_{33}$ are the principal components of the chemical shift tensor.

The isotropic chemical shift (δ_{iso}) is the average of the three principal components of the CS tensor and corresponds to the chemical shift that is observed in solution NMR

spectroscopy. The span (Ω) describes the magnitude of the chemical shift anisotropy (CSA). The skew (κ) describes the axial symmetry of the chemical shift tensor, with extreme values (± 1) reflecting the presence of rotational axes at the nuclear site. The computational calculations of the CS tensors of Sn^{IV} sites allow us to calculate the CS tensor parameters through equations (4.2)-(4.4). Plotting the ^{119}Sn isotropic chemical shift against the span for all calculated sites allows us to correlate the experimentally determined ^{119}Sn NMR signatures (Table 4.3) with our computational predictions (Figure 4.8 and 4.8). Only triply-hydrated sites are shown in Figure 4.9; the data for the doubly-hydrated Sn-sites are given in Figure A38.

Figure 4.8 shows the relationship between the calculated δ_{iso} and Ω for all dehydrated sites, including closed and defect-open T-sites, as well as the experimentally determined CSA for Sn-Beta-seed zeolites. For the closed sites (in olive green), δ_{iso} varies from -452 to -421 ppm (**T6^c** and **T9^c**, respectively), with Ω ranging from 97 to 157 ppm (**T6^c** and **T2^c**, respectively). The dehydrated defect-open sites (in orange) show δ_{iso} ranging between -417 and -375 ppm (**T9^o** and **T2^o**, respectively) with Ω varying between 101 and 361 ppm (**T9^o** and **T1^o**, respectively). Interestingly, all closed sites show δ_{iso} that are always below -420 ppm, while δ_{iso} for all open sites are above this value. One can already see that most observed sites have δ_{iso} compatible with closed sites rather than most defect-open sites in their dehydrated form, with exception of **T3^o**, and **T7^o-T9^o**, in particular **T9^o**, which has calculated CS parameters close to those of some of the closed sites.

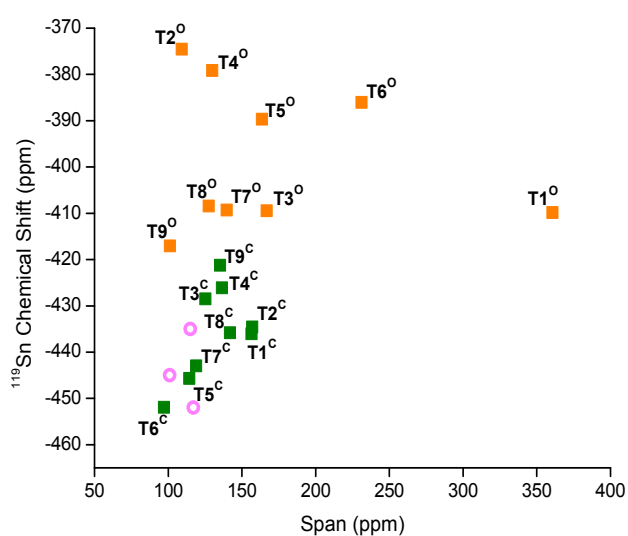


Figure 4.8. Comparison of measured and calculated ^{119}Sn NMR chemical shifts vs. spans. Calculations for a) dehydrated closed, Tn^{c} (■) and defect-open sites, Tn^{o} (■) of Sn- β . Experimental data for dehydrated Sn-Beta (○) is shown.

Mono-hydrated closed sites show ^{119}Sn δ_{iso} ranging from -586 to -558 ppm, with Ω ranging between 361 and 422 ppm. These predicted CS parameters are significantly different from the experimental data on hydrated and fully dehydrated samples of Sn- β (see Figure A39), but δ_{iso} match very well the experimental signal found at -560 ppm in partially hydrated samples.¹⁰² The results for penta-coordinated sites with two bridging OH groups, $\text{Sn}(\mu\text{-OH})_2\text{-Si}$ (Scheme 4.1e), are shown in Figure A39. The calculated ^{119}Sn NMR signatures for penta-coordinated Sn-sites (**Tn^P**) are very different to any of the collected experimental data (especially the very high calculated span of more than 400 ppm). Therefore we can exclude the presence of this type of sites in our as synthesized hydrated Sn- β samples. Calculated CS tensor parameters for doubly- and triply-hydrated closed sites are presented in Figure A38a and 4.8a, respectively, and most of them display calculated ^{119}Sn CS tensor parameters that are close to experimental data. Doubly-hydrated sites (Figure A38a, in blue) have calculated δ_{iso} ranging from -719 to -658 ppm (**T1^{C2}** and **T5^{C2}**, respectively), with Ω varying from 165 to 255 ppm (**T8^{C2}** and **T3^{C2}**, respectively). Including one water molecule in the second coordination sphere of Sn, *i.e.* a triply-hydrated site (Figure 4.9, in olive green), results in a decrease of both δ_{iso} and Ω , so that δ_{iso} varies from -741 to -684 ppm (**T4^{C3}** and **T5^{C3}**, respectively), while Ω varies from 121 to 196 ppm (**T8^{C3}** and **T5^{C3}**, respectively). The results for hydrated defect-open sites are shown in Figure A38b and Figure 4.9c (data in magenta and orange for **Tn^{O2}** and **Tn^{O3}**, respectively). For **Tn^{O2}** sites δ_{iso} ranges from -696 to -663 ppm (**T8^{O2}** and **T2^{O2}**, respectively), whereas Ω ranges from 150 and 254 ppm (**T9^{O2}** and **T3^{O2}**, respectively). Similar to the triply-hydrated closed sites, triply-hydrated defect-open sites (**Tn^{O3}**) also show ^{119}Sn NMR parameters that are, in general, lower in both δ_{iso} and Ω with respect to the doubly-hydrated ones. The δ_{iso} for these sites ranges from -724 to -691 ppm (**T1^{O3}** and **T9^{O3}**, respectively), whereas Ω ranges from 121 and 219 ppm (**T5^{O3}** and **T3^{O3}**, respectively).

We showed above that the presence of the surrounding water molecule has a strong effect on the thermodynamic stability of the different closed and defect-open sites, indicating that triply-hydrated species are more stable than mono- and double-hydrated ones. Therefore, it is expected that the different signatures for hydrated samples correspond to mainly triply-hydrated sites.

Figures 4.9c-d show the ^{119}Sn NMR signatures of the hydrolyzed-open sites of Type I and II. The Tn^{Ib} sites (Figure 4.9c) shows δ_{iso} ranging from -680 to -641 ppm (T1^{Ib} and T7^{Ib} , respectively) and Ω is between 167 and 403 ppm (T5^{Ib} and T2^{Ib} , respectively). For hydrolyzed-open sites of Type II (Figure 4.9d) δ_{iso} ranges from -690 to -619 ppm (T1^{IIa} and T1^{IIb} , respectively) and Ω ranges from 249 to 426 ppm (T1^{IIa} and T2^{IIb} , respectively). Hydrolyzing the Sn-O bond with a surrounding water molecule (Scheme 4.1c) is, in general, energetically preferred over opening the same bond with a coordinated water molecules (Scheme 4.1d). Therefore, formation of the hydrolyzed sites of Type I should be more favorable than the formation of Type II hydrolyzed species.

The computational modeling on the different Sn^{IV} -sites in both closed and open forms shows that they can be associated with specific NMR signatures. However, it is important to compute the variability of the ^{119}Sn NMR parameters (specifically δ_{iso} and Ω) with different conformations of water ligands coordinated to the Sn sites. Therefore, we investigated two geometrical descriptors: the Sn---OH₂ distance and the rotation around the Sn---OH₂ axis in the T9^{C2} model (See Text A2 and Figure A40). For the Sn---OH₂ bond distance lengthening/shortening we observed that δ_{iso} varies by 17 ppm at most, while the variation in Ω can be up to 63 ppm. For Sn---OH₂ bond rotation, the largest variation in δ_{iso} is 13 ppm, while for Ω it is 42 ppm (details of these calculations can be found in Figure A40). These results indicate that the calculated NMR parameters are sensitive to subtle changes in the local geometry of the Sn^{IV} -sites, with Ω being the most sensitive parameter. The practical consequence will be a broadening of the NMR signal and some uncertainty in the assignment of δ_{iso} and Ω to specific sites. It must also be mentioned that in some cases, the sideband manifolds extracted from the 2D MAT ^{119}Sn NMR spectra may be fit with two CS tensor parameters per isotropic shift, rather than with a single set of CS tensor parameters. These two site fits generally result in a more populated site with lower span (ca. 90 - 140 ppm) and another one with higher span (ca. 190 - 230 ppm) (see Figure A20-A24). However the population of the sites with a span larger than 190 ppm represent a minority of the Sn^{IV} centers present in all Sn- β catalysts (see two-site fits in Figure A20-A23). Rather than specifically pointing towards two types of sites, the better two-site fits show that we have likely a distribution of sites and associated CS tensor parameters for a given isotropic Sn chemical shift.

Taking into account the variability in δ_{iso} and Ω , as well as the possibility of having multiple Sn^{IV} -sites contributing to the same isotropic chemical shift, Figure 4.10a-c illustrates that several sites display ^{119}Sn NMR signatures that are close to the experimental data of the different zeolites in terms of δ_{iso} and Ω . Triply-hydrated closed (Figure 4.9a, olive green) and triply-hydrated defect-open (Figure 4.9b, orange) sites are expected to be potential active Sn^{IV} sites for the different Sn- β materials. However, the hydrolyzed-open sites, of Type I and Type II also represent some possible candidates. However, the Type II hydrolyzed-open sites (Figure 4.9d) are very unlikely in view of their very high, calculated span ($\Omega \geq 250$ ppm), compared to the experimental data.

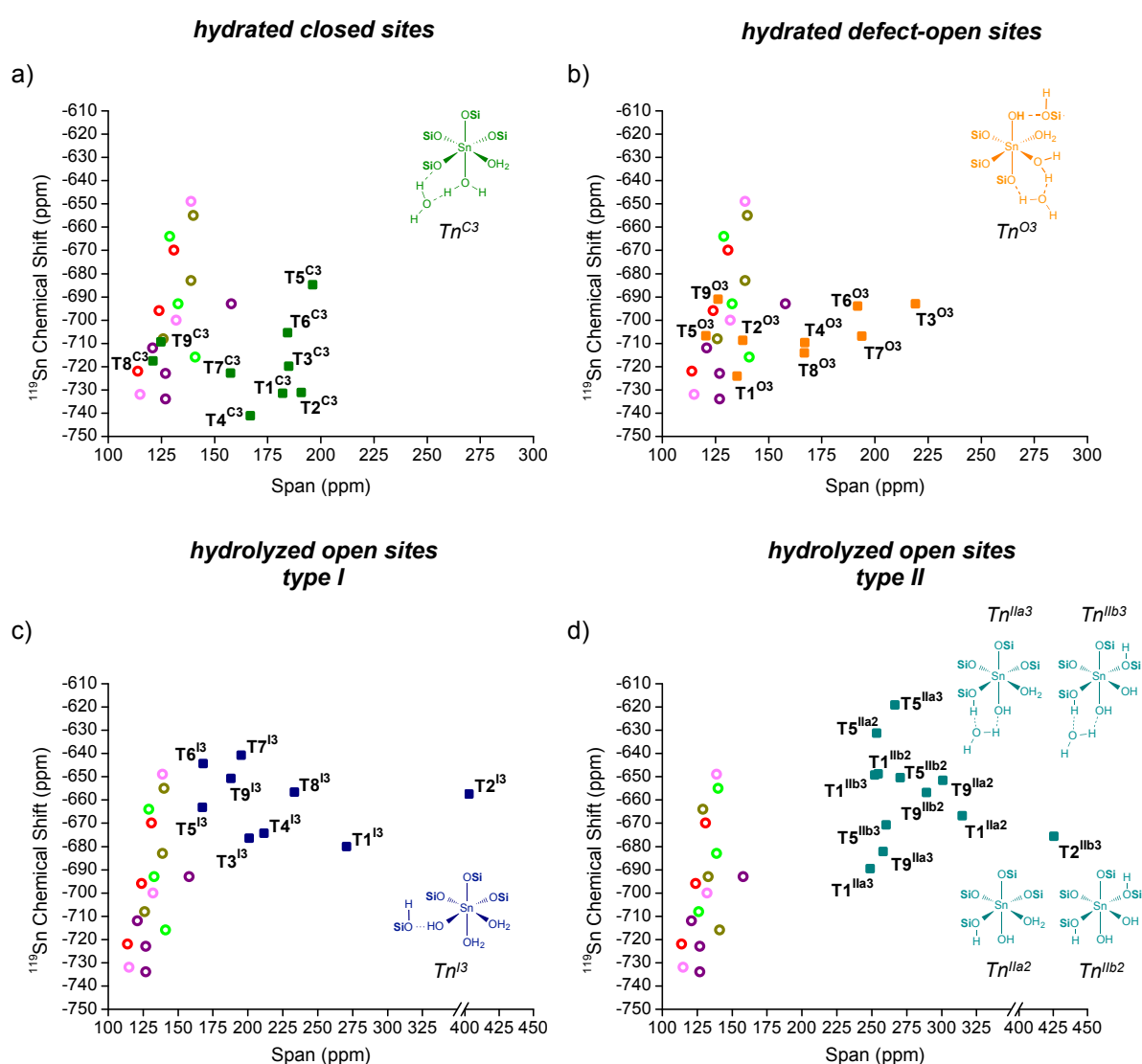


Figure 4.9. Comparison of measured and calculated ^{119}Sn NMR chemical shifts vs. spans. Calculations for a) triply-hydrated closed sites, $T_n^{\text{C}3}$ (■); b) triply-hydrated defect-open sites, $T_n^{\text{O}3}$ (■); c) hydrolyzed-open sites of type I, $T_n^{\text{I}3}$ (■) and d) hydrolyzed-open sites of type II, $T_n^{\text{II}3}$ (■) of Sn- β . Experimental data for hydrated Sn/deAl-Beta-OH-25 (●) Sn/deAl-Beta-OH-300 (●), Sn/deAl-Beta-F-30 (●), Sn-Beta-seed (●) and Sn-Beta (●) are shown.

From the calculated chemical shifts and the relative energies, one can infer general trends and discriminate between the different T-sites explored. As mentioned above, the triply-hydrated species are predicted to be the most stable among the sites with different hydration degrees, while the hydrolyzed-open sites are most likely to be formed after hydrolysis of the Sn-O bonds. In order to narrow down the assignment of NMR signatures to more specific sites, it is possible to correlate the chemical shift of dehydrated and the most stable hydrated species, i.e. triply hydrated, as illustrated in Figure 4.10. Three Sn- β materials for which ^{119}Sn NMR of dehydrated and hydrated samples have been acquired are shown: the post-synthetic material Sn/deAl-Beta-OH-25 (red box in Figure 4.10a), and both hydrothermally synthesized materials Sn-Beta-seed (violet box in Figure 4.10b) and Sn-Beta (magenta box in Figure 4.10c). Since the hydrated and dehydrated samples always show more than one NMR signature, it is *a priori* not possible to know which signals of the hydrated sample are associated with those of the dehydrated one; it is therefore more appropriate to show the possible correlation between hydrated and dehydrated sites with box-shape diagrams (Figure 4.10). The relevant T-sites will then be those where both experimental and calculated sites are found close to the *corners/intersections* of the boxes.

Starting with the Sn/deAl-Beta-OH-25 zeolite (Figure 4.10a), three different signals of the dehydrated sample were observed at -463 , -429 and -405 ppm (Table 4.3). The signal at -463 ppm can give rise to the corresponding three signals at -722 , -696 and -670 ppm in the hydrated zeolite. According to the calculations carried out in this work, the closed T6 (**T6^{C3}**) site and the T5 site as closed (**T5^{C3}**) or Type I hydrolyzed-open site (**T5^{I3}**) (Figure 4.11) show signatures closest to the signals at -696 , -722 ppm respectively. When comparing the calculated with the experimental span in hydrated samples (Figure 4.9a and c), T5 hydrolyzed-open Type I sites (**T5^{I3}**) with a chemical shift of -670 ppm is the best match. Note that in view of the calculated reaction free energies (Table 4.4) the T5 position is the most likely one to get hydrolyzed by a water molecule from the second coordination sphere (Type I). The resonance at -429 ppm can be associated with T3 and T8 closed sites (**T3^{C3}** and **T8^{C3}**) and the corresponding hydrolyzed-open sites (**T3^{I3}** and **T8^{I3}**) as well as **T4^{I3}** based on the chemical shifts observed for the dehydrated and hydrated samples. Also taking Ω (see Figure 4.8 and Figure 4.9a-c) into account, **T8^{C3}** with a hydrated chemical shift of -722 ppm represents the best fit for the active site related with a chemical shift at -429 ppm in dehydrated state. For all other possible sites the span is more than 70 ppm off. Note that this peak has the highest relative

integrated intensity in both, the hydrated and the dehydrated spectrum. The last resonance in the dehydrated sample at -405 ppm, which only has a minor contribution with a relative integral intensity of 11 % can be best associated with defect-open sites in T1, T3, T7, T8 or T9 position based on Figure 4.10a. Including the span calculations the T9 open-defect site ($T9^{O3}$, Figure 4.7b) is most likely. However, an open-defect site in T1 position is also possible ($T1^{O3}$). This shows that in Sn/deAl-Beta-OH-25 zeolite closed and open sites, both hydrolyzed-open as well as defect-open, most probably in T8, T5, and T9 location are feasible. The presence of open, in particular defect, sites is consistent with the hydrophilicity of this zeolite and the detection of Q_3 peaks in the ^{29}Si NMR spectra.

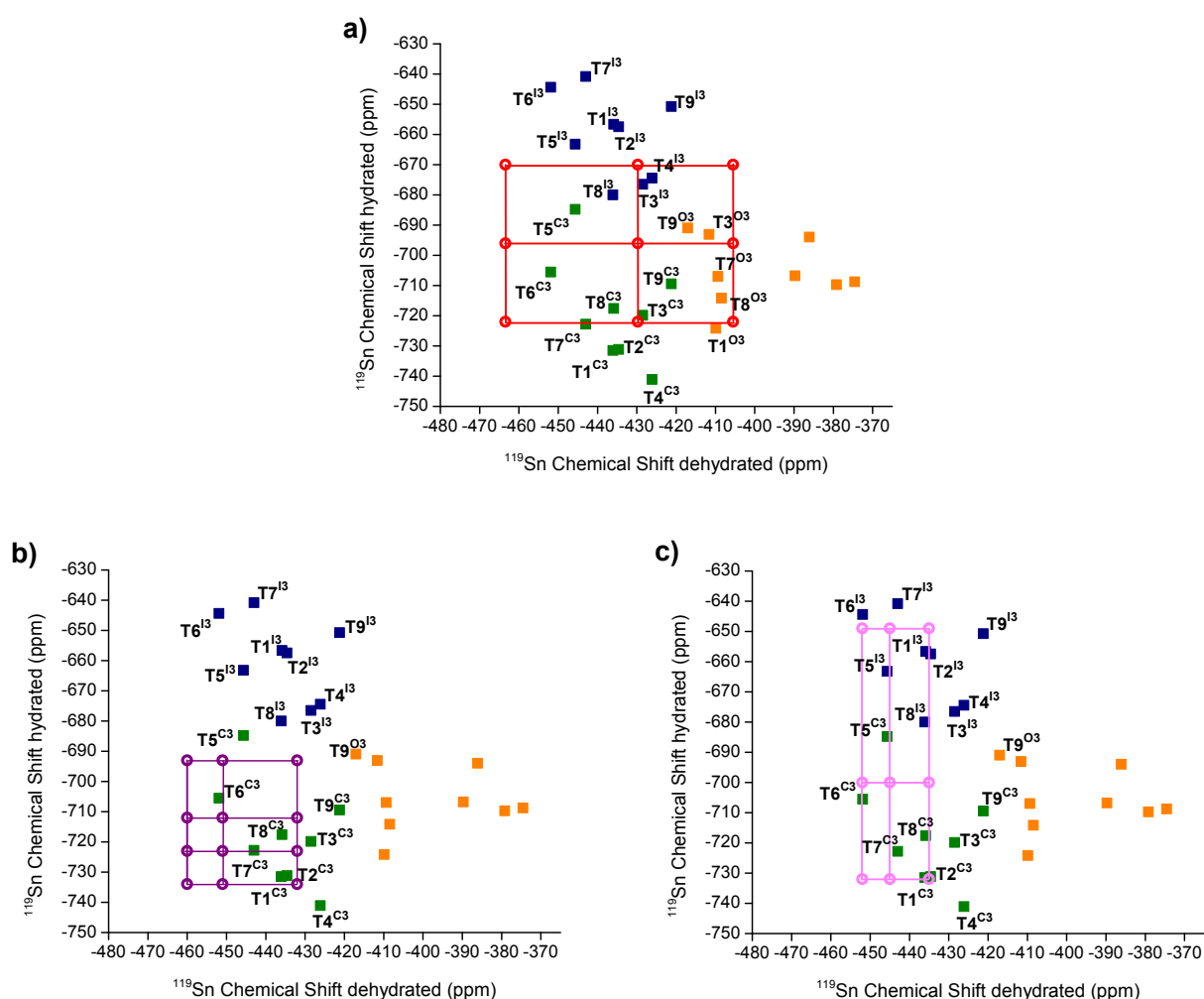


Figure 4.10. Comparison of measured and calculated ^{119}Sn NMR chemical shifts. Calculations for dehydrated vs. hydrated of closed sites (■), defect-open sites (■) and hydrolyzed-open sites of type I (■). Experimental chemical Sn chemical shifts for hydrated Sn/deAl-Beta-OH-25 (a, ○), Sn-Beta-seed (b, ○) and Sn-Beta (c, ○). The corner/intersections of the grids represent any possible combination of the chemical shifts in dehydrated and hydrated samples.

For the dehydrated Sn-Beta-seed (Figure 4.10b), three resonances at -460 , -451 and -432 ppm are present (Table 4.3). The corresponding chemical shifts for the hydrated Sn-Beta-seed sample were observed at -734 , -723 , -712 and -693 ppm. Given the number of resonances, assigning specific sites to distinct data points for Sn-Beta-seed is very difficult. For the -460 ppm peak a closed T6 site ($\mathbf{T6}^{\text{C3}}$) with a chemical shift of -712 ppm in hydrated zeolites is the best fit (see Figure 4.10b). The site with a chemical shift at -451 ppm site both $\mathbf{T5}^{\text{C3}}$ and $\mathbf{T7}^{\text{C3}}$ sites (Figure 4.11) are possible. Considering the ^{119}Sn NMR signatures for the hydrated zeolite, both $\mathbf{T5}^{\text{C3}}$ and $\mathbf{T7}^{\text{C3}}$ are in good agreement with theoretical predictions. The span is ~ 50 ppm and ~ 30 ppm off for $\mathbf{T5}^{\text{C3}}$ and $\mathbf{T7}^{\text{C3}}$, respectively. Energetically, the T7 position is predicted to be favored by 4 kcal mol^{-1} over T5. An unambiguous assignment of the chemical shift at -451 ppm to either of the two lattice positions is however not possible based on the present study. In case of the resonance at -432 ppm, which had the lowest relative integrated intensity (8 %), closed sites in Tn ($n=1-4, 8-9$) all represent plausible active sites in Sn-Beta-seed ($\mathbf{T1}^{\text{C3}}$, $\mathbf{T2}^{\text{C3}}$, $\mathbf{T3}^{\text{C3}}$, $\mathbf{T4}^{\text{C3}}$, $\mathbf{T8}^{\text{C3}}$ and $\mathbf{T9}^{\text{C3}}$) and also some hydrolyzed-open sites ($\mathbf{T3}^{\text{B3}}$, $\mathbf{T4}^{\text{B3}}$) may be present. Associating a single resonance in the dehydrated spectra with two chemical shifts of the same T-site in the hydrated spectra (closed and hydrolyzed-open) is reasonable considering that the hydrolysis of closed sites in the presence of water should be a reversible process, which results in only closed sites upon dehydration. All of these sites are also feasible in view of the span calculations. A distinct assignment for the minor resonance with chemical shift at -432 ppm is not possible. We emphasize, however, that this zeolite is likely associated with only closed sites, consistent with its high crystallinity and the NMR data (mainly Q_4 peaks in the ^{29}Si NMR spectra of the Sn-Beta-seed material, corresponding to $(\text{SiO})_4\text{Sn}$ sites, Figure 4.6).

Sn-Beta (Figure 4.10c) showed three distinct resonances at -452 , -445 and -435 ppm in its dehydrated form. The first can be associated with the T6 position, as both closed ($\mathbf{T6}^{\text{C3}}$) and hydrolyzed-open type I site ($\mathbf{T6}^{\text{B3}}$). For the resonance at -445 ppm T5 and/or T7 sites in closed and hydrolyzed-open state ($\mathbf{T5}^{\text{C3}}/\mathbf{T5}^{\text{B3}}$ and $\mathbf{T7}^{\text{C3}}/\mathbf{T7}^{\text{B3}}$) are possible. All these assignments are feasible considering ^{119}Sn NMR calculations for both dehydrated and hydrated sites (see Figure 4.8 and Figure 4.9a,c). The last resonance at -435 ppm can be best linked with T1 and/or T2 sites in closed (-732 ppm) and hydrolyzed-open type I state (-649 ppm) ($\mathbf{T1}^{\text{C3}}/\mathbf{T1}^{\text{B3}}$ and $\mathbf{T2}^{\text{C3}}/\mathbf{T2}^{\text{B3}}$). However hydrolyzed-open sites in T1/T2 lattice position can be excluded based on the very high span (>250) and the low stability predicted for these specific sites. As for Sn-Beta-seed closed $\mathbf{T3}^{\text{C3}}$, $\mathbf{T4}^{\text{C3}}$, $\mathbf{T8}^{\text{C3}}$ and $\mathbf{T9}^{\text{C3}}$ are all possible for the minor resonance (5% relative integral intensity) with a chemical

shift at -435 ppm in the dehydrated form. Note that the resonance associated with hydrolyzed-open sites (-649 ppm in the hydrated dimension) only has a minor contribution (16 %) to the ^{119}Sn NMR spectra (Figure 4.6). Hence, similarly to Sn-Beta-seed, mainly closed sites can be associated with the ^{119}Sn NMR spectra, also consistent with the ^{29}Si NMR spectra where a very minor Q_3 peak and the major Q_4 peak are observed. The highly hydrophobic nature is also in agreement with the presence of mainly closed sites in the Sn-Beta material. Some of the most relevant sites in Sn-Beta and Sn-Beta-seed are shown in Figure 9 ($\text{T5}^{\text{C3}}/\text{T5}^{\text{B}}$ and $\text{T6}^{\text{C3}}/\text{T7}^{\text{C3}}$). Comparing literature values of ^{119}Sn NMR resonances^{30,102,170} observed for hydrothermal Sn- β samples prepared in different laboratories (Figure A41) with chemical shifts of hydrothermal Sn- β samples in the present study (Figure 4.10) reveals that closed sites in T5 and T7 position can be found in all of these samples. It is worth noting that the spectra reported by Davis and co-workers¹⁵ show two resonances at -420 ppm and -445 ppm in the dehydrated sample, while the research groups of Corma^{2b} and Román-Leshkov^{18b} only observe a single shift at -445 ppm. The present data suggests that the -420 ppm resonance can be ascribed to a defect-open site with a silicon vacancy next to the Sn in contrast to an hydrolyzed-open site (with no silicon vacancies).

Combining these insights from DNP-NMR with the other characterizations performed and the catalytic activity in the aqueous phase glucose isomerization (Table 4.1) shows that the materials possessing highest catalytic activity on our series consist of predominantly closed sites in T6 and T5/T7 of a hydrophobic zeolite β framework. While the importance of hydrophobicity has already been shown for Ti- β samples prepared in both, hydroxide and fluoride media,^{75,93} we also show that different synthetic protocols lead to different active site distributions in the Sn- β materials. Hydrothermal synthesis leads to predominantly closed Sn^{IV} centers in T6 and T5/T7 position while in post-synthetic materials a closed site in T8 position is the most populated one along with the hydrolyzed-open and defect-open forms in T5 and T9 position. However, one should point that closed sites found in the as synthesized materials are likely to undergo hydrolysis to form open-hydrolyzed sites under reaction conditions.^{71,94,118,152} Therefore the overall data suggest that a highly hydrophobic framework with accessible Sn sites preferably in the outer rim of the crystal is more important for good activity in the isomerization of glucose rather than the identity of the site, i.e. closed or hydrolyzed-open.

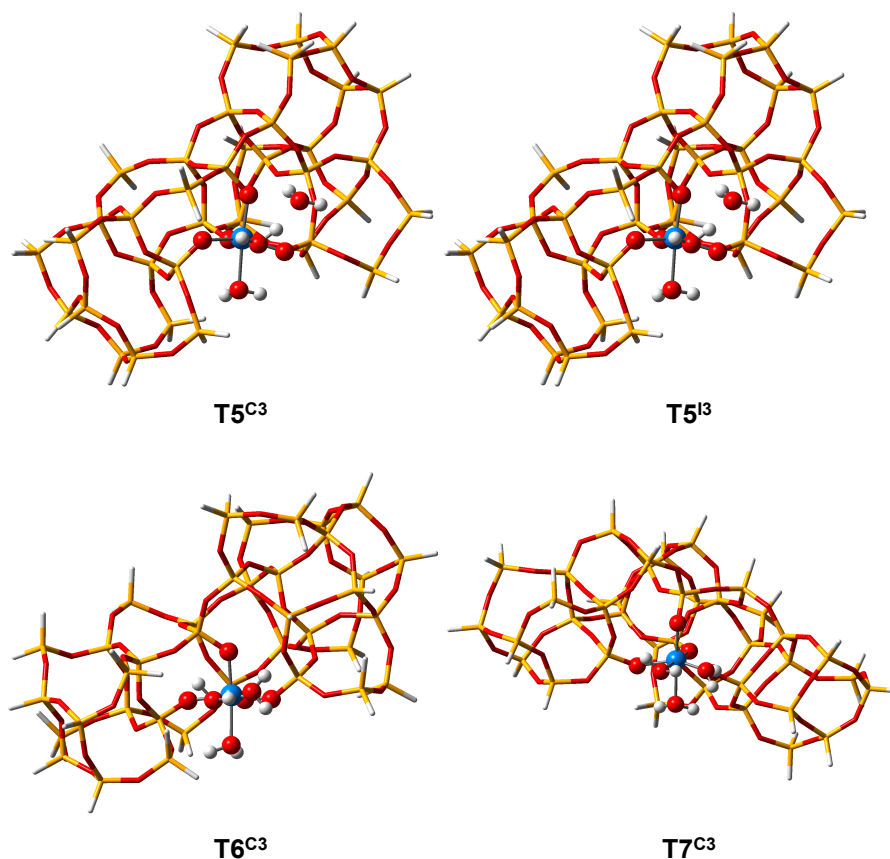


Figure 4.11. Optimized structures of some of the most feasible T sites as active sites in Sn- β : T5^{C3}/T5^{I3} (upper) and T6^{C3}/T7^{C3} (bottom).

For both hydrothermal Sn- β zeolites, which showed the highest activity, we determined little to no defects, giving rise to a hydrophobic framework, and mostly closed Sn sites in T6, and T5/T7 positions. T1-T4 and T8/T9 closed sites cannot be fully excluded, but their corresponding resonances possess the lowest relative integral intensity, so they represent a minority of the Sn sites. In the case of the Sn-Beta, a small number of the active sites can also be linked to hydrolyzed-open sites of type I in T6, and T5/T7 positions. For the post-synthetic Sn/deAl-Beta-OH-25 with a hydrophilic framework and a significant amount of defects, Sn is most likely occupying the T8 position in closed and the T5 position in hydrolyzed-open type I form. A significant amount of defect-open sites most probably in T9 lattice position are also proposed. The chemical shifts determined for dehydrated Sn- β samples from hydrothermal synthesis indicate that in absence of water, no defect-open sites are present in the zeolite and “open” sites are only created upon hydrolysis by water, which close upon dehydration.

4.5. Conclusions

Sn- β zeolites prepared *via* different synthetic protocols show different activity in the aqueous phase isomerization of glucose. For all tested catalysts an apparent activation barrier of 21-24 kcal mol⁻¹ has been observed consistent with the 1,2-hydrate shift being the rate-determining step for all materials as previously found in other studies.³⁴ Post-synthetic materials prepared by solid-state ion-exchange show a 2-5 times lower activity per Sn compared to traditional hydrothermal Sn- β . ²⁹Si NMR, X-ray diffraction and water adsorption isotherms revealed that the post-synthetic materials showing lowest activity possess a hydrophilic, defective framework, which is likely causing the low activity of these materials. On the other hand hydrothermal Sn- β zeolites and post-synthetic Sn- β prepared from a defect-free Al- β with a high Si/Al ratio display a highly hydrophobic, defect-free framework and higher activity than the hydrophilic materials. The lower activity of the defect-free, post-synthetic zeolite compared to the hydrothermal samples in the glucose isomerization is likely due to a lower accessibility of the Sn-sites or a different local geometry of the active site, since almost identical activity was observed with the smaller glyceraldehyde. In addition SEM-EDX showed a more homogeneous distribution of the Sn within the zeolite crystal in case of the post-synthetic, hydrophobic material. Moreover, the use of DNP NMR allowed the expeditious determination of NMR signatures of the sites present in a series of Sn- β zeolites; combined with DFT calculations of the CSA parameters it is possible to probe the nature of these sites present in the as-synthesized samples. Predominantly closed sites, *i.e.* Sn^{IV} centers four-fold bound to the zeolite framework, are present in the initial material. ¹¹⁹Sn NMR experiments suggest that in particular T6, and T5/T7 sites represent the most abundant species in hydrothermally synthesized Sn- β materials. In dehydrated form only closed Sn sites and no defect-open sites were found in hydrothermal Sn- β zeolites. In the presence of water, closed sites coordinate water molecules and can probably partially hydrolyze (hydrolyzed-open sites) under reaction conditions, resulting in Sn^{IV} three fold bound to the framework and a Sn-OH bond. On the other hand post-synthetic zeolite Sn- β prepared via a two-step method most probably consists of closed T8 and T5 hydrolyzed-open sites as well as T9 defect-open sites incorporated into the hydrophilic, defective framework. Overall, we can conclude that the activity of Sn- β in the aqueous phase isomerization of glucose is highly dependent on the morphology of the material, *i.e.* hydrophobicity. Moreover

accessibility and T-site positioning of the Sn-site were found to be important. Although defect-open sites (tetrahedral SnOH) can be active, the data here shows that samples constituted mainly of closed sites are also highly active. Finally, this work provides a signature map of various Sn sites and opens the possibility to determine the active site distributions in terms of nature and lattice position of the Sn centers in Sn- β zeolites, to compare the influence of synthetic protocols in the formation of specific sites, and *in fine* to rationally optimize the synthesis protocols toward the formation of the desired active sites.

Chapter 5

Conclusions and Outlook

Over recent decades, the chemical industry has established highly efficient, integrated value-chains for the synthesis of chemicals based on petrochemical resources. Within this general area, zeolites have undertaken a leading role as they efficiently catalyze chemical transformations. Nevertheless, the diminishing supply of these finite resources and the increasing environmental restrictions seek for the development of new catalytic systems that can efficiently utilize renewable feedstocks. As such, Lewis acid doped zeolites have shown great potential due to their water-tolerant catalytic behavior and the ability to efficiently activate carbonyl groups. The exploration thereof and the fundamental understanding of their catalytic activity require substantial (fundamental) research efforts until economically compatible renewable processes can be implemented.

Prior to the commencement of this thesis, alternative synthesis protocols for the preparation of Lewis acid doped zeolites were limited and a rational design of these materials was not possible due to the lack of fundamental understanding. To promote the utilization of Lewis acid zeolites on both an academic and more importantly an industrial scale, two major challenges need to be overcome that have been impedimentary so far. On the one hand, reliable and versatile synthesis procedures need to be developed that allow the synthesis of Lewis acid zeolites in a safe, efficient, reproducible and scalable way. On the other hand, there is a lack of fundamental understanding about the nature of the active sites. In particular the broad spectrum of possible metal sites and the superimposed influence of extended factors from the zeolite matrix that all contribute to the catalytic activity, make the identification of essential catalyst properties that result in high activity extremely challenging. Therefore multidisciplinary approaches need to be developed to address this problem.

5.1. Conclusions

In the present thesis a robust and versatile two-step procedure for the post-synthetic preparation of Lewis acid Sn-, Zr-, Nb- and Ti-zeolite β was established (Chapter 2). With the developed approach some of the issues associated with the conventional synthesis

such as long crystallization time, the use of toxic hydrofluoric acid and the limited amount of incorporated metal can be circumvented. This is achieved by dealumination of a parent Al- β zeolite by acid leaching and subsequent Lewis acid heteroatom-incorporation by solid-state ion-exchange (Sn, Zr) or impregnation (Nb, Ti). The resulting materials demonstrate high catalytic activity in the intramolecular 1,2-hydride shift of glyceraldehyde to dihydroxyacetone and follow the predicted trend in activity (Sn>Zr>Ti).¹⁰⁶ In the epoxidation of bulky olefins with H₂O₂ post-synthetic Ti- β showed comparable activity to hydrothermal analogues. Interestingly, the Nb-containing catalyst showed a 4 times higher activity. We believe that the convenient preparation of such Lewis acidic zeolites from readily available aluminosilicate analogues will lead to significant increases in the utilization of these materials and further to unprecedented discoveries in the application of heterogeneous Lewis acid zeolites.

In a second step, the nature of the active sites of Sn- β zeolites prepared following our developed post-synthetic approach via solid-state ion-exchange was revealed (Chapter 3). From ¹¹⁹Sn Mössbauer spectroscopy we concluded that the Sn centers in zeolite- β are hexacoordinated with a distorted octahedral geometry. ¹¹⁹Sn NMR spectra on a series of Sn- β with varying Sn loading (0.5-10 wt%) show that there are three different types of sites present in these materials, and that their relative population varies with Sn loading. One signal was assigned to extra-framework SnO₂ and the two other signals to isolated framework Sn sites. For all three sites the chemical shift anisotropy was measured to gain structural information by recording 2D cross-polarization magic-angle-turning experiments. The acquisition of ¹¹⁹Sn NMR spectra and in particular the determination of the chemical shift anisotropy was enabled by the use of dynamic nuclear polarization, which improves sensitivity, hence reduces acquisition time dramatically. To relate an active site structure to the observed NMR signatures, we calculated the ¹¹⁹Sn NMR signatures for possible active site models. Comparison of the experimental with the calculated NMR parameter lets us conclude that the main difference between the two framework sites is the coordination to the zeolite framework. Both coordinate two water molecules, but for one of the sites one of the water molecules has opened a Sn-O-Si bridge (open site). In case of the other site the Sn is still four-fold bound to the framework with two water molecules coordinated to Sn (closed site). This is the first direct spectroscopic evidence for the presence of the two framework sites, which have been proposed previously.

With a versatile synthesis procedure (Chapter 2) and a tool to characterize the active sites in Sn- β (Chapter 3) in hand we aimed to identify the influence of the synthesis protocol on the physicochemical properties and the active site distribution, hence catalytic activity of the material. In order to do so we prepared Sn- β zeolites *via* different synthetic methods. Different activities in the aqueous phase isomerization of glucose suggest a difference in the physicochemical properties and/or the nature of the active sites within the different Sn- β catalysts. The post-synthetic materials prepared by solid-state ion-exchange showed a 2-5 times lower activity per Sn compared to traditional hydrothermal Sn- β . From ^{29}Si NMR, X-ray diffraction and water adsorption isotherms we learned that a hydrophilic, defective framework was the main cause of the lower activity. Hydrothermal Sn- β zeolites and post-synthetic Sn- β prepared from a defect-free Al- β with a high Si/Al ratio, on the other hand, displayed a highly hydrophobic, defect-free framework. However, the latter still cannot compete with the activity of the hydrothermal material, suggesting a lower accessibility of the Sn-sites and/or a different local geometry of the active site to be detrimental. Therefore, we conducted ^{119}Sn NMR experiments to determine the NMR signatures of all sites present in each of the Sn- β zeolites. A combination of these experimental results with DFT calculations of the NMR parameters allowed us to provide the nature of the active sites present in the as-synthesized samples. We found that predominantly closed sites, most likely in T6 and T5/T7 are present in the highly active hydrothermal materials and that there are no or very little defect-open sites (open sites with a neighboring silicon vacancy). The less active post-synthetic materials most likely consist of closed T8 and T5 hydrolyzed-open sites as well as T9 defect-open sites. In the presence of water, closed sites coordinate water molecules and are likely to partially hydrolyze (hydrolyzed-open sites) under reaction conditions.

Overall, we can conclude that the activity of Sn- β in the aqueous phase isomerization of glucose is highly dependent on the morphology of the material, *i.e.* hydrophobicity. Moreover, accessibility and T-site positioning of the Sn-site are important. Although defect-open sites (tetrahedral SnOH) can be active, the data here shows that samples constituted mainly of closed sites are also highly active. Finally, the NMR calculations performed, provide a signature map of various Sn sites and opens the possibility to determine the active site distributions in terms of nature and lattice position of the Sn centers in Sn- β zeolites. Ultimately, this enables one to correlate the influence of

synthetic parameter on the formation of specific sites, and *in fine* to rationally optimize the synthesis protocols towards the formation of the desired active sites.

5.2. Outlook

In this thesis, achievements in the synthesis of Lewis acid β -zeolites and the determination of the precise structure of their active sites on an atomic level have been made. Nevertheless, there are still several aspects related to this work and beyond that need further dedication.

The use of DNP NMR enabled us to determine the ^{119}Sn chemical shift and the corresponding chemical shift anisotropy of natural abundance Sn- β zeolites. By combination of the so gained structural information on the active site with chemical calculations we were able to identify the nature and T-site position of the active sites in Sn- β (Chapter 4). Depending on the synthesis protocol different active site speciations were observed. We believe that by systematically investigating synthesis parameter in different synthesis protocols of Lewis acid β -zeolites and their effect on the morphology and active site speciation, a rationale design of β -zeolites with specific active sites and defined catalyst morphology can be developed. In case of the fluoride mediated synthesis of β -zeolites, interesting parameters for a systematic study and their influence on the formation of specific sites are for example the Sn loading, the seed morphology and the calcination conditions. In the case of post-synthetic materials an intriguing point to address is the influence of the method (CVD, chemical grafting, SSIE) on Sn incorporation and the effect of the Sn precursor on the active sites. Further, it would be valuable to investigate how the Al-site distribution in the parent Al- β zeolite correlates with the Sn-site distribution in the post-synthetic material. We hypothesize that Sn is placed in the T-sites that were previously occupied by Al, considering that all created silanol vacancies are filled with Sn. If this holds true, it would be possible to optimize the synthesis of Al- β toward the formation of specific sites, thus pre-defining the location of Sn in the post-synthetic material. In case less Sn is incorporated than present silanol vacancies after dealumination, the question is, if the Sn incorporated T-site specific.

Another interesting aspect is to apply our approach of combining structural information obtained from solid state NMR with computational chemistry to determine the active site distribution for Sn- β for the other heteroatoms that were

successfully incorporated into the β framework (Chapter 2). These heteroatoms include Ti, Zr and Nb. However, in contrast to ^{119}Sn , $^{47/49}\text{Ti}$, ^{91}Zr , and ^{93}Nb all consist of quadrupolar nuclei, which makes the acquisition of NMR spectra more challenging from a technical point of view. A question to approach in this regard is, how the nature of the heteroatom affects the active site distribution. Due to the different atomic radii and electronic properties of the heteroatoms that were incorporated, a difference in active site distribution in terms of both nature, *i.e.* open vs. closed and T-site position is expected.

In Chapter 4 we have observed that post-synthetic Sn- β zeolites, which possess a large number of defect sites show significantly lower activity in the isomerization of monosaccharides *via* 1,2-hydride shift compared to hydrothermal zeolites. Framework defects can originate from (i) the synthesis of the Al- β or (ii) unoccupied silanol nests created during dealumination. While the formation of silanol defects during Al- β synthesis can only be prevented by the use of a fluoride medium, the treatment of defective Sn- β with SiCl_4 could help to heal the remaining silanol nests. The introduction of a second post-synthetic step, could thus increase the hydrophobicity inside the pores of the zeolite crystal. Another possibility to increase the hydrophobicity of post-synthetic Sn- β is the functionalization of the external surface with organosilanes. This might help to exclude bulk water from the zeolite pores and lead to increased activity by reducing the extent of competitive adsorption. Further, we expect that an increase in hydrophobicity could potentially also lead to an enhanced stability of the catalyst.

The stability of Lewis acid zeolites is a property that has not obtained a lot of attention so far is an important parameter toward industrial implementation. Lari *et al.* showed the different stannosilicates experienced significant deactivation upon exposure to reaction conditions characteristic for monosaccharide isomerizations.²¹⁵ They conclude that the deactivation is mainly caused by amorphisation of the framework and a change in the coordination of the Sn center. However, the precise structure of the deactivated site was not investigated. In preliminary experiments we have also observed a drastic decrease in activity for our post-synthetic Sn/deAl-Beta-OH-25. 1Sn/deAl-Beta-OH-25 was tested in the aqueous phase isomerization of glucose at 100 °C for 4h. Recycling the catalyst from the first experiment and performing a second experiment resulted in a drop in initial activity by 50 % even when the catalyst was regenerated between the experiments. This suggests a change in the nature and/or

accessibility of the active site or the catalyst morphology. With the aim to identify the nature of the deactivated Sn species we performed ^{119}Sn DNP NMR experiments on a regenerated sample of 1Sn/deAl-Beta-OH-25 after 4 hours of reaction (Figure 5.1a). Compared to the ^{119}Sn DNP NMR spectra, the peak at -660 ppm, which we assigned to hydrolyzed-open sites showed a decreased in intensity, instead, the appearance of a peak at -718 ppm was observed. According to the NMR Signature map that we have developed, a number of different sites show a chemical shift of around -718 ppm. To assign this new site that was observed in the spectra of the deactivated material, a more thorough characterization is needed. As demonstrated in Chapter 4, structural information can be derived from the determination of the chemical shift and the chemical shift anisotropy of both dehydrated and hydrated materials. In addition to the active site structures, which were considered in Chapter 4, one could also envision a hydrolyzed defect-open site (Figure 5.1b). Further the characterization of the physicochemical properties is necessary, since these could also have a significant influence on the catalytic activity.

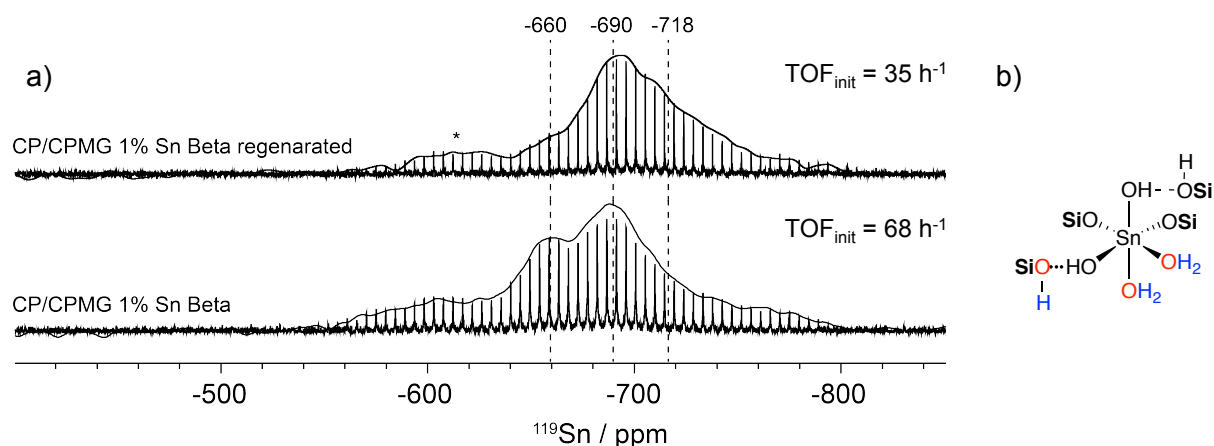


Figure 5.1. a) $105\text{ K }^{119}\text{Sn}$ DNP-CPMAS and CPMG spectra of pristine and regenerated (after 4h under reaction conditions) 1Sn/deAl-Beta-OH-25. The spectrum was acquired on a 400 MHz DNP spectrometer with a spinning frequency of 12.5 kHz. b) Schematic of a hydrolyzed defect-open site.

Not least, in our work we observed that Sn- β with predominantly closed sites show very high activity in the aqueous phase glucose isomerization (Chapter 4). In contrast, several studies both, experimental and computational suggest that the open site in Sn- β is responsible for the high activity of Sn- β in this reaction. In case of the experimental studies this hypothesis is mainly based on the characterization of Sn- β by adsorption of deuterated acetonitrile (CD_3CN), whereas computational studies focused on the calculation of the enthalpy profile over the two sites. In the adsorption of CD_3CN two distinct shifts of the $\text{C}\equiv\text{N}$ stretching vibration were observed and assigned to the

open (2316 cm^{-1}) and closed site (2308 cm^{-1}) using DFT calculations. Correlating this observation with our results raises two questions that need further dedication; (i) are the sites dynamic under reaction conditions and (ii) is the observed shift in the CD_3CN adsorption at 2316 cm^{-1} truly originating from adsorption to the open site. We believe that the first can be addressed by exposing freshly prepared Sn- β to water at reaction temperature for different times and subsequent determination of the active site speciation by measuring ^{119}Sn NMR. To approach the second point, computational chemistry presents a powerful tool. Calculations of the $\text{C}\equiv\text{N}$ shift of adsorbed CD_3CN on the different dehydrated active sites structures investigated in Chapter 4 will show, if open sites can be associated with a higher shift independent of the T-site position or if also closed sites can give rise to the signal in the FTIR spectrum at 2316 wavenumber likewise. Further, precise titration of the active sites with acetonitrile in combination with multinuclear ^{15}N - ^{119}Sn 2D experiments could proof the literature hypothesis that CD_3CN is preferably adsorbing to the open site.

In conclusion further efforts in understanding the effect of synthesis parameters on the physicochemical properties and the formation of specific active sites is necessary to establish β -zeolites as versatile industrial catalysts in the upgrading of biomass derived oxygenates and the production of fine chemicals. While our efforts were mainly focused on Sn- β , the presented approach may provide a framework for future studies on other other zeolitic materials.

Bibliography

- [1] Umile, T. P. *Catalysis for Sustainability: Goals, Challenges, and Impacts*; CRC Press: Boca Raton, **2015**.
- [2] Elkington, J. *Cannibals with Forks: The Triple Bottom Line of 21st Century Business*; Capstone, **1999**.
- [3] Anastas, P.; Eghbali, N. *Chem. Soc. Rev.* **2010**, *39*, 301-312.
- [4] Cavani, F. *Sustainable industrial processes [principles, tools and industrial examples]*; Wiley-VCH: Weinheim, **2009**.
- [5] Beller, M. *Leibnitz Perspect. - Res. Sustainable* **2007**.
- [6] Sheldon, R. A.; Arends, I.; Hanefeld, U. *Green chemistry and catalysis*; Wiley-VCH: Weinheim, **2007**.
- [7] Hagen, J. *Industrial catalysis a practical approach*; 3rd completely revised and enlarged edition ed.; Wiley-VCH: Weinheim, **2015**.
- [8] Acmite Market Intelligence *Market Report: Global Catalyst Market*, 3rd Ed., **2015**.
- [9] Rothenberg, G. In *Kirk-Othmer Encyclopedia of Chemical Technology*; John Wiley & Sons, Inc.: 2000.
- [10] Primo, A.; Garcia, H. *Chem. Soc. Rev.* **2014**, *43*, 7548-7561.
- [11] Vermeiren, W.; Gilson, J. P. *Top. Catal.* **2009**, *52*, 1131-1161.
- [12] Busca, G. *Chem. Rev.* **2007**, *107*, 5366-5410.
- [13] Kulprathipanja, S. *Zeolites in industrial separation and catalysis*; Wiley: Weinheim, **2010**.
- [14] Tanabe, K.; Holderich, W. F. *Appl. Catal., A* **1999**, *181*, 399-434.
- [15] Corma, A.; Garcia, H. *Chem. Rev.* **2003**, *103*, 4307-4365.
- [16] Yamamoto, H. *Acid catalysis in modern organic synthesis*; Wiley-VCH: Weinheim, **2008**.
- [17] Sheldon, R. A.; Bekkum, H. *Fine chemicals through heterogeneous catalysis*; Wiley-VCH: Weinheim, **2001**.
- [18] Moliner, M. *Dalton Trans.* **2014**, *43*, 4197-4208.
- [19] Hattori, H.; Ono, Y. *Solid acid catalysis from fundamentals to applications*; Pan Stanford Publishing: Singapore, **2015**.
- [20] Corma, A.; Garcia, H. *Chem. Rev.* **2002**, *102*, 3837-3892.
- [21] Luo, H. Y., Lewis, Jennifer D., Román-Leshkov, Yuriy *Annu. Rev. Chem. Biomol. Eng.* **2016**, *7*, 27.21-27.30.
- [22] *Cejka, J. r. *Introduction to zeolite science and practice*; 3rd rev. ed.; Elsevier: Amsterdam, **2007**.
- [23] Bekkum, H. *Introduction to zeolite science and practice*; Elsevier: Amsterdam etc., **1991**.
- [24] Chu, C. T. W.; Chang, C. D. *J. Phys. Chem.* **1985**, *89*, 1569-1571.

- [25] Saxton, R. J. *Top. Catal.* **1999**, *9*, 43-57.
- [26] Notari, B. *Advances in Catalysis* **1996**, *41*, 253-334.
- [27] In *Polimeri Europa Licensing Technology Brochure*.
- [28] Eilertsen, E. A.; Bordiga, S.; Lamberti, C.; Damin, A.; Bonino, F.; Arstad, B.; Svelle, S.; Olsbye, U.; Lillerud, K. P. *ChemCatChem* **2011**, *3*, 1869-1871.
- [29] Mal, N. K.; Ramaswamy, V.; Rajamohanan, P. R.; Ramaswamy, A. V. *Microporous Mater.* **1997**, *12*, 331-340.
- [30] Corma, A.; Nemeth, L. T.; Renz, M.; Valencia, S. *Nature* **2001**, *412*, 423-425.
- [31] Corma, A.; Xamena, F. X. L. I.; Prestipino, C.; Renz, M.; Valencia, S. *J. Phys. Chem. C* **2009**, *113*, 11306-11315.
- [32] Zhu, Y. Z.; Chuah, G.; Jaenicke, S. *Chem. Commun.* **2003**, 2734-2735.
- [33] Reddy, J. S.; Sivasanker, S.; Ratnasamy, P. *J. Mol. Catal.* **1991**, *69*, 383-392.
- [34] Wu, P.; Tatsumi, T. *Catal. Surv. Asia* **2004**, *8*, 137-148.
- [35] Wojtaszek-Gurdak, A.; Ziolek, M. *RSC Adv.* **2015**, *5*, 22326-22333.
- [36] Osmundsen, C. M.; Holm, M. S.; Dahl, S.; Taarning, E. *Proc. R. Soc. A* **2012**, *468*, 2000-2016.
- [37] Moliner, M.; Roman-Leshkov, Y.; Davis, M. E. *Proc. Natl. Acad. Sci. U. S. A.* **2010**, *107*, 6164-6168.
- [38] Santelli, M.; Pons, J.-M.; Lewis, G. N. *Lewis acids and selectivity in organic synthesis*; CRC: Boca Raton etc., 1996.
- [39] Leach, M. R. *Lewis acid/base reaction chemistry*; Meta-Synthesis: Brighton, **1999**.
- [40] Jensen, W. B. <<The>> *Lewis acid-base concepts an overview*; Wiley: New York, NY, **1980**.
- [41] Wu, P.; Nuntasri, D.; Ruan, J. F.; Liu, Y. M.; He, M. Y.; Fan, W. B.; Terasaki, O.; Tatsumi, T. *J. Phys. Chem. B* **2004**, *108*, 19126-19131.
- [42] Hulea, V.; Dumitriu, E. *Appl. Catal., A* **2004**, *277*, 99-106.
- [43] Kumar, S. B.; Mirajkar, S. P.; Pais, G. C. G.; Kumar, P.; Kumar, R. *J. Catal.* **1995**, *156*, 163-166.
- [44] Perego, C.; Carati, A.; Ingallina, P.; Mantegazza, M. A.; Bellussi, G. *Appl. Catal., A* **2001**, *221*, 63-72.
- [45] Ichihashi, H.; Sato, H. *Appl. Catal., A* **2001**, *221*, 359-366.
- [46] LeBars, J.; Dakka, J.; Sheldon, R. A. *Appl. Catal., A* **1996**, *136*, 69-80.
- [47] Thangaraj, A.; Kumar, R.; Ratnasamy, P. *J. Catal.* **1991**, *131*, 294-297.
- [48] Vanderpol, A. J. H. P.; Vanhooff, J. H. C. *Appl. Catal., A* **1993**, *106*, 97-113.
- [49] Boronat, M.; Corma, A.; Renz, M.; Viruela, P. M. *Chem. - Eur. J.* **2006**, *12*, 7067-7077.
- [50] Corma, A.; Domine, M. E.; Nemeth, L.; Valencia, S. *J. Am. Chem. Soc.* **2002**, *124*, 3194-3195.
- [51] Corma, A.; Renz, M. *Chem. Commun.* **2004**, 550-551.
- [52] Corma, A.; Renz, M. *Angew. Chem.-Int. Edit.* **2007**, *46*, 298-300.

- [53] Nie, Y. T.; Jaenicke, S.; Chuah, G. K. *Chem. - Eur. J.* **2009**, *15*, 1991-1999.
- [54] Nikolla, E.; Roman-Leshkov, Y.; Moliner, M.; Davis, M. E. *ACS Catal.* **2011**, *1*, 408-410.
- [55] Roman-Leshkov, Y.; Barrett, C. J.; Liu, Z. Y.; Dumesic, J. A. *Nature* **2007**, *447*, 982-985.
- [56] van Putten, R. J.; van der Waal, J. C.; de Jong, E.; Rasrendra, C. B.; Heeres, H. J.; de Vries, J. G. *Chem. Rev.* **2013**, *113*, 1499-1597.
- [57] Pacheco, J. J.; Davis, M. E. *Proc. Natl. Acad. Sci. U. S. A.* **2014**, *111*, 8363-8367.
- [58] Chang, C. C.; Cho, H. J.; Yu, J. Y.; Gorte, R. J.; Gulbinski, J.; Dauenhauer, P.; Fan, W. *Green Chem.* **2016**, *18*, 1368-1376.
- [59] Taarning, E.; Saravanamurugan, S.; Holm, M. S.; Xiong, J. M.; West, R. M.; Christensen, C. H. *ChemSusChem* **2009**, *2*, 625-627.
- [60] Holm, M. S.; Pagan-Torres, Y. J.; Saravanamurugan, S.; Riisager, A.; Dumesic, J. A.; Taarning, E. *Green Chem.* **2012**, *14*, 702-706.
- [61] Holm, M. S.; Saravanamurugan, S.; Taarning, E. *Science* **2010**, *328*, 602-605.
- [62] Wang, Y.; Lewis, J. D.; Román-Leshkov, Y. *ACS Catal.* **2016**, *6*, 2739-2744.
- [63] Van de Vyver, S.; Odermatt, C.; Romero, K.; Prasomsri, T.; Roman-Leshkov, Y. *ACS Catal.* **2015**, *5*, 972-977.
- [64] de la Torre, O.; Renz, M.; Corma, A. *Appl. Catal., A* **2010**, *380*, 165-171.
- [65] Bermejo-Deval, R.; Orazov, M.; Gounder, R.; Hwang, S. J.; Davis, M. E. *Acs Catal* **2014**, *4*, 2288-2297.
- [66] Gunther, W. R.; Wang, Y. R.; Ji, Y. W.; Michaelis, V. K.; Hunt, S. T.; Griffin, R. G.; Roman-Leshkov, Y. *Nat. Commun.* **2012**, *3*.
- [67] Tang, B.; Dai, W. L.; Wu, G. J.; Guan, N. J.; Li, L. D.; Hunger, M. *ACS Catal.* **2014**, *4*, 2801-2810.
- [68] Cambor, M. A.; Costantini, M.; Corma, A.; Gilbert, L.; Esteve, P.; Martinez, A.; Valencia, S. *Chem. Commun.* **1996**, 1339-1340.
- [69] Lewis, J. D.; Van de Vyver, S.; Roman-Leshkov, Y. *Angew. Chem.-Int. Edit.* **2015**, *54*, 9835-9838.
- [70] Kalvachev, Y.; Jaber, M.; Mavrodinova, V.; Dimitrov, L.; Nihtianova, D.; Valtchev, V. *Microporous Mesoporous Mater.* **2013**, *177*, 127-134.
- [71] Luo, H. Y.; Consoli, D. F.; Gunther, W. R.; Roman-Leshkov, Y. *J Catal* **2014**, *320*, 198-207.
- [72] Blasco, T.; Cambor, M. A.; Corma, A.; Esteve, P.; Guil, J. M.; Martinez, A.; Perdigon-Melon, J. A.; Valencia, S. *J. Phys. Chem. B* **1998**, *102*, 75-88.
- [73] Cambor, M. A.; Corma, A.; Valencia, S. *J Mater Chem* **1998**, *8*, 2137-2145.
- [74] Jansen, J. C. *Advanced zeolite science and applications*; Elsevier: Amsterdam etc., 1994.
- [75] Gounder, R.; Davis, M. E. *Aiche Journal* **2013**, *59*, 3349-3358.
- [76] Harris, J. W.; Cordon, M. J.; Di Iorio, J. R.; Vega-Vila, J. C.; Ribeiro, F. H.; Gounder, R. *Journal of Catalysis* **2016**, *335*, 141-154.
- [77] Gounder, R.; Davis, M. E. *J. Catal.* **2013**, *308*, 176-188.

- [78] Newsam, J. M.; Treacy, M. M. J.; Koetsier, W. T.; Degruyter, C. B. *P Roy Soc Lond a Mat* **1988**, *420*, 375-&.
- [79] Lew, C. M.; Rajabbeigi, N.; Tsapatsis, M. *Microporous Mesoporous Mater.* **2012**, *153*, 55-58.
- [80] Chang, C. C.; Wang, Z. P.; Dornath, P.; Cho, H. J.; Fan, W. *RSC Adv.* **2012**, *2*, 10475-10477.
- [81] Kang, Z. H.; Zhang, X. F.; Liu, H. O.; Qiu, J. S.; Yeung, K. L. *Chem Eng J* **2013**, *218*, 425-432.
- [82] Iida, T.; Sato, M.; Numako, C.; Nakahira, A.; Kohara, S.; Okubo, T.; Wakihara, T. *J. Mater. Chem. A* **2015**, *3*, 6215-6222.
- [83] Chang, C. C.; Cho, H. J.; Wang, Z. P.; Wang, X. T.; Fan, W. *Green Chem.* **2015**, *17*, 2943-2951.
- [84] Li, P.; Liu, G. Q.; Wu, H. H.; Liu, Y. M.; Jiang, J. G.; Wu, P. *J. Phys. Chem. C* **2011**, *115*, 3663-3670.
- [85] Hammond, C.; Conrad, S.; Hermans, I. *Angew. Chem.-Int. Edit.* **2012**, *51*, 11736-11739.
- [86] Dijkmans, J.; Gabriels, D.; Dusselier, M.; de Clippel, F.; Vanelderen, P.; Houthoofd, K.; Malfliet, A.; Pontikes, Y.; Sels, B. F. *Green Chem.* **2013**, *15*, 2777-2785.
- [87] van der Graaff, W. N. P.; Li, G. N.; Mezari, B.; Pidko, E. A.; Hensen, E. J. M. *ChemCatChem* **2015**, *7*, 1152-1160.
- [88] Dijkmans, J.; Demol, J.; Houthoofd, K.; Huang, S. G.; Pontikes, Y.; Sels, B. *J. Catal.* **2015**, *330*, 545-557.
- [89] Hammond, C.; Padovan, D.; Al-Nayili, A.; Wells, P. P.; Gibson, E. K.; Dimitratos, N. *ChemCatChem* **2015**, *7*, 3322-3331.
- [90] Baerlocher, C.; McCusker, L. B.; Olson, D. H.; International Zeolite Association Structure Commission *Atlas of zeolite framework types dedicated to Walter M. Meier*; 6th rev. ed.; Elsevier: Amsterdam, **2007**.
- [91] Thommes, M.; Mitchell, S.; Perez-Ramirez, J. *J. Phys. Chem. C* **2012**, *116*, 18816-18823.
- [92] Storck, S.; Bretinger, H.; Maier, W. F. *Appl. Catal., A* **1998**, *174*, 137-146.
- [93] Gounder, R. *Catal Sci Technol* **2014**, *4*, 2877-2886.
- [94] Bermejo-Deval, R.; Assary, R. S.; Nikolla, E.; Moliner, M.; Roman-Leshkov, Y.; Hwang, S. J.; Palsdottir, A.; Silverman, D.; Lobo, R. F.; Curtiss, L. A.; Davis, M. E. *Proc. Natl. Acad. Sci. U. S. A.* **2012**, *109*, 9727-9732.
- [95] Tolborg, S.; Katerinopoulou, A.; Falcone, D. D.; Sadaba, I.; Osmundsen, C. M.; Davis, R. J.; Taarning, E.; Fristrup, P.; Holm, M. S. *Journal of Materials Chemistry A* **2014**, *2*, 20252-20262.
- [96] Roy, S.; Bakhmutsky, K.; Mahmoud, E.; Lobo, R. F.; Gorte, R. J. *ACS Catal.* **2013**, *3*, 573-580.
- [97] Bermejo-Deval, R.; Gounder, R.; Davis, M. E. *ACS Catal.* **2012**, *2*, 2705-2713.
- [98] Nemeth, L.; Moscoso, J.; Erdman, N.; Bare, S. R.; Oroskar, A.; Kelly, S. D.; Corma, A.; Valencia, S.; Renz, M. *Stud. Surf. Sci. Catal.* **2004**, *154*, 2626-2631.

- [99] Dai, W.; Wang, C.; Tang, B.; Wu, G.; Guan, N.; Xie, Z.; Hunger, M.; Li, L. *ACS Catal.* **2016**, *6*, 2955-2964.
- [100] Klinowski, J. *Chem. Rev.* **1991**, *91*, 1459-1479.
- [101] Klinowski, J.; Anderson, M. W. *Magn. Reson. Chem.* **1990**, *28*, S68-S81.
- [102] Hwang, S.-J.; Gounder, R.; Bhawe, Y.; Orazov, M.; Bermejo-Deval, R.; Davis, M. *Top Catal* **2015**, 1-6.
- [103] Kolyagin, Y. G.; Yakimov, A. V.; Tolborg, S.; Vennestrøm, P. N. R.; Ivanova, I. I. *J. Phys. Chem. Lett.* **2016**, *7*, 1249-1253.
- [104] Gunther, W. R.; Michaelis, V. K.; Caporini, M. A.; Griffin, R. G.; Roman-Leshkov, Y. *J. Am. Chem. Soc.* **2014**, *136*, 6219-6222.
- [105] Boronat, M.; Concepcion, P.; Corma, A.; Renz, M.; Valencia, S. *J. Catal.* **2005**, *234*, 111-118.
- [106] Assary, R. S.; Curtiss, L. A. *J. Phys. Chem. A* **2011**, *115*, 8754-8760.
- [107] Li, G. N.; Pidko, E. A.; Hensen, E. J. M. *Catal Sci Technol* **2014**, *4*, 2241-2250.
- [108] Rai, N.; Caratzoulas, S.; Vlachos, D. G. *Acs Catal* **2013**, *3*, 2294-2298.
- [109] Conrad, S.; Verel, R.; Hammond, C.; Wolf, P.; Goltl, F.; Hermans, I. *ChemCatChem* **2015**, *7*, 3270-3278.
- [110] Sushkevich, V. L.; Palagin, D.; Ivanova, I. I. *ACS Catal.* **2015**, *5*, 4833-4836.
- [111] Sushkevich, V. L.; Vimont, A.; Travert, A.; Ivanova, I. I. *J. Phys. Chem. C* **2015**, *119*, 17633-17639.
- [112] Sastre, G.; Corma, A. *Chem. Phys. Lett.* **1999**, *302*, 447-453.
- [113] Shetty, S.; Kulkarni, B. S.; Kanhere, D. G.; Goursot, A.; Pal, S. *Journal of Physical Chemistry B* **2008**, *112*, 2573-2579.
- [114] Henry, P. F.; Weller, M. T.; Wilson, C. C. *J. Phys. Chem. B* **2001**, *105*, 7452-7458.
- [115] Hajar, C. A.; Jacubinas, R. M.; Eckert, J.; Henson, N. J.; Hay, P. J.; Ott, K. C. *J. Phys. Chem. B* **2000**, *104*, 12157-12164.
- [116] Lamberti, C.; Bordiga, S.; Zecchina, A.; Artioli, G.; Marra, G.; Spano, G. *J. Am. Chem. Soc.* **2001**, *123*, 2204-2212.
- [117] Bare, S. R.; Kelly, S. D.; Sinkler, W.; Low, J. J.; Modica, F. S.; Valencia, S.; Corma, A.; Nemeth, L. T. *J. Am. Chem. Soc.* **2005**, *127*, 12924-12932.
- [118] Montejo-Valencia, B. D.; Curet-Arana, M. C. *J Phys Chem C* **2015**, *119*, 4148-4157.
- [119] Yang, G.; Pidko, E. A.; Hensen, E. J. M. *J. Phys. Chem. C* **2013**, *117*, 3976-3986.
- [120] Shetty, S.; Pal, S.; Kanhere, D. G.; Goursot, A. *Chem. - Eur. J.* **2006**, *12*, 518-523.
- [121] Szostak, R. *Molecular sieves principles of synthesis and identification*; Van Nostrand Reinhold: New York, **1989**.
- [122] Dijkmans, J.; Dusselier, M.; Gabriëls, D.; Houthoofd, K.; Magusin, P. C. M. M.; Huang, S.; Pontikes, Y.; Trekels, M.; Vantomme, A.; Giebel, L.; Oswald, S.; Sels, B. F. *ACS Catal.* **2015**, *5*, 928-940.
- [123] Lazar, K.; Szeleczky, A. M.; Mal, N. K.; Ramaswamy, A. V. *Zeolites* **1997**, *19*, 123-127.
- [124] Jin, J. J.; Ye, X. X.; Li, Y. S.; Wang, Y. Q.; Li, L.; Gu, J. L.; Zhao, W. R.; Shi, J. L. *Dalton Trans.* **2014**, *43*, 8196-8204.

- [125] Roman-Leshkov, Y.; Davis, M. E. *ACS Catal.* **2011**, *1*, 1566-1580.
- [126] Corma, A.; Domine, M. E.; Valencia, S. *J. Catal.* **2003**, *215*, 294-304.
- [127] Boronat, M.; Corma, A.; Renz, M.; Sastre, G.; Viruela, P. M. *Chem. - Eur. J.* **2005**, *11*, 6905-6915.
- [128] Renz, M.; Blasco, T.; Corma, A.; Fornes, V.; Jensen, R.; Nemeth, L. *Chem. - Eur. J.* **2002**, *8*, 4708-4717.
- [129] Corma, A. *Catal. Rev.: Sci. Eng.* **2004**, *46*, 369-417.
- [130] Gallo, J. M. R.; Alonso, D. M.; Mellmer, M. A.; Dumesic, J. A. *Green Chem.* **2013**, *15*, 85-90.
- [131] Taarning, E.; Osmundsen, C. M.; Yang, X. B.; Voss, B.; Andersen, S. I.; Christensen, C. H. *Energ. Environ. Sci.* **2011**, *4*, 793-804.
- [132] Bai, P.; Siepmann, J. I.; Deem, M. W. *AIChE J.* **2013**, *59*, 3523-3529.
- [133] Bui, L.; Luo, H.; Gunther, W. R.; Roman-Leshkov, Y. *Angew. Chem.-Int. Edit.* **2013**, *52*, 8022-8025.
- [134] Kuwahara, Y.; Kang, D. Y.; Copeland, J. R.; Brunelli, N. A.; Didas, S. A.; Bollini, P.; Sievers, C.; Kamegawa, T.; Yamashita, H.; Jones, C. W. *J. Am. Chem. Soc.* **2012**, *134*, 10757-10760.
- [135] Kuwahara, Y.; Kang, D. Y.; Copeland, J. R.; Bollini, P.; Sievers, C.; Kamegawa, T.; Yamashita, H.; Jones, C. W. *Chem. - Eur. J.* **2012**, *18*, 16649-16664.
- [136] Anilkumar, M.; Hoelderich, W. F. *Appl. Catal., B* **2015**, *165*, 87-93.
- [137] Anilkumar, M.; Holderich, W. F. *J. Catal.* **2008**, *260*, 17-29.
- [138] Ramanathan, A.; Maheswari, R.; Barich, D. H.; Subramaniam, B. *Microporous Mesoporous Mater.* **2014**, *190*, 240-247.
- [139] Cavani, F.; Teles, J. H. *ChemSusChem* **2009**, *2*, 508-534.
- [140] Wu, P.; Tatsumi, T.; Komatsu, T.; Yashima, T. *J. Catal.* **2001**, *202*, 245-255.
- [141] Guo, Q.; Fan, F. T.; Pidko, E. A.; van der Graaff, W. N. P.; Feng, Z. C.; Li, C.; Hensen, E. J. M. *ChemSusChem* **2013**, *6*, 1352-1356.
- [142] Dzwigaj, S.; Peltre, M. J.; Massiani, P.; Davidson, A.; Che, M.; Sen, T.; Sivasanker, S. *Chem. Commun.* **1998**, 87-88.
- [143] Wu, P.; Komatsu, T.; Yashima, T. *J. Phys. Chem.* **1995**, *99*, 10923-10931.
- [144] Mania, P.; Verel, R.; Jenny, F.; Hammond, C.; Hermans, I. *Chem. - Eur. J.* **2013**, *19*, 9849-9858.
- [145] Hereijgers, B. P. C.; Parton, R. F.; Weckhuysen, B. M. *ACS Catal.* **2011**, *1*, 1183-1192.
- [146] Boronat, M.; Concepcion, P.; Corma, A.; Navarro, M. T.; Renz, M.; Valencia, S. *Phys. Chem. Chem. Phys.* **2009**, *11*, 2876-2884.
- [147] Roman-Leshkov, Y.; Moliner, M.; Labinger, J. A.; Davis, M. E. *Angew. Chem.-Int. Edit.* **2010**, *49*, 8954-8957.
- [148] Copéret, C.; Basset, J.-M. *Surface and interfacial organometallic chemistry and catalysis*; Springer: Berlin, 2005.
- [149] Lobo, R. *AIChE J.* **2008**, *54*, 1402-1409.

- [150] Dusselier, M.; Van Wouwe, P.; Dewaele, A.; Makshina, E.; Sels, B. F. *Energ. Environ. Sci.* **2013**, *6*, 1415-1442.
- [151] Corma, A.; Fornes, V.; Iborra, S.; Mifsud, M.; Renz, M. *J. Catal.* **2004**, *221*, 67-76.
- [152] Boronat, M.; Corma, A.; Renz, M. *J. Phys. Chem. B* **2006**, *110*, 21168-21174.
- [153] Boronat, M.; Concepcion, P.; Corma, A.; Renz, M. *Catal. Today* **2007**, *121*, 39-44.
- [154] Yang, G.; Pidko, E. A.; Hensen, E. J. M. *ChemSusChem* **2013**, *6*, 1688-1696.
- [155] Caër, G. L. *private communication*.
- [156] Rosay, M.; Tometich, L.; Pawsey, S.; Bader, R.; Schauwecker, R.; Blank, M.; Borchard, P. M.; Cauffman, S. R.; Felch, K. L.; Weber, R. T.; Temkin, R. J.; Griffin, R. G.; Maas, W. E. *Phys. Chem. Chem. Phys.* **2010**, *12*, 5850-5860.
- [157] Fung, B. M.; Khitrin, A. K.; Ermolaev, K. *J. Magn. Reson.* **2000**, *142*, 97-101.
- [158] Zagdoun, A.; Casano, G.; Ouari, O.; Schwarzwaldler, M.; Rossini, A. J.; Aussenac, F.; Yulikov, M.; Jeschke, G.; Coperet, C.; Lesage, A.; Tordo, P.; Emsley, L. *J. Am. Chem. Soc.* **2013**, *135*, 12790-12797.
- [159] Hu, J. Z.; Wang, W.; Liu, F.; Solum, M. S.; Alderman, D. W.; Pugmire, R. J.; Grant, D. M. *J. Magn. Reson. Ser. A* **1995**, *113*, 210-222.
- [160] Long, G. J. *Mössbauer spectroscopy applied to inorganic chemistry*; Plenum Press: New York London, **1984**.
- [161] Tetrahedral Sn^{IV} is expected with significant negative value ($\delta = -0.2$ mm s⁻¹), corroborating the hexacoordination of Sn in the sample
- [162] Maly, T.; Debelouchina, G. T.; Bajaj, V. S.; Hu, K. N.; Joo, C. G.; Mak-Jurkauskas, M. L.; Sirigiri, J. R.; van der Wel, P. C. A.; Herzfeld, J.; Temkin, R. J.; Griffin, R. G. *J. Chem. Phys.* **2008**, *128*.
- [163] Zagdoun, A.; Rossini, A. J.; Gajan, D.; Bourdolle, A.; Ouari, O.; Rosay, M.; Maas, W. E.; Tordo, P.; Lelli, M.; Emsley, L.; Lesage, A.; Coperet, C. *Chem. Commun.* **2012**, *48*, 654-656.
- [164] Zagdoun, A.; Casano, G.; Ouari, O.; Lapadula, G.; Rossini, A. J.; Lelli, M.; Baffert, M.; Gajan, D.; Veyre, L.; Maas, W. E.; Rosay, M.; Weber, R. T.; Thieuleux, C.; Coperet, C.; Lesage, A.; Tordo, P.; Emsley, L. *J. Am. Chem. Soc.* **2012**, *134*, 2284-2291.
- [165] Gajan, D.; Schwarzwaldler, M.; Conley, M. P.; Gruning, W. R.; Rossini, A. J.; Zagdoun, A.; Lelli, M.; Yulikov, M.; Jeschke, G.; Sauvee, C.; Ouari, O.; Tordo, P.; Veyre, L.; Lesage, A.; Thieuleux, C.; Emsley, L.; Coperet, C. *J. Am. Chem. Soc.* **2013**, *135*, 15459-15466.
- [166] Lesage, A.; Lelli, M.; Gajan, D.; Caporini, M. A.; Vitzthum, V.; Mieville, P.; Alauzun, J.; Roussey, A.; Thieuleux, C.; Mehdi, A.; Bodenhausen, G.; Coperet, C.; Emsley, L. *J. Am. Chem. Soc.* **2010**, *132*, 15459-15461.
- [167] Lelli, M.; Gajan, D.; Lesage, A.; Caporini, M. A.; Vitzthum, V.; Mieville, P.; Heroguel, F.; Rascon, F.; Roussey, A.; Thieuleux, C.; Boualleg, M.; Veyre, L.; Bodenhausen, G.; Coperet, C.; Emsley, L. *J. Am. Chem. Soc.* **2011**, *133*, 2104-2107.
- [168] Rossini, A. J.; Zagdoun, A.; Lelli, M.; Lesage, A.; Coperet, C.; Emsley, L. *Acc. Chem. Res.* **2013**, *46*, 1942-1951.

- [169] Protesescu, L.; Rossini, A. J.; Kriegner, D.; Valla, M.; de Kergommeaux, A.; Walter, M.; Kravchuk, K. V.; Nachttegaal, M.; Stangl, J.; Malaman, B.; Reiss, P.; Lesage, A.; Emsley, L.; Coperet, C.; Kovalenko, M. V. *ACS Nano* **2014**, *8*, 2639-2648.
- [170] Gunther, W. R.; Michaelis, V. K.; Caporini, M. A.; Griffin, R. G.; Román-Leshkov, Y. *Journal of the American Chemical Society* **2014**, *136*, 6219-6222.
- [171] van der Wel, P. C. A.; Hu, K. N.; Lewandowski, J.; Griffin, R. G. *J. Am. Chem. Soc.* **2006**, *128*, 10840-10846.
- [172] Rossini, A. J.; Zagdoun, A.; Hegner, F.; Schwarzwald, M.; Gajan, D.; Coperet, C.; Lesage, A.; Emsley, L. *J. Am. Chem. Soc.* **2012**, *134*, 16899-16908.
- [173] Lafon, O.; Thankamony, A. S. L.; Kobayashi, T.; Carnevale, D.; Vitzthum, V.; Slowing, I. I.; Kandel, K.; Vezin, H.; Amoureux, J. P.; Bodenhausen, G.; Pruski, M. *J. Phys. Chem. C* **2013**, *117*, 1375-1382.
- [174] Rossini, A. J.; Zagdoun, A.; Lelli, M.; Canivet, J.; Aguado, S.; Ouari, O.; Tordo, P.; Rosay, M.; Maas, W. E.; Coperet, C.; Farrusseng, D.; Emsley, L.; Lesage, A. *Angew. Chem.-Int. Edit.* **2012**, *51*, 123-127.
- [175] Rossini, A. J.; Zagdoun, A.; Lelli, M.; Gajan, D.; Rascon, F.; Rosay, M.; Maas, W. E.; Coperet, C.; Lesage, A.; Emsley, L. *Chem. Sci.* **2012**, *3*, 108-115.
- [176] Herzfeld, J.; Berger, A. E. *J. Chem. Phys.* **1980**, *73*, 6021-6030.
- [177] Choudhary, V.; Pinar, A. B.; Sandler, S. I.; Vlachos, D. G.; Lobo, R. F. *ACS Catal.* **2011**, *1*, 1724-1728.
- [178] Corma, A.; Domine, M. E.; Nemeth, L.; Valencia, S. *J Am Chem Soc* **2002**, *124*, 3194-3195.
- [179] Vjunov, A.; Fulton, J. L.; Huthwelker, T.; Pin, S.; Mei, D. H.; Schenter, G. K.; Govind, N.; Camaioni, D. M.; Hu, J. Z.; Lercher, J. A. *J Am Chem Soc* **2014**, *136*, 8296-8306.
- [180] Dijkmans, J.; Dusselier, M.; Janssens, W.; Trekels, M.; Vantomme, A.; Breynaert, E.; Kirschhock, C. E. A.; Sels, B. F. *Acs Catal* **2016**, *6*, 31-46.
- [181] Parvulescu, A. N.; Müller, U.; Teles, J. H.; Vautravers, N.; Uhl, G.; Hermans, I.; Wolf, P.; Hammond, C. WO2015067654 A1, **2015**.
- [182] Valencia, S. V.; Corma, A. C. US5968473 **2001**.
- [183] Rouquerol, J.; Llewellyn, P.; Rouquerol, F. In *Studies in Surface Science and Catalysis*; P.L. Llewellyn, F. R.-R. J. R., Seaton, N., Eds.; Elsevier: 2007; Vol. Volume 160, p 49-56.
- [184] Kubicki, D. J.; Rossini, A. J.; Porea, A.; Zagdoun, A.; Ouari, O.; Tordo, P.; Engelke, F.; Lesage, A.; Emsley, L. *J Am Chem Soc* **2014**, *136*, 15711-15718.
- [185] Pines, A.; Waugh, J. S.; Gibby, M. G. *J Chem Phys* **1972**, *56*, 1776-&.
- [186] Metz, G.; Wu, X. L.; Smith, S. O. *J Magn Reson Ser A* **1994**, *110*, 219-227.
- [187] Dixon, W. T.; Schaefer, J.; Sefcik, M. D.; Stejskal, E. O.; McKay, R. A. *J Magn Reson* **1982**, *49*, 341-345.
- [188] Hu, J. Z.; Alderman, D. W.; Ye, C. H.; Pugmire, R. J.; Grant, D. M. *J Magn Reson Ser A* **1993**, *105*, 82-87.
- [189] Frisch, M. J.; Trucks, G. W.; Schlegel, H. B.; Scuseria, G. E.; Robb, M. A.; Cheeseman, J. R.; Scalmani, G.; Barone, V.; Mennucci, B.; Petersson, G. A.; Nakatsuji, H.; Caricato, M.; Li, X.; Hratchian, H. P.; Izmaylov, A. F.; Bloino, J.; Zheng, G.;

- Sonnenberg, J. L.; Hada, M.; Ehara, M.; Toyota, K.; Fukuda, R.; Hasegawa, J.; Ishida, M.; Nakajima, T.; Honda, Y.; Kitao, O.; Nakai, H.; Vreven, T.; Montgomery, J. A.; Peralta, J. E.; Ogliaro, F.; Bearpark, M.; Heyd, J. J.; Brothers, E.; Kudin, K. N.; Staroverov, V. N.; Kobayashi, R.; Normand, J.; Raghavachari, K.; Rendell, A.; Burant, J. C.; Iyengar, S. S.; Tomasi, J.; Cossi, M.; Rega, N.; Millam, J. M.; Klene, M.; Knox, J. E.; Cross, J. B.; Bakken, V.; Adamo, C.; Jaramillo, J.; Gomperts, R.; Stratmann, R. E.; Yazyev, O.; Austin, A. J.; Cammi, R.; Pomelli, C.; Ochterski, J. W.; Martin, R. L.; Morokuma, K.; Zakrzewski, V. G.; Voth, G. A.; Salvador, P.; Dannenberg, J. J.; Dapprich, S.; Daniels, A. D.; Farkas, Foresman, J. B.; Ortiz, J. V.; Cioslowski, J.; Fox, D. J. Wallingford CT, **2009**.
- [190] Vosko, S. H.; Wilk, L.; Nusair, M. *Can J Phys* **1980**, *58*, 1200-1211.
- [191] Lee, C. T.; Yang, W. T.; Parr, R. G. *Phys. Rev. B* **1988**, *37*, 785-789.
- [192] Becke, A. D. *J. Chem. Phys.* **1993**, *98*, 5648-5652.
- [193] Stephens, P. J.; Devlin, F. J.; Chabalowski, C. F.; Frisch, M. J. *J. Phys. Chem.* **1994**, *98*, 11623-11627.
- [194] Grimme, S.; Antony, J.; Ehrlich, S.; Krieg, H. *J. Chem. Phys.* **2010**, *132*.
- [195] Grimme, S.; Ehrlich, S.; Goerigk, L. *J Comput Chem* **2011**, *32*, 1456-1465.
- [196] Wadt, W. R.; Hay, P. J. *J Chem Phys* **1985**, *82*, 284-298.
- [197] Hay, P. J.; Wadt, W. R. *J Chem Phys* **1985**, *82*, 299-310.
- [198] Hay, P. J.; Wadt, W. R. *J. Chem. Phys.* **1985**, *82*, 270-283.
- [199] Schreckenbach, G.; Ziegler, T. *J. Phys. Chem.* **1995**, *99*, 606-611.
- [200] Krykunov, M.; Ziegler, T.; Van Lenthe, E. *Int J Quantum Chem* **2009**, *109*, 1676-1683.
- [201] te Velde, G.; Bickelhaupt, F. M.; Baerends, E. J.; Guerra, C. F.; Van Gisbergen, S. J. A.; Snijders, J. G.; Ziegler, T. *J. Comput. Chem.* **2001**, *22*, 931-967.
- [202] Van Lenthe, E.; Baerends, E. J. *J Comput Chem* **2003**, *24*, 1142-1156.
- [203] Wolff, S. K.; Ziegler, T. *J Chem Phys* **1998**, *109*, 895-905.
- [204] Wolff, S. K.; Ziegler, T.; van Lenthe, E.; Baerends, E. J. *J. Chem. Phys.* **1999**, *110*, 7689-7698.
- [205] Conley, M. P.; Rossini, A. J.; Comas-Vives, A.; Valla, M.; Casano, G.; Ouari, O.; Tordo, P.; Lesage, A.; Emsley, L.; Coperet, C. *Phys Chem Chem Phys* **2014**, *16*, 17822-17827.
- [206] Brunauer, S.; Deming, L. S.; Deming, W. E.; Teller, E. *J Am Chem Soc* **1940**, *62*, 1723-1732.
- [207] Cambor, M. A.; Corma, A.; Valencia, S. *Chem Commun* **1996**, 2365-2366.
- [208] Lippens, B. C.; Deboer, J. H. *J Catal* **1965**, *4*, 319-323.
- [209] Pines, A.; Gibby, M. G.; Waugh, J. S. *J Chem Phys* **1973**, *59*, 569-590.
- [210] Dixon, W. T. *J Chem Phys* **1982**, *77*, 1800-1809.
- [211] Antzutkin, O. N.; Song, Z. Y.; Feng, X. L.; Levitt, M. H. *J Chem Phys* **1994**, *100*, 130-140.
- [212] Kulkarni, B. S.; Krishnamurty, S.; Pal, S. *J Mol Catal a-Chem* **2010**, *329*, 36-43.

- [213] Corma, A.; Moliner, M.; Cantin, A.; Diaz-Cabanas, M. J.; Lorda, J. L.; Zhang, D. L.; Sun, J. L.; Jansson, K.; Hovmoller, S.; Zou, X. D. *Chem Mater* **2008**, *20*, 3218-3223.
- [214] Christianson, J. R.; Caratzoulas, S.; Vlachos, D. G. *Acs Catal* **2015**, *5*, 5256-5263.
- [215] Lari, G. M.; Dapsens, P. Y.; Scholz, D.; Mitchell, S.; Mondelli, C.; Perez-Ramirez, J. *Green Chem.* **2016**, *18*, 1249-1260.
- [216] Zhao, Y.; Truhlar, D. G. *Theor. Chem. Acc.* **2008**, *120*, 215-241.
- [217] M. J. Frisch, G. W. Trucks., H. B. Schlegel, G. E. Scuseria, M. A. Robb, J. R. Cheeseman, G. Scalmani, V. Barone, B. Mennucci, G. A. Petersson, H. Nakatsuji, M. Caricato, X. Li, H. P. Hratchian, A. F. Izmaylov, J. Bloino, G. Zheng, J. L. Sonnenberg, M. Hada, M. Ehara, K. Toyota, R. Fukuda, J. Hasegawa, M. Ishida, T. Nakajima, Y. Honda, O. Kitao, H. Nakai, T. Vreven, J. A. Montgomery, Jr., J. E. Peralta, F. Ogliaro, M. Bearpark, J. J. Heyd, E. Brothers, K. N. Kudin, V. N. Staroverov, T. Keith, R. Kobayashi, J. Normand, K. Raghavachari, A. Rendell, J. C. Burant, S. S. Iyengar, J. Tomasi, M. Cossi, N. Rega, J. M. Millam, M. Klene, J. E. Knox, J. B. Cross, V. Bakken, C. Adamo, J. Jaramillo, R. Gomperts, R. E. Stratmann, O. Yazyev, A. J. Austin, R. Cammi, C. Pomelli, J. W. Ochterski, R. L. Martin, K. Morokuma, V. G. Zakrzewski, G. A. Voth, P. Salvador, J. J. Dannenberg, S. Dapprich, A. D. Daniels, O. Farkas, J. B. Foresman, J. V. Ortiz, J. Cioslowski, and D. J. Fox; Gaussian, Inc.: Wallingford CT, **2010**.
- [218] Hollwarth, A.; Bohme, M.; Dapprich, S.; Ehlers, A. W.; Gobbi, A.; Jonas, V.; Kohler, K. F.; Stegmann, R.; Veldkamp, A.; Frenking, G. *Chem. Phys. Lett.* **1993**, *208*, 237-240.
- [219] Guerra, C. F.; Snijders, J. G.; te Velde, G.; Baerends, E. J. *Theor. Chem. Acc.* **1998**, *99*, 391-403.
- [220] ADF 2012, S. *Theor. Chem. Acc., Vrije Universiteit, Amsterdam, The Netherlands*, <http://www.scm.com>.
- [221] van Lenthe, E.; Ehlers, A.; Baerends, E. J. *J. Chem. Phys.* **1999**, *110*, 8943-8953.
- [222] Vanlenthe, E.; Baerends, E. J.; Snijders, J. G. *J. Chem. Phys.* **1994**, *101*, 9783-9792.
- [223] Vanlenthe, E.; Baerends, E. J.; Snijders, J. G. *J. Chem. Phys.* **1993**, *99*, 4597-4610.
- [224] Bagno, A.; Casella, G.; Saielli, G. *J. Chem. Theory. Comput.* **2006**, *2*, 37-46.

Appendix A

Annexes

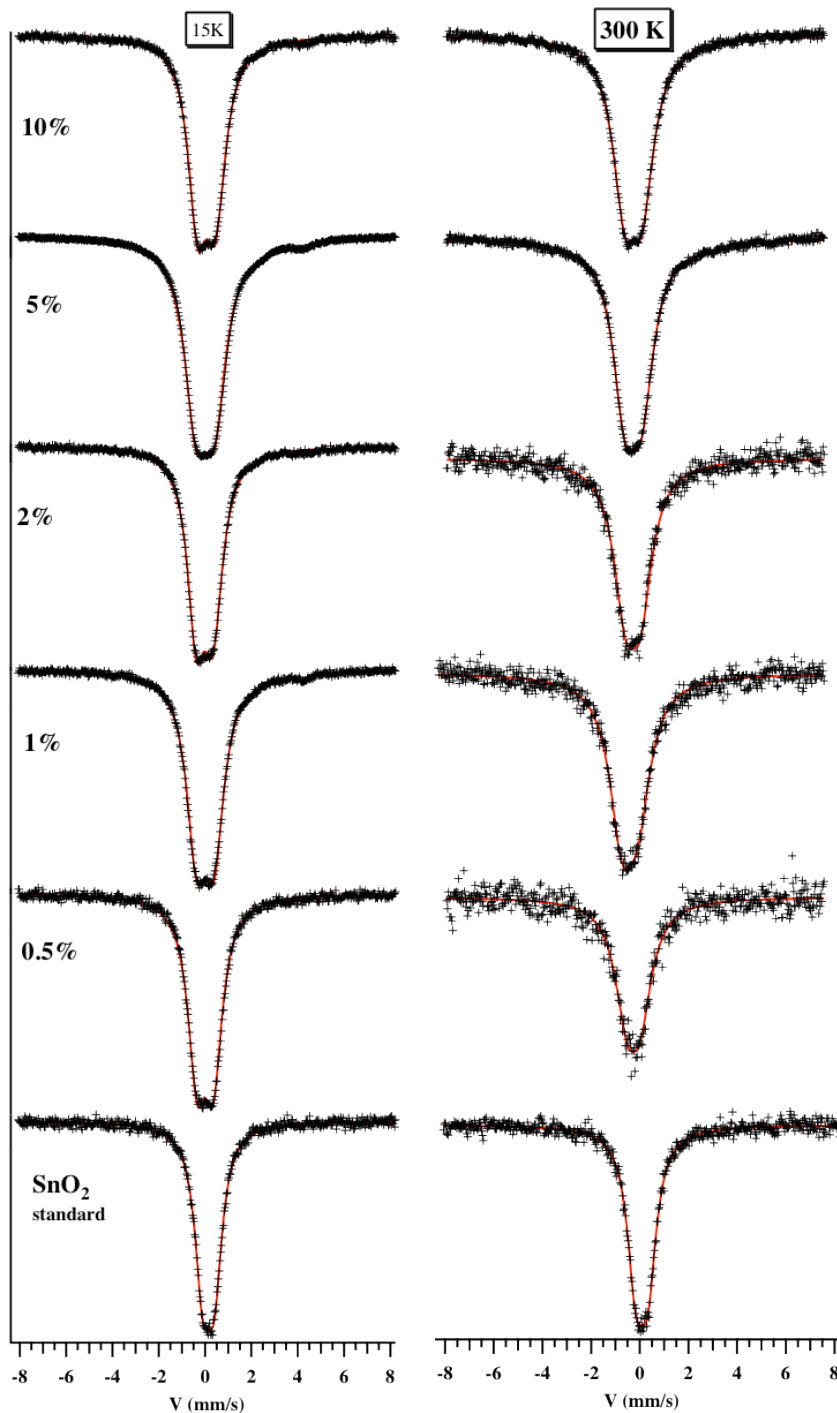


Figure A1. ^{119}Sn Mossbauer spectra of $\text{Sn-}\beta$ samples with various Sn loadings. Samples were recorded at 300 (right) and 15 K (left). A reference measurement of pure SnO_2 was also performed. Red curves represent the fitted spectra, based on a least squares method program assuming Lorentzian peaks.

Table A1. Mossbauer data extracted from 300 and 15 K spectra of Sn/deal-Beta-OH-25 zeolites with different Sn-loading^[a,b] and SnO₂ as a standard. Values in brackets show impurities of tin (II) from the tin precursor.

Entry	Sn-loading (wt %)	300 K					15 K					dln[A _{agg} ^o /A _{ref}]/dT x 10 ⁻² [g]
		G (mm/s)	IS (mm/s)	EQ (mm/s)	S (%)	A (a.u.)	G (mm/s)	IS (mm/s)	EQ (mm/s)	S (%)	A (a.u.)	
1	10	1.24	-0.06	0.74	100	7.9	1.00 (0.80)	-0.02 (3.31)	0.77 (1.83)	98 (2)	25.1	0.4
2	5	1.24	-0.1	0.73	100	12.3	1.19 (1.15)	-0.08 (3.19)	0.81 (1.93)	96 (4)	43.1	0.44
3	2	1.20	-0.08	0.65	100	2.7	0.94	-0.10	0.72	100	11.9	0.52
4	1	1.26	-0.08	0.67	100	3.4	1.02 (1.08)	-0.08 (3.04)	0.75 (2.09)	97 (3)	13.5	0.5
5	0.5	1.23	-0.08	0.59	100	2.0	0.94	-0.08	0.71	100	7.9	0.49
6 ^[d]	N/A	0.85	0	0.49	100	6.8	0.83	0.06	0.5	100	9.3	0.11

[a] G: FWHM; IS: isomer shift; QS: quadrupole splitting; S: relative spectral area; and A: intensity relative to the base line. [b] The estimated accuracy of positional data is ± 0.04 mm/s. [c] Correlated with the recoilless fractions of components (Parish, R.V. in "Mossbauer Spectroscopy Applied to Inorganic Chemistry", Vol. 1 (Ed. G.J. Long) Plenum Press, New York, 1984, p. 527). [d] pure SnO₂.

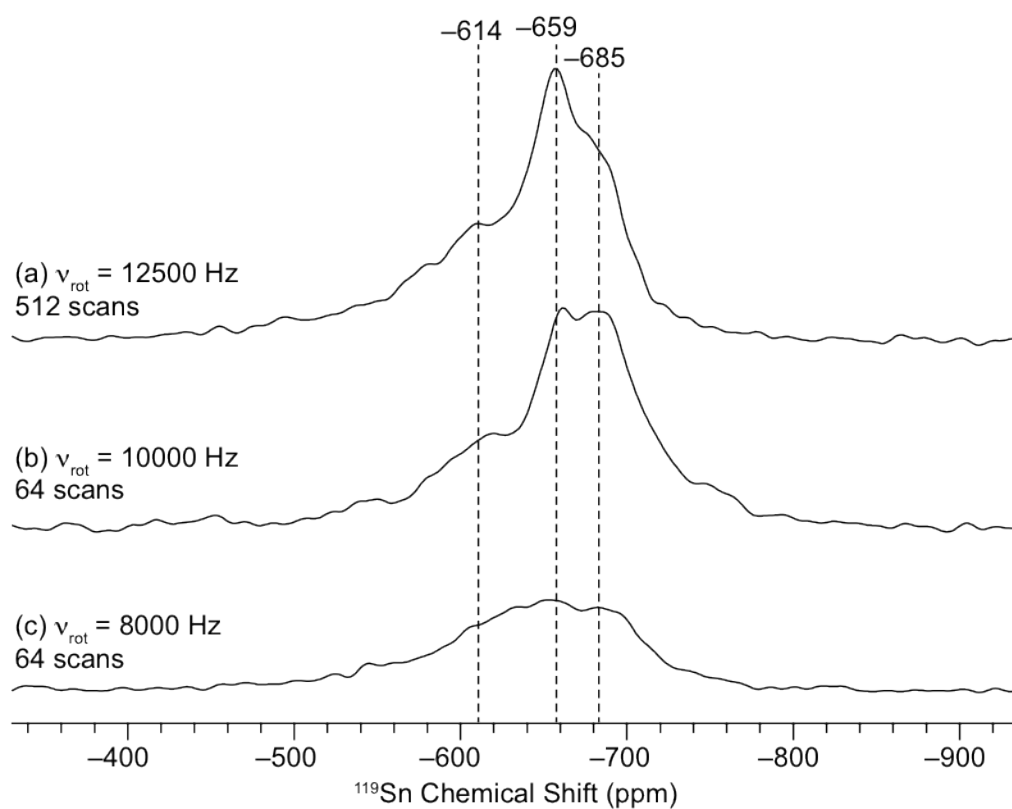


Figure A2. DNP enhanced ^1H - ^{119}Sn CP-CPMG spectra of 5Sn/deAl-Beta-OH-25 zeolite acquired with MAS spinning rates of a) 12.5 kHz, b) 10 kHz and c) 8 kHz. A contact time of 3.5 ms and polarization delay of 5 sec were applied in all cases

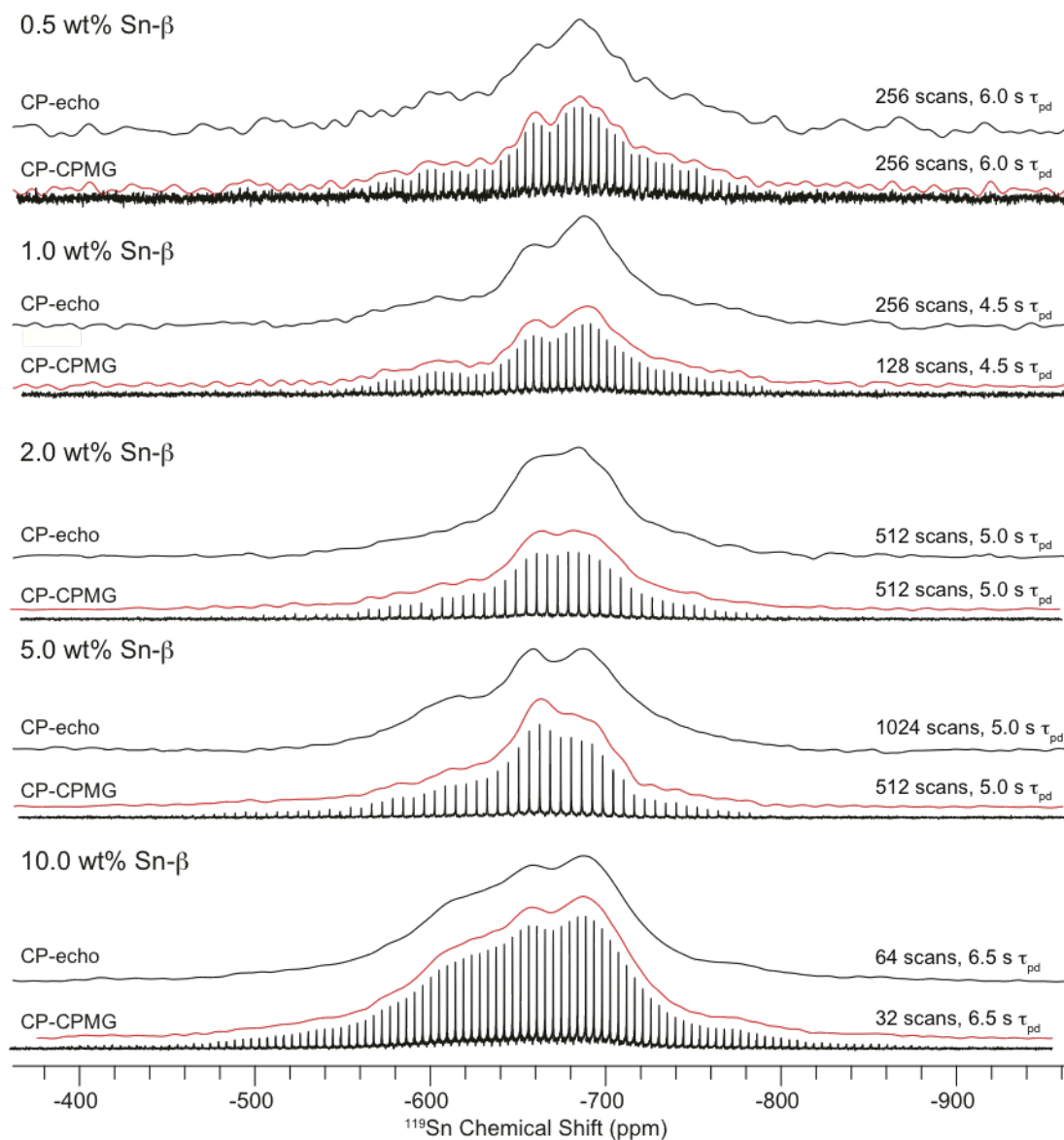


Figure A3. Comparison of DNP enhanced CP-echo (upper trace) and CP-CPMG (lower traces) ^{119}Sn solid-state NMR spectra for different loading levels of Sn/deAl-Beta-OH-25. All spectra were acquired with a 12500 Hz MAS frequency. For the CP-CPMG spectra both the spikelet (black) and echo (red trace) spectra are shown. The echo CP-CPMG spectra were obtained by summing all of the individual echoes in the FID in the time domain, followed by truncation to a single summed echo, which was then Fourier transformed. Between 20 and 30 individual echoes were acquired in the CP-CPMG experiments. The number of scans and polarization delay (τ_{pd}) are indicated for each spectrum.

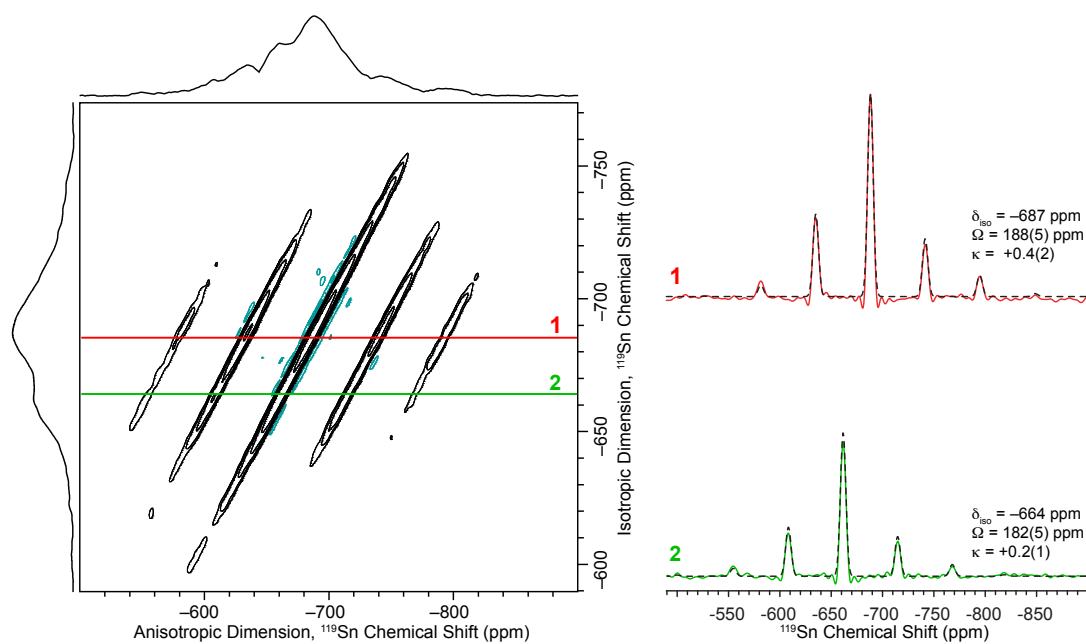


Figure A4. DNP enhanced ^1H - ^{119}Sn CP-MAT spectrum of 1Sn/deAl-Beta-OH-25 zeolite. The spectrum was acquired with a CP contact time of 4 ms, a polarization delay of 5 s, 224 scans per t_c increment and 52 t_c increments were acquired. A MAS frequency of 8000 Hz was used. Fits to the sideband manifolds are shown for the two isotropic peaks (dashed lines) and the CS tensor parameters obtained from the fits are indicated.

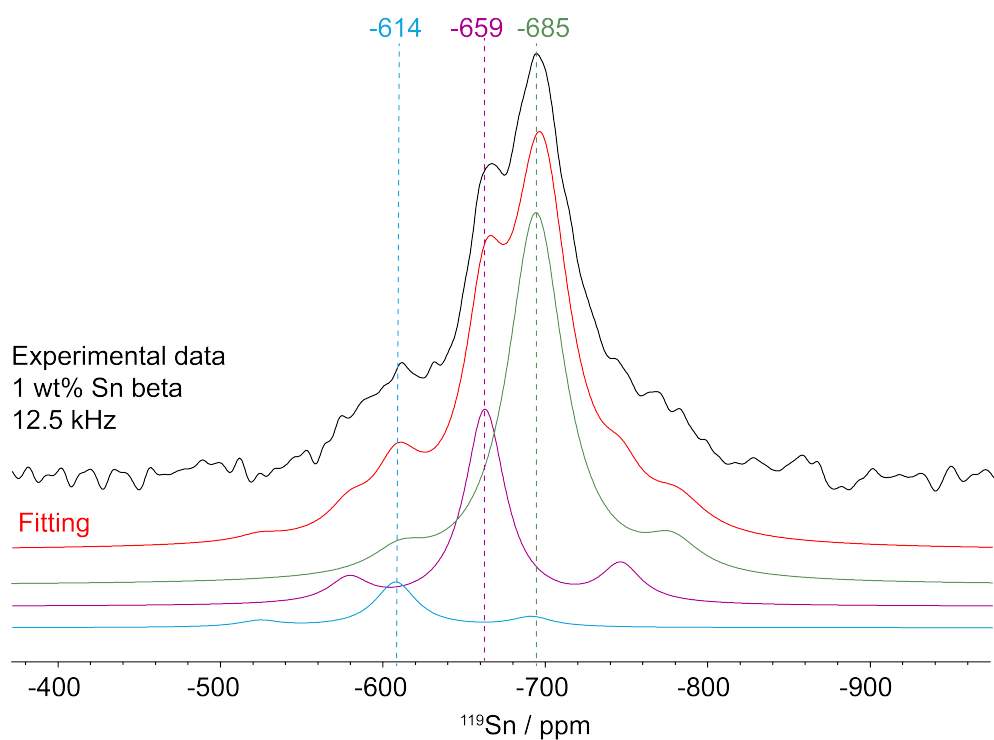


Figure A5. DNP enhanced ^1H - ^{119}Sn CPMAS spectrum of 1Sn/deAl-Beta-OH-25 acquired with an MAS frequency of 12.5 kHz, polarization delay of 5 s and CP contact time of 4 ms. The total fit of the spectrum is shown as the red trace. The lower traces show the contributions of the three different sites to the total spectrum. The sideband intensities of each set were set to the values determined from the analysis of the MAT.

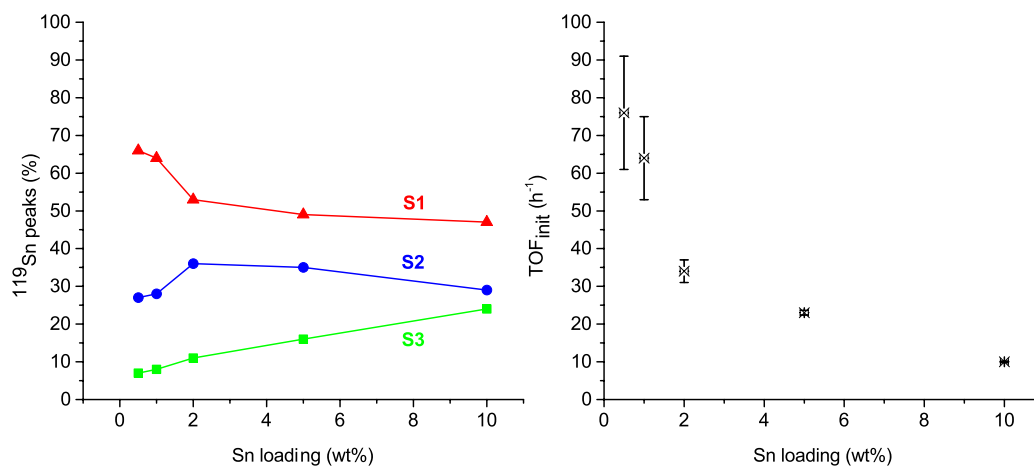


Figure A6. (*left*) Sn site distribution obtained from the deconvolution of the DNP enhanced ^1H - ^{119}Sn CPMAS spectra as a function of Sn-loading. (*right*) initial TOF in the aqueous-phase glucose isomerization versus Sn-loading. Error estimated based on the ICP-determined Sn-loading.

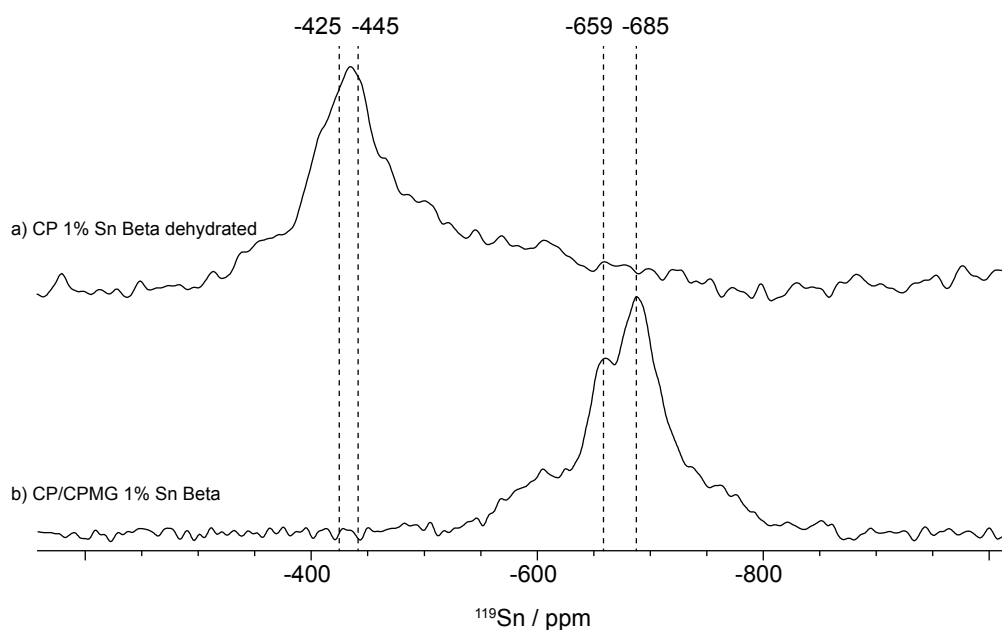


Figure A7.9.4 T 105 K ^1H - ^{119}Sn DNP SENS magic angle spinning cross-polarization spin echo spectra of (a) dehydrated 1Sn/deAl-Beta-OH-25, the number of scans was 512 scans, the polarization delay was set to 8 sec and the proton DNP enhancements ($\bullet\text{H}$) measured with separate ^1H spin echo experiments was 120 b) 2Sn/deAl-Beta-OH-25, the number of scans was 256 scans, the polarization delay was set to 4.5 sec and the proton DNP enhancements ($\bullet\text{H}$) measured with separate ^1H spin echo experiments was 61. All spectra were acquired with a MAS frequency of 12.5 kHz and CP contact times between 3.0 and 3.5 ms. Sample (a) was dehydrated at 300 °C for 5 hours under high vacuum (10⁻⁵ mbar) and stored in water and oxygen free atmosphere glovebox where it was impregnated with a solution of 16 mM TEKPol in freshly distilled 1,1,2,2-tetrachloroethane. Sample (b) was impregnated with a 16 mM TEKPol 1,1,2,2-tetrachloroethane solution.

Text A1. Modeling the active sites by means of *ab initio* calculations.

All structures were optimized at the Mo6²¹⁶ level with Gaussian09,²¹⁷ using the LANL2DZ pseudopotential¹⁹⁸ with *d* polarization functions for Sn²¹⁸ and the 6-31g(d,p) basis set for Si, O and H. The NMR parameters (isotropic chemical shift and CSA) were obtained with the NMR module^{199,204} of the ADF code^{201,219,220} with the ZORA method²²¹⁻²²³ using spin-orbit correction and B₃LYP¹⁹¹⁻¹⁹³-D₃¹⁹⁴/TZP since relativistic effects and spin-orbit coupling are needed for accurate ¹¹⁹Sn chemical shift values.²²⁴ The small cluster, where the zeolite framework is replaced by OSiH₃ substituents, already shows a clear trend (Scheme A1): from the initial tetrahedral site with a calculated chemical shift of –373 ppm, which is already close to the experimental values (–420 / –446 ppm, *vide supra*), the next two additional water molecules, making Sn penta- and hexacoordinated, induce a decrease of the chemical shift value by *ca.* 100 ppm for each H₂O, whether H₂O remains coordinated or opens an SiOSn bridge. Additional water molecules in the second coordination sphere that interact through H-bonding further decrease the chemical shift to reach a value as low as –638 ppm (see Table A2, Scheme A1 and Figure A8). In order to obtain a more accurate description, large models of the T₁ site were investigated on selected examples, in particular for the hexacoordinated Sn sites. Due to the much larger size of these models, NMR shifts were calculated without including relativistic effects (RE) and spin orbit coupling (SOC), and then corrected with a scaling factor since we found a close to perfect correlation between chemical shift values calculated with and without RE+SOC (Table A3 and Figure A9-Figure A11).

Scheme A1. Computed ^{119}Sn isotropic chemical shifts in ppm (upper numbers outside of parenthesis) for the small clusters, in which four SiH_3 groups have substituted the zeolite framework. Calculations were also performed for a more accurate substituted zeolite framework model and the calculated isotropic chemical shift, span and skew (δ_{iso} , W , and k , respectively) are shown in parenthesis. The zeolite framework is depicted for two selected structures.

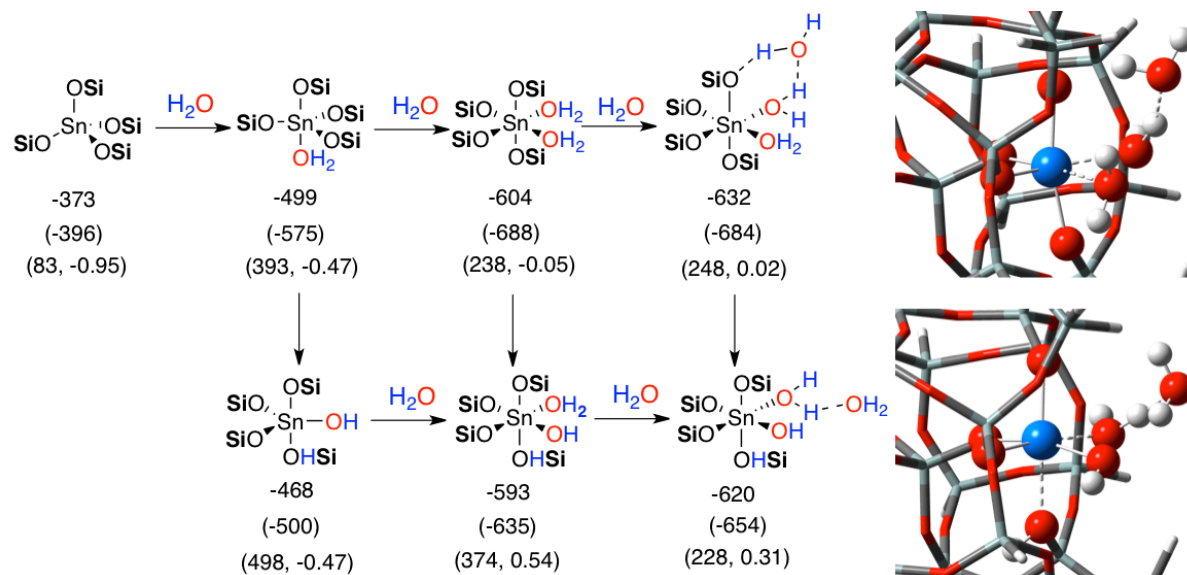
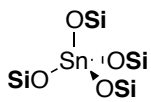
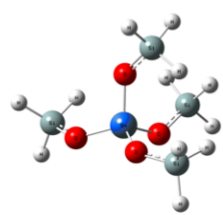
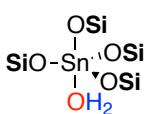
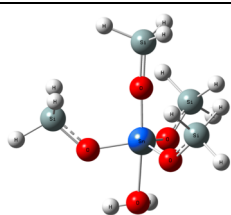
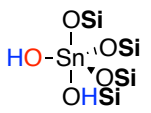
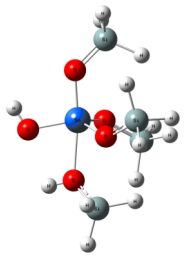
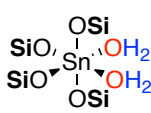
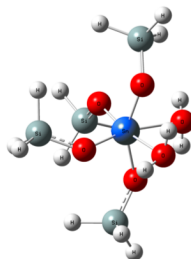
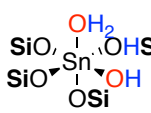
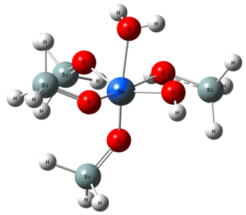

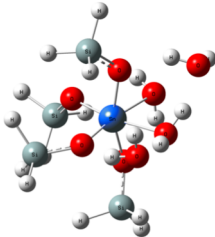
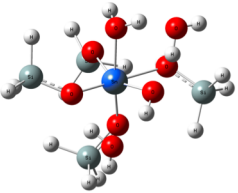


Table A2. Computational results for the small clusters of the Sn- β zeolite.

Entry	Schematic picture	Optimized Geometry	NMR data
A			
1			$\delta_{iso} = -373$ ppm $\Omega = 129$ ppm $\kappa = 0.47$
A + 1 H₂O			
2			$\delta_{iso} = -499$ ppm $\Omega = 507$ ppm $\kappa = -0.55$
3			$\delta_{iso} = -468$ ppm $\Omega = 429$ ppm $\kappa = -0.41$
A + 2 H₂O			
4			$\delta_{iso} = -604$ ppm $\Omega = 225$ ppm $\kappa = 0.16$
5			$\delta_{iso} = -593$ ppm $\Omega = 168$ ppm $\kappa = -0.34$

Entry	Schematic picture	Optimized Geometry	NMR data
6			$\delta_{iso} = -595 \text{ ppm}$ $\Omega = 207 \text{ ppm}$ $\kappa = -0.30$
A + 2 H₂O			
7			$\delta_{iso} = -617 \text{ ppm}$ $\Omega = 465 \text{ ppm}$ $\kappa = -0.30$
8			$\delta_{iso} = -596 \text{ ppm}$ $\Omega = 211 \text{ ppm}$ $\kappa = -0.86$
9			$\delta_{iso} = -596 \text{ ppm}$ $\Omega = 197 \text{ ppm}$ $\kappa = -0.30$
10			$\delta_{iso} = -565 \text{ ppm}$ $\Omega = 254 \text{ ppm}$ $\kappa = -0.04$
A + 3 H₂O			
11			$\delta_{iso} = -632 \text{ ppm}$ $\Omega = 265 \text{ ppm}$ $\kappa = 0.33$

Entry	Schematic picture	Optimized Geometry	NMR data
12	$ \begin{array}{c} \text{OH}_2 \\ \\ \text{SiO}_2 \text{---} \text{Sn} \text{---} \text{HSi} \\ \quad \quad \\ \text{SiO} \quad \quad \text{OH} \\ \\ \text{OSi} \end{array} + \text{H}_2\text{O} $		$\delta_{\text{iso}} = -620 \text{ ppm}$ $\Omega = 144 \text{ ppm}$ $\kappa = -0.79$
A + 4 H ₂ O			
13	$ \begin{array}{c} \text{OSi} \\ \\ \text{SiO}_2 \text{---} \text{Sn} \text{---} \text{OH}_2 \\ \quad \quad \\ \text{SiO} \quad \quad \text{OH}_2 \\ \\ \text{OSi} \end{array} + 2\text{H}_2\text{O} $		$\delta_{\text{iso}} = -638 \text{ ppm}$ $\Omega = 199 \text{ ppm}$ $\kappa = 0.18$
14	$ \begin{array}{c} \text{OH}_2 \\ \\ \text{SiO}_2 \text{---} \text{Sn} \text{---} \text{HSi} \\ \quad \quad \\ \text{SiO} \quad \quad \text{OH} \\ \\ \text{OSi} \end{array} + 2\text{H}_2\text{O} $		$\delta_{\text{iso}} = -624 \text{ ppm}$ $\Omega = 206 \text{ ppm}$ $\kappa = 0.26$

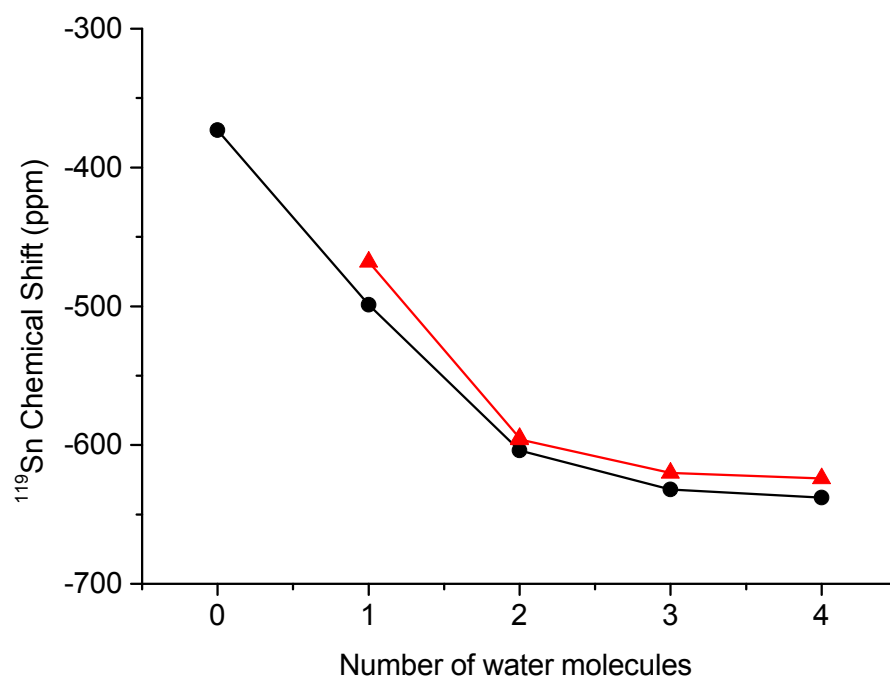


Figure A8. Variation of the ^{119}Sn NMR Chemical shift when including a successive number of water molecules. The first two water molecules are coordinated to Sn whereas the third and the fourth ones remain on the second coordination sphere via hydrogen bonding. With only water molecules coordinated (•) and with a water molecule split on one SnOSi (▲) forming one SiOHSn group.

Table A3. Computational results for the intermediate model of the T1 site of the Sn- β zeolite. The dangling bonds were terminated with hydrogen atoms. Sn is highlighted in blue. The Sn coordination sphere is highlighted with ball and stick models.

Entry	Schematic picture	Optimized Geometry	NMR data
A			
1			$\delta_{iso} = -413 \text{ ppm}$ $\Omega = 136 \text{ ppm}$ $\kappa = 0.45$
A + 1H₂O			
2			$\delta_{iso} = -543 \text{ ppm}$ $\Omega = 365 \text{ ppm}$ $\kappa = -0.46$
3			$\delta_{iso} = -504 \text{ ppm}$ $\Omega = 443 \text{ ppm}$ $\kappa = -0.55$
4			$\delta_{iso} = -507 \text{ ppm}$ $\Omega = 542 \text{ ppm}$ $\kappa = -0.17$

Entry	Schematic picture	Optimized Geometry	NMR data
A + 2 H₂O			
5			$\delta_{iso} = -645 \text{ ppm}$ $\Omega = 318 \text{ ppm}$ $\kappa = 0.50$
6			$\delta_{iso} = -670 \text{ ppm}$ $\Omega = 342 \text{ ppm}$ $\kappa = 0.24$
A + 3 H₂O			
7			$\delta_{iso} = -677 \text{ ppm}$ $\Omega = 265 \text{ ppm}$ $\kappa = 0.65$
8			$\delta_{iso} = -677 \text{ ppm}$ $\Omega = 236 \text{ ppm}$ $\kappa = 0.16$

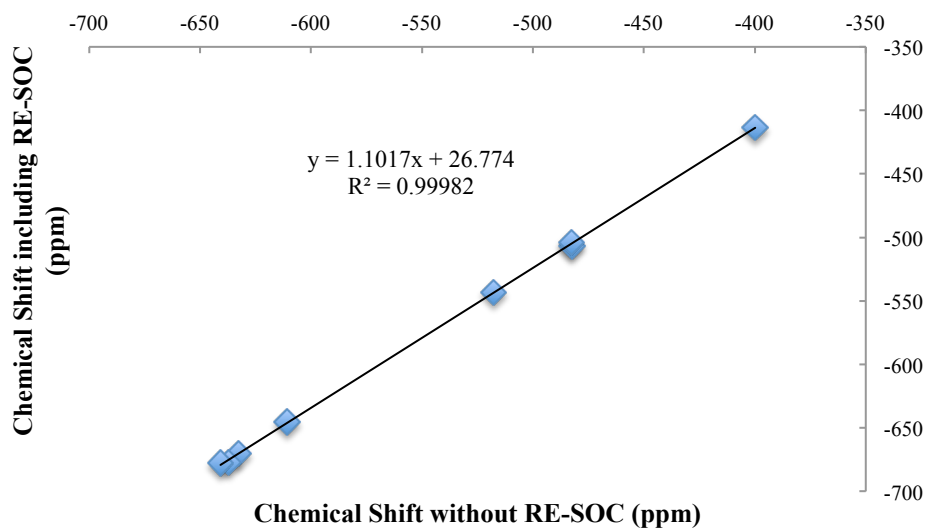


Figure A9. Correlation between the calculated NMR chemical shifts with and without relativistic effects and spin-orbit coupling (RE-SOC) for the intermediate model of T1 site of the Sn- β zeolite.

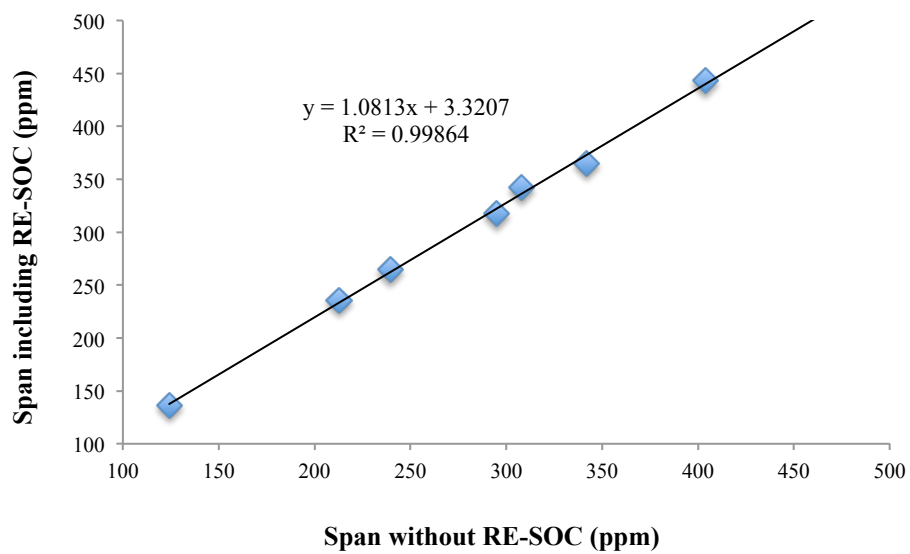


Figure A10. Correlation between the calculated span with and without relativistic effects and spin-orbit coupling (RE-SOC) for the intermediate model of T1 site of the Sn- β zeolite.

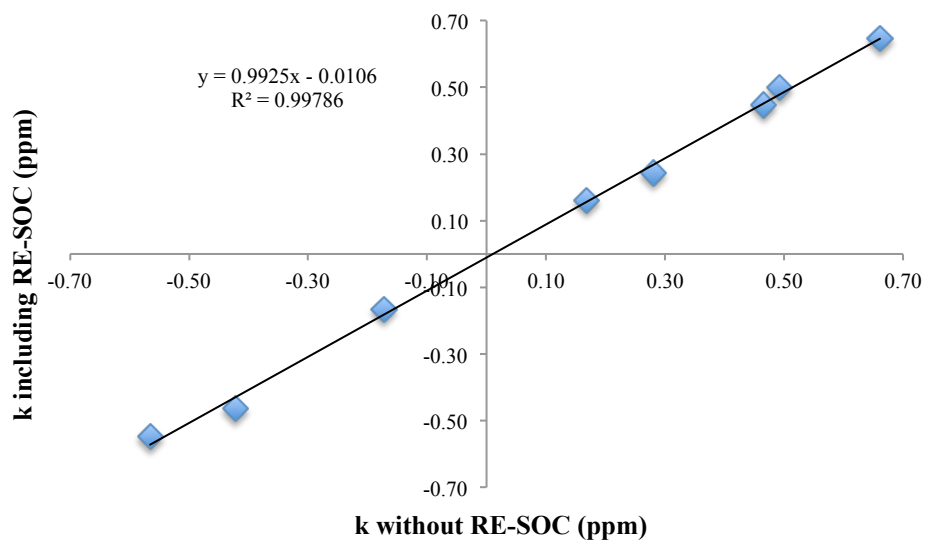
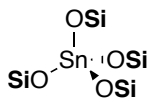
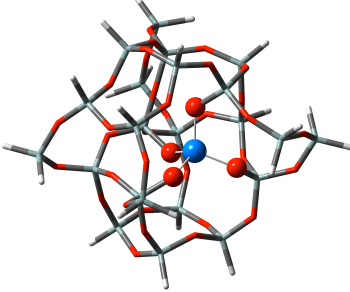
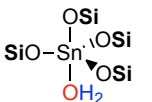
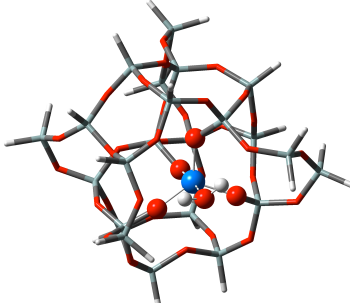
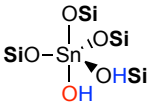
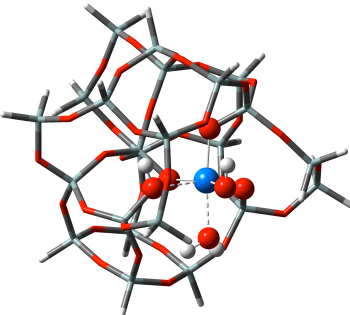
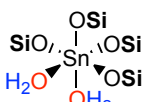
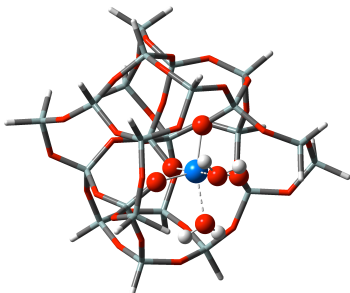


Figure A11. Correlation between the calculated κ with and without relativistic effects and spin-orbit coupling (RE-SOC) for the intermediate model of T₁ site of the Sn- β zeolite.

Table A4. Computational results for the T1 site of the Sn- β zeolite. The clusters were cut from the zeolite structure with at least 4 SiO_4 units around Sn and maintaining all the related cages. The dangling bonds were terminated with hydrogen atoms. Sn is highlighted in blue. The Sn coordination sphere is highlighted with ball and stick models. Relativistic effects and spin-orbit couplings were included by means of the equations shown in Figure S7, S8 and S9 for the chemical shift, span and κ , respectively.

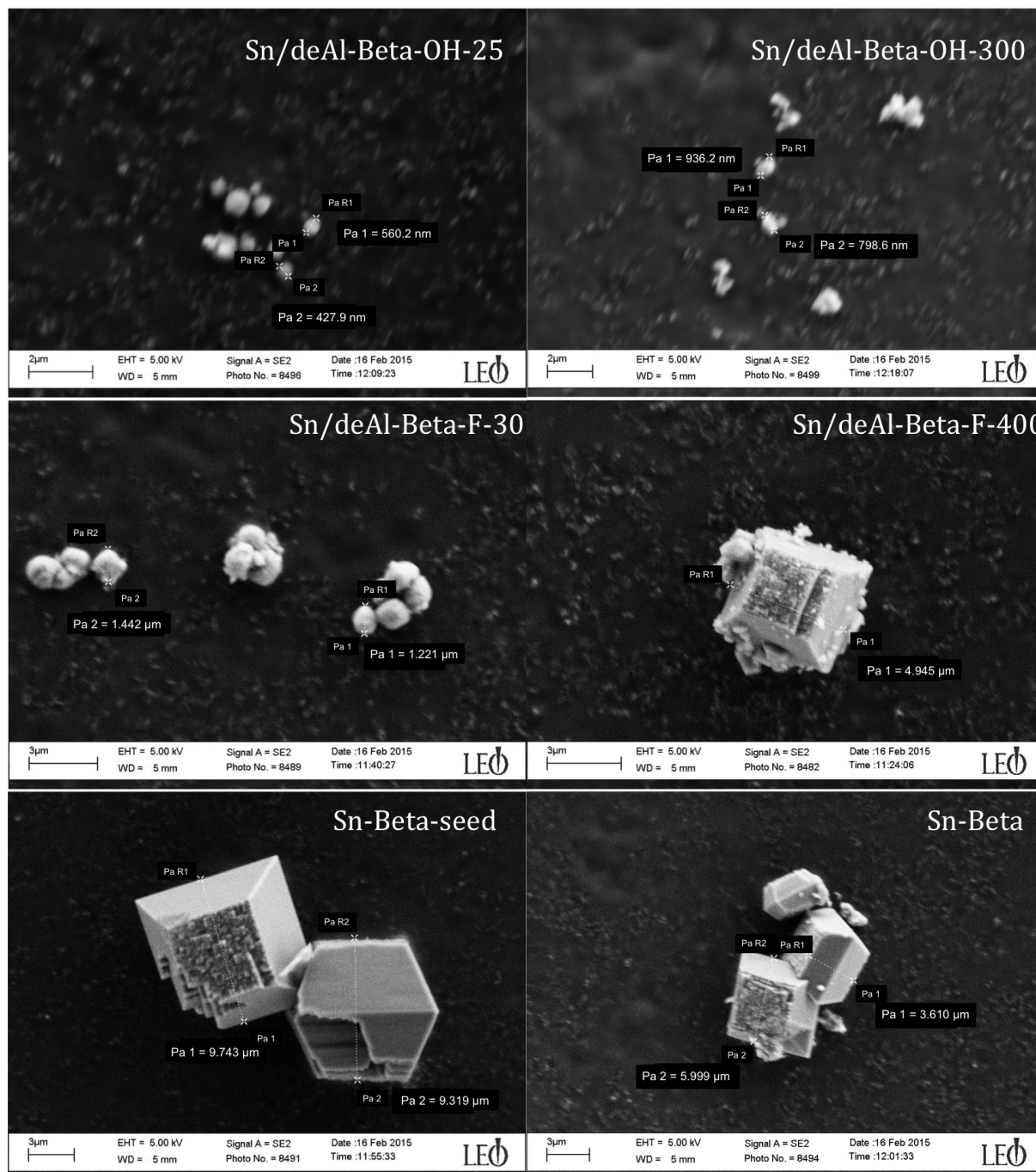
Entry	Schematic picture	Optimized Geometry	NMR data
A			
1			$\delta_{\text{iso}} = -396 \text{ ppm}$ $\Omega = 83 \text{ ppm}$ $\kappa = -0.95$
A + 1 H₂O			
2			$\delta_{\text{iso}} = -575 \text{ ppm}$ $\Omega = 393 \text{ ppm}$ $\kappa = -0.47$
3			$\delta_{\text{iso}} = -500 \text{ ppm}$ $\Omega = 498 \text{ ppm}$ $\kappa = -0.47$
A + 2 H₂O			
4			$\delta_{\text{iso}} = -688 \text{ ppm}$ $\Omega = 238 \text{ ppm}$ $\kappa = -0.05$

Entry	Schematic picture	Optimized Geometry	NMR data
A + 2 H₂O			
5			$\delta_{150} = -635 \text{ ppm}$ $\Omega = 374 \text{ ppm}$ $\kappa = 0.54$
A + 3 H₂O			
6			$\delta_{150} = -684 \text{ ppm}$ $\Omega = 248 \text{ ppm}$ $\kappa = 0.02$
7			$\delta_{150} = -654 \text{ ppm}$ $\Omega = 228 \text{ ppm}$ $\kappa = 0.31$

Table A5. Physicochemical properties of different Sn- β zeolites.

Catalyst	Crystallinity ^a [%]	BET ^b [m ² g ⁻¹]	V _{micro} ^c [mL g ⁻¹]	V _{meso} ^c [mL g ⁻¹]	S _{ext} ^c [m ² g ⁻¹]	Si/Sn ^d	SiO ₂ /Al ₂ O ₃ ^e	H ₂ O _{ads} ^f [mmol g ⁻¹]	H ₂ O _{ads} ^g [mmol g ⁻¹]
Sn- β From Post-Synthetic Incorporation									
Sn/deAl-Beta-OH-25	53	616	0.18	0.18	166.9	163	25	1.22	12.0
Sn/deAl-Beta-OH-300	52	637	0.20	0.17	151.0	178	300	1.28	10.1
Sn/deAl-Beta-F-30	61	651	0.20	0.14	151.1	160	32	0.54	7.9
Sn/deAl-Beta-F-400	85	554	0.20	0.05	32.5	196	398	0.33	2.3
Sn- β From Hydrothermal Synthesis									
Sn-Beta-seed	100	650	0.23	0.04	53.3	197	-	0.27	2.5
Sn-Beta	78	610	0.21	0.07	66.7	182	-	0.26	2.4

^a Calculated from integration of the d₃₀₂-reflection at 22.4 2 θ . ^b Brunauer-Emmett-Teller area; linear range of p/p₀ = 0.005-0.03 chosen following Rouquerol et al.⁸³ ^c Micropore, mesopore volume and external surface area derived from the t-plot. ^d Determined by ICP-AES. ^e Si/Al ratio of parent zeolite determined by ICP-AES. ^f quantity of water adsorbed in the micropores; p/p₀ = 0.10. ^g at p/p₀ = 0.82.

Figure A12. Scanning Electron Micrographs of the various Sn- β samples

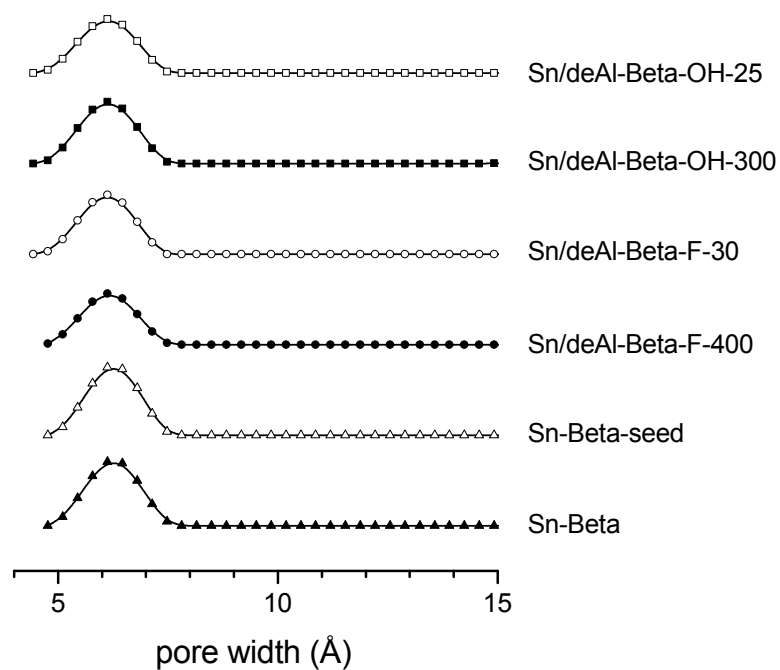


Figure A13. DFT pore size distribution derived from Ar adsorption isotherms at 87 K for various Sn- β catalysts.

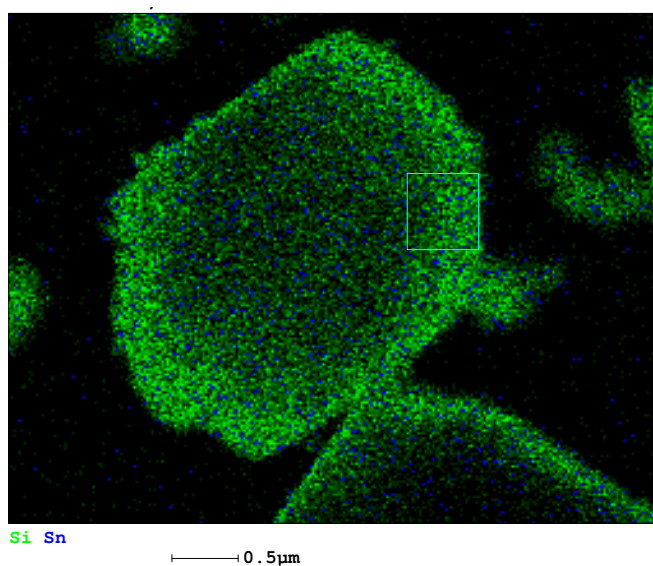


Figure A14. SEM-EDX of Sn/deAl-Beta-F400 showing the homogeneous distribution of Sn in the crystal.

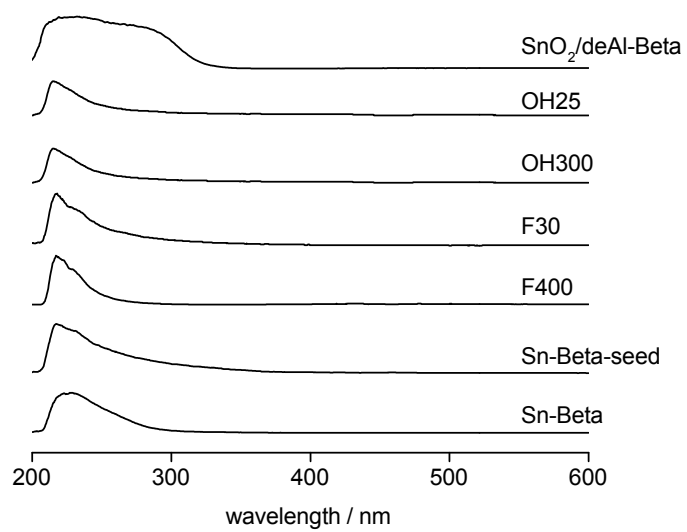


Figure A15. DR-UV/Vis spectra of SnO₂ on deAl-Beta and the different Sn-β zeolites showing the absence of SnO₂ in the prepared Sn-β samples.

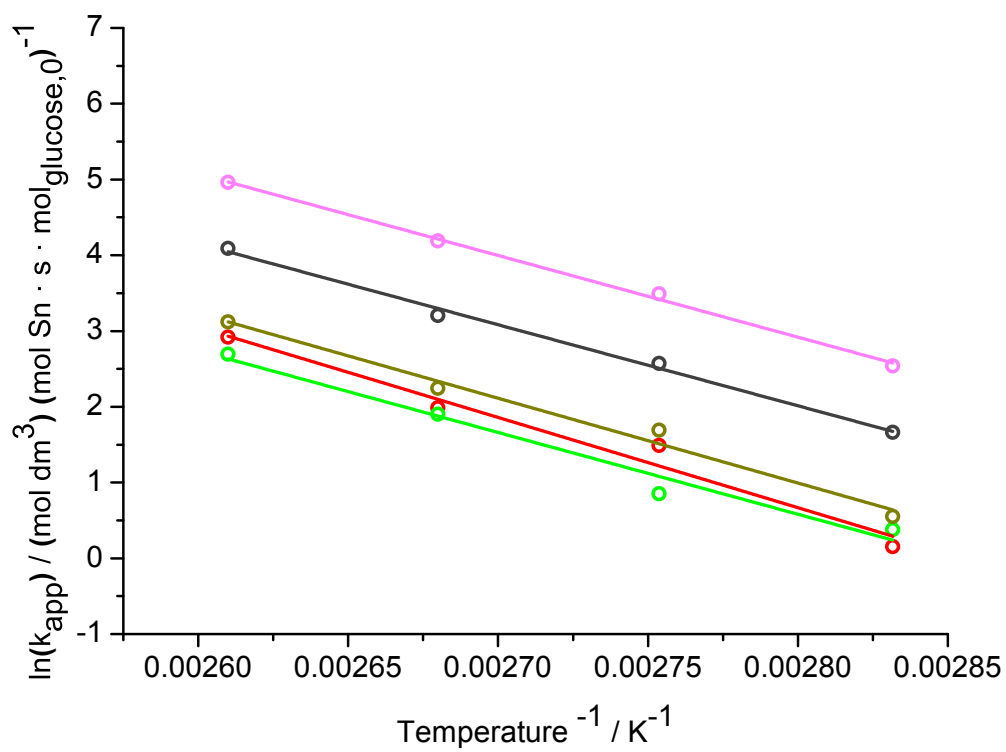


Figure A16. Arrhenius plot for the isomerization of glucose with different Sn- β zeolites in the temperature range of 353-383K. Sn/deAl-Beta-OH-25 (○) Sn/deAl-Beta-OH-300 (○), Sn/deAl-Beta-F-30 (○), Sn-Beta-F-400 (○) and Sn-Beta (○)

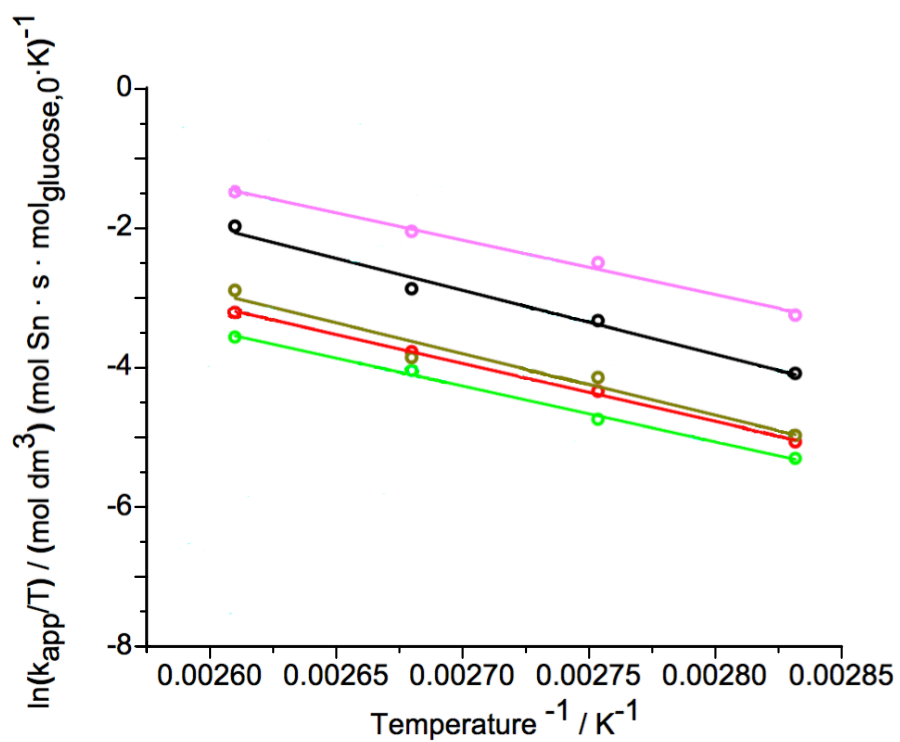


Figure A17. Eyring plot for the isomerization of glucose with different Sn- β zeolites in the temperature range of 353-383K. Sn/deAl-Beta-OH-25 (○) Sn/deAl-Beta-OH-300 (○), Sn/deAl-Beta-F-30 (○), Sn-Beta-F-400 (○) and Sn-Beta (○)

Table A6. Activity and activation energies of different Sn- β zeolites in the aqueous phase isomerization reaction of glyceraldehyde.^{a,f}

Entry	Catalyst ^b	Activity per Sn _{init} ^{c,d} [h ⁻¹]	DHA Yield ^e [%]	DHA Selectivity ^e [%]	E_{app}^f [kcal mol ⁻¹]	Pre-exponential factor $A^{f,g}$
<i>Sn-β From Post-Synthetic Incorporation</i>						
1	Sn/deAl-Beta-OH-25	144 ± 18	13	>99	21.3 ± 0.8	22 ± 1.0
2	Sn/deAl-Beta-F-400	868 ± 107	43	95	18.5 ± 0.5	19.5 ± 0.6

^aReaction conditions: 27 mg of catalyst in 5 mL of a 0.3 M aqueous glyceraldehyde solution at 70 °C.

^bSn/deAl-Beta: tin incorporated into dealuminated β by solid-solid ion-exchange; OH: parent Al-Beta zeolite synthesized in hydroxide media; F: parent Al-Beta zeolite synthesized in fluoride media; 25: SiO₂/Al₂O₃ ratio of parent zeolite; Sn-Beta: hydrothermally synthesized Sn- β zeolite; seed: β seed crystals added to the synthesis gel. ^cDefined as the mole product generated per mole Sn per hour calculated at the initial stage of the reaction. ^dError based on ICP-OES determined Sn-loading. ^eAfter 20 min of reaction.

^frates are measured in mole product formed per second normalized per total mole metal in the catalyst; temperatures for Arrhenius plot range from 50-80 °C. ^g units: (mol · dm³)(mol Sn · s · mol glyceraldehyde)⁻¹

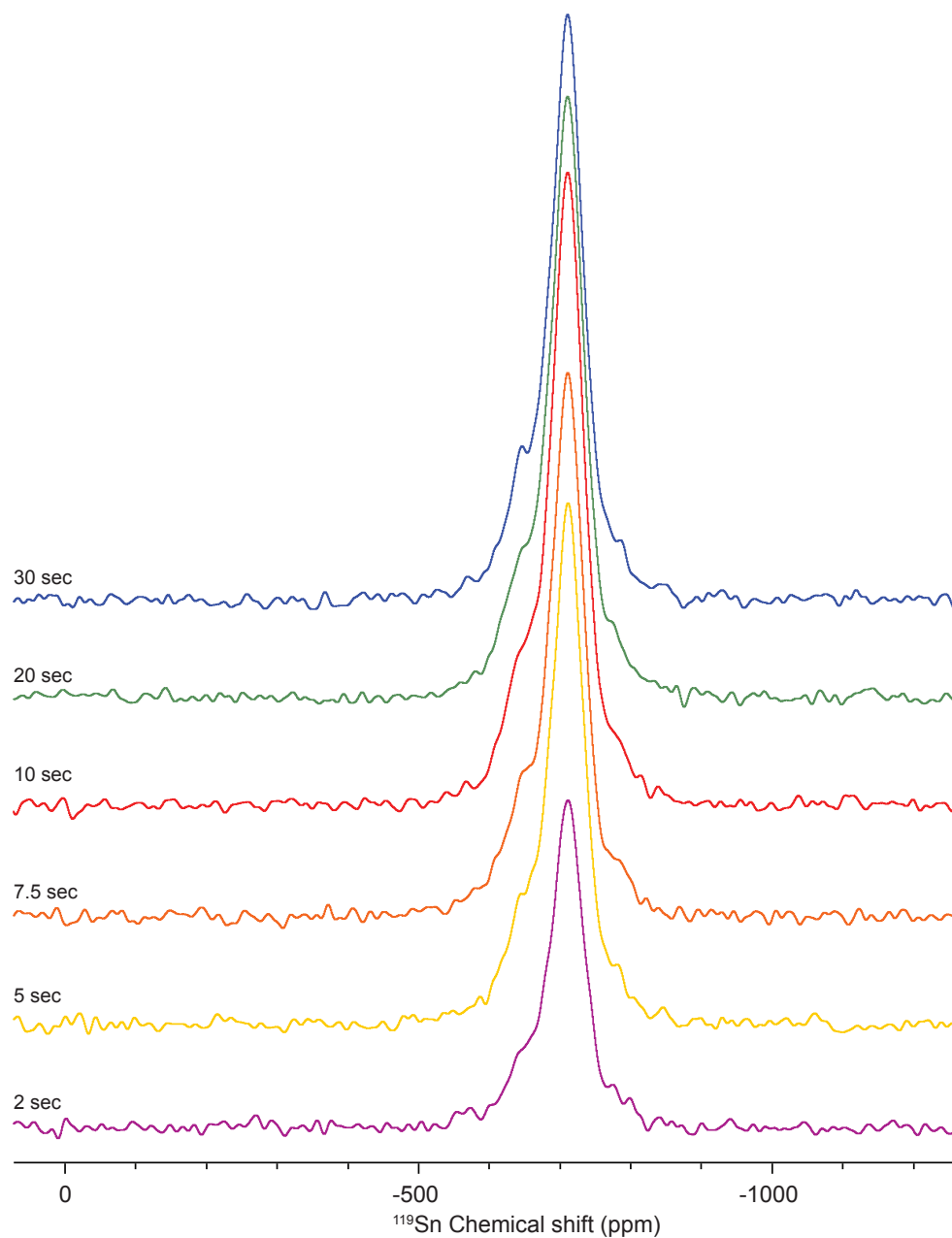


Figure A18. DNP enhanced ^1H - ^{119}Sn CP-echo spectrum of Sn/deAl-Beta-OH-25 with polarization delays between 2.0 to 30 s. The spectra were acquired with a CP contact time of 3.5 ms, a t_1 increment of 12.50 μs , 280 scans per t_1 increment and 132 t_1 increments were acquired. A MAS frequency of 4000 Hz was used.

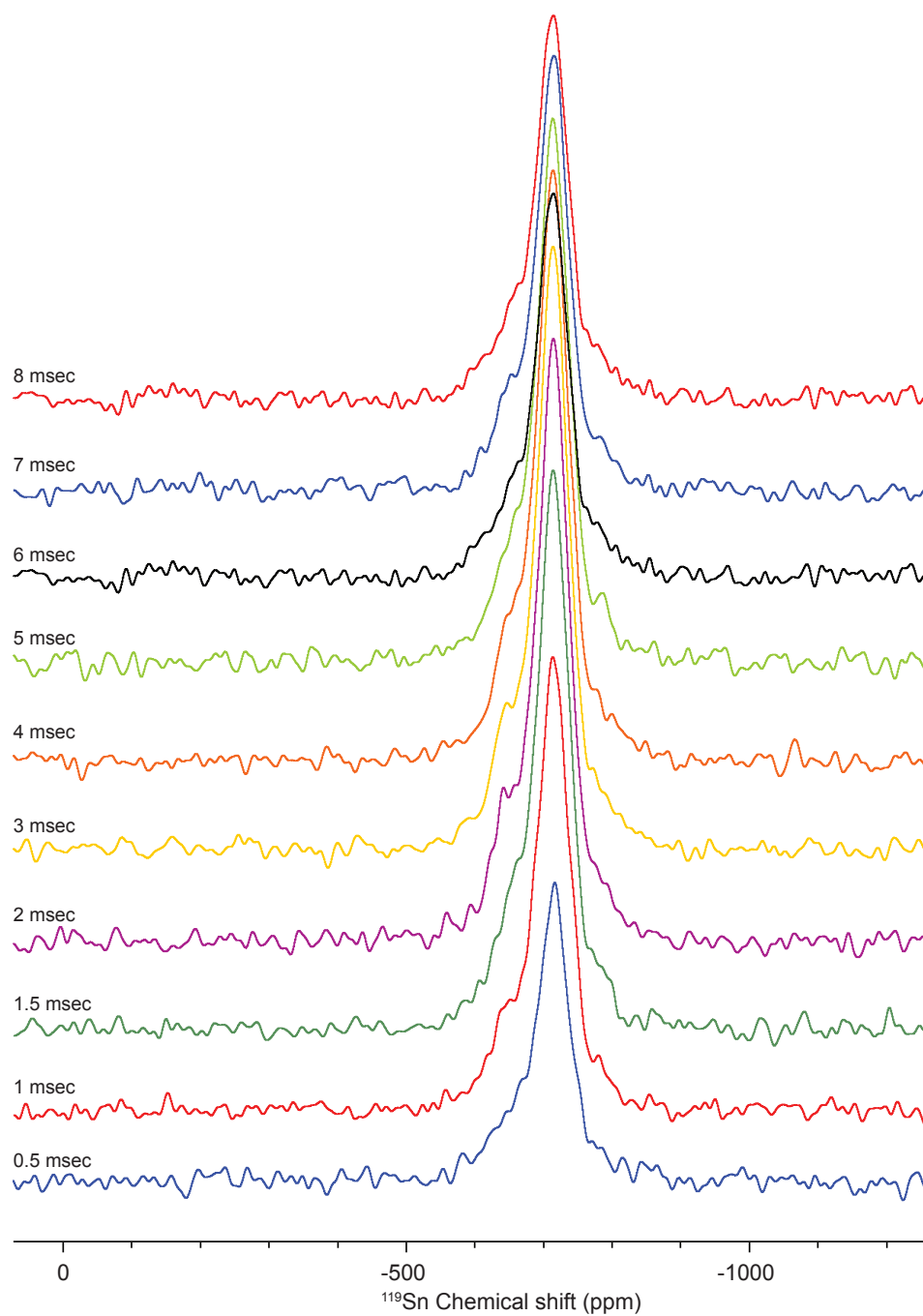


Figure A19. DNP enhanced DNP enhanced ^1H - ^{119}Sn CP-echo spectrum of Sn/deAl-Beta-OH-25 with different CP contact times. The spectra were acquired with a polarization delay of 3.5 s, a t_1 increment of 12.50 μs , 280 scans per t_1 increment and 132 t_1 increments were acquired. A MAS frequency of 4000 Hz was used.

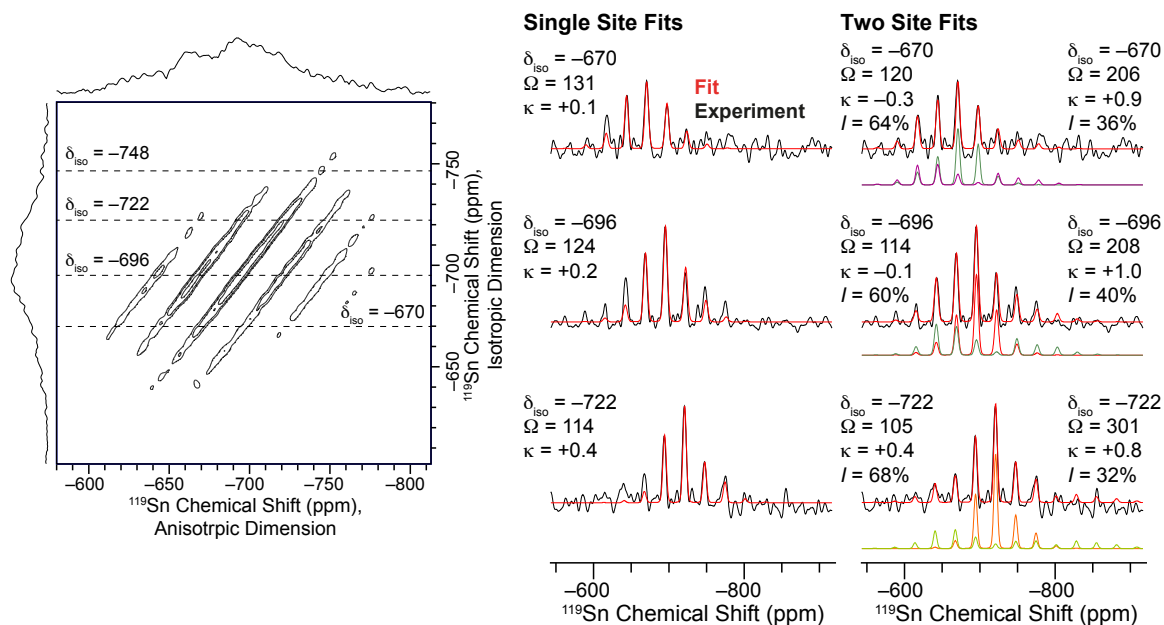


Figure A20. DNP enhanced ^1H - ^{119}Sn CP-MAT spectrum of Sn/deAl-Beta-OH-25. The spectrum was acquired with a CP contact time of 3.5 ms, a polarization delay of 2.2 s, a t_1 increment of 12.50 μs , 280 scans per t_1 increment and 132 t_1 increments were acquired. A MAS frequency of 4000 Hz was used. Fits to the sideband manifolds are shown for the three most intense isotropic peaks (dashed lines) and the CS tensor parameters obtained from the fits for both a single-site and a two-site fit are indicated. The site at -748 ppm with a relative integral intensity of only 6% cannot be properly fitted.

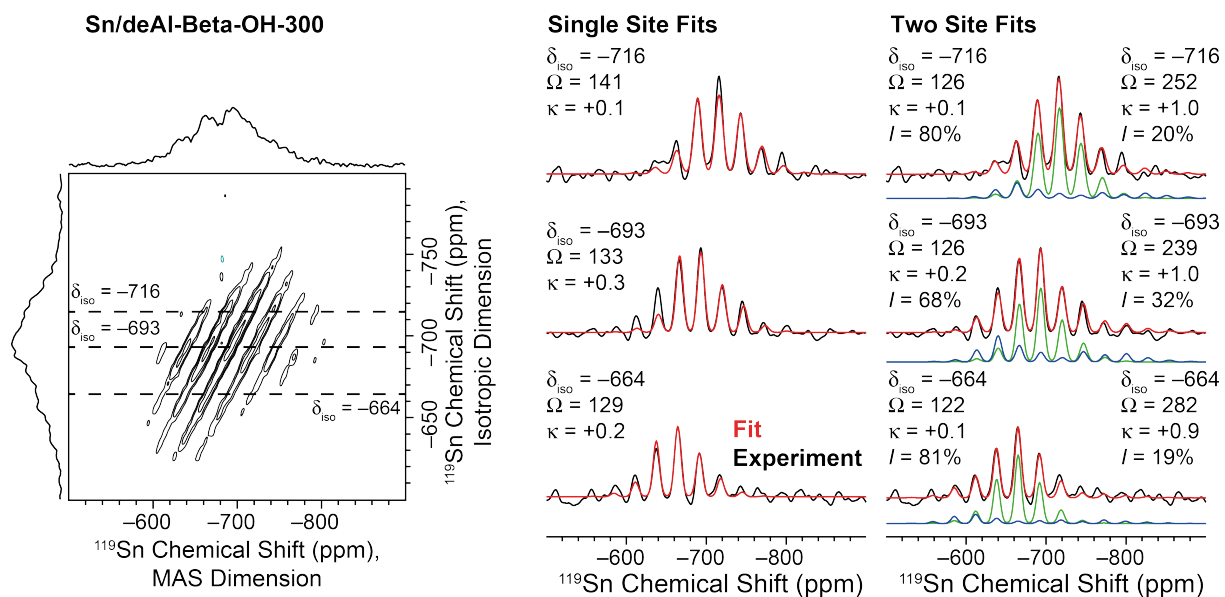


Figure A21. DNP enhanced ^1H - ^{119}Sn CP-MAT spectrum of Sn/deAl-Beta-OH-300. The spectrum was acquired with a CP contact time of 3 ms, a polarization delay of 3.2 s, a $25\ \mu\text{s}$ t_r increment, 112 scans per t_r increment and 56 t_r increments were acquired. A MAS frequency of 4000 Hz was used. A MAS frequency of 4000 Hz was used. Fits to the sideband manifolds are shown for the three isotropic peaks (dashed lines) and the CS tensor parameters obtained from the fits for both a single-site and a two-site fit are indicated.

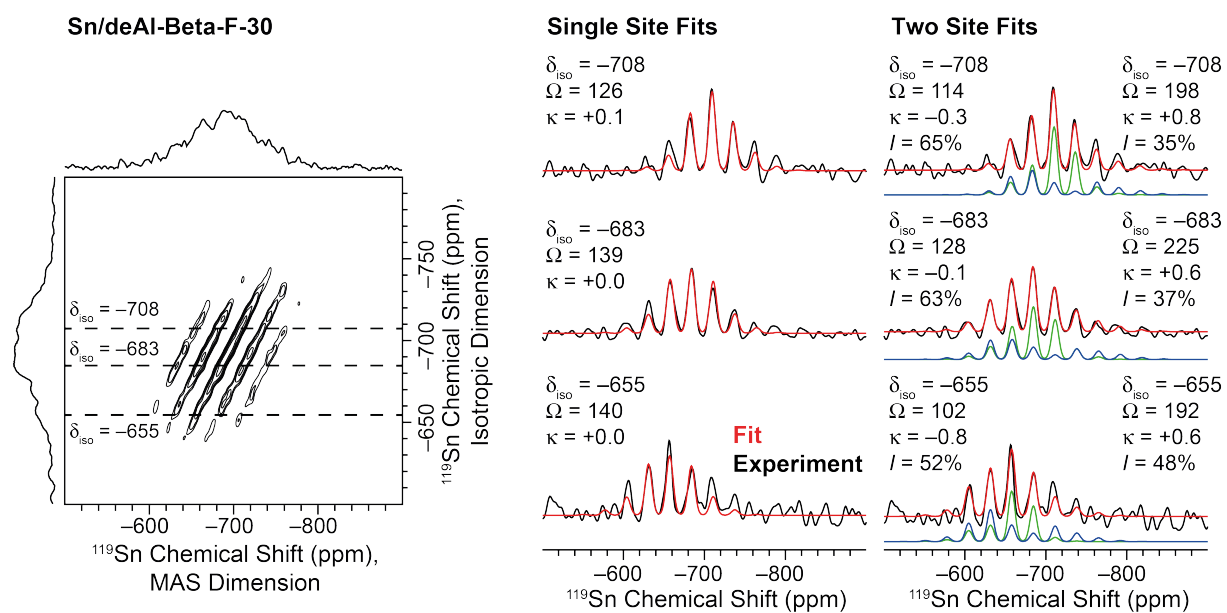


Figure A22. DNP enhanced ^1H - ^{119}Sn CP-MAT spectrum of Sn/deAl-Beta-F-30. The spectrum was acquired with a CP contact time of 3 ms, a polarization delay of 3.2 s, a $25\ \mu\text{s}$ t_r increment, 56 scans per t_r increment and 90 t_r increments were acquired. A MAS frequency of 4000 Hz was used. Fits to the sideband manifolds are shown for the two isotropic peaks (dashed lines) and the CS tensor parameters obtained from the fits for both a single-site and a two-site fit are indicated.

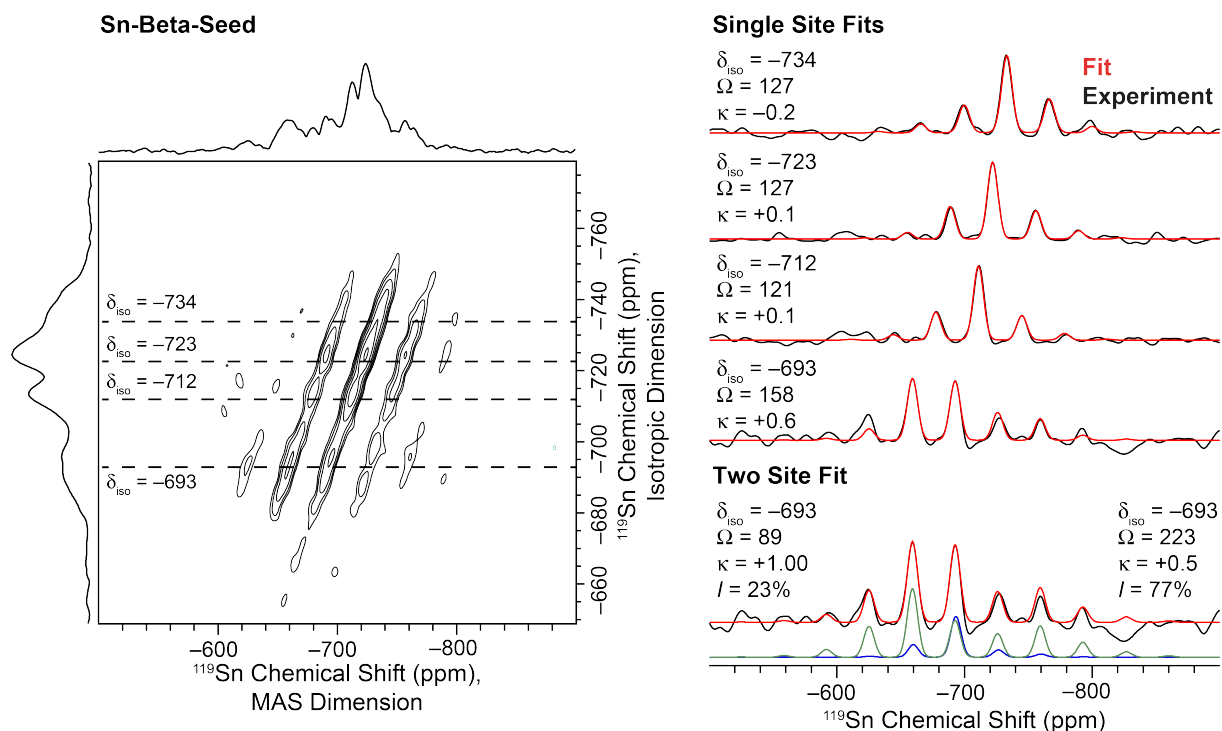


Figure A23. DNP enhanced ^1H - ^{119}Sn CP-MAT spectrum of Sn-Beta-Seed. The spectrum was acquired with a CP contact time of 3 ms, a polarization delay of 7 s, a $34.7 \mu\text{s}$ t , increment, 56 scans per t , increment and 132 t , increments were acquired. A MAS frequency of 5000 Hz was used. Fits to the sideband manifolds are shown for the two isotropic peaks (dashed lines) and the CS tensor parameters obtained from the fits for a single-site. For the peak at $\delta_{\text{iso}} = -693$ ppm a two-site fit is also shown.

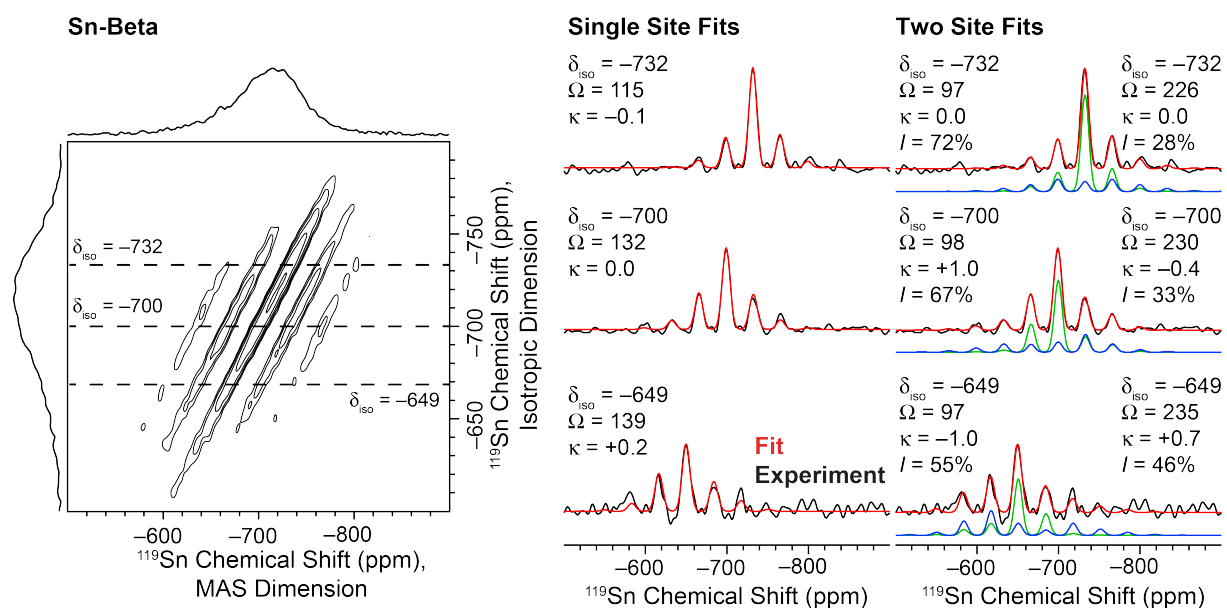


Figure A24. DNP enhanced ^1H - ^{119}Sn CP-MAT spectrum of Sn-Beta. The spectrum was acquired with a CP contact time of 3 ms, a polarization delay of 5 s, a $12.5 \mu\text{s}$ t_1 increment, 140 scans per t_1 increment and 80 t_1 increments were acquired. A MAS frequency of 5000 Hz was used. Fits to the sideband manifolds are shown for the two isotropic peaks (dashed lines) and the CS tensor parameters obtained from the fits for both a single-site and a two-site fit are indicated.

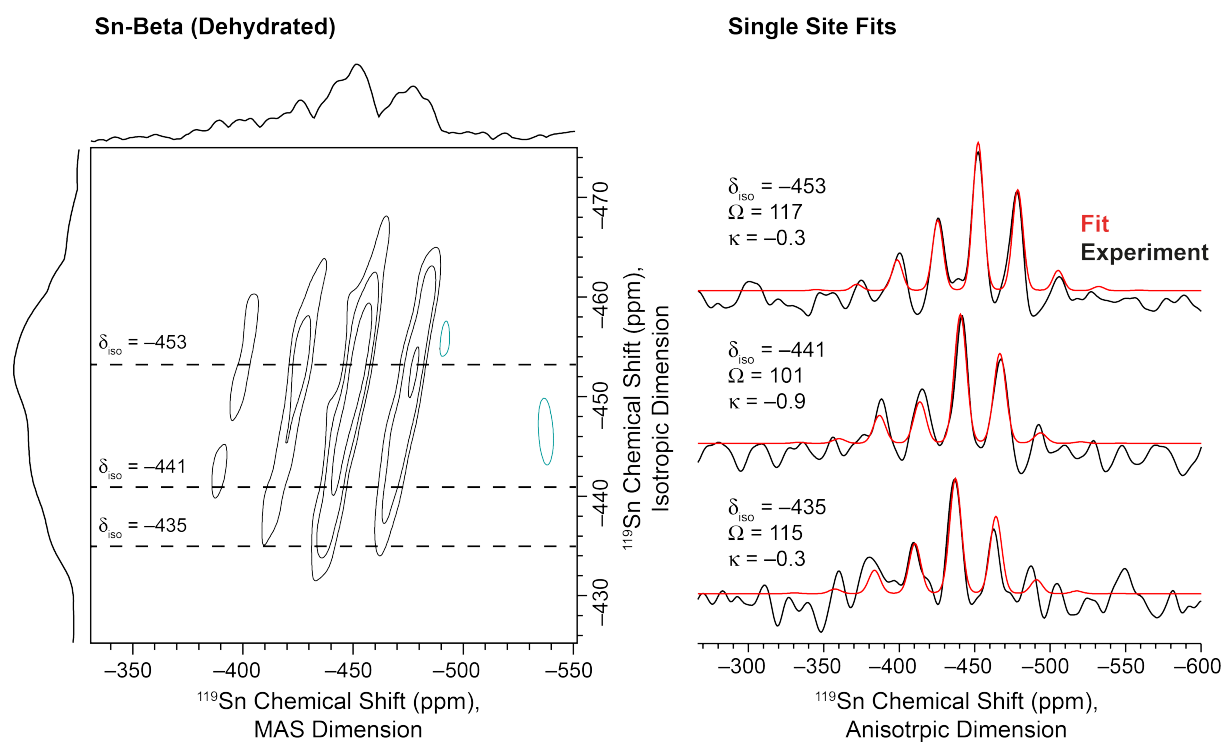


Figure A25. DNP enhanced ^1H - ^{119}Sn CP-MAT spectrum of Sn-Beta dehydrated. The spectrum was acquired with a CP contact time of 5.5 ms, a polarization delay of 15 s, a $77.4 \mu\text{s}$ t_c increment, 392 scans per t_c increment and 28 t_c increments were acquired. A MAS frequency of 4500 Hz was used. Fits to the sideband manifolds are shown for the two isotropic peaks (dashed lines) and the CS tensor parameters obtained from the fits for a single-site.

Table A7. Calculated main average geometrical parameters of all dehydrated T sites in Sn- β . Average distances are given in Å and average angles in degrees.

Site	Closed sites				Defect-open sites				
	Sn-O	Sn-Si	O-Sn-O	Sn-O-Si	Sn-OH	Sn-O	Sn-Si	O-Sn-O	Sn-O-Si
T1	1.894	3.235	109.5	132.8	1.886	1.904	3.299	109.3	138.5
T2	1.895	3.234	109.5	132.9	1.889	1.905	3.210	109.5	129.5
T3	1.894	3.242	109.4	133.6	1.904	1.892	3.251	109.5	133.8
T4	1.894	3.232	109.4	133.1	1.906	1.895	3.209	109.5	129.5
T5	1.888	3.273	109.5	129.5	1.923	1.888	3.216	109.5	132.8
T6	1.886	3.291	109.4	140.8	1.903	1.895	3.270	109.5	136.2
T7	1.890	3.248	109.5	135.9	1.921	1.890	3.241	109.5	136.0
T8	1.893	3.226	109.5	133.3	1.904	1.898	3.225	109.4	133.3
T9	1.894	3.213	109.4	131.9	1.918	1.893	3.229	109.4	133.7

Table A8. Main average geometrical parameters of all mono-hydrated closed sites formed in Sn- β . O atoms with “w” superscript correspond to O atoms of the water ligands. Distances are given in Å and angles in degrees.

Site	Sn-O	Sn-O ^w	Sn-Si	O-Sn-O	O-Sn-O ^w	Sn-O-Si
T1 ^{C1}	1.913	2.278	3.251	118.0	178.1	133.5
T2 ^{C1}	1.910	2.300	3.282	117.8	173.3	136.5
T3 ^{C1}	1.907	2.334	3.286	117.0	173.0	138.0
T4 ^{C1}	1.911	2.315	3.284	116.8	175.8	137.4
T5 ^{C1}	1.908	2.289	3.330	116.9	170.2	143.8
T6 ^{C1}	1.904	2.275	3.331	117.5	175.8	142.1
T7 ^{C1}	1.911	2.303	3.259	116.9	174.5	135.2
T8 ^{C1}	1.914	2.330	3.254	116.2	172.8	135.2
T9 ^{C1}	1.912	2.331	3.258	116.4	174.8	135.3

Table A9. Main average geometrical parameters of all doubly-hydrated closed sites formed in Sn- β . O atoms with “w” superscript correspond to O atoms of the water ligands. Distances are given in Å and angles in degrees

	Sn-O	Sn-O ^{w1}	Sn-O ^{w2}	Sn-Si	O-Sn-O	O-Sn-O ^w	Sn-O-Si
T1 ^{C2}	1.939	2.251	2.174	3.290	96.3	171.3	129.7
T2 ^{C2}	1.933	2.255	2.223	3.303	96.9	166.3	142.5
T3 ^{C2}	1.931	2.253	2.292	3.297	98.0	170.5	140.1
T4 ^{C2}	1.934	2.260	2.274	3.337	99.8	171.5	140.7
T5 ^{C2}	1.940	2.266	2.296	3.247	99.7	174.8	131.4
T6 ^{C2}	1.945	2.242	2.266	3.264	97.9	172.2	133.0
T7 ^{C2}	1.944	2.258	2.218	3.289	99.5	175.5	135.3
T8 ^{C2}	1.950	2.219	2.219	3.263	98.6	174.3	132.8
T9 ^{C2}	1.945	2.202	2.270	3.275	99.3	168.6	134.1

Table A10. Main average geometrical parameters of all triply-hydrated closed sites formed in Sn- β . O atoms with “w” superscript correspond to O atoms of the water ligands. Distances are given in Å and angles in degrees

	Sn-O	Sn-O ^{w1}	Sn-O ^{w2}	Sn-Si	O-Sn-O	O-Sn-O ^w	Sn-O-Si
T1 ^{C3}	1.945	2.271	2.127	3.304	95.4	169.5	138.3
T2 ^{C3}	1.943	2.174	2.180	3.302	95.3	170.7	141.0
T3 ^{C3}	1.939	2.168	2.289	3.302	97.0	173.2	139.4
T4 ^{C3}	1.947	2.164	2.260	3.359	98.2	170.1	141.7
T5 ^{C3}	1.948	2.191	2.284	3.285	98.7	173.5	133.9
T6 ^{C3}	1.955	2.221	2.197	3.270	96.9	168.9	132.7
T7 ^{C3}	1.953	2.180	2.236	3.290	98.4	176.5	134.6
T8 ^{C3}	1.960	2.159	2.219	3.268	97.5	174.7	132.4
T9 ^{C3}	1.957	2.134	2.279	3.274	97.9	168.8	132.9

Table A11. Main average geometrical parameters of all doubly-hydrated defect-open sites formed in Sn- β . O atoms with “w” superscript correspond to O atoms of the water ligands. Distances are given in Å and angles in degrees.

	Sn-OH	Sn-O	Sn-O ^{w1}	Sn-O ^{w2}	Sn-Si	O-Sn-O	O-Sn-O ^w	Sn-O-Si
T1 ^{O2}	1.967	1.935	2.288	2.154	3.348	98.1	169.7	143.1
T2 ^{O2}	1.925	1.953	2.189	2.266	3.289	96.8	167.2	138.3
T3 ^{O2}	1.960	1.956	2.218	2.198	3.315	97.4	171.4	134.4
T4 ^{O2}	1.951	1.938	2.304	2.262	3.307	100.7	177.2	144.1
T5 ^{O2}	1.990	1.939	2.177	2.287	3.303	99.3	170.9	136.9
T6 ^{O2}	1.948	1.959	2.227	2.250	3.289	97.8	167.7	134.3
T7 ^{O2}	1.958	1.943	2.292	2.245	3.295	99.9	174.9	135.8
T8 ^{O2}	1.989	1.943	2.219	2.233	3.293	98.4	176.5	135.4
T9 ^{O2}	1.953	1.946	2.276	2.264	3.300	100.1	165.1	136.2

Table A1. Main average geometrical parameters of all triply-hydrated defect-open sites formed in Sn- β . O atoms with “w” superscript correspond to O atoms of the water ligands. Distances are given in Å and angles in degrees.

	Sn-OH	Sn-O	Sn-O ^{w1}	Sn-O ^{w2}	Sn-Si	O-Sn-O	O-Sn-O ^w	Sn-O-Si
T1 ^{O3}	1.970	1.942	2.177	2.127	3.398	96.0	170.8	154.0
T2 ^{O3}	1.982	1.955	2.154	2.172	3.332	96.3	174.8	138.3
T3 ^{O3}	1.957	1.972	2.130	2.225	3.326	95.8	173.4	135.9
T4 ^{O3}	1.959	1.947	2.174	2.250	3.341	98.7	177.4	140.5
T5 ^{O3}	1.995	1.949	2.119	2.275	3.312	97.8	171.2	137.0
T6 ^{O3}	1.934	1.974	2.145	2.300	3.297	97.4	170.5	133.6
T7 ^{O3}	1.984	1.952	2.206	2.230	3.306	98.2	174.4	136.1
T8 ^{O3}	1.985	1.955	2.157	2.240	3.310	97.2	176.1	137.3
T9 ^{O3}	1.964	1.954	2.147	2.238	3.308	97.7	172.0	137.1

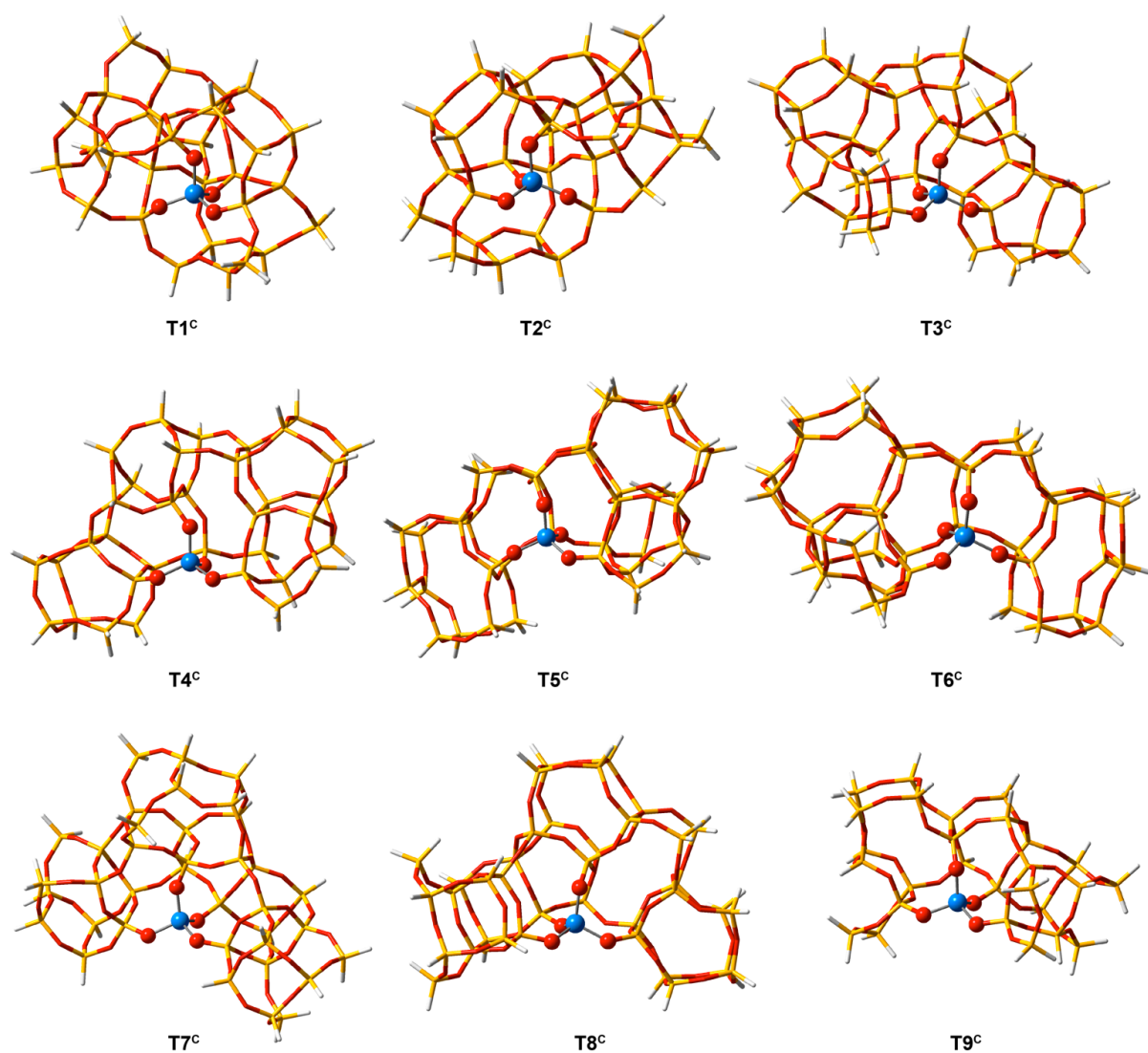


Figure A26. Optimized structures of all dehydrated closed sites of Sn-β. The Sn atom and its first coordination sphere are highlighted with ball and sticks model. Sn atoms are shown in blue, oxygen in red, silicon in yellow and hydrogen in white.

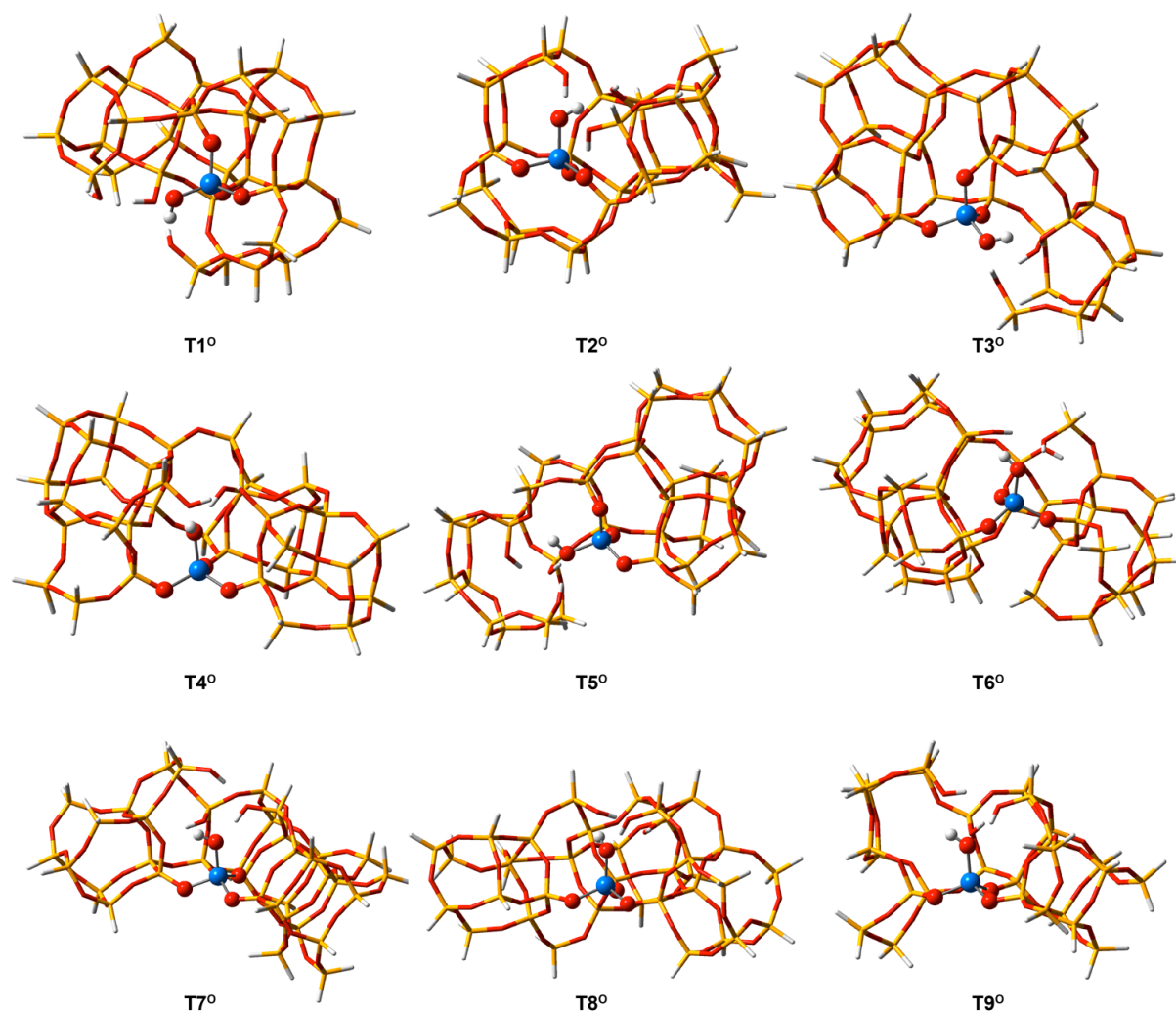


Figure A27. Optimized structures of all dehydrated defect-open sites of Sn-β. The Sn atom and its first coordination sphere are highlighted with ball and sticks model. Sn atoms are shown in blue, oxygen in red, silicon in yellow and hydrogen in white.

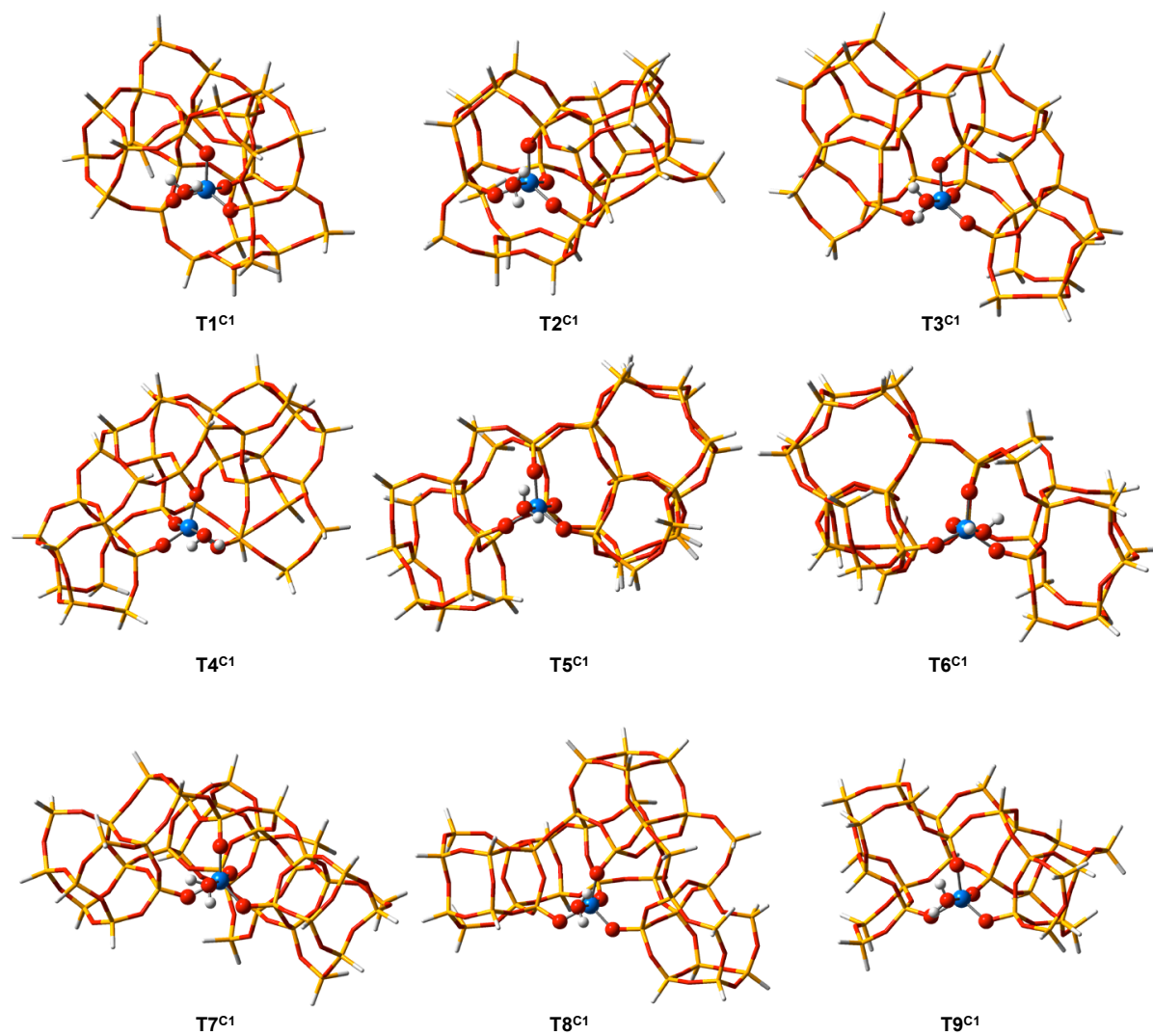


Figure A28. Optimized structures of all mono-hydrated closed sites of Sn- β . The Sn atom and its first coordination sphere are highlighted with ball and sticks model. Sn atoms are shown in blue, oxygen in red, silicon in yellow and hydrogen in white.

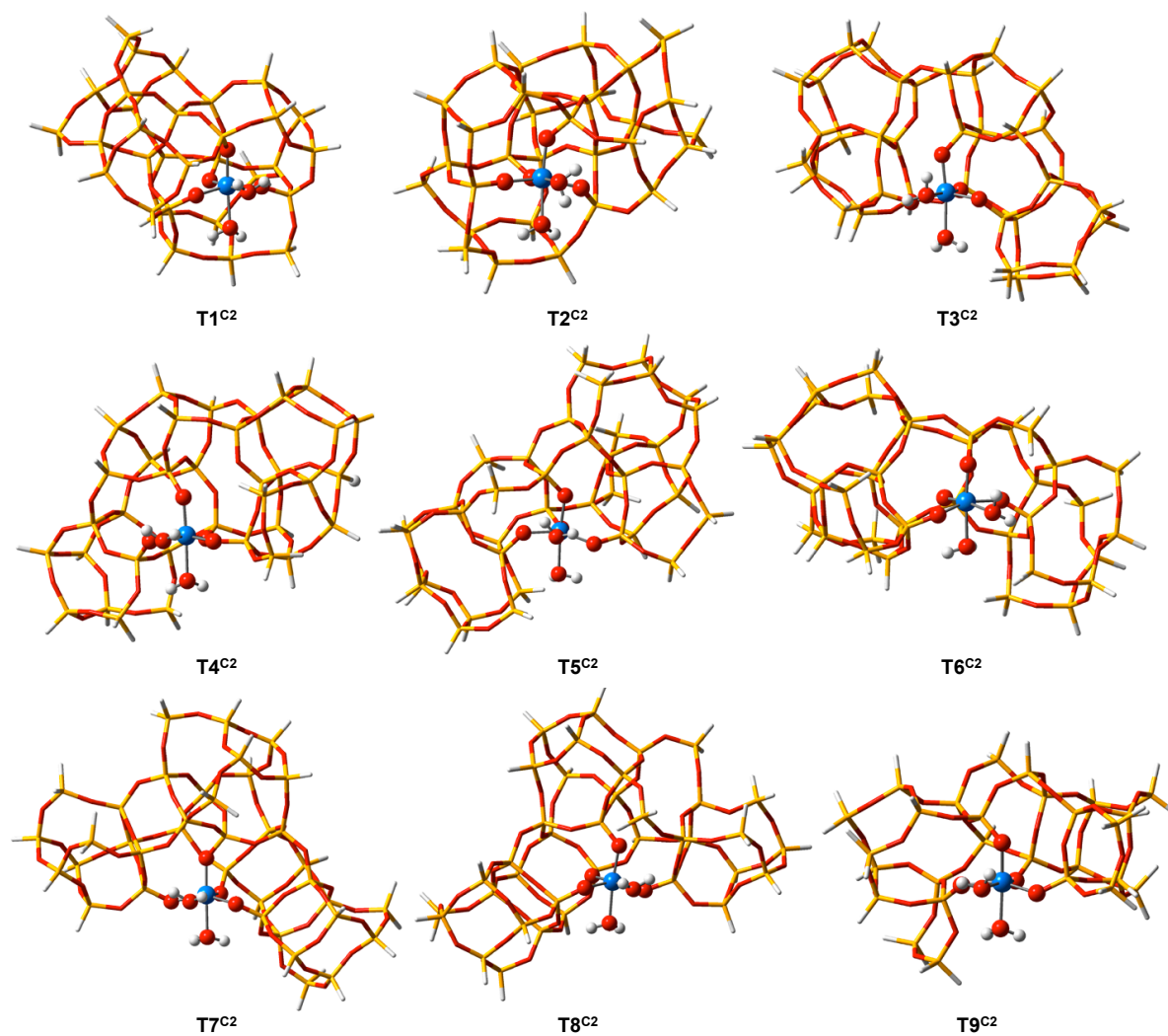


Figure A29. Optimized structures of all doubly-hydrated closed sites of Sn- β . The Sn atom and its first coordination sphere are highlighted with ball and sticks model. Sn atoms are shown in blue, oxygen in red, silicon in yellow and hydrogen in white.

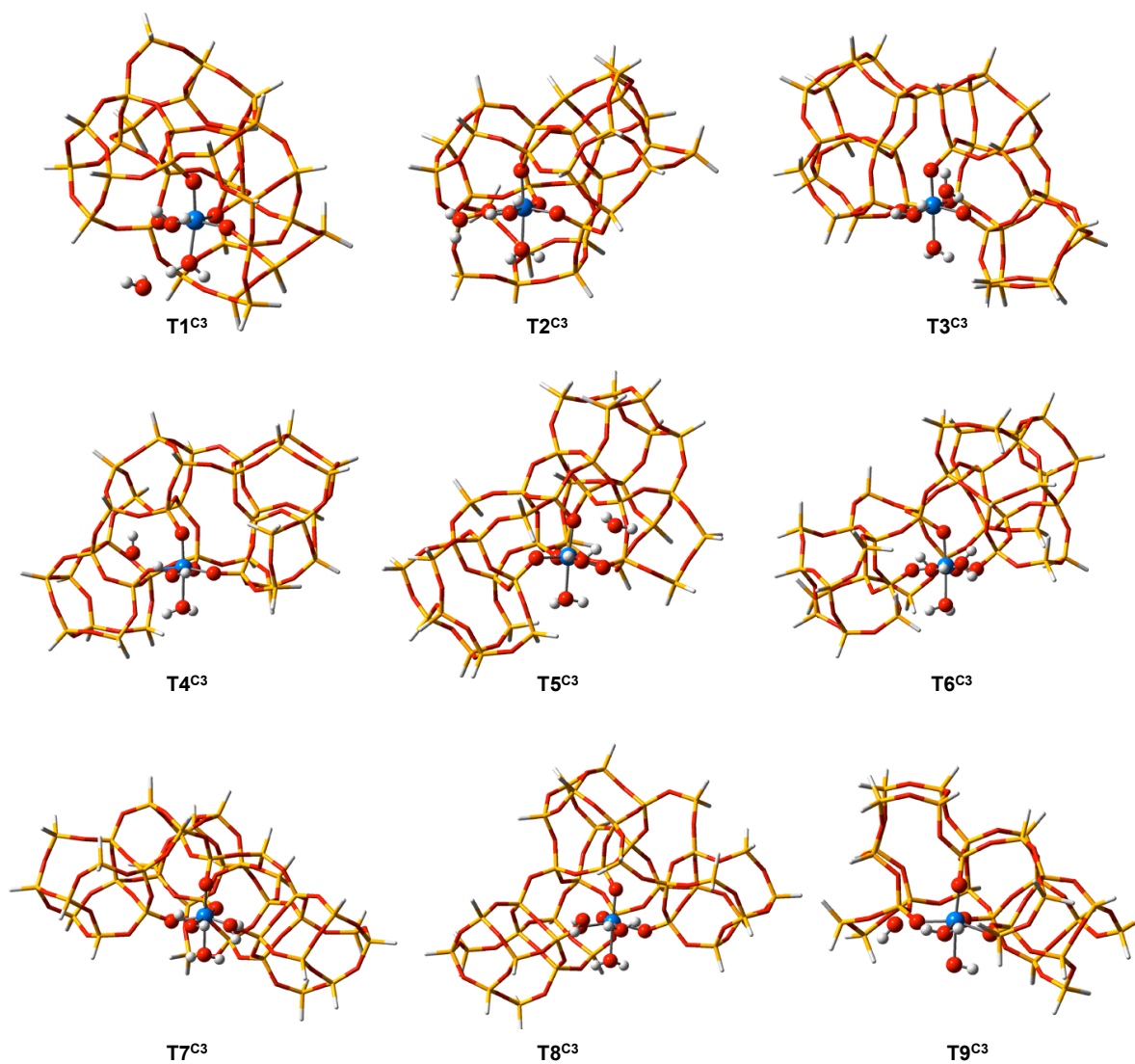


Figure A30. Optimized structures of all triply-hydrated closed sites of Sn- β . The Sn atom and its first coordination sphere are highlighted with ball and sticks model. Sn atoms are shown in blue, oxygen in red, silicon in yellow and hydrogen in white.

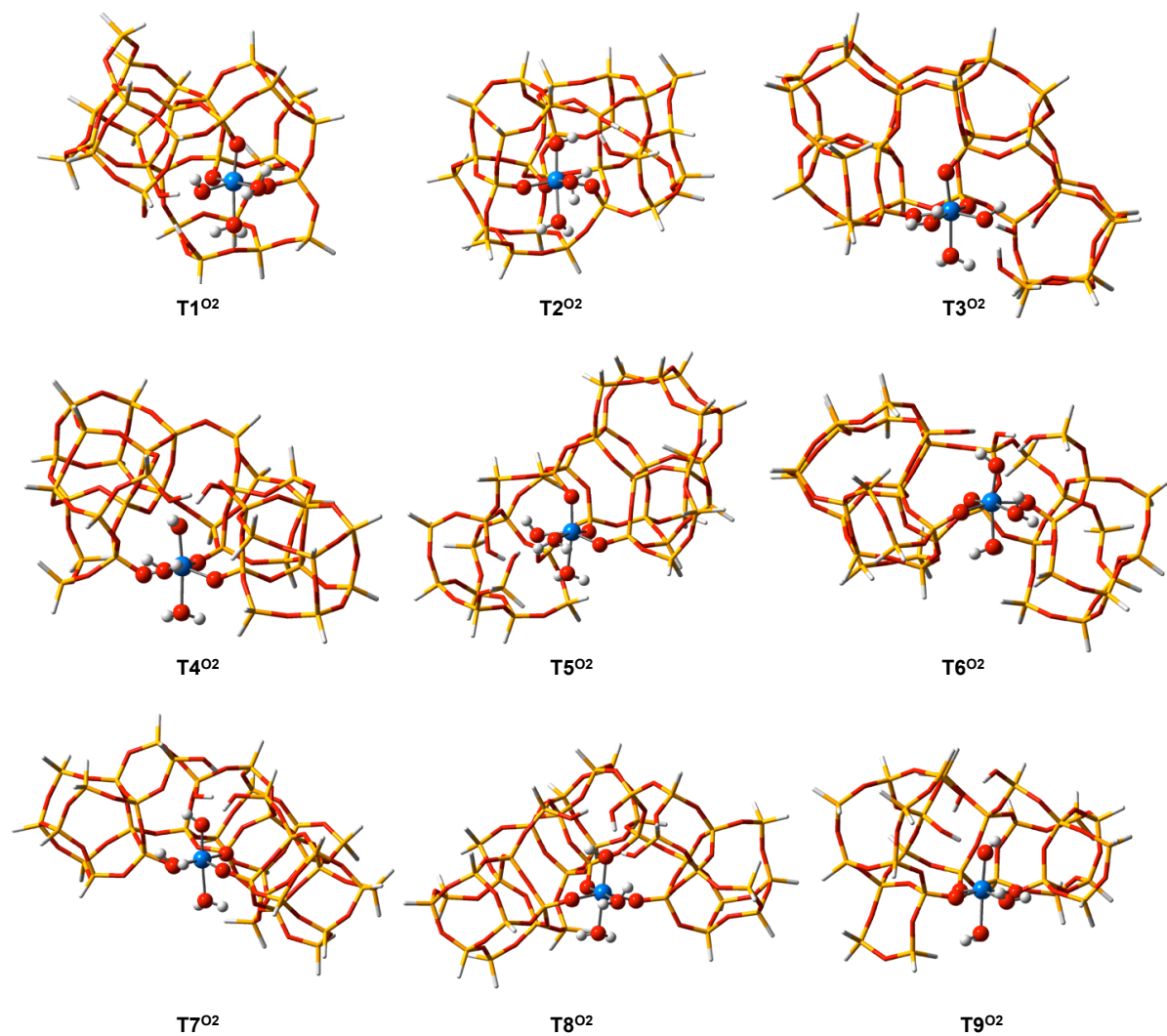


Figure A31. Optimized structures of all doubly-hydrated defect-open sites of Sn- β . The Sn atom and its first coordination sphere are highlighted with ball and sticks model. Sn atoms are shown in blue, oxygen in red, silicon in yellow and hydrogen in white.

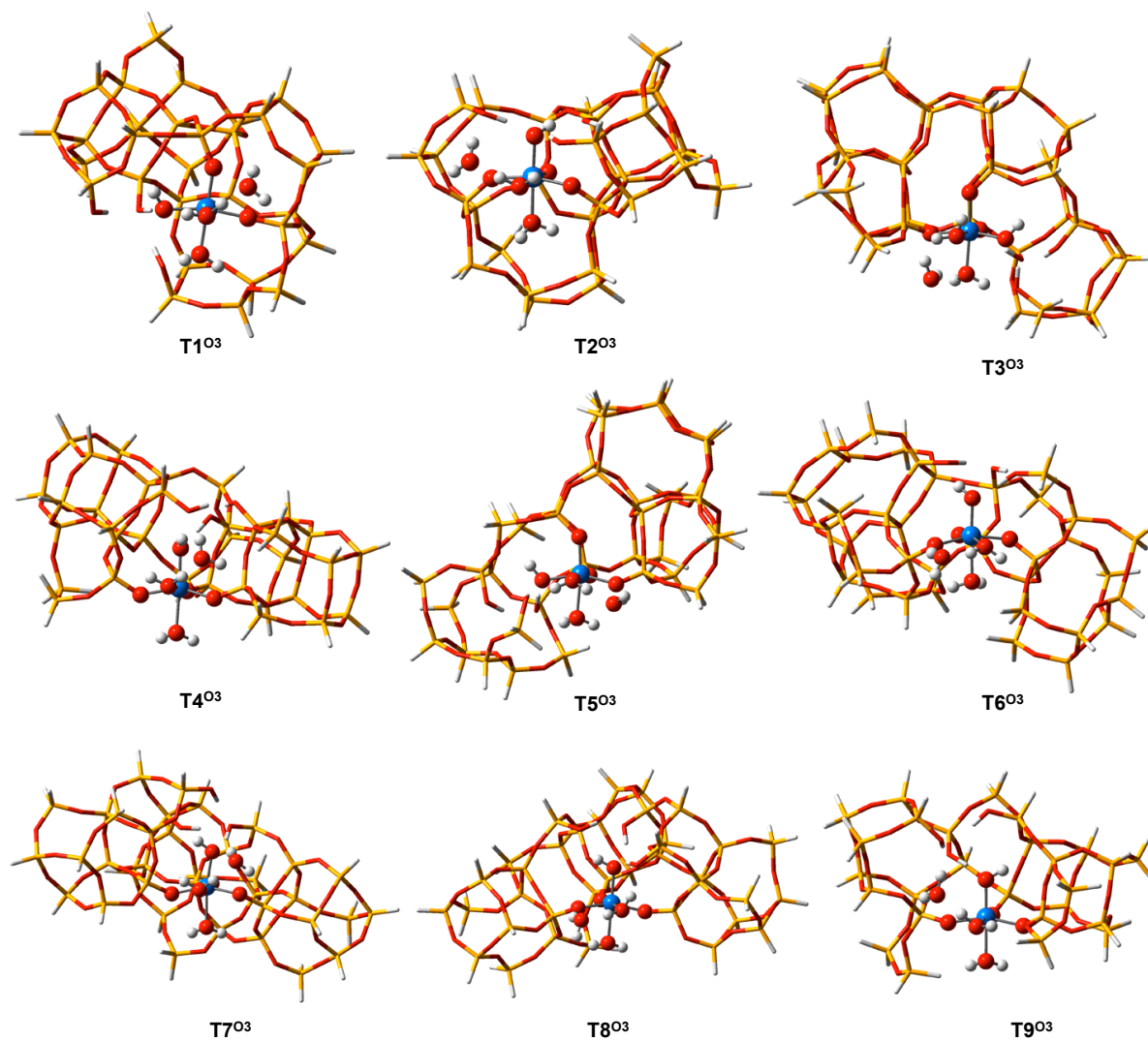


Figure A32. Optimized structures of all triply-hydrated defect-open sites of Sn- β . The Sn atom and its first coordination sphere are highlighted with ball and sticks model. Sn atoms are shown in blue, oxygen in red, silicon in yellow and hydrogen in white.

Table A2. Relative stabilities of the different T sites in cluster models of Sn- β . The DE energies correspond to electronic energies calculated with the B₃LYP with dispersion corrections (B₃LYP-D₃). Energies are given in kcal·mol⁻¹

Site	ΔE
T1	0.0
T2	1.4
T3	3.4
T4	3.7
T5	6.9
T6	6.3
T7	2.9
T8	3.5
T9	3.2

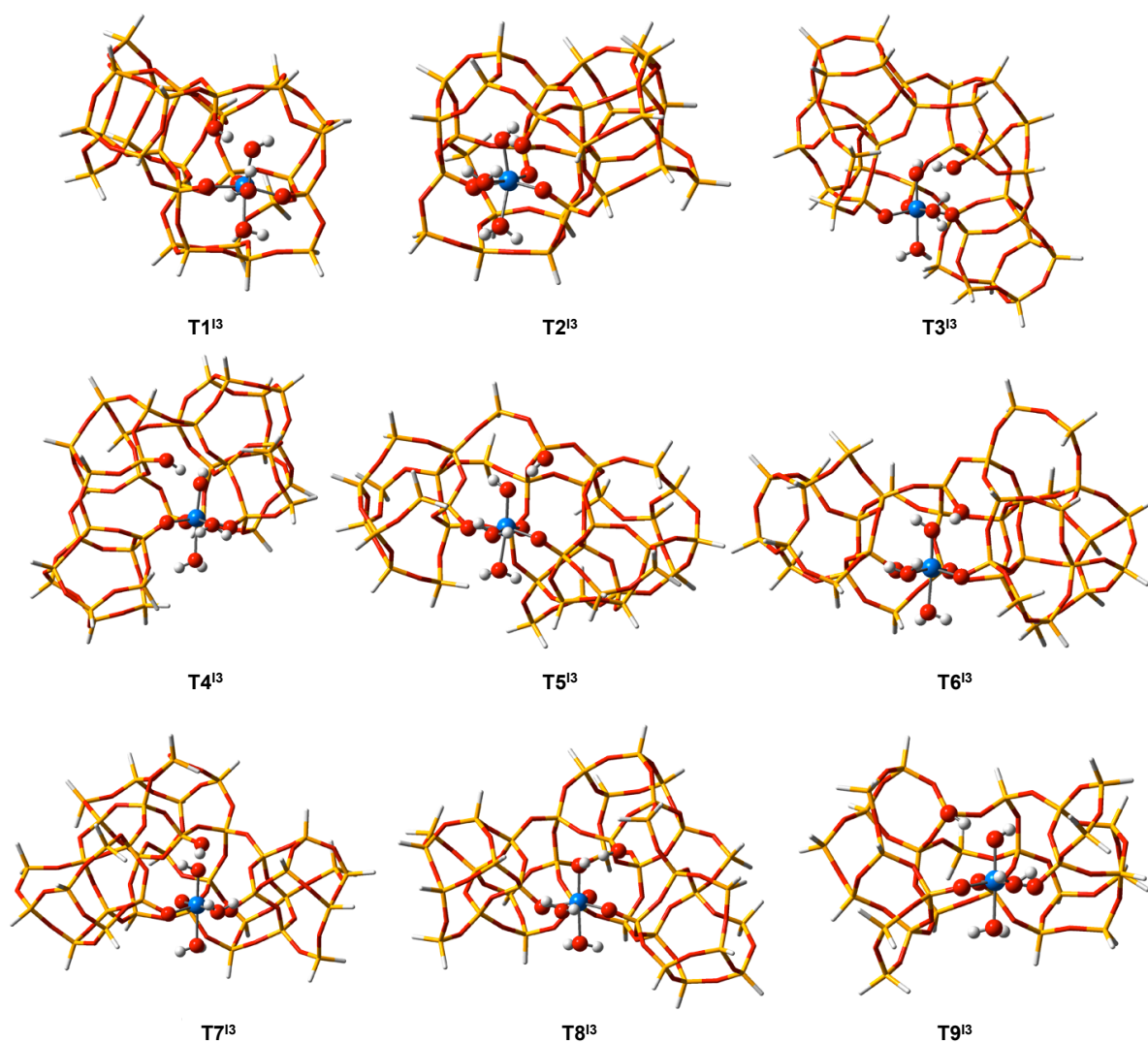


Figure A33. Optimized structures of hydrolyzed-open sites of Type I of Sn- β . The Sn atom and its first coordination sphere are highlighted with ball and sticks model. Sn atoms are shown in blue, oxygen in red, silicon in yellow and hydrogen in white.

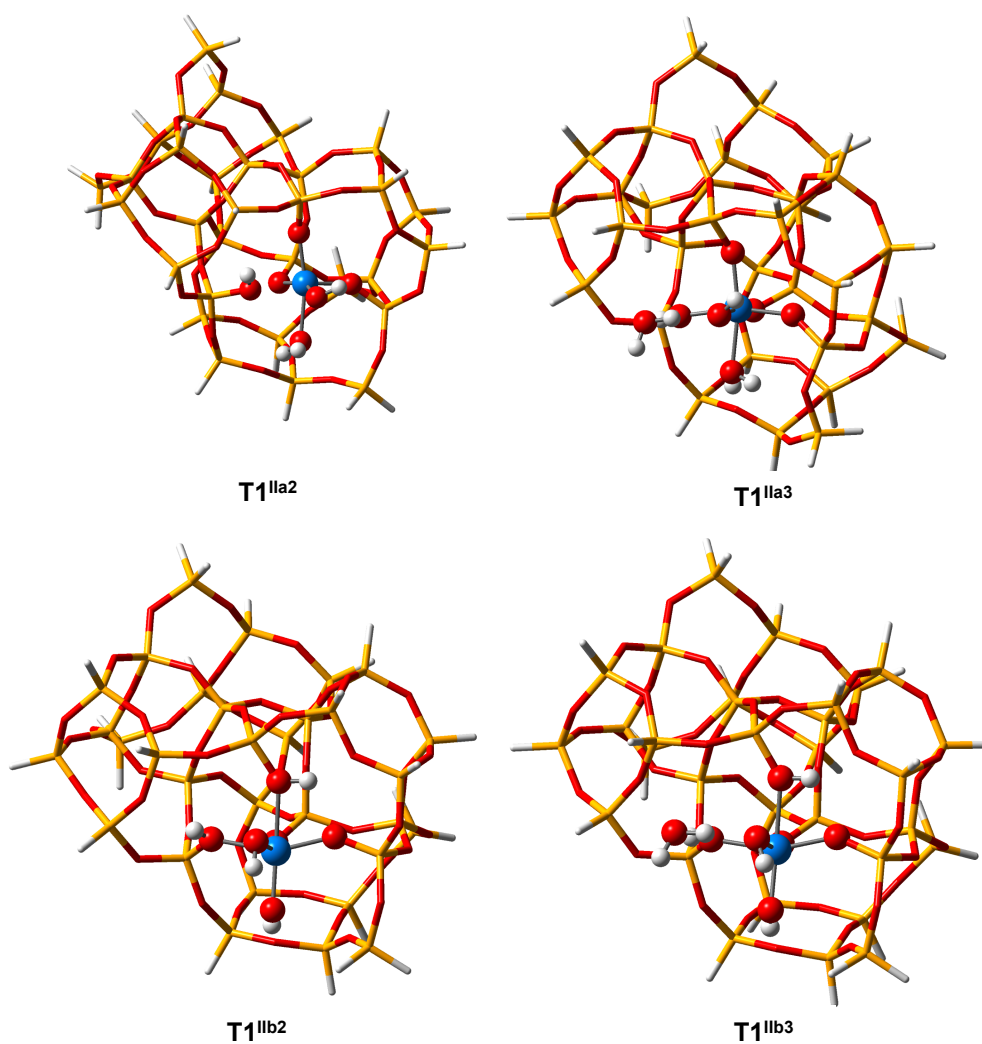


Figure A34. Optimized structures of T1 hydrolyzed-open sites of Type II of Sn-β. The Sn atom and its first coordination sphere are highlighted with ball and sticks model. Sn atoms are shown in blue, oxygen in red, silicon in yellow and hydrogen in white.

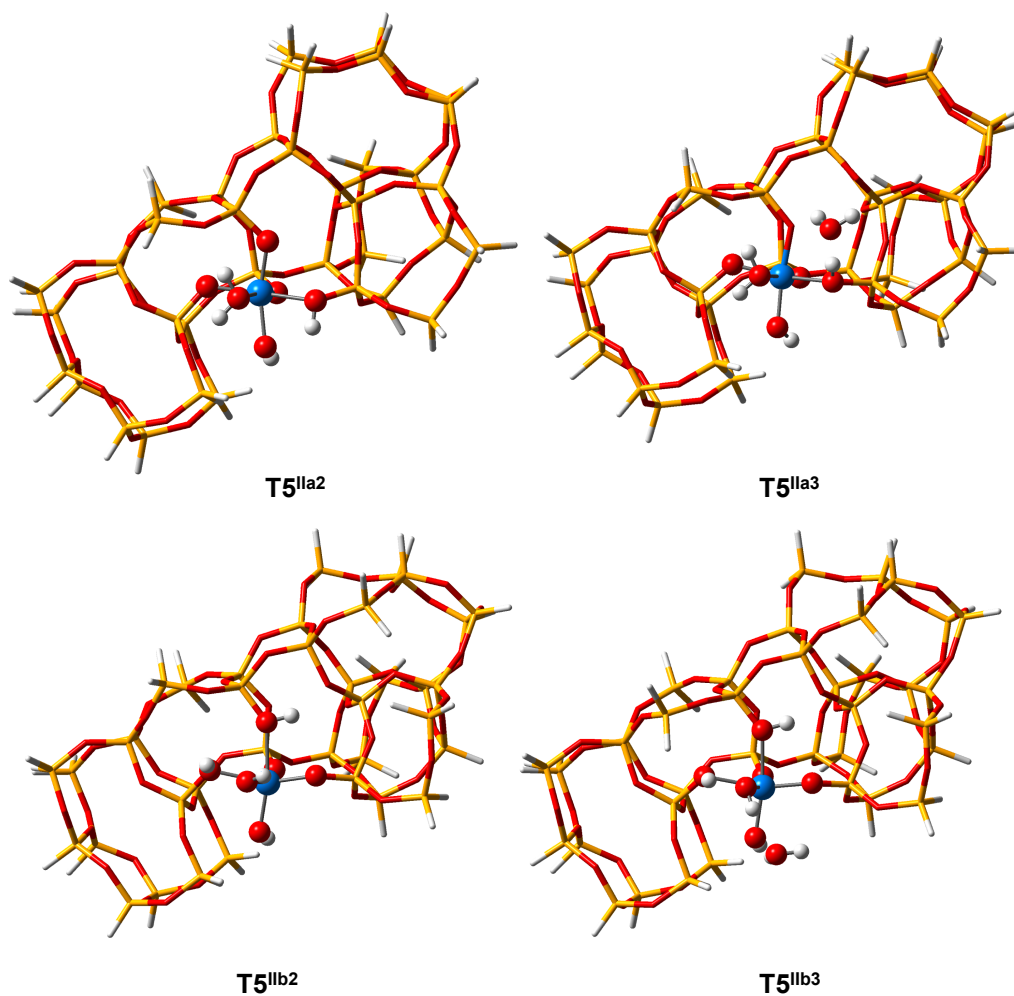


Figure A35. Optimized structures of T5 hydrolyzed-open sites of Type II of Sn-β. The Sn atom and its first coordination sphere are highlighted with ball and sticks model. Sn atoms are shown in blue, oxygen in red, silicon in yellow and hydrogen in white.

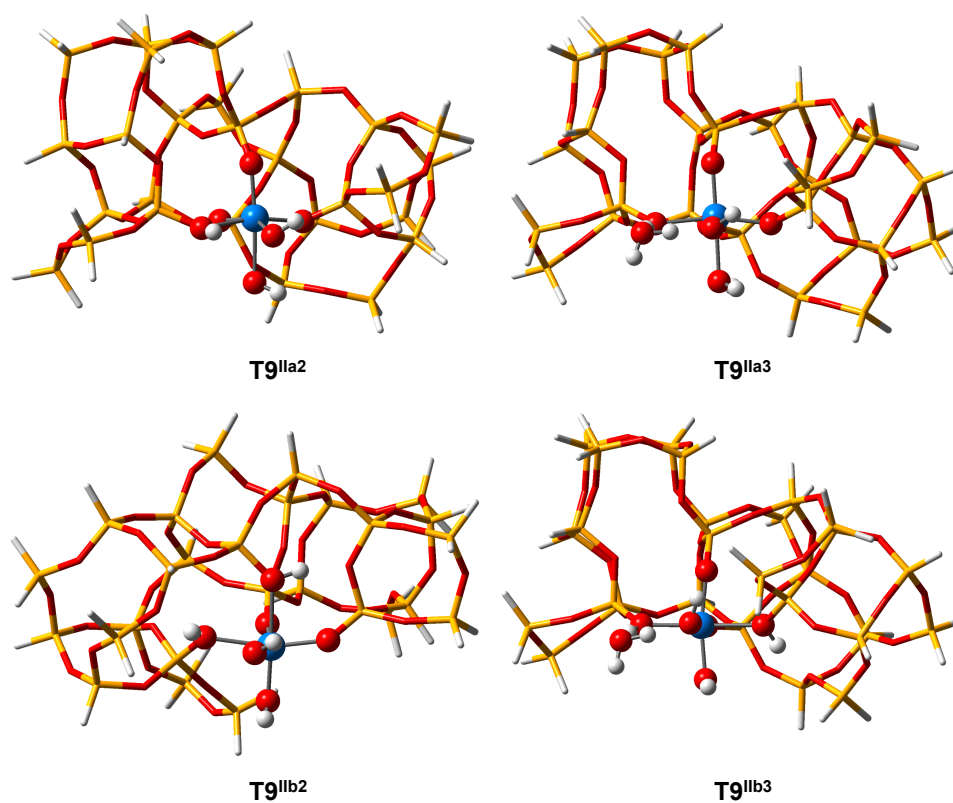


Figure A36. Optimized structures of T9 hydrolyzed-open sites of Type II of Sn- β . The Sn atom and its first coordination sphere are highlighted with ball and sticks model. Sn atoms are shown in blue, oxygen in red, silicon in yellow and hydrogen in white.

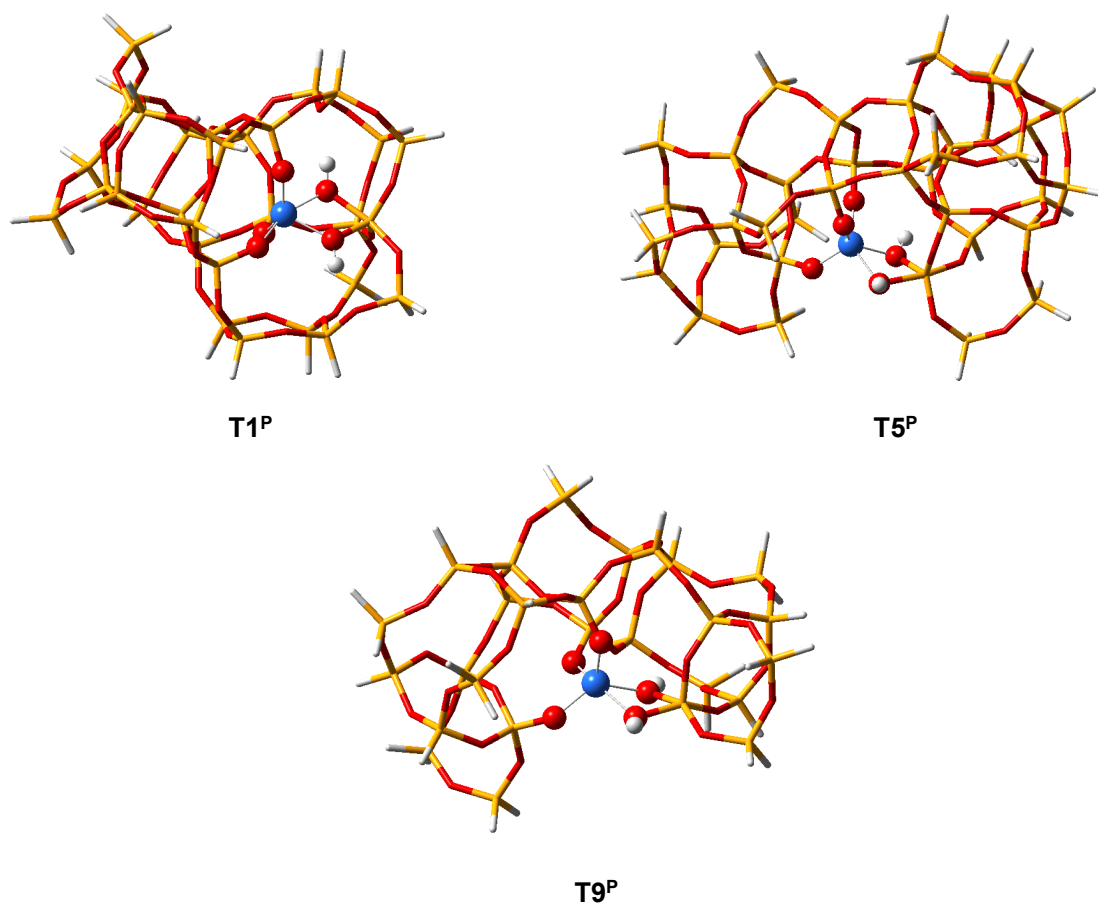


Figure A37. Optimized structures of T1, T5 and T9 penta-coordinated sites of Sn-β. The Sn atom and its first coordination sphere are highlighted with ball and sticks model. Sn atoms are shown in blue, oxygen in red, silicon in yellow and hydrogen in white.

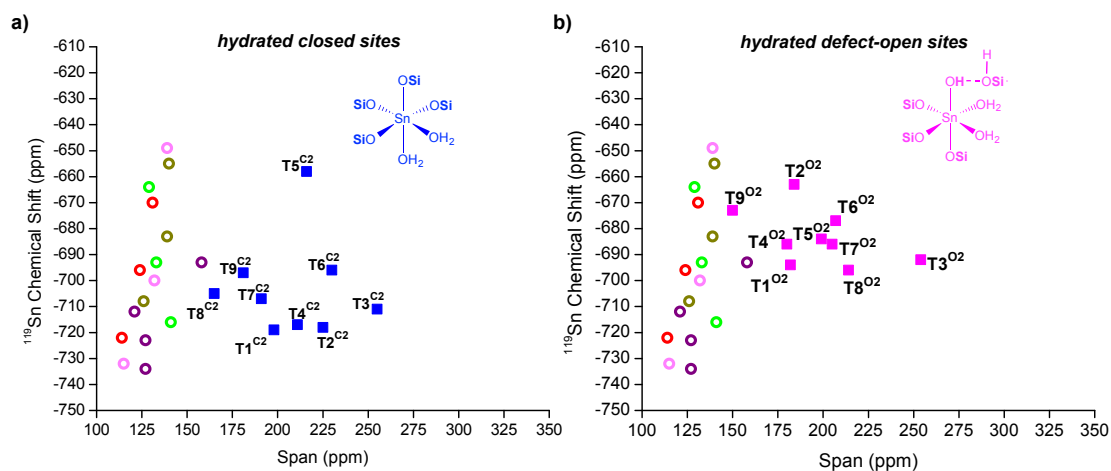


Figure A38. Comparison of measured and calculated ^{119}Sn NMR chemical shifts vs. spans. Calculations for a) double-hydrated $\text{Tn}^{\text{C}2}$ (■) closed sites; b) double-hydrated $\text{Tn}^{\text{O}2}$ (■) Experimental data are shown for hydrated Sn/deAl-Beta-OH-25 (○), Sn/deAl-Beta-OH-300 (○), Sn-Beta-F-30 (○), Sn-Beta-seed (○) and Sn-Beta (○).

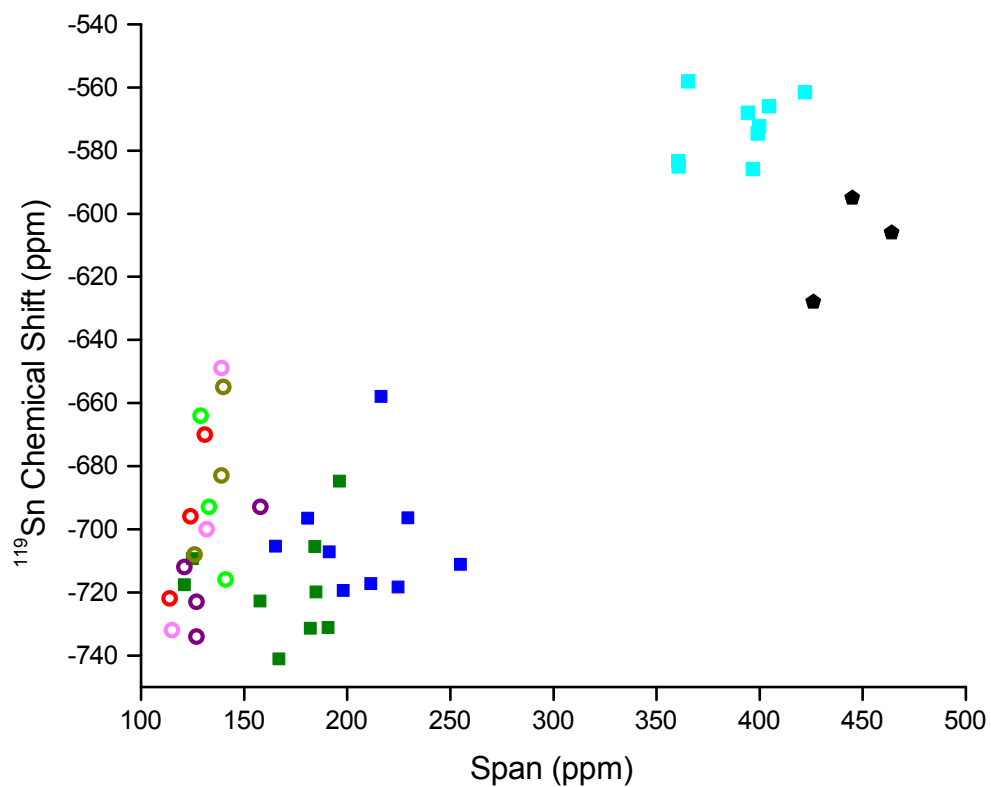


Figure A39. ^{119}Sn NMR chemical shift vs. span for mono-hydrated-hydrated Tn^{C1} (■), double-hydrated Tn^{C2} (■), triply-hydrated Tn^{C3} (■) closed sites and pentacoordinated hydrated sites (◆). Experimental data for hydrated Sn/deAl-Beta-OH-25 (○), Sn/deAl-Beta-OH-300 (○), Sn/deAl-Beta-F-30 (○), Sn-Beta seeded (○) and Sn-Beta unseeded (○) are also shown for comparison.

Text A2. Effect of water ligand conformations on the ^{119}Sn NMR signatures

We investigated the effect of variations of the water ligand on the ^{119}Sn NMR signatures of Sn- β . To this end, we decided to explore the NMR spectra of ^{119}Sn in constrained structures, that is, by selecting different degrees of freedom (geometrical parameters) involving the water molecules and calculate the NMR signatures for certain fixed values of those parameters. We chose two different parameters: the distance between Sn and the water molecule (Sn-OH₂) and the Sn-OH₂ rotational axis, as shown in Figure A40 (top). Exemplarily, we carried out the calculations only for the T9^{C2} site and explored the movement of only one water ligand, by fixing the mentioned parameters and freely optimizing the rest of the cluster. For the first parameter, the Sn-OH₂ bond distance, we explored eight structures by increasing/decreasing the Sn-OH₂ equilibrium distance four times by 0.05 Å, while for the second parameter, the Sn-OH₂ rotational axis, we explored seven points resulting from the rotation of the Sn-OH₂ bond around by 45°.

The results of these calculations are shown in Figure A40(bottom). We observed in Figure A40a that the energetic variation of both processes is low compared to the equilibrium structure (eq). For the Sn-OH₂ bond distance the variation is at most 2.5 kcal·mol⁻¹, while for the Sn-OH₂ rotation the energy change for most of the explored structures compared to the equilibrium structure (eq) is below 1.5 kcal·mol⁻¹ (only two points are about 3.0 kcal·mol⁻¹ from the equilibrium structure). This means that the water ligand can actually fluctuate from the equilibrium distance with very low energetic cost. This result is in agreement with a recent *Ab initio* Molecular Dynamics (AIMD) study on the water absorption to the T2 site of the Sn- β . At T=300K, it was found that the water molecule prefers to coordinate to the heteroatom (Sn) and that the Sn-OH₂ bond distance fluctuate with an average value of 2.44 Å.¹¹⁹

Figure A1b shows the variation of the ^{119}Sn NMR parameters (δ_{iso} and Ω) for the explored structures. For the Sn-OH₂ bond distance variation we observed that δ_{iso} only varies by 17 ppm at most (eq and point 8), while the variation in Ω is more drastic, with a window of 63 ppm (points 1 and 8). In the case of the Sn-OH₂ rotational axis, the variation in δ_{iso} and Ω is random. The largest variation in δ_{iso} is only 13 ppm, while that for Ω is 42 ppm.

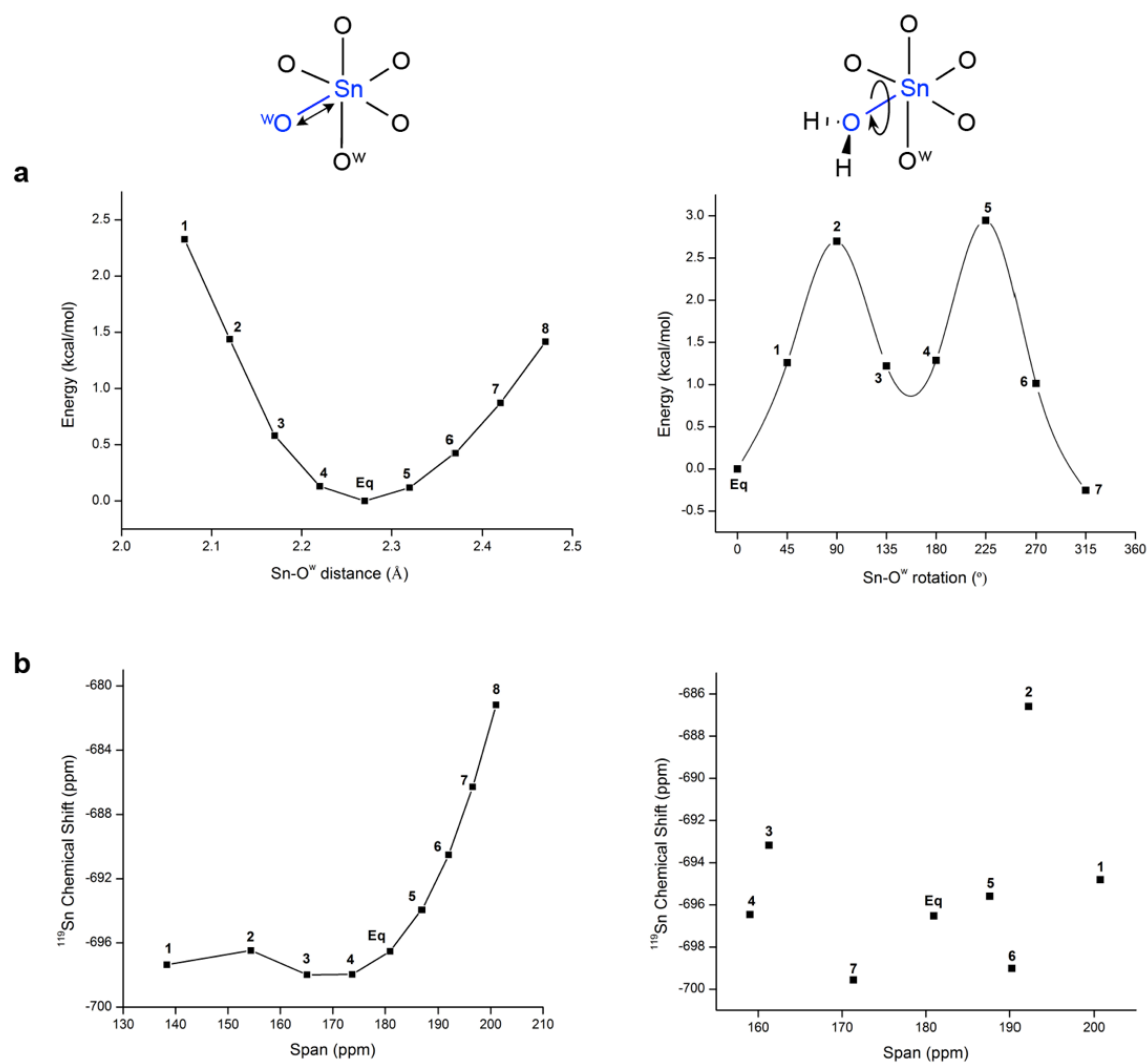


Figure A40. a) Electronic energy profiles for the Sn---OH₂ bond distance variation (left) and rotation (right) in the T_g^{C2} site; b) ¹¹⁹Sn NMR parameters for the variation of the Sn-OH₂ bond distance variation (left) and rotation (right) in the T_g^{C2} site.

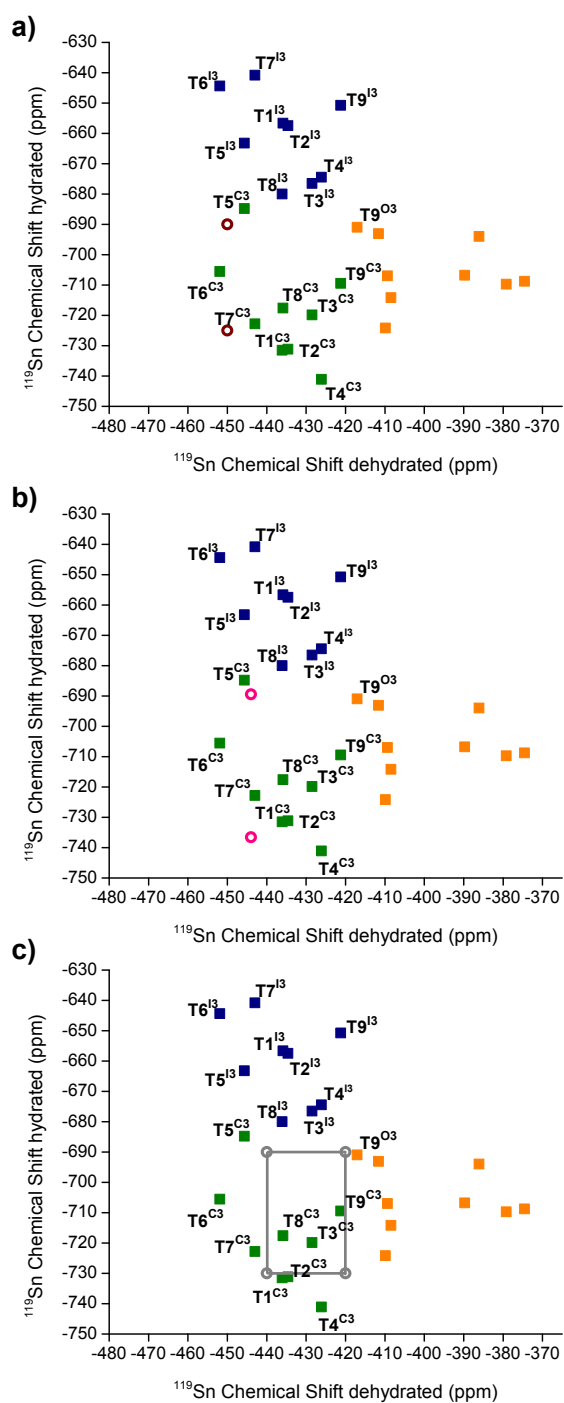


Figure A41. Comparison of experimental ^{119}Sn NMR chemical shifts found in literature with computational ^{119}Sn NMR. Calculations for dehydrated vs. hydrated of closed sites (■), defect-open sites (■) and hydrolyzed-open sites of type I (■). Experimental chemical Sn chemical shifts for hydrothermal Sn- β samples from different research labs: (a) Román-Leshkov et al.¹⁷⁰ (b) Corma et al.³⁰ (c) Davis et al.¹⁰² The corner/intersections of the grids represent any possible combination of the chemical shifts in dehydrated and hydrated samples.

Appendix B

List of Publications

B. Hernández, J. Iglesias, G. Morales, M. Paniagua, C. López-Aguado, J. L. García Fierro, P. Wolf,^{*} I. Hermans, J. A. Melero

Influence of Hydrophilicity on the Sn β -Catalyzed Baeyer-Villiger Oxidation of Cyclohexanone with Aqueous Hydrogen Peroxide

ChemCatChem **2016**, doi:10.1002/cctc.201600893.

B. Hernández, J. Iglesias, G. Morales, M. Paniagua, C. López-Aguado, J. L. García Fierro, P. Wolf,^{*} I. Hermans, J. A. Melero

One-pot cascade transformation of xylose into γ -valerolactone (GVL) over bifunctional Brønsted-Lewis Zr-Al-beta zeolite

Green Chemistry **2016**, *18*, 5777-5781.

P. Wolf,^{*} W.-C. Liao,^{*} T. C. Ong,^{*} M. Valla, J. W. Harris, R. Gounder, W. N. P. van der Graaff, E. A. Pidko, E. J. M. Hensen, P. Ferrini, B. Sels, I. Hermans, C. Copéret

Identifying Sn Site Heterogeneities Prevalent in Sn-Beta Zeolites

Helvetica Chimica Acta **2016**, doi:10.1002/hlca.201600234.

P. Wolf,^{*} M. Valla,^{*} F. Núñez-Zarur,^{*} A. Comas-Vives,^{*} A. J. Rossini,^{*} C. Firth, H. Kallas, A. Lesage, L. Emsley, C. Copéret, I. Hermans

Correlating Synthetic Methods, Morphology, Atomic-Level Structure and Catalytic Activity of Sn- β Catalysts

ACS Catalysis **2016**, *6*, 4047-4063. (Chapter 5)

P. Müller, P. Wolf, I. Hermans

Insights into the Complexity of Heterogeneous Liquid-Phase Catalysis: Case Study on the Cyclization of Citronellal

ACS Catalysis **2016**, *6*, 2760-2769.

S. Conrad, R. Verel, C. Hammond, P. Wolf, F. Göttl, I. Hermans

Silica-Grafted Sn^{IV}-Catalysts in Hydrogen-Transfer Reactions

ChemCatChem **2015**, *7*, 3188-3403. (front cover)

P. Wolf,* M. Valla,* A. J. Rossini,* Aleix Comas-Vives,* F. Núñez-Zarur,* B. Malaman, A. Lesage, L. Emsley, C. Copéret, I. Hermans
NMR Signatures of the active sites in Sn- β zeolites
Angew. Chem. Int. Ed. **2014**, *53*, 10179-10183. (Chapter 4)

P. Wolf, C. Hammond, S. Conrad, I. Hermans
Post-Synthetic Preparation of Sn-, Ti-, Zr- β : A Facile Route to Water-Tolerant, Highly Active Lewis Acidic Zeolites
Dalton Trans. **2014**, *43*, 4515-4519. (Chapter 3)

A. N. Parvulescu, U. Müller, N. Vautravers, G. Uhl, I. Hermans, P. Wolf, C. Hammond
A Tin-Containing zeolitic Material Having a BEA Framework Structure
WO 2015/067654 A1.

C. Aellig, F. Jenny, D. Scholz, P. Wolf, I. Giovinazzo, F. Kollhoff, I. Hermans
Combined 1,4-Butanediol Lactonization and Transfer Hydrogenation/Hydrogenolysis of Furfural-Derivatives under Continuous Flow Conditions
Catal. Sci. Technol. **2014**, *4*, 2326-2331.

* these authors contributed equally

Appendix C

Presentations

24th North American Catalysis Society Meeting

Pittsburgh (PA), United States, 2015

Towards the Understanding of the Active Site Distribution in Sn-Beta

P. Wolf, M. Valla, F. Núñez-Zarur, A. Comas-Vives, A. J. Rossini, C. Firth, H. Kallas, A. Lesage, L. Emsley, C. Copéret, I. Hermans

248th ACS National Meeting and Exposition

San Francisco (CA), United States, 2014

Talk: “Progress in the Synthesis of Site-Isolated Lewis Acidic Catalysts”

P. Wolf, M. Valla, A. J. Rossini, Aleix Comas-Vives, F. Núñez-Zarur, B. Malaman, A. Lesage, L. Emsley, C. Copéret, I. Hermans

Advisory Board Meeting – Chemistry Department

Madison (WI), United States, 2014

Poster: “Spectral Signatures of the Active Sites in Sn- β Zeolite”

P. Wolf, M. Valla, A. J. Rossini, Aleix Comas-Vives, F. Núñez-Zarur, Bernard Malaman, A. Lesage, L. Emsley, C. Copéret, I. Hermans

Catalysis Club of Chicago – Spring Symposium

Chicago (IL), United States, 2014

Talk: “Continuous Flow Transfer-hydrogenations for the reductive upgrading of Biomass”

P. Wolf, C. Aellig, I. Hermans

Appendix D

Curriculum Vitae

Name	Patrick Wolf
Date of birth	April 20 th , 1989
Place of birth	Schweinfurt, Bavaria
Nationality	German

Education

2014-2016	External Doctoral Studies under the supervision of Prof. Dr. Ive Hermans and Prof. Dr. Christophe Copéret at the University of Wisconsin-Madison, Madison (WI), United States
2012-2016	Ph. D. under the supervision of Prof. Dr. Ive Hermans and Prof. Dr. Christophe Copéret at ETH Zurich, Zurich, Switzerland
2012	Master Thesis under the supervision of Prof. Dr. Yuriy Román-Leshkov at Massachusetts Institute of Technology (MIT), Cambridge (MA), United States
2011-2012	M. Sc. Studies in Chemical & Bioengineering at ETH Zurich, Zurich, Switzerland
2008-2011	B. Sc. Studies in Chemical & Bioengineering at ETH Zurich, Zurich, Switzerland